



Journal of Science

Volume: 17, Issue: 3, Year: 2021

Contact

Manisa Celal Bayar University
Institute of Natural and Applied Sciences
Campus of Şehit Prof Dr İlhan Varank 45140 Yunussemre – MANİSA, TURKEY
Tel: (00 90) 236 201 27 05
Fax: (00 90) 236 241 21 49
e-mail: cbujos@gmail.com
Web: <https://dergipark.org.tr/tr/pub/cbayarfbe>

“CBU Journal of Science is indexed by ULAKBIM-TUBITAK TR-DIZIN”



ISSN 1305-130X

E-ISSN 1305-1385

CBUJOS is published quarterly at Manisa Celal Bayar University Printing House

“CBU Journal of Science is a refereed scientific journal”



Celal Bayar University Journal of Science

Owner

Manisa Celal Bayar University,

Editors : Assoc. Prof. Dr. Kamil ŞİRİN

Assoc. Prof. Dr.. Emine KEMİKLİOĞLU

Assistant Editor: Assoc. Prof. Dr. Mustafa AKYOL

Layout Editor & Secretary

Dr. İlker Çetin KESKİN

International Scientific Advisory Board

Prof. Dr. Arianit REKA; State University of Tetova, Macedonia

Prof. Dr. Tomasz NIEMIEC; Warsaw University of Life Sciences, Poland

Prof. Dr. Alyani ISMAIL; Universiti Putra, Malaysia

Prof. Dr. Iuliana APRODU; Dunarea de Jos University, Romania

Assoc. Prof. Dr. Johanan Christian PRASANNA; Madras Christian College, South India

Assoc. Prof. Dr. Noureddine ISSAOUI; Université de Monastir, Tunisie.

Assoc. Dr. Edward Albert UECKERMANN; North-West University, South Africa

Assoc. Dr. Zhi-Qiang ZHANG; The University of Auckland, Holland

Assist. Prof. Dr. Young Ki KIM; Pohang University of Science and Technology, South Korea

Assist. Prof. Can BAYRAM; University of Illinois, USA

Assist. Prof. Dr. Mona MIRHEydARI; Rutgers University, USA

Assist. Prof. Dr. Donatella ALBANESE; Università Degli Studi Di Salerno, Italy

Assist. Prof. Dr. Jinghua JIANG; The University of Memphis, USA

Assist. Prof. Dr. Jens OLDELAND; University of Hamburg, Germany

Dr. Cheng CHENG; Apple Inc., USA

Dr. Sajedah AFGHAH; Microsoft Corporation, USA

Dr. Jinghua JIANG; The University of Memphis

National Scientific Advisory Board

Prof. Dr. Mustafa Ersöz; Selçuk University

Prof. Dr. Oğuz Gürsoy; Mehmet Akif University

Prof. Dr. Mehmet Çevik; İzmir Katip Çelebi University

Prof. Dr. Sezgin Çelik; Yıldız Teknik University

Prof. Dr. Osman Dayan; Çanakkale Onsekiz Mart University

Prof. Dr. Serdar İplikçi; Pamukkale University

Prof. Dr. Yasin Üst; Yıldız Teknik University

Prof. Dr. Mahmut Kuş; Konya Teknik University

Prof. Dr. Ertuğ Gundüz; Hacettepe University

Prof. Dr. Tülin Aydemir; Manisa Celal Bayar University

Prof. Dr. Sezai Taşkın; Manisa Celal Bayar University

Prof. Dr. Fatma Şaşmaz Ören; Manisa Celal Bayar University

Assoc. Prof. Dr. Fatih Doğan; Çanakkale Onsekiz Mart University

Assoc. Prof. Dr. Erol Akpınar; Abant İzzet Baysal University

Assoc. Prof. Dr. Yeliz Yıldırım; Ege University

Assoc. Prof. Dr. Serap Derman; Yıldız Teknik University

Assoc. Prof. Dr. Hayati Mamur; Manisa Celal Bayar University

Assoc. Prof. Dr. Fatih Selimefendigil; Manisa Celal Bayar University

Assoc. Prof. Dr. Özlem Çağındı; Manisa Celal Bayar University

Assoc. Prof. Dr. Osman Çulha; Manisa Celal Bayar University

Assoc. Prof. Dr. Ali Demir; Manisa Celal Bayar University

Assoc. Prof. Dr. Ali Konuralp; Manisa Celal Bayar University

Assist. Prof. Dr. Nil Mansuroğlu; Ahi Evran University

Assist. Prof. Dr. Zeynep Çipiloğlu Yıldız; Manisa Celal Bayar University



CBU Journal of Science

Celal Bayar University Journal of Science (CBUJOS) covers scientific studies in the fields of Engineering and Science and publishes accounts of original research articles concerned with all aspects of experimental and theoretical studies. CBU Journal of Science is a refereed scientific journal published four times annually (March, June, September and December) by Institute of Natural and Applied Sciences of Manisa Celal Bayar University. CBU Journal of Science considers the original research articles written in English for evaluation.

CBU Journal of Science is indexed by TUBİTAK ULAKBİM TR-DİZİN, and also is included in DOAJ, Cite Factor, Journal TOCS, Advanced Science Index and OAJI databases. Digital Object Identifier (DOI) number will be assigned for all the articles being published in CBU Journal of Science.

Instructions for Authors and Article Template can be found on the main page of MCBU Institute of Natural and Applied Sciences (<http://fbe.cbu.edu.tr>)





Vol: 17, Issue: 3, Year: 2021

Contents

Research Article




Pages

- Validation and Verification of Cavitation in Microchannels by using an Open Source Computational Tool
DOI: 10.18466/cbayarfbe.828275
Gökçe Özkazanç Güç, Levent Ünlüsoy, E. Yegan Erdem 223-227
- Evaluation of Proficiency Test Results in Tensile Test of Elastomer Materials
DOI: 10.18466/cbayarfbe.884874
Kemal Kuş, Bülent Aydemir 229-233
- Effects of the nickel, copper, silver and tin coating on S235JR, 21NiCrMo2, C45 and 42CrMo4 steels for radiation shielding performance
DOI: 10.18466/cbayarfbe.874287
İdris Karagöz, Erdem Şakar, Murat Türemiş, Mehmet Büyükyıldız 235-244
- Modification of Asphalt Binder with Waste Expanded Polystyrene (EPS) Foam
DOI: 10.18466/cbayarfbe.885696
Kürşat Yıldız, Harun Kınacı, Mert Atakan 245-252
- Internet of Things Technology Based Agricultural Spraying Drone Design for Remote Farming Applications
DOI: 10.18466/cbayarfbe.781368
Cemil Altın, Hasan Ulutaş, Eyyüp Orhan, Orhan Er, Volkan Akdoğan 253-260
- Design and Manufacturing of The Prototype System for Recycling Waste Generated in 3 Dimensional Production to Filaments by Fused Deposition Modeling Method
DOI: 10.780314/cbayarfbe.869473
İlker Ertuna, Uğur Can Topçu, Çağrı Yalçınkaya, Defne Açıkgöz, Ezgi Cırık, Ceren Göde 261-266
- Experimental and response surface methodology investigation of cast material obtained by melting and recycling of chips
DOI: 10.18466/cbayarfbe.898972
Harun Akkuş, Harun Yaka 267-273
- Determination of the Effect of Cooling Rate and Strontium Amount on Eutectic Si Modification Performance of A356 Alloy via Casting Simulation
DOI: 10.801544/cbayarfbe.869010
Batuhan Doğu, Onur Ertuğrul, Uğur Aybarç, Serkan Gündoğdu 275-283
- Synthesis, Spectroscopic Characterization, Crystal Structure and Theoretical Studies on New Organic Single Crystal of 1-(3,5-Difluorophenyl)-3-(2-Nitrophenyl)Urea
DOI: 10.18466/cbayarfbe.887714
Tuğba Güngör, Tuncay Karakurt, Zarife Sibel Şahin 285-295
- Experimental and Theoretical Investigation of a new β -Diketiminat Derivative
DOI: 10.18466/cbayarfbe.825395
İlkay Yıldırım 297-304
- Investigation of the effects on dose calculations of correction-based algorithms in different tissue medium
DOI: 10.18466/cbayarfbe.841547
Serhat Aras 305-311



- On Iteration Method to The Solution of More General Volterra Integral Equation in Two Variables and a Data Dependence Result
DOI: 10.18466/cbayarfbe.837062
Samet Maldar 313-318
- The Effects of Magnetic Iron oxide Nanoparticles (Fe_3O_4) on Some Biological Aspects of *Galleria mellonella* L. (Lepidoptera: Pyralidae)
DOI: 10.18466/cbayarfbe.920637
Ayşe Nazan Eskin, Şahlan Öztürk, Ata Eskin 319-324
- In vitro Micropropagation of Duckweed (*Lemna minor* L.) Plant with Temporary Immersion System Bioreactors
DOI: 10.18466/cbayarfbe.848369
Uğur Sıdal, Zehra Ergönül 325-335

Validation and Verification of Cavitation in Microchannels by using an Open Source Computational Tool

Gökçe Özkazanç Güç¹ , Levent Ünlüsoy² , E. Yegan Erdem^{1,3*} 

¹ Mechanical Engineering Department, Bilkent University, Ankara, Turkey

² Roketsan A.Ş., Ankara, TURKEY

³ National Nanotechnology Research Center (UNAM), Ankara, Turkey

*yeganerdem@bilkent.edu.tr

*Orcid No: 0000-0001-9852-2293

Received: 20 November 2020

Accepted: 26 July 2021

DOI: 10.18466/cbayarfb.828275

Abstract

Cavitation is mostly unwanted in applications due to its unpredictable and distorting effect on fluid flow. On the other hand, its modelling is expensive in terms of time and computational power in general. Regarding this a tendency for using an open source software such as OpenFOAM is emerging as a promising tool for both predicting and analyzing cavity formation. In this study, validation and verification of an OpenFOAM solver is investigated for cavitation in microchannels. Experiments are carried out as well for comparison with computational results. During the experiments the cavity formation was efficiently captured by observing the fluorescent particle flow. Overall, computational and experimental results are compared to investigate the capability of OpenFoam for the chosen conditions.

Keywords: Cavitation, Computational Fluid Dynamics, Microchannels, Open Source,

1. Introduction

Cavitation, as a chaotic phenomenon and is generally defined as the phase change of the fluid flow by nucleation, growth, and collapse of a vapor bubble in regions where pressure drop is rapid and high [1]. Its damaging effects are undesired in most of the applications that include high speed fluid flow such as nozzles [2], hydraulic machinery [3] and diesel engines [4].

On the other hand, cavity formation within a microchannel can have several applications in particle and cell manipulation due to the vortex formation around them. Some studies in literature focused on forming microvortices within microfluidic channels by utilizing a cavity-like channel geometry for such applications [5-9]. For instance, Kamalakshakurup showed the controlled formation of microvortices to trap microparticles [5], Shen et al. studied the circulating particles in microvortices [6], Kim et al. utilized the formation of vortices for rapid mixing of reagents in production of hybrid nanoparticles [7], Shen et al. showed trapping of particles by using microcavities within a microchannel [8, 9]. Formation of cavity by controlling flow can also be useful for these

studies which would eliminate the need for complex geometries.

Cavitating flow in microchannels has been investigated by researchers; some of this work was experimental [10, 11]; while most of them were focused on the numerical modelling of this phenomenon [12-14]. Rooze et al, studied pressure gradients in $100 \times 100 \mu\text{m}^2$ channels with cavitation by using computational fluid dynamics software [12]; Egerer et al. performed large-eddy simulations for studying cavity formation in a throttle geometry where turbulence behavior is analyzed and compared with experimental work [13], and Ghorbani et al. studied cavitating nozzle flow in microchannels with high Reynolds numbers by numerical methods [14], Osterman et al. investigated the effect of channel aspect ratio on the formation of cavities by both numerically and experimentally where they used COMSOL Multiphysics software [15].

However, modeling of cavitation is expensive in terms of both computational power and time. To minimize this cost, usage of an Open-Source software is emerging [16, 18]. OpenFOAM, is becoming one of the most preferred tools due to its compatibility with C++ language and user-friendly structure [19].

Different than the studies in literature, this work uses the OpenFOAM solver *interPhaseChangeFOAM* to examine cavity formation and verification in microchannels. Its findings can also be extended for applications in microchannels as well as in industry where a quick and low-cost analysis is required.

2. Materials and Methods

2.1 Computational Model

For solving the cavitating flow, the geometry shown in Figure 1 is used which is a modification of the former geometries studied in the literature [20-21]. Solution domain is given in Figure 1 with its dimensions. Microchannels with this geometry are fabricated for obtaining experimental results used for comparison.

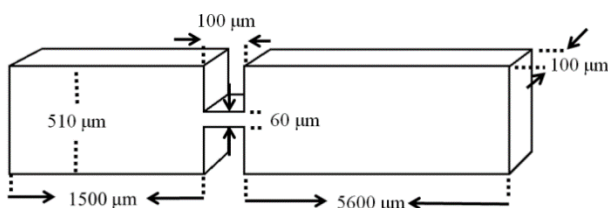


Figure 1. Geometry used for experimental and computational studies.

Mesh is generated with using OpenFOAM's *blockMesh* and *refineMesh* utilities. Since the solution of the wall is only of interest in throttle section, first layer thickness is calculated, and cells are generated regarding the minimum thickness; then refinement levels are used for solving the model. There are around $360e^3$ cells at the final mesh. Generated mesh is shown in Figure 2.

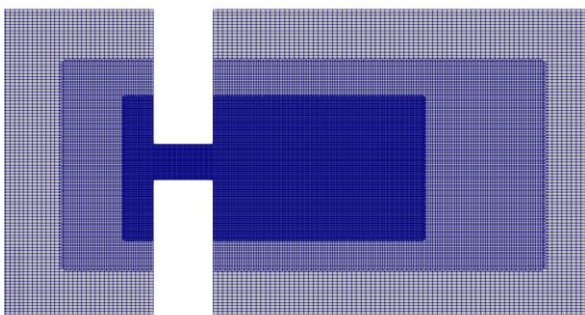


Figure 2. Mesh generated for computational solution.

Among the OpenFoam's several different solvers *interPhaseChangeFoam* is chosen for this case with using total pressure as inlet, static pressure as outlet and no slip as wall boundary conditions.

2.2 Experimental Set-Up and Fabrication

Experimental set-up used for observing the cavitation phenomena includes a pressure pump to maintain a constant fluid flow and a high-speed camera for capturing the images of flow. The schematic of the set-up is shown in Figure 3.

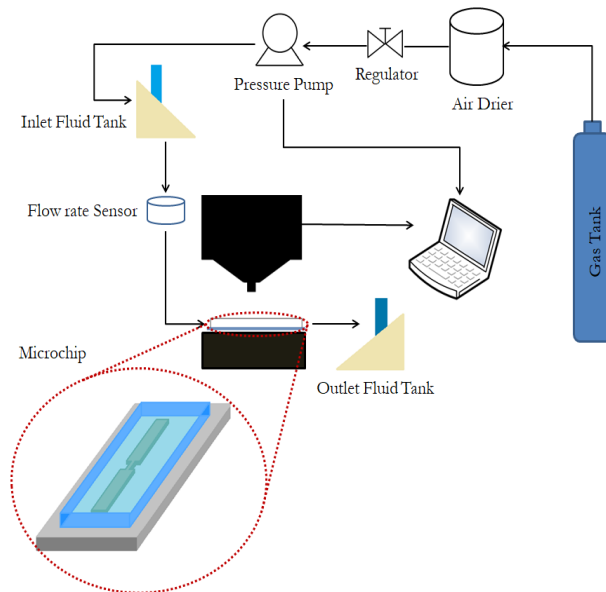


Figure 3. Schematic of the experimental set-up.

Microfluidic devices were fabricated with a conventional soft-lithography technique where initially a master mold is made in clean room by using negative photoresist SU-8 and later pouring polydimethylsiloxane (PDMS) into this mold and finally curing to obtain the channel geometry. At the last step, these channels are bonded to a glass slide for encapsulation. Figure 4 shows the fabricated PDMS channel under the optical microscope.

3. Results and Discussion

During the experiments, high speed camera was used to capture the fluid flow at a rate of 8-16 frames per second. Flow was maintained by supplying an input pressure at the channel entrance with a pressure pump where the value was varied from 1 bar to 6.5 bars. It is seen that for lower input pressure values, flow does not encounter any phase change, therefore cavity does not form. Representation of these flows are given in Figure 4 for 3 bars. It is seen that these flows have a regular steady state flow behavior.

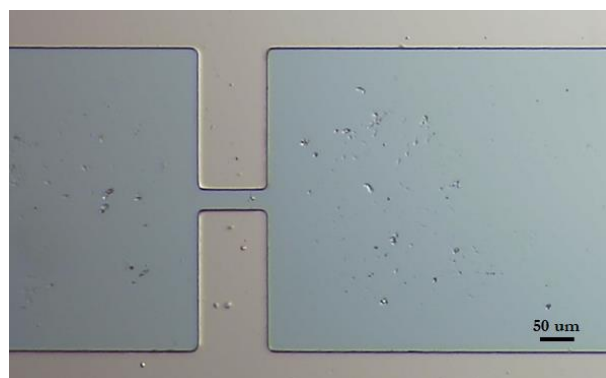


Figure 4. Steady flow with 3 bars input pressure without cavity formation.

As the input pressure is increased however, flow characteristics change. For example, for higher pressure values (4-5 bars), bubbles begin to occur and fade away. The moment at which a bubble occurs is captured and marked in Figure 5.

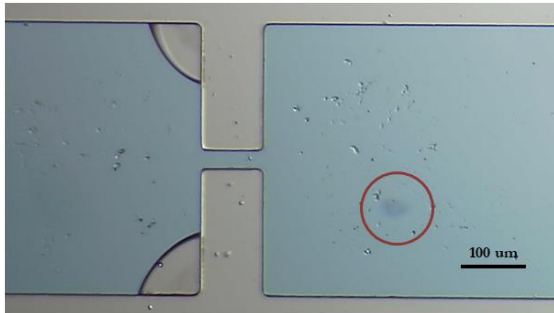
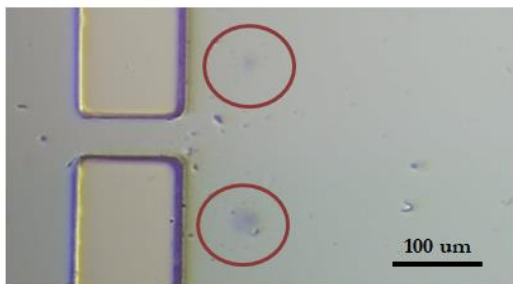
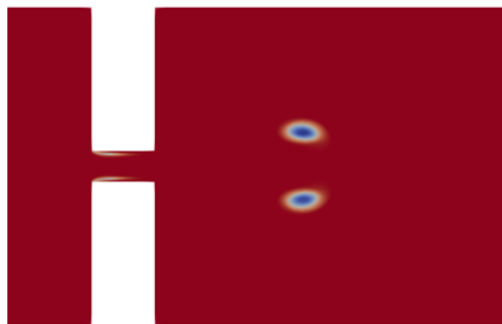


Figure 5. Vapor bubble occurrence at 4 bars.

For 5-6 bars at the inlet, number of bubbles double. Same behavior is also observed in computational results. Figure 6a shows the experimental results while Figure 6b shows the CFD results for multiple cavity formation.



(a)



(b)

Figure 6. Comparison of simulation and experimental results. (a) Cavity formation observed during an experiment, (b) cavity formation observed in computational work.

For the higher velocities, formation of bubbles increases since pressure drops to lower values however since the flow is highly chaotic bubbles occur and disappear suddenly. Same pattern is also observed in the simulation results. An image obtained during an

experiment with high velocity is given in Figure 7. From both experimental and the simulation visuals, it is seen that the flow forms a symmetrical elliptic pattern, which shows that the model is solving the flow field correctly and the given boundary conditions are satisfying the experimental conditions.

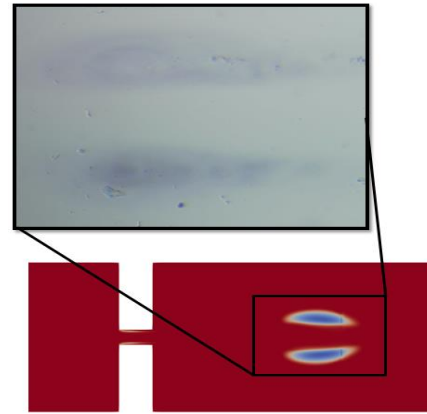


Figure 7. Low-density zones observed in experiment and simulation.

Cavitation behavior is also investigated using fluorescent latex beads, which are yellow-green carboxylate-modified polystyrene; this clarified the formation of cavity and enabled a better comparison with simulation results. With this way streamline is clearly observed unlike regular high speed camera visuals. This method has shown better performance in visualizing the experiments than any previously suggested methods in literature.

In this manner, from Figure 8a, the region of vortex is clearly seen at the initial time steps and the movement of the vortex region is shown in Figure 8b. The cavity formation is observed with a darker region, where there is no liquid flow and therefore no fluorescent bead.

4. Conclusion

In this study, both simulations and experiments were conducted under the same boundary conditions to observe cavity formation in a microfluidic channel. The experimental set-up consisted of a pressure pump, a microfluidic chip and a high-speed camera.

The visualization of flow was facilitated by using fluorescent particles dissolved in water; which presents a novel approach for capturing the low-pressure zones in the flow.

When the experiments were compared with simulations, it is seen that there is a great resemblance between the two results. However, since cavitation is a chaotic flow, these similarities were only captured at the regions closer to the formation zone. Therefore, as a future work, by adding local pressure and velocity sensors,

numerical data for these low-pressure regions can be obtained in addition to the image-based comparisons presented in this paper.

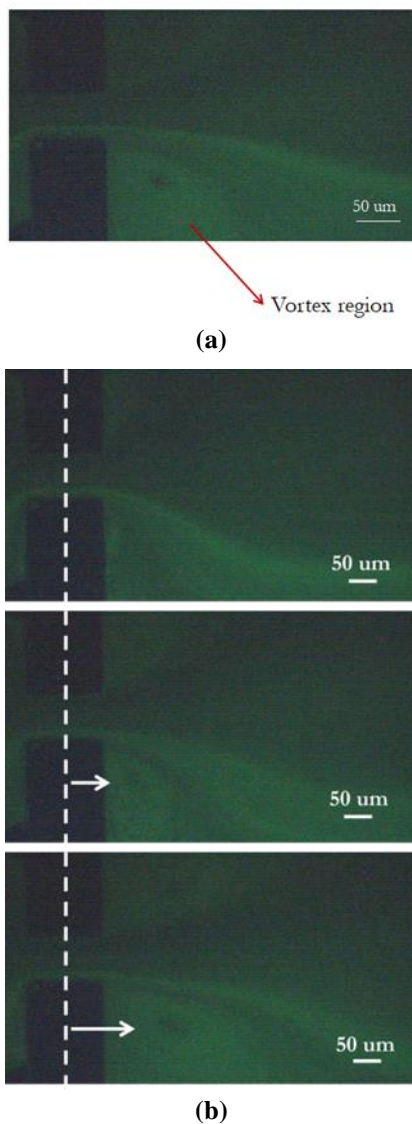


Figure 8. (a) Vortex region and (b) its movement with fluid flow.

Acknowledgement

Authors acknowledge the support from the Researcher Training Program for Defense Industry Program (SAYP) supported by the Presidency of Defense Industries in cooperation with Roketsan AŞ.

Author's Contributions

Gökçe Özkazanç Güç: Fabricated the microreactor, performed the experimental and computational work. Helped in the manuscript preparation.

Levent Ünlüsoy: Advised the research part on simulations and helped the formation of the computational model. Reviewed the final versions of the manuscript.

E. Yegan Erdem: Designed the microreactor and the experimental steps. Prepared the manuscript and the revised version.

Ethics

There are no ethical issues after the publication of this manuscript.

References

1. Brennen, C. E. Cavitation and bubble dynamics: Cambridge University Press, 2014; pp. 6.
2. Tamaki, N., Shimizu, M., Nishida, K., Hiroyasu, H. 1998. Effects of cavitation and internal flow on atomization of a liquid jet. *Atomization and Sprays*; 8 (2): 247-254.
3. Arndt, R. E. Cavitation in fluid machinery and hydraulic structures. 1981. *Annual Review of Fluid Mechanics*; 13(1): 273-326.
4. Aoyama, T., Suzuki, S., Kawamoto, A., Noda, T., Ozasa, T., Kato, T., Ito, T. 2007. Preventive design and analysis of cavitation noise on diesel engine. *R&D Review of Toyota CRDL*; 40(1): 36-42.
5. Kamalakshakurup, G., Aghaamoo, M., Ataei, M., Zhang, N., Lee, A. P. 2021. Shear-dependent microvortices in liquid-liquid flow-focusing geometry: A theoretical, numerical, and experimental study. *Physics of Fluids*; 33: :032016.
6. Shen, F., Li, Z., Xue, S., Li, M., Liu, Z. 2021. Particle recirculating orbits within microvortices using microfluidics. *J. Phys. D: Appl. Phys.*; 54: 025401.
7. Kim, Y. T., Chung, B. L., Ma, M., Mulder, W. J. M., Fayad, Z. A., Farokhzad, O. C., Langer, R. 2012. Mass production and size control of lipid-polymer hybrid nanoparticles through controlled microvortices. *Nano Letters*; 12(7): 3587-3591.
8. Shen, F., Xu, M., Wang, Z., Liu, Z. M. 2017. Single-particle trapping, orbiting, and rotating in a microcavity using microfluidics. *Applied Physics Express*; 10(9): 097301.
9. Shen, F., Xue, S., Zhou, B., Xu, M., Xiao, P., Liu, Z. 2018. Evolution of single-particle recirculating orbits within a hydrodynamic microvortex. *J. Micromech. Microeng.*; vol. 28(8): 085018.
10. Ayela, F., Cherief, W., Colombet, D., Ledoux, G., Martini, M., Mossaz, S., Podbevsek, D., Qiu, X., Tillement, O. 2017. Hydrodynamic cavitation through "labs on a chip": from fundamentals to applications. *Oil Gas Sci. Technol.*; 72(19): 1-12.
11. Ghorbani, M., Chen, H., Villanueva, L. G., Grishenkov, D., Koşar, A. 2018. Intensifying cavitating flows in microfluidic devices with poly(vinyl alcohol) (PVA) microbubbles. *Physics of Fluids*, 30: 102001.
12. Rooze, J., André, M., van der Gulik, G.-J. S., Fernandez-Rivas, D., Gardeniers, G. E., Rebrov, E. V., Schouten, J. C., Keurentjes, J. T. F. 2012. Hydrodynamic cavitation in micro channels with channel sizes of 100 and 750 micrometers. *Microfluid. Nanofluid.*; 12: 499-508.
13. Egerer, C. P., Hickel, S., Schmidt, S. J., Adams, N. A. 2014. Large-eddy simulation of turbulent cavitating flow in a micro channel. *Phys. of Fluids*; 26(8): 085102.
14. Ghorbani, M., Yildiz, M., Gozuacik, D., Kosar, A. 2016. Cavitating nozzle flows in micro- and minichannels under the

- effect of turbulence. *Journal of Mechanical Science and Technology*; 30(6): 2565-2581.
15. Osterman, N., Derganc, J., Svenšek, D. 2016. Formation of vortices in long microcavities at low Reynolds number. *Microfluid Nanofluid*; 20(33): 1-10.
 16. Cazzoli, G. Falfari, S., Bianchi, G. M., Forte, C., Catellani, C. 2016. Assessment of the cavitation models implemented in openfoam® under di-like conditions. *Energy Procedia*; 101: 638-645.
 17. Asnaghi, A., Feymark, A. Bensow, R. E. Numerical simulation of cavitating flows using openfoam, proceedings of the 18th Numerical Towing Tank Symposium, Cortona, Italy, 2015.
 18. Zeng, Q., Gonzales-Avila, S. R., Ohl, C.-D. 2020. Splitting and jetting of cavitation bubbles in thin gaps. *J. Fluid Mech.*: 896: A28.
 19. Weller, H. G., Tabor, G., Jasak, H., Fureby, C. 1998. A tensorial approach to computational continuum mechanics using object-oriented techniques. *Computers in Physics*; 12 (6): 620-631.
 20. Medrano, M., Zermatten, P., Pellone, C., Franc, J.-P., Ayela, F. 2011. Hydrodynamic cavitation in microsystems. I. Experiments with deionized water and nanofluids. *Physics of Fluids*, 23(12): 127103.
 21. Medrano, M., Pellone, C., Zermatten, P., Ayela, F. 2012. Hydrodynamic cavitation in microsystems. II. Simulations and optical observations. *Physics of Fluids*; 24(4): 047101.

Evaluation of Proficiency Test Results in Tensile Test of Elastomer Materials

Kemal Kuş^{1*} , Bülent Aydemir² 

¹ VESTEL Beyaz Eşya Tic.San.A.Ş., Keçili/Şehzadeler / MANİSA, TÜRKİYE

² TÜBİTAK Ulusal Metroloji Enstitüsü (TÜBİTAK UME), Gebze/Kocaeli, TÜRKİYE

*kemal.kus@vestel.com.tr

*Orcid: 0000-0001-8189-0196

Received: 22 February 2021

Accepted: 6 September 2021

DOI: 10.18466/cbayarfbe.884874

Abstract

Testing laboratories need to verify their test procedures and testing capability for reliable results. In this study, equivalent samples are prepared with elastomer materials. This paper has described the evaluation of tensile test results of elastomer material specimens tested according to ISO 37 and DIN 53504 standards. The proficiency test conditions, test equipment and the results were evaluated according to TS EN ISO/IEC 17043 standard. Finally, the Z scores of the participant laboratories were presented.

Keywords: Proficiency test (PT), plastic material, tensile test, ISO 37, DIN 53504, EN ISO/IEC 17043

1. Introduction

General conditions for the competence of test and calibration laboratories TS EN ISO / IEC 17025 standard has been defined. It includes the evaluation, approval and subsequent inspection of the technical competence of the laboratory according to the necessary criteria by an internationally recognized and authorized organization to ensure that the tests and analyzes are carried out with TS EN ISO / IEC 17025 accreditation [1].

A proficiency test is defined as one of the accreditation requirements. Interlaboratory comparisons and proficiency tests (PT) are important tools in assessing the technical competence of calibration and experimental laboratories. This issue is specified in TS EN ISO / IEC 17025, TS EN ISO / IEC 17043 and ASTM E 1301 standards [1-3] and TURKAK document [4]. It is a requirement of TURKAK that accredited laboratories or laboratories applying for accreditation participate in the PT program and / or inter-laboratory comparisons regarding the measurement sizes within the scope of accreditation and achieve successful results.

In this study, the proficiency test was carried out in the field of tensile testing of elastomer materials in accordance with ISO 37 and DIN 53504 [5,6] standards. Participating laboratories have carried out the required experiments using their material testing machines. The

measurement results were sent to the Vestel laboratory in the required format, and Vestel prepared the proficiency test report by evaluating the results from the laboratories.

In this study, the results obtained during the proficiency test were discussed, in particular, an analysis was applied in accordance with the TS EN ISO / IEC 17043 standard to evaluate the differences between the average values of test results from different laboratories.

2. Technical Protocol

First of all, proficiency test technical protocol was prepared and sent to all participating laboratories. The technical protocol is prepared to include the preparation of test samples, distribution to laboratories, timetable for tests, test reports and test requirements according to ILAC P9 and ISO/IEC Guide 43-2 [7,8].

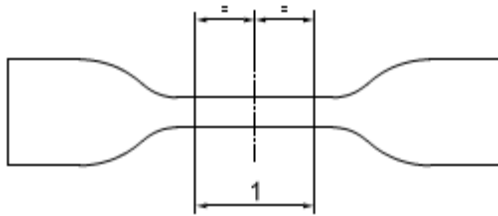
2.1. Participants

Three different test laboratories in Turkey participated in this proficiency test. The proficiency test was started on 15.06.2020 and completed on 29.06.2020. Measurements were completed in accordance with the planned time schedule.

2.2. Samples and Test Conditions

The sample materials are the standard raw material used in the washing machine gaskets obtained from rubber

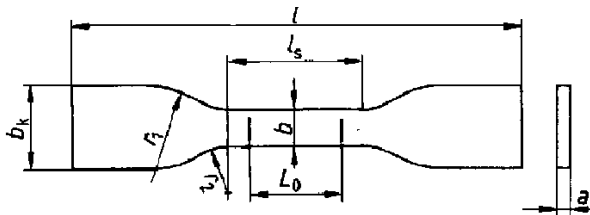
known as EPDM-01 A in the market. The samples were prepared from elastomer material with the same chemical composition and dimensions in accordance with ISO 37 Type-2 and DIN 53504 S2 (Figures 1a and 1b). The samples were cut by stamping using the appropriate cutting die in the standard. 5 samples were sent to each participant by numbering appropriately. After the prepared samples are transferred to the relevant laboratory, the laboratory has been made to test as soon as possible. The parameters given in ISO 37 and DIN 53504 standards were used for the necessary conditions during the proficiency tests. In the tests, the elongation measurements were obtained from the values obtained from the moving table of the machine and the stress values were obtained by dividing the values obtained from the force measuring device on the machine by the test sample cross-sectional area. The test speed was used as 500 mm/min. The grip to grip distance was used taken 50 mm.



Test sample type	Type 1	Type 1A	Type 2	Type 3	Type 4
Test sample length (1) (mm)	25 ± 0,5	20 ± 0,5*	20 ± 0,5	10 ± 0,5	10 ± 0,5

*The length of the test should not exceed the length of the narrow part of the test piece. (Dimension of C in Table 2).

Figure 1a. Tensile test specimen type - Type 2 (ISO 37)



Test sample type	S 1	S 2	S 3	S 3A
Dimension (mm)				
length, l	115	75	35	50
b _k	25	12,5	6	8,5
l _s	33	25	12	16
b	6	4	2	4
r ₁	25	12,5	3	10
r ₂	14	8	3	7,5
a	2 ± 0,2	2 ± 0,2	1 ± 0,1	2 ± 0,2
L ₀	25	20	10	10

Figure 1b. Tensile test specimen type - S2 (DIN 53504)



Figure. 1c. Tensile test device photo, sample, extensometer and force measuring device

Laboratories that have the infrastructure and that are or will be accredited by TURKAK participated in the proficiency test. In order to keep their identities confidential, the results are given with the lab code

3. Results and Discussion

After completing the tests by each laboratory, the test reports were sent to the Vestel laboratory. Vestel laboratory evaluated all test reports according to TS EN ISO / IEC 17043 and ISO 13528 [9]. standards. In given figures and tables, each laboratory is represented with a letter as A, B, C. The measurement results are prepared using documents from the laboratories participating in the proficiency test and the distributions between the values declared by the participants are given in the tables below. In addition, statistical data and results were created in accordance with the requirements of the TS EN ISO / IEC 17043 standard. Homogeneity and stability tests were carried out for the samples according to ISO 5725-1 ,ISO 5725-2 and ISO 5725-4 [10,11,12] standarts. However, the details are not given in this study.

Measurement results of participating laboratories in accordance with the ILAC-P10 [13] policy; calculated according to the following formula specified in the standard of TS EN ISO / IEC 17043.

Z score is taken as an assessment method of the evaluated results. The Z score is calculated according to below equation:

$$z = \frac{x - X}{\sigma} \quad (3.1)$$

X : Reference value
 x : Participating in the laboratory result
 σ : Standard deviation for proficiency testing evaluation

Criteria for performance evaluation should be established after taking into account whether the performance measure involves certain features. The features of z scores for performance evaluation are as follows;

| z | < 2.0 shows adequate performance and does not generate a warning signal.

2.0 < | z | < 3.0 shows questionable performance and generates a warning signal, the problem should be investigated.

| z | > 3.0 shows poor performance and corrective action should be implemented.

The robust test method was used to determine the assigned value. After the proficiency test program was completed, the robust method was applied statistically to the results obtained. While applying the method, regardless of the value, the results were not eliminated and used as they were, but the assigned value was determined by reducing the effect of the extreme values with the help of the method. The following steps were followed during the implementation process. The p pieces of data (delivered results) belonging to the participants are listed in ascending order from smallest to largest as follows:

$$x_1, x_2, \dots, x_i, \dots, x_{p-1}, x_p$$

The robust mean (x*) and robust standard deviation (s*) premise values of these data are calculated as follows:

$x^* = xi$ median (median) of the data (i = 1,2,... p) The median of the values

$$s^* = 1,483 (| xi - x^* | (i = 1,2,... p))$$

After these preliminary values are calculated, the robust mean (x*) and robust standard deviation (s*) increased values are calculated using the following formulas:

$\delta = 1.5 s^*$ is calculated and using these values, xi^* values are calculated again for each xi (i = 1,2,... p) value as follows::

$$x_i^* = \begin{cases} x^* - \delta, & \text{if } x_i < x^* - \delta \\ x^* + \delta, & \text{if } x_i > x^* + \delta \\ x_i, & \text{or} \end{cases}$$

Using these new values, the new robust mean (x*) and robust standard deviation (s*) are calculated as follows:

$$x^* = \sum x_i^* / p \quad (3.2)$$

$$s^* = 1,134 \sqrt{\sum (x_i^* - x^*)^2 / (p - 1)} \quad (3.3)$$

For deviating values, after making the necessary corrections according to the above evaluation process, new mean (x*) and standard deviation (s*) values are calculated. The x* and s* values are repeated until no correction is required. The correction process may need to be repeated several times. The repetition process is continued until the 3rd digit after the x* and s* comma remains constant. Thus, deviating values are corrected and included within the acceptance range. These last determined values are followed by an iterative calculation method until they converge, and the third significant figure in both values is considered to have converged as soon as there is no change from one iteration to the other. After these calculations, the last average value that is not corrected is accepted as the assigned value.

Table 1. Tensile strength values participant results

Lab Code	σ_{max} Values (MPa)				
	1	2	3	4	5
A	6,90	8,00	8,40	8,60	8,70
B	8,33	8,17	8,50	8,95	9,58
C	8,30	7,50	7,80	8,10	8,30

Table 2. Performance values of participants for tensile strength

Lab. Code	Mean Value	σ_{max} Values (MPa)		Z-Score
		x*	s*	
A	8,12	8,09	0,283	0,11
B	8,71	0	9	2,18
C	8,00			-0,32

Table 3. Elongation values at break participant results

Lab Code	ϵ_R Values (%)				
	1	2	3	4	5
A	513	536	563	564	565
B	678	630	672	704	712
C	568	586	590	595	601

Table 4. Performance values of participants for elongation at break

ϵ_R Values (%)				
Lab. Code	Mean Value	x^*	s^*	Z-Score
A	548,2	592,7	52,039	-0,86
B	679,2			1,66
C	588,0			-0,09

Table 5. 100% modulus values participant results

σ_{100} Values (MPa)					
Lab Code	1	2	3	4	5
A	2,00	2,00	2,10	2,10	2,10
B	1,81	1,76	1,79	1,86	1,88
C	2,30	2,10	2,10	2,20	2,20

Table 6. Performance values of participants for 100% modulus

σ_{100} Values (MPa)				
Lab. Code	Mean Value	x^*	s^*	Z-Score
A	2,06	2,04	0,148	0,14
B	1,82			-1,49
C	2,20			0,95

Table 7. 300% modulus values participant results

σ_{300} Values (MPa)					
Lab Code	1	2	3	4	5
A	3,60	3,70	3,70	3,70	3,70
B	3,19	3,07	3,12	3,18	3,23
C	4,00	3,80	3,80	3,90	3,90

Table 8. Performance values of participants for 300% modulus

σ_{300} Values (MPa)				
Lab. Code	Mean Value	x^*	s^*	Z-Score
A	3,68	3,73	0,305	-0,16
B	3,16			-1,87
C	3,88			0,49

4. Evaluation of Performance

Performance evaluation is based on the following performance criteria.

1) $|z| < 2.0$ shows adequate performance and does not generate a warning signal. $2.0 < |z| < 3.0$ shows questionable performance and generates a warning signal, the problem should be investigated. $|z| > 3.0$ underperforms and generates a signal of action and corrective action should be implemented. The

differences between the participants are given in the result section of the participants.

2) In the case of Z Score warning signal and activity signal, possible sources of error are given below.

- the test equipment has not been calibrated.
- the test equipment is not calibrated within its operating range,
- the test equipment did not carry out intermediate checks
- Test technical person is not getting enough education
- used a different method as a test method.

3) If the Z Score value is greater than 10, it makes it impossible to evaluate the results and interpret the performance. For this reason, participant values with a Z-Score value greater than 10 were not included in the calculations.

As a result of the evaluation of the Z score, the tensile strength (σ_{max}) value of Lab B was found to be questionable as $2 < z < 3$. This can often be caused by test equipment, test personnel, and test method differences. According to the results of this study, Lab B personnel should examine these parameters that affect the results in detail and determine the cause of the error. After the conditions that created the error are eliminated, Lab B should join the proficiency test again and get a successful result.

5. Conclusion

The laboratories, one of which is accredited by TURKAK and the other two of which will be accredited with existing infrastructure, participated in the proficiency test in order to perform the test. The experiments were carried out in accordance with the schedule. Based on the results obtained from the laboratories, this final report was prepared by the Vestel Washing Machine Incoming Quality laboratory.

As a result of the evaluation of the Z score, only the tensile strength (σ_{max}) value of the Lab B would be questionable; It has been determined that the proficiency test measurements of all laboratories in the parameters of the tensile strength (σ_{max}), elongation at break (ϵ_R), 100% modulus and 300% modulus are as " $z < 2$ sufficient = successful"

In order to verify the testing capability of the test laboratories, the proficiency tests are very important for the assessment of the tensile test measurement capabilities of all laboratories and they should be repeated periodically.

Table 9. Overall Z score assessment

Z-Score	$ z < 2$		$2 < z < 3$		$ z \geq 3$	
	Num.of Lab	%	Num.of Lab	%	Num.of Lab	%
σ_{max}	3	75	1	25		
ϵ_R	4	100				
σ_{100}	4	100				
σ_{300}	4	100				

determination of the trueness of a standard measurement method, 2020.

13. ILAC P10 , ILAC Policy on Metrological Traceability of Measurement Results ;2020.

Author's Contributions

Kemal Kuş: Drafted and wrote the manuscript, performed the experiment and result analysis.

Bulent Aydemir: Assisted in analytical analysis on the structure, supervised the experiment's progress, result interpretation and helped in manuscript preparation.

Ethics

There are no ethical issues after the publication of this manuscript.

References

1. TS EN ISO/IEC 17025, Deney ve Kalibrasyon Laboratuvarlarının Yeterliliği İçin Genel Şartlar, TSE, 2017.
2. TS EN ISO/IEC 17043: 2013, Uygunluk değerlendirmesi - Yeterlilik deneyi için genel kurallar, TSE, 2017.
3. ASTM E1301, Standard Guide for Proficiency Testing by Interlaboratory Comparisons ,1995.
4. P704, TURKAK Yeterlilik Deneyleri ve Laboratuvarlararası Karşılaştırma Programları Prosedürü, Rev 10, 2019.
5. ISO 37, Rubber, vulcanized or thermoplastic - Determination of tensile stress-strain properties, International Organization for Standardization, 2017.
6. DIN 53504, Testing of rubber - Determination of tensile strength at break, tensile stress at yield, elongation at break and stress values in a tensile test, 2017.
7. ILAC P9 , Policy for Participation in Proficiency Testing Activities; 2014
8. ISO/IEC Guide 43-2 , Proficiency testing by interlaboratory comparisons — Part 2: Selection and use of proficiency testing schemes by laboratory accreditation bodies; ISO,1997.
9. ISO 13528, Statistical methods for use in proficiency testing by interlaboratory comparison, International Organization for Standardization, 2015.
10. ISO 5725-1; Accuracy (trueness and precision) of measurement methods and results — Part 1: General principles and definitions, 1994
11. ISO 5725-2, Accuracy (trueness and precision) of measurement methods and results — Part 2: Basic method for the determination of repeatability and reproducibility of a standard measurement method, 2019
12. ISO 5725-4, Accuracy (trueness and precision) of measurement methods and results — Part 4: Basic methods for the

Effects of the nickel, copper, silver and tin coating on S235JR, 21NiCrMo2, C45 and 42CrMo4 steels for radiation shielding performance

İdris Karagöz¹, Erdem Şakar², Murat Türemiş^{3*}, Mehmet Büyükyıldız³

¹Faculty of Engineering, Department of Polymer Materials Engineering, Yalova University, Yalova, Turkey

²Faculty of Science, Department of Physics, Ataturk University, 25240 Erzurum, Turkey

³Faculty of Engineering and Natural Sciences, Department of Physics, Bursa Technical University, Bursa, Turkey

* muratturemis@hotmail.com

*Orcid: 0000-0001-8849-4364

Received: 4 February 2021

Accepted: 11 August 2021

DOI: 10.18466/cbayarfbe.874287

Abstract

In this study, S235JR (1.0037), 21NiCrMo2 (1.6523), C45 (1.0503), 42CrMo4 (1.7225) steels were coated with nickel, copper, silver, and tin. Then, the radiation shielding performances of the uncoated and coated steels were investigated. The steels were firstly designed by the coating processes via electrolytic plating method on behalf of Ni, Cu, Ag and Sn metals. The samples were then irradiated by radioactive sources for transmission of the gamma rays at photon energies in the range 81–383 keV photon energies to measure linear and mass attenuation coefficients (LAC- μ , MAC- μ/ρ) of the pure and coated steels by Ni, Cu, Ag and Sn. Half and tenth value of layers (HVL and TVL) of investigated materials were then calculated at the same studied photon energies. The materials were compared with each other as well as with some shielding concretes in terms of mean free paths (MFP) wherever possible. The coated steels were found to be better shielding materials than the concretes due to lower MFP values they had, and they showed also better shielding than reference materials up to 35.31% relative difference in MFP. It was concluded that coating processes improved the shielding properties of the steels.

Keywords: Coating, radiation shielding, steel

1. Introduction

The steels are generally known as iron-carbon alloys, have different types based on iron alloys on behalf of mechanical, physical, and chemical properties required to use. They are widely utilized in various areas such as engineering, security systems in military, public and private buildings, nuclear power plants, shipbuilding, structural materials etc. due to their well physical and mechanical quantities. On the other hand, with the increasing use of the X- and/or gamma rays in different fields such as nuclear plants, medical facilities and laboratories, it is frequently required the new types of materials against the hazardous radiations. For this aim, we can use the concretes, glasses, heavy metals, different steels etc. The resistance of steels to radiation damage gains importance especially when their strength, chemical composition, resistance to corrosion, weldability and ductility properties are taken into account [1,2].

Some steels have been generally investigated in some X- and/or gamma ray energies for shielding applications in the literature. And the studies have experimental and/or theoretical values and can show radiation shielding properties of the materials. They can also explain linear attenuation coefficient (cm^{-1} , μ , LAC), mass attenuation coefficient ($\text{cm}^2.\text{gr}^{-1}$, μ_m , MAC), mean free path (cm, MFP), half values of layer (cm, HVL), tenth values of layer (cm, TVL), effective atomic number (Z_{eff}), effective electron density (N_{eff}) and buildup factors for steels [3-14]. Alım et al. [15] have recently determined radiation parameters of AISI-coded stainless steels (Part 1) both experimentally and theoretically at different photon energies. And AISI 300 austenitic stainless-steel series containing Ni have been found superior when compared to the other materials in the study. Gamma charged particle and fast neutron interactions of AISI-302, 304, 321 and 430 stainless steels have been calculated and evaluated in terms of shielding performance [16]. And authors said that

studied steels had excellent shielding properties than shielding concretes.

It is considered that materials such as 1.0037 (S235JR), 1.6523 (21NiCrMo2), 1.0503 (C45), 1.7225 (42CrMo4) steels, which are frequently used in machine industry and structural elements in the industry, can be used in the production of reactor components or control equipment when their chemical contents are taken into account. But the surface quality, corrosion resistance, machinability and weldability of steel materials are important in applications or usage because they can affect the physical properties of the materials [17,18]. However, the fact that the corrosion resistance of these materials is not as well as stainless steels constitutes a disadvantage [19]. The corrosion resistance of steels can be increased by the coating method applied for purposes such as adding aesthetic properties to materials, increasing the lifetime of materials by increasing their surface hardness and providing abrasion resistance, and conductivity. Metal coating methods or designs that are commonly used for this purpose in the industry are zinc coating, TiN coating, silver coating, nickel coating, and copper coating methods [20]. These operations can change or improve some properties of the materials. So, some physical properties of the materials can be changed after coating, and it should be important to determine these possible changes in the materials for applications. But radiation shielding capability or effectiveness of materials after coating processes have not been taken into consideration in literature as far as is determined. Whereas radiation shielding capabilities of the materials may be changed, even improved after coating processes via useful designs. This is the motivation of the present study. In the present study, 1.0037 (S235JR), 1.6523 (21NiCrMo2), 1.0503 (C45), 1.7225 (42CrMo4) steels were coated with Ni, Cu, Ag and Sn to investigate possible developments of the coatings on radiation shielding properties.

2. Materials and Methods

2.1. Sample preparation

The prepared samples were plated by the electrolytic plating method and chemical compositions and formulas of the samples were given at Table 1. In general, the sequential steps presented in Figure 1 were followed in all coating processes. In the copper plating process, the samples, which were first subjected to the pre-degreasing process, were etched with acid using 30% HCL and 1% inhibitor after washing. The samples that were washed after etching were subjected to 5% degreasing salt, cathodic 4-8 A/dm² and electrolytic degreasing for 3 minutes. The copper plating process was performed for 10 minutes using 60 °C, 2-3 Volt, 0.5-1 A/dm² plating parameters. The samples, which were washed again for 10 seconds after the neutralization process in 10% H₂SO₄ solution, were dried with hot air.

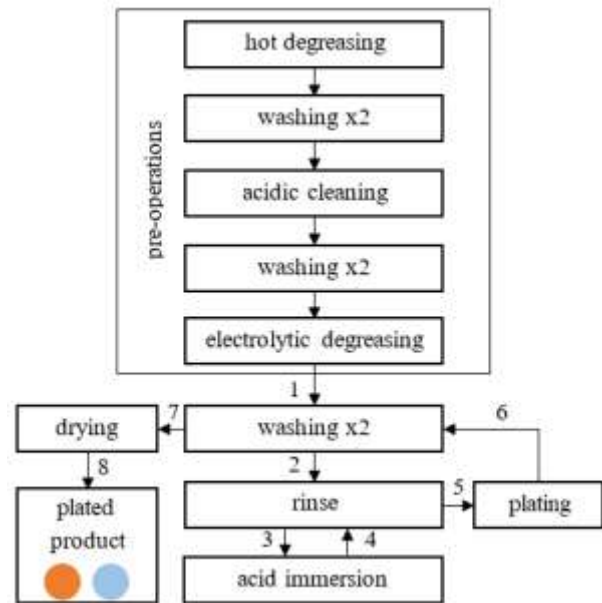


Figure 1. Followed in all coating processes.

The samples subjected to the polishing process in the silver-plating process were cleaned using hot mechanical lubricants. The cleaned samples were subjected to the oxide removal process in the solution containing 100 gr/l NaCN. After the oxide removal process, 5% degreasing salt, cathodic 4-8 A/dm² and electrolytic degreasing for 3 minutes were applied. The washed samples were subjected to the neutralization process for 20 seconds in the solution containing 100 gr/l potassium. The neutralized samples were pre-plated with silver for 2 minutes using 120 gr/l silver powder, 0.02-0.01 A/dm². The pre-silver-plated samples were silver plated using 180 gr/l silver powder, 4 gr/l silver cleaner, and 4 gr/l silver moisturizer. After silver plating, the samples were washed in hot water at 70 °C for 3 minutes.

In the nickel-plating process, the samples were first subjected to the pre-degreasing process, and after washing, they were etched with acid using 10% H₂SO₄ solution. The electrolytic degreasing process was applied to the samples that were washed after etching. The nickel-plating process was performed for 10 minutes using 25 gr/l nickel chloride, 60 °C, 2-3 Volt, 0.5-3 A/dm² plating parameters. In the tin plating process, the samples were immersed in the alkaline caustic solution and degreased. Then, the electrolytic degreasing process was performed for 11 A/dm² and 3 minutes. After washing, the samples were etched with acid using 30% HCL and 1% inhibitor. The samples that were washed after etching were tin-plated in 300 gr/l tin concentrate, at room temperature for 4.3-10.76 A/dm² and 20 minutes.

Table 1. Codes, formulas and chemical compositions of the steels.

Code	DIN	C	N	Si	P	S	Mn	Cr	Ni	Mo	Rest
1.0037	S235JR	0.13	0.002	-	0.023	0.027	0.80	-	-	-	Fe
1.6523	21NiCrMo2	0.19	-	0.04	0.015	0.025	0.74	0.56	0.65	0.23	Fe
1.0503	C45	0.43	-	0.40	0.020	0.027	0.73	-	-	-	Fe
1.7225	42CrMo4	0.45	-	0.40	0.023	0.024	0.76	0.98	-	0.24	Fe

Table 2. Some physical properties of the investigated materials. RM: Reference Materials)(%).

	Sample	Mass (gr)	Thickness (cm)	Diameter (cm)	Radius (cm)	Volume (cm ³)	Density (g/cm ³)
RM	S235JR	5.30	0.210	2.000	1.000	0.660	8.034
	21NiCrMo2	4.90	0.215	1.970	0.985	0.655	7.477
	C45	4.08	0.180	2.010	1.005	0.571	7.143
	42CrMo4	4.84	0.195	2.020	1.010	0.625	7.745
Ni Coated	S235JR	4.70	0.190	2.000	1.000	0.597	7.874
	21NiCrMo2	4.60	0.210	1.950	0.975	0.627	7.335
	C45	5.04	0.205	2.000	1.000	0.644	7.826
	42CrMo4	4.97	0.205	2.100	1.050	0.710	7.000
Ag Coated	S235JR	4.68	0.200	2.000	1.000	0.628	7.448
	21NiCrMo2	4.36	0.195	1.955	0.978	0.585	7.448
	C45	4.78	0.200	2.000	1.000	0.628	7.608
	42CrMo4	5.28	0.220	2.020	1.010	0.705	7.489
Cu Coated	S235JR	4.68	0.195	2.000	1.000	0.613	7.639
	21NiCrMo2	4.63	0.200	1.950	0.975	0.597	7.752
	C45	5.30	0.215	2.000	1.000	0.675	7.847
	42CrMo4	5.26	0.210	2.020	1.010	0.673	7.816
Sn Coated	S235JR	4.91	0.195	2.000	1.000	0.613	8.015
	21NiCrMo2	4.59	0.200	1.956	0.978	0.601	7.638
	C45	5.22	0.220	2.000	1.000	0.691	7.553
	42CrMo4	5.02	0.200	2.020	1.010	0.641	7.832

2.2. Radiation shielding process

After the coating processes, S235JR, 21NiCrMo2, C45, 42CrMo4 steels were irradiated by Ba-133 (10 mCi) radioactive sources having 81-383 keV energies to measure the LACs via the Beer-Lambert law (Figure. 2) and equation (Eq. 2.1);

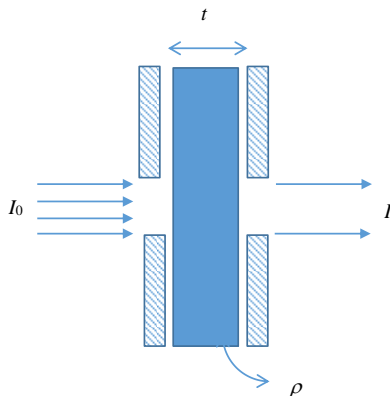


Figure 2. The experimental arrangement for transmission geometry

$$I = I_0 e^{-\mu x}, \mu = \frac{\ln(I_0/I)}{x} \quad (2.1)$$

where I_0 and I are unattenuated and attenuated photon intensities. MAC of any steel, which is a measure of the relative dominance of various interactions, was then determined via density (ρ , g.cm⁻³) of the relevant material; $\mu_m = \mu/\rho$ (cm².g⁻¹). A HPGe detector of 10 mm crystal length, 16 mm diameter and 200 mm² active area was used to detect gamma rays. These HPGe detectors are known to have high detection efficiency at high energies. It has a resolution of ~182 eV at 5.9 keV and its working voltage is -1500 V. A Tennelec 244 model amplifier was used and the measurement time for each sample was set to 1800s. Each sample has been measured at least three times and the results are given as the mean values along with standard deviation. Experimental geometry and a sample spectrum are given in Figures 3 and 4.

Half-value layer (HVL, cm) and tenth-value layer (TVL, cm) are the thickness of the material at which the intensity of radiation entering it is reduced by one half and one tenth, and they were determined by;

$$HVL = \frac{\ln(2)}{\mu} = \frac{0.693}{\mu} \text{ and } TVL = \frac{\ln(10)}{\mu} = \frac{2.302}{\mu} \quad (2.2)$$

Mean free path (MFP, cm), which is the average distance between two successive interactions, was calculated using the LAC (μ , cm⁻¹) of the steel from the equation;

$$MFP = 1/\mu \quad (2.3)$$

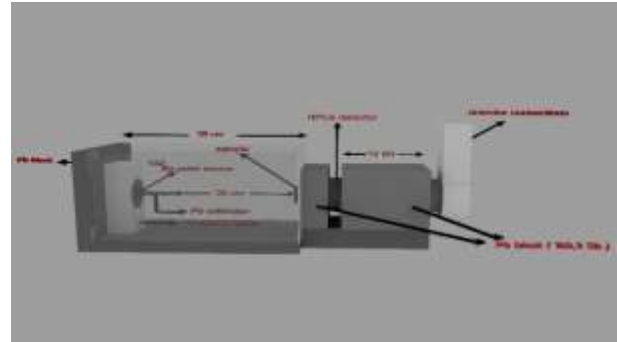


Figure 3. Experimental geometry

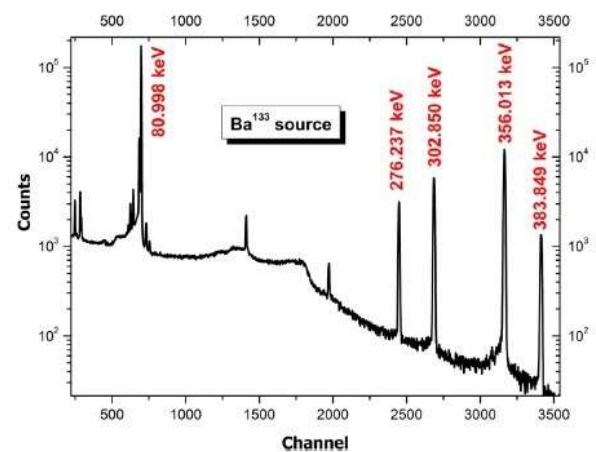


Figure 4. A sample spectrum for RM at studied energies

3. Results and Discussion

The reference materials (RM) 1.0037 (S235JR), 1.6523 (21NiCrMo2), 1.0503 (C45), 1.7225 (42CrMo4) steels were firstly coated with Ni, Cu, Ag and Sn heavy metals via mentioned processes. Mass (gr), thickness (cm), diameter (cm), radius (cm), volume (cm³) and density (g.cm⁻³) of coated materials were then determined using the Archimedes' principle using distilled water as an immersion liquid and a digital balance of sensitivity 10⁻⁴ g. Measurements were repeated five times with an error of < 0.1%. And the values are listed in Table 2. After the physical measurements, LACs of the investigated reference and coated steels were measured with standard deviation as shown in Table 3. Pure (RM) S235JR, 21NiCrMo2, C45, 42CrMo4 steels and its coated (by heavy metals) forms were listed from Ni to Sn coated values to discuss the results in order. In addition, each steel and its coated forms were tabulated with increasing photon energy in the left column for evaluations.

Table 3. LACs of the pure (RM) and different coated steels

Energy (keV)	S235JR					Std. Deviation				
	RM	Ni	Cu	Ag	Sn	RM	Ni	Cu	Ag	Sn
81	4.410	4.426	4.428	4.516	4.923	0.002	0.033	0.007	0.010	0.001
160	1.383	1.551	1.542	1.638	1.697	0.049	0.025	0.011	0.008	0.016
276	0.924	0.932	0.941	0.964	1.092	0.022	0.050	0.003	0.025	0.054
302	0.836	0.841	0.845	0.852	0.959	0.002	0.012	0.018	0.006	0.038
356	0.755	0.761	0.767	0.787	0.873	0.008	0.003	0.006	0.017	0.003
383	0.747	0.752	0.759	0.777	0.853	0.045	0.053	0.007	0.005	0.021
Energy (keV)	21NiCrMo2					Std. Deviation				
	RM	Ni	Cu	Ag	Sn	RM	Ni	Cu	Ag	Sn
81	4.106	4.104	4.343	4.441	4.823	0.001	0.012	0.007	0.003	0.007
160	1.271	1.517	1.560	1.586	1.719	0.061	0.008	0.099	0.004	0.034
276	0.817	0.911	0.933	0.938	0.998	0.026	0.021	0.015	0.005	0.003
302	0.782	0.801	0.830	0.846	0.853	0.001	0.029	0.009	0.001	0.014
356	0.747	0.747	0.779	0.780	0.807	0.022	0.007	0.026	0.007	0.003
383	0.700	0.710	0.750	0.760	0.801	0.064	0.048	0.027	0.017	0.007
Energy (keV)	C45					Std. Deviation				
	RM	Ni	Cu	Ag	Sn	RM	Ni	Cu	Ag	Sn
81	3.820	4.231	4.258	4.419	4.440	0.005	0.011	0.010	0.015	0.003
160	1.235	1.491	1.515	1.535	1.557	0.017	0.004	0.044	0.024	0.051
276	0.815	0.903	0.907	0.920	0.945	0.003	0.015	0.022	0.006	0.029
302	0.732	0.818	0.817	0.819	0.842	0.006	0.008	0.004	0.059	0.003
356	0.679	0.748	0.744	0.755	0.768	0.001	0.004	0.010	0.010	0.002
383	0.669	0.738	0.736	0.745	0.758	0.027	0.069	0.105	0.023	0.015
Energy (keV)	42CrMo4					Std. Deviation				
	RM	Ni	Cu	Ag	Sn	RM	Ni	Cu	Ag	Sn
81	4.162	4.163	4.672	4.701	4.926	0.017	0.016	0.000	0.003	0.008
160	1.306	1.321	1.485	1.583	1.670	0.012	0.017	0.022	0.032	0.021
276	0.885	0.890	0.991	0.999	1.099	0.007	0.017	0.000	0.008	0.016
302	0.847	0.841	0.929	0.931	0.952	0.009	0.011	0.026	0.018	0.036
356	0.757	0.757	0.825	0.830	0.890	0.005	0.007	0.014	0.006	0.001
383	0.725	0.722	0.753	0.813	0.859	0.006	0.097	0.026	0.053	0.012

This method was also used for the other presentations of the parameters both figures and tables. When Table 3 is analyzed, energy dependences and coating effects on LAC values for the studied steels can be clearly seen found. So, LAC is decreasing with increasing photon energy as known, and values of LAC increase as atomic number of heavy coating metals at each photon energy from Table 3.

MAC values of the studied materials were then determined using densities of the materials from Table 2 as $\mu_m = \mu/\rho$. From this equation, it is clear that μ_m (MAC, mass attenuation coefficient) is proportional the μ (LAC, linear attenuation coefficient) for any material at the same photon energy. Thus, MAC values of the

materials have the same energy dependences and the atomic number of coating heavy metal as seen from Figure 5 (a-d). MAC is a measure of the average number of interactions between incident photons and matter or is a measurement of how strongly a matter absorbs or scatters at a specific energy, per unit mass. And this parameter is a function of photon energy. It is also the fundamental property utilized in computations of the penetration of X-and/or gamma rays for different types of materials such as shielding, health or the others. MAC values increase generally with increasing atomic number of coated metals from Ni to Sn in the worked photon energies [21,22]. In the light of this information, the more atomic number of coated heavy metals is higher, the more MAC is the higher at any specific photon energy from Figure 5 (a-d). It can consequently

be said that coating process affects positively the MAC values of 1.0037 (S235JR), 1.6523 (21NiCrMo2), 1.0503 (C45), 1.7225 (42CrMo4) steels from the figure.

HVL and TVL are the significant thicknesses of the materials in terms of the radiation entering to matter. So, these parameters of the materials were obtained by using Eq. 2.2 at the investigated energies. Also, Table 4 shows HVLs and TVLs of the reference materials and the coated forms by heavy metals. HVL and TVL are inversely proportional to LAC. So, HVL and TVL values increase with increasing energy from 81 to 383 keV for any materials due to relations between these parameters and LACs. On the other hand, values of HVL and TVL reduce with rising atomic number of coated metals to the reference materials because of increasing LACs from Ni to Sn at each energy. And in this point, relations between HVL-TVL and LACs show its significance again on the radiation entering or shielding. As a result, coating process developed the HVL and TVL properties of the 1.0037 (S235JR), 1.6523 (21NiCrMo2), 1.0503 (C45), 1.7225 (42CrMo4) steels owing to diminishing HVL-TVL values from Ni to Sn coated metals at the studied energies.

MFP is one of the most significant parameters of materials on behalf of radiation attenuation or radiation shielding capability. The lower MFP values are desired for radiation shielding capability for any material thanks to its meaning. In other words, the less MFP is, the better radiation shielding capability is. Thus, MFP values of the materials were calculated by using Eq. 2.3 at the investigated photon energies. For this aim, values of LAC were utilized from Table 3, and the results were given in Figure 6 (a-d). MFP values are rising with increasing photon energy from 81 to 383 keV for RMs (S235JR, 21NiCrMo2, C45, 42CrMo4) and its coated forms as shown in the figure. This is because of fact that MFP is function of LAC, and LAC are reducing with rising photon energy (from Table 3) for the materials. On the other hand, the studied materials were compared with some standard shielding concretes (Ordinary, Hematite-serpentine, Ilmenite-limonite, Basalt-magnetite, Ilmenite [23]) on behalf of MFP at possible energy (356 keV) as seen in Figure 7 (a-d). It is clearly seen from the figure, both RMs (S235JR, 21NiCrMo2, C45, 42CrMo4) and its coated forms (by heavy metals: from Ni to Sn) have lower MFP values than standard shielding concretes at 356 keV. Therefore, one can say that investigated materials display the better radiation shielding capability than standard shielding concretes due to lower MFP values. Differences (%) between RMs and coated forms on MFP values should be very important to describe improvements of materials. So, differences (%) were calculated by $diff. (\%) = \frac{MFP_{RM} - MFP_{coated}}{MFP_{coated}} \times 100$ at the photon energies.

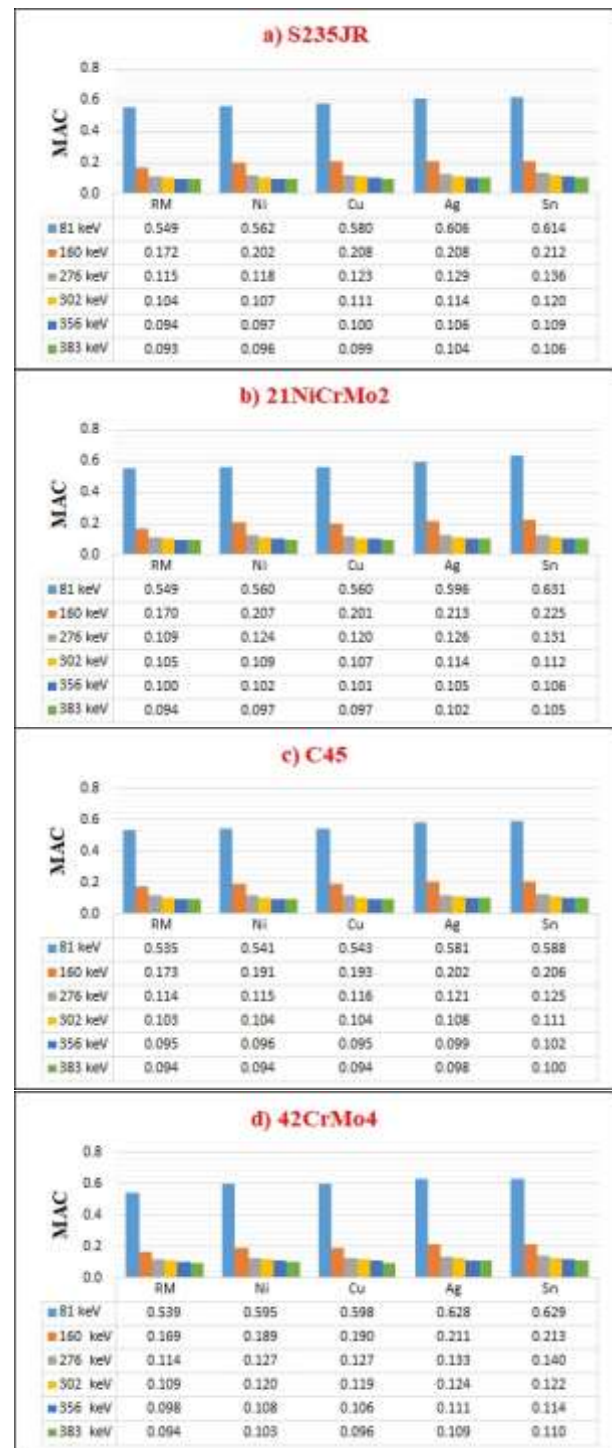


Figure 5. MACs ($\text{cm}^2.\text{g}^{-1}$) of coated steels at investigated energies.

Table 4. HVLs and TVLs of the pure (RM) and different coated steels.

Energy (keV)	HVL					TVL				
	RM	Ni	Cu	Ag	Sn	RM	Ni	Cu	Ag	Sn
S235JR										
81	0.157	0.157	0.157	0.153	0.141	0.522	0.520	0.520	0.510	0.468
160	0.501	0.450	0.447	0.423	0.409	1.664	1.493	1.485	1.406	1.357
276	0.751	0.744	0.737	0.719	0.635	2.493	2.470	2.447	2.388	2.108
302	0.829	0.824	0.821	0.814	0.723	2.753	2.736	2.726	2.703	2.402
356	0.918	0.910	0.904	0.881	0.794	3.049	3.024	3.002	2.927	2.636
383	0.928	0.922	0.913	0.892	0.812	3.082	3.062	3.033	2.963	2.699
21NiCrMo2										
81	0.169	0.169	0.160	0.156	0.144	0.561	0.561	0.530	0.519	0.477
160	0.546	0.457	0.444	0.437	0.403	1.812	1.518	1.476	1.452	1.339
276	0.848	0.761	0.743	0.739	0.695	2.818	2.527	2.469	2.455	2.308
302	0.887	0.865	0.835	0.820	0.813	2.946	2.875	2.774	2.723	2.701
356	0.928	0.928	0.889	0.888	0.859	3.084	3.082	2.955	2.951	2.853
383	0.991	0.977	0.925	0.913	0.866	3.291	3.245	3.072	3.031	2.876
C45										
81	0.181	0.164	0.163	0.157	0.156	0.603	0.544	0.541	0.521	0.519
160	0.561	0.465	0.458	0.452	0.445	1.864	1.544	1.520	1.500	1.479
276	0.850	0.767	0.764	0.753	0.733	2.824	2.549	2.538	2.502	2.436
302	0.946	0.848	0.848	0.847	0.823	3.144	2.816	2.818	2.813	2.734
356	1.021	0.927	0.931	0.919	0.903	3.393	3.080	3.093	3.051	3.000
383	1.036	0.940	0.941	0.931	0.915	3.441	3.122	3.127	3.092	3.040
42CrMo4										
81	0.167	0.167	0.148	0.147	0.141	0.553	0.553	0.493	0.490	0.467
160	0.531	0.525	0.467	0.438	0.415	1.763	1.743	1.550	1.455	1.379
276	0.783	0.779	0.699	0.694	0.631	2.603	2.586	2.323	2.305	2.095
302	0.819	0.824	0.746	0.745	0.728	2.720	2.737	2.480	2.475	2.418
356	0.915	0.916	0.840	0.835	0.779	3.041	3.042	2.791	2.775	2.587
383	0.956	0.960	0.920	0.853	0.807	3.177	3.190	3.056	2.833	2.680

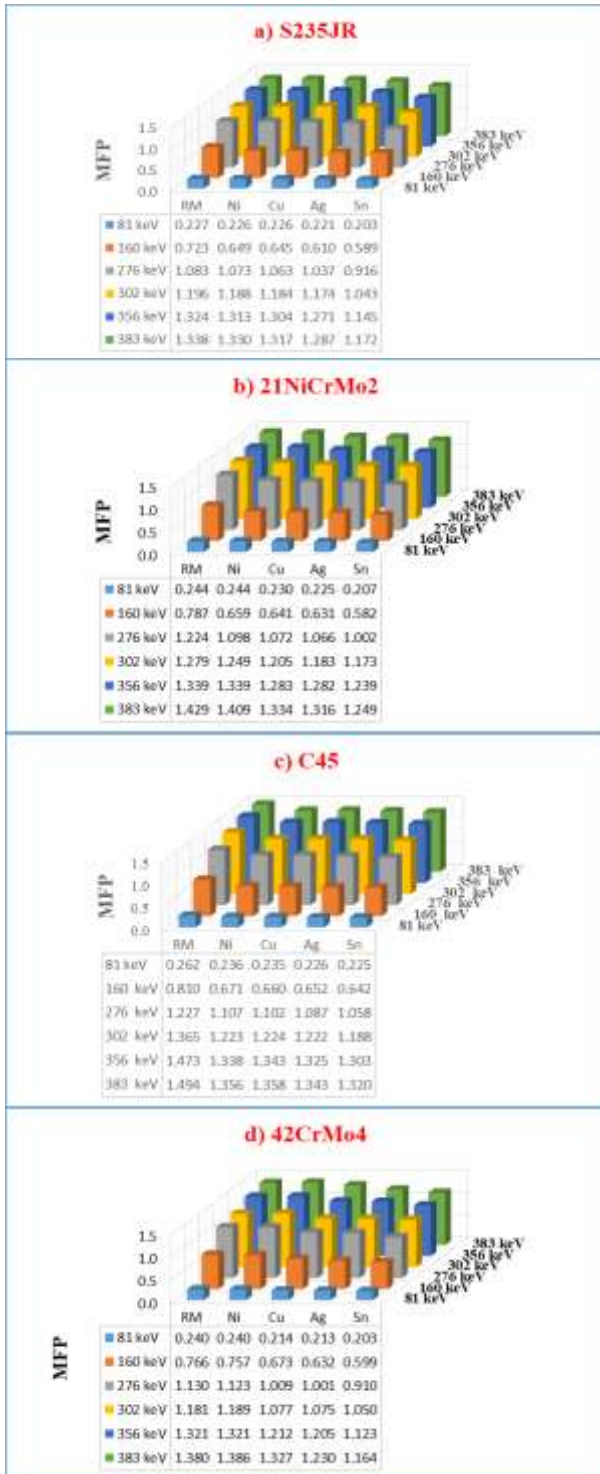


Figure 6. MFPs (cm) of coated steels at investigated energies

Relative differences were generally increased from Ni to Sn coating forms of the materials, and maximum relative difference was determined to be 35.31% for Sn coated 1.6523 (21NiCrMo2) steel. This shows that coating process used has positively affected the RM materials on account of MFP which is very significant feature of radiation shielding applications.

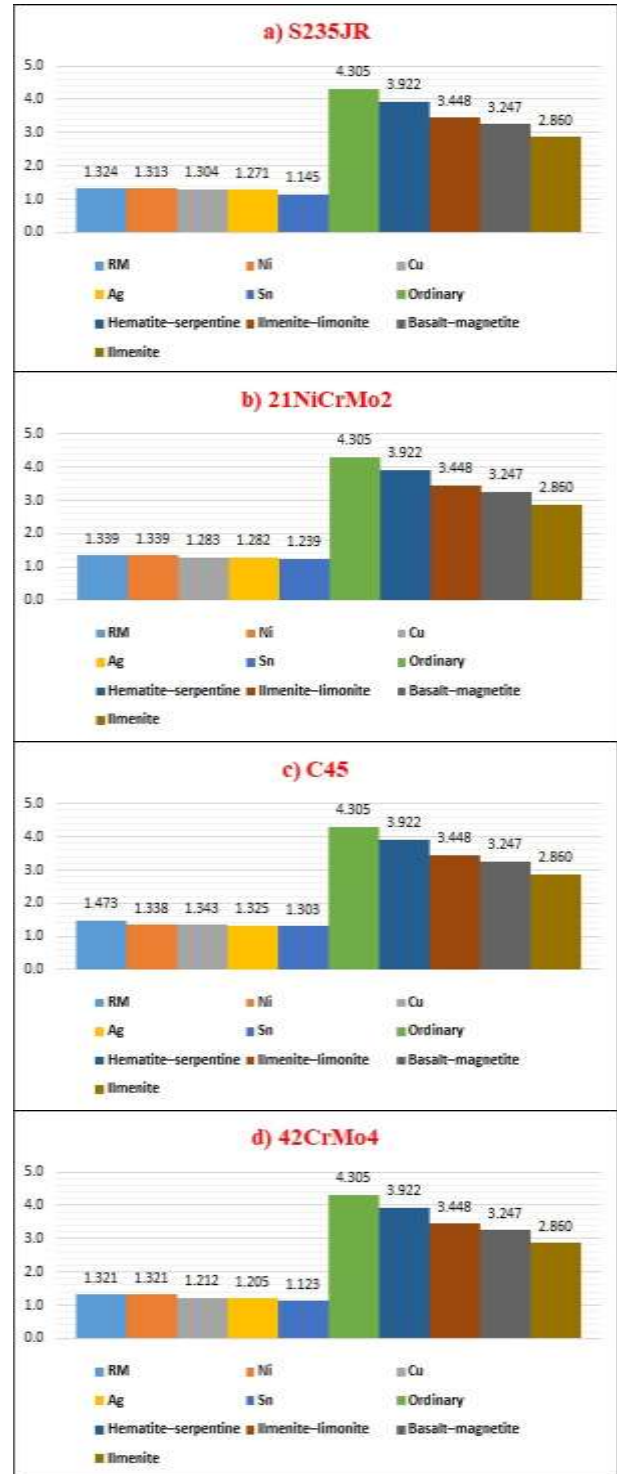


Figure 7. MFPs (cm) of coated steels and some standard shielding concretes at 356 keV photon energy

4. Conclusion

It was aimed to improve 1.0037 (S235JR), 1.6523 (21NiCrMo2), 1.0503 (C45), 1.7225 (42CrMo4) steels using coating process the materials in terms of the radiation shielding capability as much as possible in the present study. 1.0037 (S235JR), 1.6523 (21NiCrMo2),

1.0503 (C45), 1.7225 (42CrMo4) pure steels were coated by Ni, Cu, Ag and Sn heavy metals via electrolytic plating method to measure radiation attenuation properties. The pure and coated samples were then irradiated by radioactive sources for transmission of the gamma rays at 81–383 keV photon energies to measure linear and mass attenuation coefficients ($LAC-\mu$, $MAC-\mu/\rho$). Mean free path (MFP), Half and tenth value of layers (HVL and TVL) of investigated materials were then calculated at the same studied photon energies. The coated steels were found to be better shielding materials than the concretes due to higher LACs and MACs, and lower MFP values. Coated steels were also better shielding than reference materials up to 35.31% relative difference in MFP. One can obviously say that coating processes improve the radiation shielding capability of the studied steels, and the materials have excellent shielding features against the rays according to standard concretes.

Author's Contributions

İdris Karagöz: Sample preparation, characterization progresses, methodology.

Erdem Şakar: Made the experiments, data curation, software.

Murat Türemiş: Data curation, investigation, helped in manuscript preparation.

Mehmet Büyükyıldız: Made literature search, writing - review & editing.

Ethics

There are no ethical issues after the publication of this manuscript.

References

1. Raj, B, Mudali, UK, Vijayalakshmi M, Mathew MD, Bhaduri, AK, Chellapandi, P, Venugopal, S, Sundar, CS, Rao, BPC, Venkataraman, B. 2013. Development of stainless steels in nuclear industry: with emphasis on sodium cooled fast spectrum reactors: history, technology and foresight. *Advanced Materials Research*; 794: 3-25. <https://doi.org/10.4028/www.scientific.net/AMR.794.3>
2. Cattant, F, Crusset, D, Féron, D. 2008. Corrosion issues in nuclear industry today. *Materials Today*; 11(10): 32-37. [https://doi.org/10.1016/S1369-7021\(08\)70205-0](https://doi.org/10.1016/S1369-7021(08)70205-0)
3. El-Kateb, AH, Rizk, RAM., Abdou-Kader, AM. 2000. Determination of atomic cross-sections and effective atomic numbers for some alloys. *Annals of Nuclear Energy*; 27(14), 1333-1343. [https://doi.org/10.1016/S0306-4549\(99\)00121-8](https://doi.org/10.1016/S0306-4549(99)00121-8)
4. Akkurt, I. 2009. Effective atomic and electron numbers of some steels at different energies. *Annals of Nuclear Energy*; 36(11-12): 1702-1705. <https://doi.org/10.1016/j.anucene.2009.09.005>
5. Medhat, ME, Wang, Y. 2015. Investigation on radiation shielding parameters of oxide dispersion strengthened steels used in high temperature nuclear reactor applications. *Annals of Nuclear Energy*; 80: 365-370. <https://doi.org/10.1016/j.anucene.2015.01.044>
6. Singh, VP, Medhat, ME, Shirmardi, SP. 2015. Comparative studies on shielding properties of some steel alloys using Geant4, MCNP, WinXCOM and experimental results. *Radiation Physics and Chemistry*; 106: 255-260. <https://doi.org/10.1016/j.radphyschem.2014.07.002>
7. Yıldırım, S, Tuğrul, AB, Büyük, B, Demir, E. 2016. Gamma Attenuation properties of some aluminum alloys. *Acta Physica Polonica A*; 129(4): 813-815 (2016). <https://doi.org/10.12693/APhysPolA.129.813>
8. Büyükyıldız, M, Kurudirek, M, Ekici, M, İçelli, O, Karabul, Y. 2017. Determination of radiation shielding parameters of 304L stainless steel specimens from welding area for photons of various gamma ray sources. *Progress in Nuclear Energy*; 100: 244-254. <https://doi.org/10.1016/j.pnucene.2017.06.014>
9. Büyükyıldız, M.. 2018. Effect of current intensity on radiological properties of joined 304L stainless steels for photon interaction. *Nuclear Science Techniques*; 29:8. <https://doi.org/10.1007/s41365-017-0353-1>
10. Akman, F, Sayyed, MI, Kaçal MR, Tekin, HO. 2019. Investigation of photon shielding performances of some selected alloys by experimental data, theoretical and MCNPX code in the energy range of 81 keV-1333 keV. *Journal of Alloys and Compounds*; 772: 516-524. <https://doi.org/10.1016/j.jallcom.2018.09.177>
11. Yılmaz, D, Aktaş, B, Çalık, A, Aytar, OB. 2019. Boronizing effect on the radiation shielding properties of Hardox 450 and Hardox HiTuf steels. *Radiation Physics and Chemistry*; 161: 55-59. <https://doi.org/10.1016/j.radphyschem.2019.04.019>
12. Li, J, Huang, M, Hou, R, Ouyang, X. 2019. Photon attenuation coefficients of oxide dispersion strengthened steels by Geant4, XCOM and experimental data. *Radiation Physics and Chemistry*; 161: 23-28. <https://doi.org/10.1016/j.radphyschem.2019.03.042>
13. Şakar, E, Büyükyıldız, M, Alım, B, Şakar, BC, Kurudirek, M. 2019. Leaded brass alloys for gamma-ray shielding applications. *Radiation Physics and Chemistry*; 159: 64-69. <https://doi.org/10.1016/j.radphyschem.2019.02.042>
14. Akman, F, Kaçal, MR, Sayyed MI, Karataş HA. 2019. Study of gamma radiation attenuation properties of some selected ternary alloys. *Journal of Alloys and Compounds*; 782: 315-322. <https://doi.org/10.1016/j.jallcom.2018.12.221>
15. Alım, B, Şakar, E, Baltakesmez, A, Han, İ, Sayyed, MI, Demir, L. 2020. Experimental investigation of radiation shielding performances of some important AISI-coded stainless steels: Part I. *Radiation Physics and Chemistry*; 166: 108455. <https://doi.org/10.1016/j.radphyschem.2019.108455>
16. Alım, B, Şakar, E, Han, İ, Sayyed, MI. 2020. Evaluation the gamma, charged particle and fast neutron shielding performances of some important AISI-coded stainless steels: Part II. *Radiation Physics and Chemistry*; 166: 108454. <https://doi.org/10.1016/j.radphyschem.2019.108455>
17. Sterne, JrRH, Steele, LE. 1969. Steels for commercial nuclear power reactor pressure vessels. *Nuclear Engineering and Design*; 10(3): 259-307. [https://doi.org/10.1016/0029-5493\(69\)90066-1](https://doi.org/10.1016/0029-5493(69)90066-1)
18. Neff, D, Saheb, M, Monnier, J, Perrin, S, Descostes, M, L'Hostis, V, Crusset, D, Millard, A, Dillmann, P. 2010. A review of the archaeological analogue approaches to predict the long-term corrosion behaviour of carbon steel overpack and reinforced concrete structures in the French disposal systems. *Journal of Nuclear Materials*; 402: 196-205. <https://doi.org/10.1016/j.jnucmat.2010.05.003>
19. Finniston, HM. 1974. The sixth royal society technology lecture: Nuclear energy for the steel industry. *Proceedings of the Royal Society A*; 340: 139-146. <http://www.jstor.org/stable/78625>



- [20]. Standish, T, Chen, J, Jacklin, R, Jakupi, P, Ramamurty, S, Zagidulin, D, Keech, P, Shoesmith, D. 2016. Corrosion of copper-coated steel high level nuclear waste containers under permanent disposal conditions. *Electrochimica Acta*; 211: 331-342. <https://doi.org/10.1016/j.electacta.2016.05.135>
- [21]. Seltzer, SM, Hubbell, JH. Tables and Graphs of Photon Mass Attenuation Coefficient and Mass Energy-Absorption Coefficients for Photon Energies 1 keV to 20 MeV for Elements Z = 1 to 92 and Some Dosimetric Materials, Appendix to invited plenary lecture by J.H. Hubbell "45 Years (1950-1995) with X-Ray Interactions and Applications" presented at the 51st National Meeting of the Japanese Society of Radiological Technology, April 14-16, Nagoya, Japan, 1995.
- [22]. Gerward, L, Guilbert, N, Jensen, KB, Leving, H. 2004. WinXCom-a program for calculating X-ray attenuation coefficients. *Radiation Physics and Chemistry*; 71:(3-4): 653-654. <https://doi.org/10.1016/j.radphyschem.2004.04.040>
- [23]. Bashter, II. 1997. Calculation of radiation attenuation coefficients for shielding concretes. *Annals of Nuclear Energy*; 24(17): 1389-1401. [https://doi.org/10.1016/S0306-4549\(97\)00003-0](https://doi.org/10.1016/S0306-4549(97)00003-0)

Modification of Asphalt Binder with Waste Expanded Polystyrene (EPS) Foam

Kürşat Yıldız¹ , Harun Kınacı² , Mert Atakan^{3*} 

¹ Gazi University, Faculty of Technology, Department of Civil Engineering, Ankara, Turkey

² Faculty of Economics and Administrative Sciences, Erciyes University, Kayseri, Turkey

³ Gazi University, Faculty of Technology, Department of Civil Engineering, Ankara, Turkey

*mertatakan@gazi.edu.tr

*Orcid: 0000-0003-1878-2111

Received: 28 February 2021

Accepted: 26 July 2021

DOI: 10.18466/cbayarfb.885696

Abstract

Waste polymers are widely used in asphalt modification, especially, in order to reduce their detrimental effect on the environment. This study discusses the usability of waste expanded polystyrene (EPS) foam in asphalt modification. In this respect, the EPS foam, which produces waste in both production and use stages, was mixed with bitumen by weight at the ratios of 2%, 4%, 6%, and 8%, and dry modification method was employed. The penetration, ductility, softening point, flash point, and specific gravity values of virgin bitumen were compared with waste EPS foam modified bitumen. The comparison was made by both graphical and statistical methods. A strong correlation between the physical properties of modified asphalt and the ratio of EPS foam was observed. A drop was observed in penetration and ductility values. Besides, it was found by statistical analyses that 2% of the increase in the additive ratio is not sufficient to make a significant difference in the physical properties of bitumen, therefore, the increase should be at least 4%. Overall, it is concluded that EPS foam additive can be used in bitumen modification for hot regions where low penetration is required.

Keywords: Asphalt Binder, Bitumen Modification, EPS, Polystyrene Foam, Statistical Evaluation.

1. Introduction

Hot bituminous mixtures (HBMs) are the most common type of material using in pavement constructions. HBMs are preferred due to their service life performance, stability, durability, water-resistance, and comfort criteria. Recently increased traffic volume and axle loads have created a great necessity to improve these criteria [1].

It is a well-known fact that the rheological behavior of bitumen is significantly heat-related and low thermal susceptibility is vital for the bitumen. Bitumen at low temperatures is brittle due to its high stiffness which makes it vulnerable to thermal and fatigue cracking. On the other hand, bitumen at high temperatures tends to flow which gives rise to permanent deformations under traffic loads such as rutting [2]. Accordingly, polymers modification in bitumen enhances its performance at high, low, and intermediate temperatures. They can reduce thermal and fatigue cracking at low temperatures

in the asphalt mixture. Also, they can increase the resistance to permanent deformation at high temperatures [2–4].

Today, with the development of the petroleum industry, synthetic polymers such as polypropylene (PP), polyethylene (PE), and polystyrene (PS) have become indispensable parts of our lives. This brought about the environmental waste problem. PS foam represents 70% of the total plastic waste in the oceans due to its low recycling rate. Approximately 3 million tons of PS waste are threatening the environment due to their chemical stability [5–8]. Although this threat is tried to be eliminated through landfills and incineration, landfill brings an extra cost, and incineration results in toxic gas emissions, which is detrimental to the environment [5]. Polymeric materials are also considered a good bitumen modifier because of their chemical structure composed of mostly carbon elements [7]. Thus, many studies have been done on asphalt modification with polymeric materials such as PP [9], PE [10], and PS [8,11–14]. For

instance, Vila-Cortavitar et al. (2018) has performed a life cycle assessment on waste PS modified bitumen and they suggest that using modified bitumen might reduce its environmental impact significantly because it provides longer performance life [14]. In another study, bitumen has been modified with PS and trans-polyoctenamer in the presence of a cross-linking agent [12]. They have reported that modified bitumen has provided good storage stability, improved in elastic recovery, and showed better overall performance compared to virgin asphalt.

The expanded polystyrene (commonly referred to as EPS) has great impact strength, acoustic and heat isolation properties. Also, its lightness is another advantage. Therefore, EPS is generally used in the package and packaging sector as well as in the building industry as heat or acoustic isolation material [15,16]. EPS comprises small PS beads that are obtained from styrene by the polymerization process. Once polymerization is completed, EPS is infused with a blowing agent (e.g., pentane and hexane). After that, small volumes of gas are entrapped between polystyrene beads, and expansion is achieved [17]. EPS contains more than 95% of air which makes it difficult to accumulate as waste. Besides, its recycling process is complicated and costly due to its high volume [3]. Thus, using EPS in asphalt modification can contribute to handling this environmental pollutant. Also, EPS starts to soften at a temperature above 100 °C [18]. That is why it can stay durable at service temperatures of asphalt pavements.

Nciri et al. (2020) have studied the chemical background of asphalt modification with waste EPS, and they have suggested that waste EPS can be used as a bitumen modifier [16]. However, the limitation of their study is not to address the physical properties of the asphalt. On the other hand, some studies have been done relating to the effect of EPS modification on the physical and rheological properties of asphalt binder [3,19,20]. They have suggested that waste EPS modification enhances asphalt's physical performance. For instance, Mahida et al. (2021) have studied waste EPS modified asphalt with mechanical analysis (e.g., penetration, softening point, viscosity), rheological tests, electron microscopy, infrared stereoscopy, and Marshall stability [3]. They have demonstrated incorporation of waste PS in bitumen modification at different percentages significantly improves the properties as compared to virgin bitumen. They have got satisfactory results in rutting and fatigue parameters in dynamic shear rheometer (DSR). Besides, they have reported an increase in stiffness of the bitumen with waste PS according to penetration and softening point results. The raise in the stiffness is also supported by other studies [19–21]. Although several studies have been carried out on EPS modification of asphalt binder,

no single study exists that uses statistical evaluation methods.

This study investigates the effect of waste EPS foam on the physical properties of the asphalt binder. In line with this purpose, 50/70 penetration grade of asphalt cement was modified with waste EPS at the ratio of 2%; 4%; 6%, and 8%. The penetration, ductility, softening point, flash point, and specific gravity tests were performed according to related standards. The reason to choose these tests was to evaluate stiffness, temperature susceptibility, and safety of the modified bitumen. Obtained results are interpreted and evaluated with statistical methods differently from other studies.

2. Materials and Methods

In this study, 50/70 penetration grade bitumen, which was supplied from İzmit Tüpraş refinery, was used, and the properties of the bitumen are given in Table 1.

EPS was used in the study. Generally, their density varies from 0.028-0.045 g/cm³. In this study EPS, whose density is 0.032 g/cm³, was used. Typical properties of the PS are given in Table 2. The dry method, which is one of the modified bitumen preparation methods, was used in the study. In this method, virgin bitumen and waste EPS foam were mixed in a steel bowl before melting the EPS (Figure 1).

Table 1. Properties of the bitumen [22].

Parameters	Value from the Supplier	Laboratory Tests Results
Penetration (0.1 mm)	50/70	66.3
Softening Point (°C)	46-54	50.4
Flash Point (°C)	230 (Min)	314
Solubility (%)	99 (Min)	-
Softening point rise (°C)	9 (Max)	-
Resistance to hardening (a) at 163 °C		-
- Loss on heating (%)	0.5 (Max)	
- Penetration after heating (%)	50 (Min)	
- Softening point after heating (° C)	48 (Min)	

Table 2. Typical properties of PS [3].

Property	Value
IUPAC name	Poly(1-phenylethene)
Common name	Thermocol
CAS number	9003-53-6
Abbreviations	PS
Chemical formula	(C ₈ H ₈) _n
Density	0.96–1.04 g/cm ³
Melting point	~ 240 °C

The waste EPS was added into the bowl, which contains 150°C hot bitumen, at certain percentages of bitumen weight (2%, 4%, 6%, and 8%). These ratios were selected based on previous studies where additive ratios are below 10% [16,19–21]. Then, EPS and the bitumen

mixed homogeneously. Next, the mixture was added to the oven whose temperature was adjusted to 150° C. The mixture was kept in the oven for 2 hours in order to provide EPS to melt, and thus obtain a homogeneous mixture. Once EPS was softened and mixed with bitumen, entrapped air in the EPS was disappeared. In other words, EPS became normal PS. After that, the homogeneous mixture was taken into test equipment within the standards following; penetration (ASTM D5-D5M-13), ductility (AASHTO T 51-09), softening point (AASHTO T 53), flash point (ASTM D 92-18), and specific gravity. Some stages of the experimental process are demonstrated in Figure 2.



Figure 1. The process of mixing EPS foam into the bitumen.

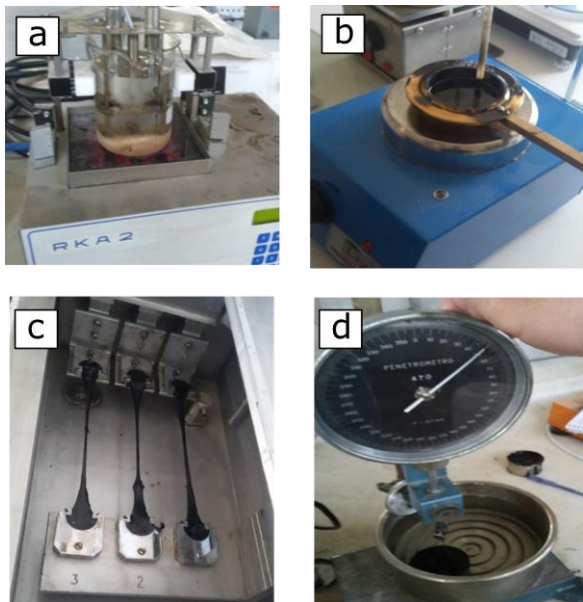


Figure 2. Experimental process a) Softening Point b) Flash Point c) Ductility d) Penetration.

3. Results and Discussion

The changes in physical properties of EPS modified bitumen were evaluated and interpreted compared to the 50/70 penetration virgin bitumen. The findings are given in Table 3. The data presented here are the means

of the values obtained as a result of three experiments for penetration, ductility, and softening point, respectively. Standard deviations of the results are illustrated in Figure 3 as error bars. Table data were interpreted by graphing for each physical property and using statistical methods.

Table 3. Modified Bitumen Physical Properties (Modified Bitumen Physical Properties).

Physical Properties	Standard	Polystyrene rate (%)				
		0%	2%	4%	6%	8%
Penetration (x 0.1 mm)	ASTM D5-D5M-13	66.3	62.7	61.3	57.7	49.7
Ductility (cm)	ASHTO T 51-09	122	114	109	102	83
Softening point (°C)	ASHTO T 53	50.4	49.8	49.5	49.3	49.1
Flash Point (°C)	ASTM D 92-18	314	320	342	354	360
Specific gravity (g/cm ³)	ASTM-D 70-03	1.030	1.036	1.050	1.058	1.065
Penetration Index (PI)	Pfeiffer and Van Doormaal (1936) [23]	-0.41	-0.71	-0.84	-1.04	-1.44

3.1 Penetration

When the penetration data are examined in Table 3, the modified bitumen penetration values decreased as the EPS percentage increased. The amount of this change is given in Figure 3a graphically. When each polystyrene additive percentage increased by 2%, it was observed that pure bitumen penetration decreased by 5.53%, 7.53%, 13.53%, and 25.13%, respectively.

In order to determine the statistical significance of this decrease, the correlation value between the polystyrene percentage and the penetration value was calculated, and a strong negative value of -0.958 was obtained. The p-value of the correlation value is 0.01 (Table 4). It is concluded that the correlation coefficient is significant for the case where the meaning level is 0.05 [24]. From these results, it is interpreted that as the percentage of polystyrene additive increases, the penetration value decreases.

It is clear that this decrease in the penetration values of bitumen will lead to an increase in viscosity. According to reference [25], this increase makes workability difficult, in other words, compaction of the asphalt mixture becomes more difficult. But the decrease in penetration provides higher resistance against deformations such as rutting as stated in reference [26]. Besides, it is thought that the penetration value can be adjusted by using polystyrene additive in hot climates where low penetration is required. When it comes to the rheology, rheological properties of the modified bitumen were not completely evaluated in this study.

However, this issue is addressed by Mahida (2021) [3]. They have stated that PS modified bitumen showed better rutting performance and its elastic properties largely increased.

Table 4. Correlation Analysis Results

First Variable	Second Variable	Correlation Coefficient	p-Value
Penetration (x 0.1 mm)	EPS Ratio (%)	-0.958	0.010*
Ductility (cm)		-0.963	0.009*
Softening point (°C)		-0.967	0.007*
Flash Point (°C)		0.979	0.004*
Specific gravity (g/cm ³)		0.992	0.001*

*Meaningful at 0.05 significance level

3.2 Ductility

When ductility values are examined in Table 3, the ductility values of modified bitumen decreased as the additive ratio increased. The amount of this change is shown in Figure 3c graphically. In each 2% increase of polystyrene additive, it was observed a decrease of 6.56%, 10.66%, 16.40%, and 31.97% in ductility of pure bitumen, respectively.

In order to determine the statistical significance of this decrease, the correlation value between polystyrene percentage and ductility value was calculated, and a strong negative correlation value of -0.963 was obtained. The p-value of the correlation value found is 0.009 (Table 4). It is concluded that the correlation coefficient is significant for the case where the meaning level is 0.05. From these results, it is interpreted that the ductility value decreases with polystyrene additives.

The ductility test is commonly accepted as a controversial test because of its empirical nature, low reproducibility, and the unclear relationship between the measured results and basic material characteristics [27]. However, field data support that there is a good correlation between asphalt ductility and pavement cracking. Cracks are more likely to occur as ductility decrease [28,29]. Therefore, the decrease in ductility may not be interpreted as good especially in cold regions. Nonetheless, ductility values of the modified bitumen are met with the specification limits except for the value for 8% additive. That is why it might be used for hot regions up to 6% for a similar reason with penetration values.

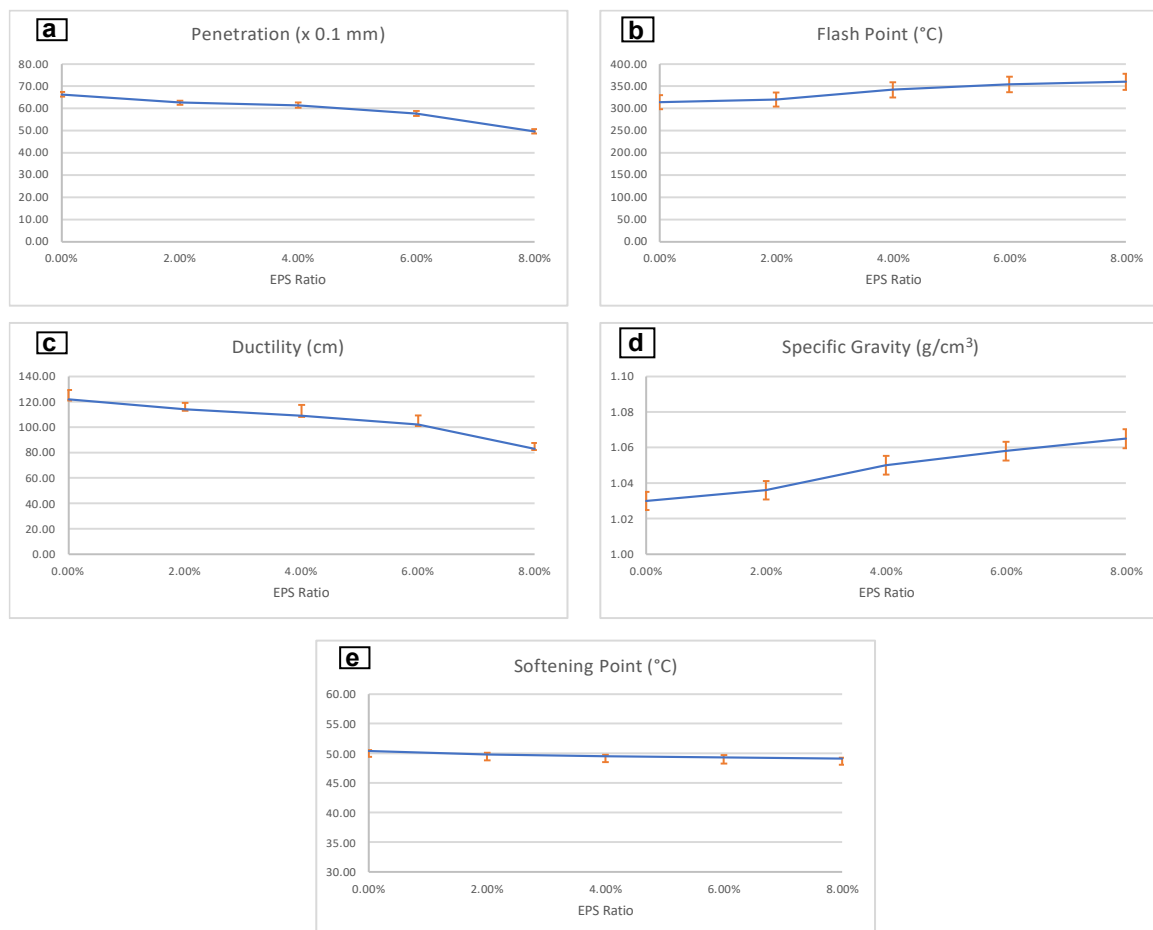


Figure 3. Change of the physical properties a) Penetration b) Flash Point c) Ductility d) Penetration e) Softening Point

3.3 Softening Point

When the softening point values are examined in Table 3, the softening point values of modified bitumen decreased as the EPS ratio increased. The amount of this change is shown in Figure 3e graphically. Each 2% increase of polystyrene additive caused a decrease of 1.19%, 1.88%, 2.18%, and 2.57%, respectively, in the softening point of the pure bitumen.

In order to determine the statistical significance of this decrease, the correlation value between polystyrene percentage and softening point value was calculated, and a strong negative value of -0.967 was obtained. The p-value of the correlation value found is 0.007 (Table 4). It is concluded that the correlation coefficient is significant for the case where the meaning level is 0.05. From these results, it is interpreted that the softening point value decreases as the percentage of polystyrene additive increases.

The softening point test measures the temperature value where bitumen reaches a certain softness. Bitumen has an approximately penetration value of 800 or absolute viscosity of 13 000 poises when it is at its softening point [30]. Therefore, softening point test reveals the relationship between viscosity and temperature of the bitumen. In other words, the viscosity of the bitumen depends on the difference between its temperature and softening point. The slight decrease in the softening point of modified bitumen may affect badly its performance especially in hot regions due to low viscosity. However, this decrease is slight and remains in the limitation of base bitumen. Therefore, the modified bitumen can be used, because it can contribute to reclaim waste EPS and reduce bitumen consumption.

Furthermore, the softening point can be used along with penetration to calculate the temperature susceptibility of the bitumen. For this purpose, Penetration Index (PI) was defined by Pfeiffer and Van Doormaal (1936) [23]. By assuming bitumen has a penetration of 800 at softening point, PI values were calculated for each PS ratio (Table 3). These calculation steps are well explained in reference [30]. There was a constant decrease in PI values which means a rise in temperature susceptibility. However, this decrease remained within the limits of normal bitumen. Because bitumen with PI values between -2 and 2 can be referred to as normal bitumen [30,31].

3.4 Flash Point

The change of flash point values with the EPS ratio is given in Table 3. It illustrates that flash point values of modified bitumen increased, as the additive ratio increased. The amount of change, according to the EPS ratio, is graphically demonstrated in Figure 3b. Each 2% increase in the EPS ratio gives rise to an ascend in flash

point by 1.91%, 8.91%, 12.73%, and 14.64%, respectively.

In order to determine the statistical significance of this increase, the correlation value between the polystyrene percentage and flash point value was calculated, and a strong positive correlation value of 0.979 was obtained. The p-value of the correlation value found is 0.004 (Table 4). It is concluded that the correlation coefficient is significant for the case where the meaning level is 0.05.

From these results, it is interpreted that the flash point value increases as the percentage of polystyrene additive increases. When the results are evaluated in the light of literature, the determination of the flash point of petroleum products or flammable materials is a crucial parameter that should be determined in terms of safety and environmental damage [32]. In this respect, polystyrene-modified bitumen shows good behavior. This situation also increases the safety range by meeting the requirements for the transportation of bitumen and HBM.

3.5 Specific Gravity

When the specific gravity values of bitumen are examined in Table 3, the specific gravity of modified bitumen increases as the additive ratio increases. The amount of change of the specific gravity according to the additive ratio is given in Figure 3d. Each 2% increase in the EPS ratio is caused to a rise in the bitumen specific gravity value by 0.58%, 1.94%, 2.71%, and 3.39%, respectively.

In order to determine the statistical significance of this increase, the correlation value between polystyrene percentage and specific gravity value was calculated, and a strong positive correlation value of 0.992 was obtained. The p-value of the correlation value is 0.001 (Table 4). It is concluded that the correlation coefficient is significant for the case where the meaning level is 0.05. From these results, it is interpreted that the specific gravity value increases as the percentage of polystyrene additive increases.

The specific gravity value of the asphalt binder is essential to determine the volumetric specifications of the asphalt mix. Because while preparing asphalt-mix, mixing ratios are often expressed as percent by weight. In another aspect, the specific gravity value is particularly important for the determination of the critical characteristic of the asphalt mixture, such as bitumen film thickness [33]. In this respect, it is concluded that polystyrene-modified bitumen is within the specification limits and denser than pure bitumen. This can contribute to bitumen stability positively, as well as to increase durability.

3.6 Inferential Statistics

Another point that needs to be addressed with this experimental study is the significance of the differences between the values in different amounts of polystyrene for each variable (penetration ductility, etc.). With these tests, it is possible to obtain information about how much the amount of penetration should be increased to make a significant difference according to the relevant parameter.

For this purpose, the significance of changes in the penetration, ductility, and softening point values obtained by three different experiments according to different polystyrene ratios were evaluated by Kruskal-Wallis Test and the p-values obtained as 0.011, 0.031, and 0.022, respectively. Penetration, ductility, and softening point values are interpreted separately for different polystyrene values where all of these values are less than 0.05 meaning level. Post hoc tests were also performed for different polystyrene values to determine the ratios between these differences.

Table 5. Results of Kruskal-Wallis Test

Group Variables	Dependent Variables	Kruskal-Wallis Test p-values	Leven's Test p-values
EPS Ratio (5 Groups)	Penetration	0.011*	0.743**
	Ductility	0.031*	0.810**
	Softening Point	0.022*	0.547**
* Meaningful at 0.05 significance level			
** Not meaningful at 0.05 significance level (Homogeneous variances)			

There are several Post Hoc tests in the literature. These are divided into two main groups according to whether the variances of the variables to be compared are equal or not. For this purpose, homogeneity of variances was tested by Levene's test, and p-values were obtained as 0.743, 0.810, and 0.547 according to the variables of penetration, ductility, and softening point, respectively (Table 5). When the meaning level is above 0.05, it is interpreted that they have the same variance according to different polystyrene values for each variable. In this case, the Post Hoc test should be selected from the tests that run under the assumption that the variances are equal. For this reason, the Scheffe test, which provides this feature, was applied for binary comparisons (Table 6).

In the paired comparisons for the penetration variable, the penetration value was statistically insignificant only when the polystyrene ratio was between 2% and 4% (p-value = 0.726). In other words, the use of polystyrene at the ratio of 2% or 4% does not cause a statistically significant difference in the penetration value. In all other possible binary comparisons, penetration values for different polystyrene ratios were found to be different (Table 6).

Table 6. Scheffe Post Hoc test results of penetration, ductility, and softening point

EPS Ratio (%)		p-Value for Penetration	p-Value for Ductility	p-Value for Softening Point
0	2	0.036*	0.716	0.048*
	4	0.005*	0.302	0.002*
	6	0.000*	0.056	0.001*
	8	0.000*	0.001*	0.000*
2	4	0.726	0.928	0.290
	6	0.005*	0.371	0.114
	8	0.000*	0.004*	0.020*
4	6	0.036*	0.800	0.996
	8	0.000*	0.012*	0.458
6	8	0.000*	0.073	0.809
*Meaningful at 0.05 significance level				

The ratio of polystyrene in binary comparisons for the ductility variable is shown in Table 6. The corresponding p-values are given in the table. According to the results obtained, the difference in ductility values was statistically insignificant when the additive ratio is 2% or 4%. It was concluded that the additive ratio should be at least 6% in order to affect the ductility of the virgin asphalt. Furthermore, according to the results, the polystyrene ratio should change at least 4% (e.g., from 4% to 8%) in order to have a significant change in ductility value.

Binary comparisons of the EPS ratio for the softening point are listed in Table 6. The corresponding p-values are given in the table. The table demonstrates that the softening point values where the polystyrene ratio is 0% are different from other polystyrene ratios. Therefore, the addition of EPS causes a meaningful change in the softening point. However, if the polystyrene rate is 2% or more, the polystyrene rate must be changed at least 4% to create a meaningful change in the softening point.

4. Conclusions

Waste utilization is an issue that should be considered in almost all activities of developed and developing countries. That is why, both in the world and in Turkey, many non-governmental and governmental organizations continue their activities by looking for new utilization fields of wastes. In this respect, using waste EPS in asphalt modification was studied, and this paper not only aims to solve an engineering problem but also employs an environmentalist approach. The following conclusions can be drawn from this study:

- EPS modification of AC 50/70 penetration grade bitumen with the additive ratio of 2%, 4%, and 6% remain within the limit values of ASTM D5-D5M-13 standard, but 8% additive ratio exceeded the limits of the standard.
- Ductility of the pure bitumen decreased with EPS additive, which is considered a negative result

usually. But it may give rise to a decrease in thermal sensitivity, which is a good point in hot climates.

- The EPS additive does not significantly affect the softening point.
- Flash point of the pure bitumen raised with EPS additive, which may improve storing, transport, and environmental sensitivity in terms of safety.
- It has been observed that the addition of EPS increases the specific gravity of the bitumen, which may affect the service life positively.
- There is a strong correlation between the physical properties of asphalt cement and EPS ratios. It is a known fact that physical properties are affected by each other. This reality is especially strong between ductility and softening point.
- It is found that a 2% increase in the EPS ratio had no significant effect on the physical properties of the asphalt. Thus, considering inferential statistical analysis, an optimum increase ratio should be determined as 4% instead of 2% in further optimizing research.
- If the bitumen is modified with a 4% EPS ratio, 1.25 m³ waste EPS can be reclaimed for every ton of bitumen usage. In other words, an average truckload waste EPS can be recycled with 16 tons of bitumen.

The study makes a baseline level discussion of using EPS to modification of asphalt. Further research may be done in order to improve its results, such as the aging or fatigue behavior of EPS modified asphalt. One of the limitations of this study is the number of specimens. That is why further research can be done with more specimens in order to drop the error in statistical analyses. In this way, the results could approximate practical applications. Besides, more broadly, research is needed to determine morphological characteristics of modified bitumen.

Author's Contributions

Kürşat Yıldız: Study conception and design, data collection, analysis and interpretation of results, draft manuscript preparation

Harun Kınacı: Analysis and interpretation of results, draft manuscript preparation,

Mert Atakan: Analysis and interpretation of results, draft manuscript preparation,

Ethics

There are no ethical issues after the publication of this manuscript.

References

1. Papagiannakis, A.T. and Masad, E.A. *Pavement Design and Materials*; John Wiley & Sons, Inc.: Hoboken, New Jersey, 2008.
2. García-Morales, M., Partal, P., Navarro, F.J., Martínez-Boza, F., Gallegos, C., González, N., González, O., and Muñoz, M.E. 2004. Viscous properties and microstructure of recycled eva modified bitumen. *Fuel*. 83 (1): 31–38.
3. Mahida, S., Shah, Y.U., and Sharma, S. 2021. Analysis of the Influence of Using Waste Polystyrene in Virgin Bitumen. *International Journal of Pavement Research and Technology*. (0123456789):
4. Kalantar, Z.N., Karim, M.R., and Mahrez, A. 2012. A review of using waste and virgin polymer in pavement. *Construction and Building Materials*. 33 55–62.
5. Baytekin, B., Baytekin, H.T., and Grzybowski, B.A. 2013. Retrieving and converting energy from polymers: Deployable technologies and emerging concepts. *Energy and Environmental Science*. 6 (12): 3467–3482.
6. Hearon, K., Nash, L.D., Rodriguez, J.N., Lonneckker, A.T., Raymond, J.E., Wilson, T.S., Wooley, K.L., and Maitland, D.J. 2014. A high-performance recycling solution for polystyrene achieved by the synthesis of renewable poly(thioether) networks derived from d -limonene. *Advanced Materials*. 26 (10): 1552–1558.
7. Pol, V.G. 2010. Upcycling: Converting waste plastics into paramagnetic, conducting, solid, pure carbon microspheres. *Environmental Science and Technology*. 44 (12): 4753–4759.
8. Mohamed, N., Maharaj, R., and Ramlochan, D. 2017. Rutting and fatigue cracking susceptibility of polystyrene modified asphalt. *Am J Appl Sci*. 14 (5): 583–591.
9. Casey, D., McNally, C., Gibney, A., and Gilchrist, M.D. 2008. Development of a recycled polymer modified binder for use in stone mastic asphalt. *Resources, Conservation and Recycling*. 52 (10): 1167–1174.
10. Polacco, G., Berlincioni, S., Biondi, D., Stastna, J., and Zanzotto, L. 2005. Asphalt modification with different polyethylene-based polymers. *European Polymer Journal*. 41 (12): 2831–2844.
11. Baker, M.B., Abendeh, R., Abu-Salem, Z., and Khedaywi, T. 2016. Production of sustainable asphalt mixes using recycled polystyrene. *International Journal of Applied Environmental Sciences*. 11 (1): 183–192.
12. Padhan, R.K., Sreeram, A., and Gupta, A. 2020. Evaluation of trans-polyoctenamer and cross-linking agents on the performance of waste polystyrene modified asphalt. *Road Materials and Pavement Design*. 21 (4): 1170–1182.
13. Barzegari, M.R., Yousefi, A.A., and Zeynali, M.E. 2002. Bitumen modification via PS/PB Blend. *Iranian Journal of Polymer Science and Technology (Persian)*.
14. Vila-Cortavitarte, M., Lastra-González, P., Calzada-Pérez, M.Á., and Indacoechea-Vega, I. 2018. Analysis of the influence of using recycled polystyrene as a substitute for bitumen in the behaviour of asphalt concrete mixtures. *Journal of Cleaner Production*. 170 1279–1287.
15. Samper, M.D., Garcia-Sanoguera, D., Parres, F., and López, J. 2010. Recycling of expanded polystyrene from packaging. *Progress in Rubber, Plastics and Recycling Technology*. 26 (2): 83–92.
16. Nciri, N., Shin, T., and Cho, N. 2020. Towards the Use of Waste

Expanded Polystyrene as Potential Modifier for Flexible Road Pavements. *Materials Today: Proceedings*. 24 763–771.

17. SohrabVeiseh and Yousefi, A.A. 2021. Compressive behavior and thermal conductivity-density correlation of expanded polystyrene thermal insulators. *Iranian Polymer Journal*. (0123456789):
18. Ramli Sulong, N.H., Mustapa, S.A.S., and Abdul Rashid, M.K. 2019. Application of expanded polystyrene (EPS) in buildings and constructions: A review. *Journal of Applied Polymer Science*. 136 (20): 1–11.
19. Nassar, I.M., Kabel, K.I., and Ibrahim, I.M. 2012. Evaluation of the Effect of Waste Polystyrene on Performance of Asphalt Binder. *ARPN Journal of Science and Technology*. 2 (10): 927–935.
20. Al-Haydari, I.S.J. and Masued, G.G. 2017. Benefit of Using Expanded Polystyrene Packaging Material To Improve Pavement Mixture Properties. *Applied Research Journal*. 3 (11): 332–342.
21. Murana, A.A., Akilu, K., and Olowosulu, A.T. 2021. Use of expanded polystyrene from disposable food pack as a modifier for bitumen in hot mix asphalt. *Nigerian Journal of Technology*. 39 (4): 1021–1028.
22. TÜPRAŞ 2020. Product Specification.
23. Pfeiffer, J.P. and Van Doormaal, P.M. 1936. The rheological properties of asphaltic bitumens. *Journal of the Institute of Petroleum Technologists*. 22 414–440.
24. Fisher, R.A. 1992. Statistical methods for research workers. in: *Breakthroughs in Statistics*, Springer: pp. 66–70.
25. Bennert, T., Reinke, G., Mogawer, W., and Mooney, K. 2010. Assessment of workability and compactability of warm-mix asphalt. *Transportation Research Record*. (2180): 36–47.
26. Fontes, L.P.T.L., Trichês, G., Pais, J.C., and Pereira, P.A.A. 2010. Evaluating permanent deformation in asphalt rubber mixtures. *Construction and Building Materials*. 24 (7): 1193–1200.
27. Tabatabaee, H., Clopotel, C., Arshadi, A., and Bahia, H. 2013. Critical problems with using the Asphalt ductility test as a performance index for modified binders. *Transportation Research Record*. (2370): 84–91.
28. Ruan, Y., Davison, R.R., and Glover, C.J. 2003. An investigation of asphalt durability: Relationships between ductility and rheological properties for unmodified asphalts. *Petroleum Science and Technology*. 21 (1–2): 231–254.
29. Arslan, D., Gürü, M., and Çubuk, M.K. 2013. Bitüm ve Bitümlü Karışımların Performans Özelliklerinin Organik Esaslı Çinkofosfat Bileşiği İle Geliştirilmesi. *Gazi Üniversitesi Mühendislik Mimarlık Fakültesi Dergisi*. 27 (2):.
30. Elkholy, S.A., Abd El-Rahman, A.M.M., El-Shafie, M., and Abo-Shanab, Z.L. 2018. Physical and rheological properties of modified sulfur asphalt binder. *International Journal of Pavement Research and Technology*. 11 838–845.
31. Firoozifar, S.H., Foroutan, S., and Foroutan, S. 2011. The effect of asphaltene on thermal properties of bitumen. *Chemical Engineering Research and Design*. 89 (10): 2044–2048.
32. Alsheyab, M.A.T. and Khedaywi, T.S. 2013. Effect of electric arc furnace dust (EAFD) on properties of asphalt cement mixture. *Resources, Conservation and Recycling*. 70 38–43.
33. Read, J. and Whiteoak, D. *The Shell Bitumen Handbook Fifth edition, Exhibit 1008*; Thomas Telford Publishing: 2003.

Internet of Things Technology Based Agricultural Spraying Drone Design for Remote Farming Applications

Cemil Altın^{1*} , Hasan Ulutaş¹ , Eyyüp Orhan¹ , Orhan Er¹ , Volkan Akdoğan¹ 

¹ Yozgat Bozok University

*cemil.altin@bozok.edu.tr

*Orcid: 0000-0001-8892-2795

Received: 16 August 2020

Accepted: 15 September 2021

DOI: 10.18466/cbayarfbe.781368

Abstract

Internet of things and Drones are two new promising innovative technologies that are inevitable in the internet era. These technologies provide modern solutions for many fields. One of these fields is agriculture. Agriculture plays a pivot role for humankind because more than half of the World's population depends on agriculture. In this study internet of things, technology is applied to a drone that is capable of doing agricultural works like spraying, carrying, and real-time monitoring. An onboard android device that is mounted on the drone is used to manage the drone over the internet by a graphical user interface software designed within the study. The farmer communicates with onboard android device over the internet by remote desktop application to manage drone and get data. The drone will help farmers by getting live data from the farm and do necessary works remotely. This study aims to enable farmers to do remote farming. Agricultural activities have declined in recent years with the increase in migration from the village to the city. Thus, farmers will be able to make remote farming.

Keywords: IoT, Precise Farming, Remote Farming, Smart Farming, UAV

1. Introduction

The future of the smart World will be based on the Internet of Things (IoT). IoT is a vision about everyday systems and devices being connected to the internet[1]. This facilitates tracking, monitoring, data collection, analysis, and control. Another technology that is popular today is unmanned aerial vehicles (UAV) or drones. Drones are unmanned flying aircraft. The fact that drones have some advantages over other aircraft has brought drones forward. Drone's improved mobility enabled them to be used in every field. Today, drones are used in the military, construction, security, energy, agriculture, entertainment, etc. After referring to the IoT and drones that are up to date in the technology, it is necessary to conduct studies on the usability of these two technological products to facilitate and help human life. In other words in which sectors these two products can be used should be studied. To begin with, it is useful to take a look at the sectors that people are dealing with the most. According to the international labor organization, the largest share of the world population (29.6 percent) is engaged in agriculture, forestry, hunting, and fishing. In other words, it can be said that the number of agricultural workers is higher than in other sectors.

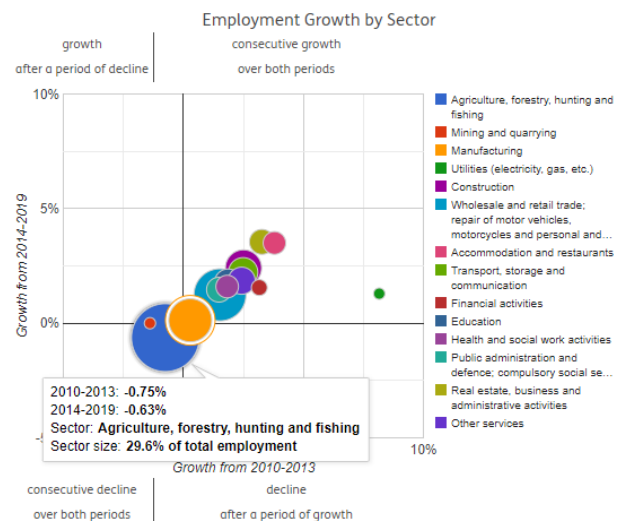


Figure 1. World's employment populations[2].

Figure 1 shows that agriculture has the biggest share. For this reason, the agriculture sector was chosen for the application.

After selecting the sector, it is necessary to identify existing problems in the relevant sector. The problem is

that agriculture decreases significantly as industrialization increases. As seen in the international labor organization report in Figure 1, the rate of those employed in agriculture has decreased continuously in the period between 2010-2013 (-0.75) and 2014-2019 (-0.63). The human population is increasing day by day and thus the need for food increases [3]. Food is a must for the human being to survive.

In recent studies, it is predicted that the world population and food demand will increase rapidly until 2050 [4,5,6]. Studies support each other that food production should increase significantly by 2050. Therefore, it is important to maintain and increase agricultural production. By using the technology in agriculture, it can easily find a solution to the increasing food demand.

Almost all drones are managed by short-range remote controllers. Due to the short-range problem, drones can only be controlled when they are within view. However, remote farming cannot be done with visual line of sight (VLOS) drones. For remote farming, beyond visual line of sight (BVLOS) drones are needed. Thus, the drone can be controlled even from a very long distance. BVLOS drones are usually drones that can be controlled via the internet. Currently, both agricultural drones and internet-controlled drones are available commercially. The term agricultural drone is a very comprehensive term. Because there are drones used in a wide variety of agricultural work. Agricultural drones in the literature search; it has been used in jobs such as seed sowing [7], pest detection[8], data acquisition[9], irrigation management[10], plant health monitoring[11,12,13], yield estimation[14], soil analysis[15] and spraying[16,17,18]. Although there are many spraying drones in the literature, IOT-based spraying drones have not been encountered. Existing drones are either spraying drones that can be managed by short-range remote controllers, or IOT based drones especially used for crop monitoring or data acquisition. For this reason, an IOT based spraying drone was designed to be used in spraying jobs in this study.

Multicopter drones are the most suitable unmanned aerial vehicle structure for spraying due to their ability to hang in the air, move slowly and push the drug towards the plant with the help of propellers. For this reason, a multicopter drone was used in the study.

In this paper, a product that is pioneered the use of technology in agriculture and which is important and necessary in the field of agriculture was developed. The main objective of this study is the design of a spraying drone that allows the use of technology in agriculture with affordable price and superior features. Since the designed drone has direct IoT technology, it provides superiority to drones managed over the internet via remote control. Its high carrying capacity of 20 liters is higher than the carrying capacity of many drones.

2. Materials and Methods

2.1. Chassis Design

Spraying drones are large-sized drones that can lift a heavy load because they carry several liters of liquid and spraying system components. In this study, a drone that can handle approximately 20lt of liquid was designed. Therefore, the chassis must be strong, durable, and light. Aluminum was used in chassis construction because it is durable, cheap, light, and easily available. Drones are multi-rotor unmanned aerial vehicles. Generally, drones with 4, 6, or 8 rotors are available. The number of rotors changes according to the weight of the load to be lifted or according to the motor-propeller pair used. It has been calculated that a 6 rotor drone can handle the designed structure when using a predetermined motor-propeller pair according to price and performance. The designed body consists of only 6 aluminum rods. 6 aluminum rods are uniquely assembled to create a large area in the middle where parts of the drone and spray system can be placed.

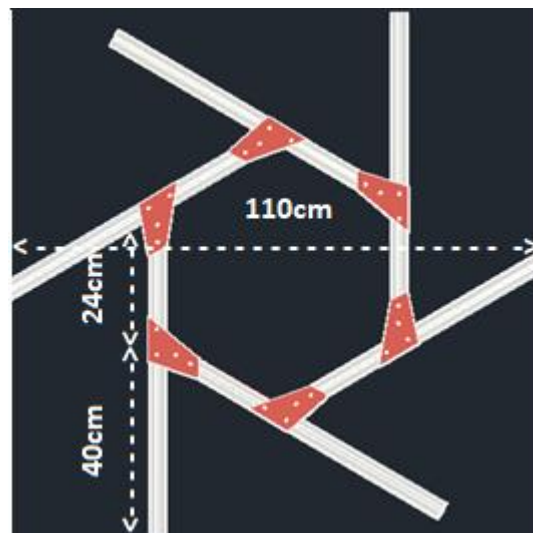


Figure 2. CAD drawing of the unique chassis.

The drone chassis shown in Figure 2 is of a unique structure and is very simple, robust, and reliable. By changing the connection points of the 6 rods to each other, the size of the area in the center can be adjusted easily. The rods are fixed to each other so that the 20lt liquid drum can be easily mounted in the center of the drone. The distance between two opposing rotors is 110cm. The drone dimensions are shown in Figure 2.

2.2. Wiring Diagram and Controller

The drone has 6 rotors (hexacopter structure) and its electrical connection diagram is given in Figure 3. As seen in Figure 3, brushless motors are used in the drone. Electronic speed controllers (ESC) are used to control brushless motors, and the PWM signal required for ESCs is sent by the microprocessor through the flight software.

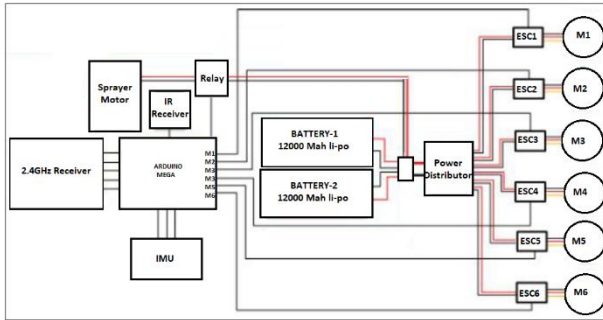


Figure 3. Electrical wiring diagram of the drone.

Flight software is not commercial software, it is original software developed by our team. Therefore, in case of any additions or changes, it can be easily overcome. Thus, a flexible working environment is provided. Thanks to the electrical power distributor, the necessary electrical power is given to the ESCs and motors. For spraying, a motor and a relay for turning the motor on and off were used. Commands from the IoT system are transmitted to the drone control system via an infrared receiver. In addition to being able to control the drone over the internet, it can also be controlled with a short-range remote control. For this, a 2.4 GHz radiofrequency (RF) receiver is integrated into the system.

The wiring diagram has been introduced, and now information about drone control and controller design will be given.

Drones are vehicles that move in x, y, and z axes. Control is based on controlling the angle the drone chassis has to do with the axes. As in Figure 4, it is thought that the center of the drone is placed in the origin, the front-rear direction of the drone is placed in the x-axis direction, the right-left direction of the drone is placed in the y axis direction. The angle between the front-rear direction of the drone and the x-axis is called pitch angle, the angle between the right-left direction of the drone and y-axis is called roll angle and the angle of the drone center with the origin in the z-axis is called the yaw angle.

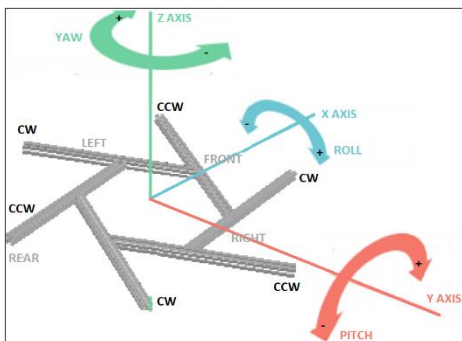


Figure 4. Yaw, pitch, roll angles, and motor rotation directions.

Yaw, pitch, and roll angles are controlled by rotating the drone rotors at different speeds. For example, if the motors on the left are rotated faster than the motors on the right, the drone moves to the right by making a roll angle in the + direction. Likewise, if the motors in the front are rotated faster than the rear ones, the drone makes a pitch attitude in the - direction and moves back. Or if the clockwise rotating motors are rotated faster than the counter-clockwise rotating motors, the drone would turn in the - yaw direction and turn counterclockwise.

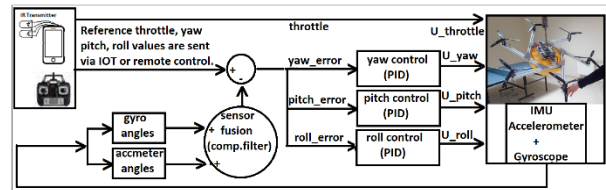


Figure 5. Control system flow chart.

Figure 5 shows the control system flow diagram. PID controller is used as the controller. The PID controller tries to eliminate the error by comparing the reference input values with the current values of the system. PID works in the same way on the drone. After the reference yaw, pitch, and roll angles are sent by the user, PID works to eliminate the error by comparing reference angles with the current angles of the drone measured by the inertial measurement system (IMU). PID controller performs these operations mathematically with the following equation.

$$u(t) = K_p e + K_i \int_0^t e dt + K_d \frac{d}{dt} e \quad (2.1)$$

PID stands for proportional, integral, and derivative. Here, the error (e) is multiplied by the K_p coefficient and approached to the reference. The error is eliminated over time by taking the integral of the error and multiplying it by the K_i coefficient. The sudden changes of the error are absorbed by taking the derivative of the error and multiplying it by the K_d coefficient. Many systems can be controlled with the PID controller. However, the K_p , K_i , and K_d coefficients are different for each different system. It is important to adjust these coefficients correctly, because the more accurate the adjustment is, the better the design of the controller. There are many different combinations of K_p , K_i , and K_d values for flight. However, one of them is the most ideal one. Adjusting means finding the most ideal coefficients, or those closest to it. Although these parameters are calculated by methods such as the Ziegler-Nichols method, it is more effective to adjust by experimenting in practice. While adjusting by experimenting, random values are determined first, then the coefficients are increased or decreased according to system response. While adjusting, it should be noted that K_p is responsible for the system speed, K_i for error elimination, and K_d for eliminating fluctuations in the

system response. It is very difficult to adjust these coefficients experimentally in some systems, especially in non-stationary moving systems. Drones are one of these systems because of their three-dimensional movement. Because the coefficients should be in the range of coefficients required for a successful flight. If coefficients are chosen outside of this range, the drone will crash and be damaged so it will damage the environment and living things. Thus, drone production will be very costly and dangerous. To avoid such disadvantages, an adjustment should be made on a test platform. On the test platform, the drone is free as if flying in the air, but it cannot change position. In other words, it performs yaw, pitch, and roll movements, but the changing position is prevented. Within the scope of the study, a unique test platform has been developed as shown in figure 6.



Figure 6. Drone test platform.

The test platform is designed in such a way that the drone can make its yaw, pitch, and roll movements without changing its position. To do this, the drone is attached to the flexible joint from the center. The flexible joint used is the car joint rod shaft. Thanks to the test platform, the controller parameters can be adjusted easily and the drone has been made to fly without damaging anything.

The last thing to mention is the IMU. With IMU, the instantaneous yaw, pitch, and roll angles of the drone are fed back to the controller as shown in Figure 5. The controller controls the drone from this information that comes with feedback. The IMU includes a gyroscope and an accelerometer to calculate the angles. The accelerometer measures linear accelerations, while the gyroscope measures angular acceleration. The data of the two sensors are combined with sensor fusion algorithms to obtain the drone's yaw, pitch, and roll angles. Many sensor fusion algorithms are available. Some of those; Kalman Filter, first-order complementary filter, second-order complementary filter, and yaw compensated complementary filter [19]. Although these sensor fusion algorithms do the same job, they differ in speed and immunity to noise. In the tests performed, it was observed that the most successful one of these algorithms for the designed drone is the yaw compensated complementary filter. Mathematically, how angles are obtained by combining raw sensor data is presented with the following

equations. The calculations in the following equations are made for roll angle only, calculations for other angles are similar.

Gyro rate to gyro angle integration;

$$roll_{integration} = roll_{angle} + roll_{gyro_{raw}} * dt \quad (2.2)$$

Yaw rate integration to roll angle;

$$\int roll_{integration} + roll_{angle} * \frac{\pi}{180} * yaw_{gyro_{raw}} * dt \quad (2.3)$$

Error correction with roll accelerometer data

$$roll_{error} = roll_{accel} - roll_{integration} \quad (2.4)$$

$$roll_{angle} = roll_{integration} + time_{cons} * roll_{error} \quad (2.5)$$

Here the time constant is chosen between 0 and 1.

2.3. IoT System

One of the most important devices of the IoT revolution is smartphones that have become a part of our lives. For this reason in this study, IoT application was carried out using an onboard smartphone. The implemented system is presented in Figure 7 and is unique.

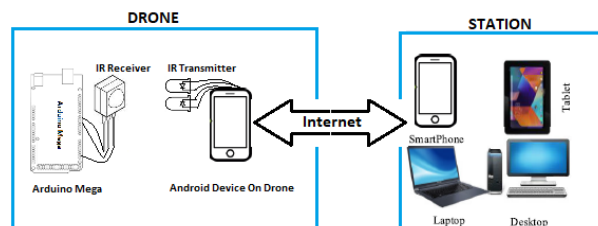


Figure 7. The implemented IoT system.

As seen in Figure 7, there is a smartphone on the drone. When the user wants to control the drone, he/she accesses the smartphone on the drone via another smartphone, tablet computer, or PC that can connect to the internet. This inter-device access is realized with the remote desktop application. Thanks to remote desktop access, it is possible to use the phone on the drone and send commands to the drone using it. It is not possible to do this directly. It is also necessary to establish a connection between the phone on the drone and the microprocessor containing the drone flight software. This connection can be made by wi-fi or Bluetooth. For this, it is necessary to attach a wi-fi or Bluetooth module to the microprocessor. It is possible to see many studies or applications in the literature that make connections in this way. This causes extra costs and can lead to negativity due to disconnection problems. In this case, the unmanned aerial vehicle will travel freely or even crash. A unique system has been proposed to overcome these problems. Wi-fi or Bluetooth is not used in the proposed system. Therefore, there is no problem of connection or disconnection. The proposed system is the same as the communication between television and remote control. This communication is infrared (IR)

communication. The receiver is always ready to receive data from the transmitter. As soon as data is sent from the transmitter, the receiver starts to receive the data, and communication is established. This system is very useful, reliable, cheap, and simple. Its cost is also very low because it consists of one IR receiver LED and two IR transmitter LEDs. In this system, the encoded audio file played from the smartphone is converted to infrared waves. In other words, the smartphone gains infrared remote controller features like a TV remote controller. One IR receiver is attached to the microprocessor on the drone. Two IR transmitter LEDs are used in the circuit that converts the audio data from the smartphone's headphone output to IR signal, as in Figure 8.

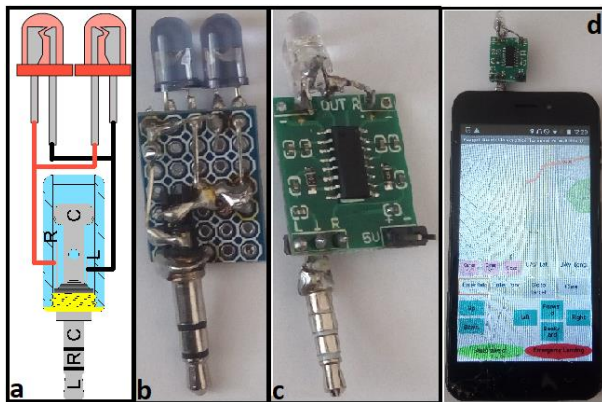


Figure 8. The circuit that converts encoded sound waves to IR waves.

The circuit that converts the sound to the IR signal is simple and it has two types. The first circuit is the circuit given in figure 8.b and is the same as the circuit given in figure 8.a. This circuit is for the sound card electrically powerful. It can be used by plugging it directly into the headphone jack. The second circuit is given in figure 8.c. The difference between this circuit and the other circuit is that it is used with a mini audio amplifier. It is necessary to apply external 5V DC to this circuit. From the moment the circuit is attached to the smartphone, it is possible to manage the device that works with an IR remote controller. Figure 8.d shows the circuit connected to the headphone output of the smartphone. In other words, the smartphone has become a remote control that manages many electronic devices such as televisions, air conditioners, and stereos. All that needs to be done is to convert the different IR signals emitted by the original remote controller keys into an audio file. Because the designed circuit is a circuit that converts audio signals into IR signals. How this conversion process is done can be learned in detail from this reference[20].

2.4. Smartphone User Interface Application Design

A useful user interface design has been developed within the framework of the study. The application is an android based application. The android platform was

chosen because it is widely used, easy to develop, and cheap. The application is installed on the android smartphone on the drone. This application sends encoded audio to the device that converts the audio to IR. It is also an application that easily accesses the hardware such as the camera and GPS of the android phone it is installed on. The user uses this application by accessing the smartphone on the drone with a remote desktop connection from a computer, tablet, or other smartphones. Many remote desktop applications are available. TeamViewer application was used in the experiments. It can be downloaded for free on the Android market. Thanks to the remote desktop software, another paired device can be accessed and managed. In this study, the drone is also managed with the user interface developed by accessing the smartphone on the drone via the remote desktop application wherever you are in the world.



Figure 9. Android-based user interface application.

Figure 9 shows the screenshot of the designed user interface. To mention briefly; the Camera_1 button opens the rear camera of the smartphone on the drone, this camera shows the earth while the drone is air. The Camera_2 button opens the front camera of the phone, this camera shows the sky when the drone is in the air. The camera view is instantly seen in the upper left half of the user interface. The camera view is closed with the Close button. In the upper right half of the user interface, the Google Maps application instantly shows the position of the drone on the map, the coordinate information is also shown just below. For this, it is necessary to have a GPS sensor in the onboard android phone. With the control buttons on the lower half of the user interface, the drone is moved in the directions written on the buttons. These buttons are assigned differently coded sound waves. Pressing the button

plays a short sound from the phone's music player. The played sound is converted into IR waves with the device connected to the headphone output and a command is sent to the drone. Since the response of the command generated by each key is pre-coded into the drone flight software, the drone knows which button is pressed and acts accordingly.

2.5. Spraying system

The spraying system consists of one yellow-colored 20 lt water container mounted under the drone (shown in Figure 6), one small water motor in the container, and six sprinklers. The durable water container, which has a large surface area, is also used as a stand.

While designing the spraying drone, elements with a high price/performance ratio were preferred. The most important of these elements are electric motors. As a result of the market research, 380 kV motors with a power of 2665 W, operating with 22.4 V, which have a higher price-performance ratio than their competitors, were preferred. The thrust of these electric motors determined the other elements of the aircraft and the load it could handle. The thrust force of the selected electric motor and propeller pairs was calculated with the following formula.

$$T = [(\eta x P)^2 x 2 \pi x r^2 \rho]^{1/3} \quad (2.6)$$

Here;

η : propeller efficiency (between 0.7-0.9), preferred:0.8

P : electric motor power (Watt), preferred:2665 Watt

r : radius of propellers (m), preferred:0.203 m

ρ : air density (1.22 kg/m³)

Calculated thrust is =112.2 N,

1 N=0.101972 kgf

Then thrust is = 11.421 kgf for one electric motor.

The UAV has 6 motors, so total thrust generated by all motors is 6x11.421=68.526 kg.

This means that the preferred electric motors and propellers can handle a total load of 68,526 kg. However, for a successful flight, electric motors need to provide 1.5-2 times the thrust of the total weight of the aircraft. According to this calculation, the total weight of the aircraft should be at most 68.526/2=34.263 kg. Since the curb weight of the aircraft is 16,161 kg, it can carry 34.263-16.161=18.102 kg = 18.102 lt (water) cargo. Of course, this is the case when the factor of safety 2 is selected. If the safety factor is chosen between 1.5 and 2, there will be a carrying capacity of around 20 liters, so a 20lt tank has been selected.

For loads up to 20 lt, the desired amount of pesticide can be placed in the container and spraying can be done without making any changes. It is not suitable for loads more than 20 liters due to the maximum carrying limit of the aircraft.

Since the spraying process is not done autonomously, the success of the spraying depends on the user experience and the characteristics of the pesticide. The pesticide will be sprayed by the user at the optimum level.

2.6. Cost of the System

The cost of the total system is given in Table 1.

Table 1. Cost of the system.

	Product	Qty	Unit(\$)	Total (\$)
1	20lt Container	1	4,1	4,1
2	Aluminium sigma rod 35x35	6mt	65	65
3	Connection parts	1	12	12
4	22.2V Li-Po Battery 12000mAh 25C-6s	2	282	564
5	Atmel microprocessor	1	30	30
6	9 Axis IMU	1	37	37
7	380KV Brushless Motor	6	62,89	377,34
8	200A ESC	6	36,11	216,66
9	3-blade Propeller 16x10	6	18,98	113,88
10	IR transmitter LEDs	2	0,25	0,5
11	IR receiver	1	0,5	0,5
12	PAM8403 mini Audio amplifier	1	1	1
13	2.4 GHz Remote Controller	1	59,5	59,5
14	Water pump	1	10	10
15	Li-po charger	1	58	58
16	Old android smartphone	1	---	---
TOTAL				1549,48\$

3. Results and Discussion

As a result, a drone with different features than existing drones in the literature was designed and successfully flown.



Figure 10. An image from the test flight.

Especially the chassis design and IOT system are different and unique from existing drones. The center of the chassis is designed to expand and contract easily according to the water container to be mounted. Thus, for a heavy lift drone, there is easily place for all the elements. Using an onboard android system for the IoT system and controlling it with a remote desktop application has provided a lot of flexibility and convenience. The most important of these facilities is that the applications available in the android market and used for agricultural purposes are easily and instantly installed and the plant or field is analyzed and intervened quickly. In addition, a user with an android phone can have an IoT system at no extra cost. Thanks to the recommended plug-and-use audio-infrared converter, the user will be able to control drones from anywhere in the world. Thanks to the android smartphone, the user will not spend money on expensive equipment such as a camera, GPS, modem. In the IoT system, the communication between the internet provider device and the microprocessor responsible for flight is unique in that it eliminates connection problems and communication problems. Thanks to the developed original flight software and test platform, all-purpose development and updates can be made.

3.1. Comparison With Other Agricultural UAVs

Compared to other prominent agricultural drone manufacturers, the prototype sprayer drone reveals that it is the most economical UAV in its class with a 20-liter payload and IOT technology.

	Manufacturer	IOT	Capacity	Price (\$)
1	Our UAV	Directly with UAV	20 l	1549.48\$
2	DJI Agras T20	Via Remote controller	20 l	16511.9\$
3	Xaircraft P20	Via Pilot Phone	10 l	21500\$
4	RPA Pelicano	Via Remote controller	16 l	No information
5	SHIYANLI	Via Remote controller	20 l	19054\$
6	IHA TR 5	Via Remote controller	20l	21186\$

Comparison made in terms of IoT, tank capacity and price. Except for these drones, drones with lower specifications are not included in the comparison. Fixed-wing unmanned aerial vehicles and helicopters are also not included in the comparison. The compared drones consist of drones that dominate the market with similar features to the drone we have designed. Our drone is an affordable drone compared to other drones. As can be seen, all drones can be connected to the internet and controlled via their remote controllers. In other words, there is an intermediary remote controller between the internet and the drone. Although these drones are controlled over the internet, they cannot go out of the remote controller range. In other words, this system works when the remote controller is close to the

drone. But in our design, the drone is directly connected to the internet and there is no need for an intermediary remote controller. It doesn't matter if the remote controller is near or far. In addition to the price advantage, the advantage of direct internet connection makes our drone superior.

4. Conclusion

In a conclusion, a product has been designed to lead the fusion of technology and agriculture in recent years, when agriculture 4.0 has been spoken in the world with industry 4.0. An innovation that makes agriculture easy and attractive beyond traditional farming methods has been introduced. Thanks to this innovative technology, time and labor are saved. Spraying in agriculture is one of the most important and difficult jobs. The spraying process, which is done by diluting with tons of water with traditional spraying methods, has been ended and it has been possible to spray without wasting water. Thus, waste of water is prevented. In the traditional method, due to the difficulty of spraying, the whole field was sprayed, but thanks to the proposed product, regional spraying was provided instead of the whole. Thus, the environment was protected and expenses were reduced by preventing excessive use of the drug. The proposed system allows comfortable spraying, especially in difficult, rugged, and hilly terrain. Due to the ease of spraying, there is an increase in yield. In addition to these, the difficulty of going to the field for spraying and other works has been eliminated, and it has become possible to obtain information about the field and spraying without leaving the house. Since the product makes it easier to do agricultural work remotely via the internet, agriculture is continued even if there are migrations to big cities.

Novelty of this study is the design of a spraying drone that allows the use of technology in agriculture with affordable price and superior features. Since the designed drone has direct IoT technology, it provides superiority to drones managed over the internet via remote control. Its high carrying capacity of 20 liters is higher than the carrying capacity of many drones. Another original aspect is that it offers sustainable and budget-friendly solutions for precision agriculture. Sending commands to the drone with remote desktop connection through the android interface developed by us by converting the audio signal into infrared signals is unique.

Acknowledgement

This study was supported by Yozgat Bozok University with the BAP project number 6602b-MMF/18-194.

Author's Contributions

Cemil ALTIN: Drafted and wrote the manuscript, performed the experiment and result analysis.

Hasan ULUTAŞ: Performed material purchase and assembly works.

Eyyüp ORHAN: Performed the chassis design and CAD drawing.

Orhan ER: Supervised the study's progress.

Volkan AKDOĞAN: Assisted in some works.

Ethics

There are no ethical issues after the publication of this manuscript.

References

1. S. K. Mohapatra, J. N. Bhuyan, P. Asundi, and A. Singh, 2016. "A Solution Framework For Managing Internet Of Things (Iot)," *The International Journal of Computer Networks & Communications.*; 8(6):73-87 doi: 10.5121/ijcnc.2016.8606.
2. "World Employment and Social Outlook: Which sector will create the most jobs?" https://www.ilo.org/global/about-the-ilo/multimedia/maps-and-charts/WCMS_337082/lang-en/index.htm (accessed Jul. 22, 2020).
3. R. Vidhya and K. Valarmathi, 2018. "Survey on Automatic Monitoring of Hydroponics Farms Using IoT," in *Proceedings of the 3rd International Conference on Communication and Electronics Systems ICCES 2018*; 2018: 125-128. doi: 10.1109/CESYS.2018.8724103.
4. B. Basnet and J. Bang, 2018. "The State-of-the-Art of Knowledge-Intensive Agriculture: A Review on Applied Sensing Systems and Data Analytics," *Journal of Sensors*; 2018: 1-13. doi: 10.1155/2018/3528296.
5. K. W. Jaggard, A. Qi, and E. S. Ober, 2010. "Possible changes to arable crop yields by 2050," *Philosophical Transactions of the Royal Society B: Biological Sciences*; 365(1554): 2835-2851. doi: 10.1098/rstb.2010.0153.
6. S. Chakraborty and A. C. Newton, 2011. "Climate change, plant diseases and food security: An overview," *Plant Pathology*; 60(1): 2-14. doi: 10.1111/j.1365-3059.2010.02411.x.
7. M. A. Jubair, S. Hossain, M. A. Al Masud, K. M. Hasan, S. H. S. Newaz, and M. S. Ahsan, 2018. "Design and development of an autonomous agricultural drone for sowing seeds," *IET Conference Publications*; 2018 (CP750): 6-9. doi: 10.1049/cp.2018.1598.
8. D. Gao, Q. Sun, B. Hu, and S. Zhang, 2020. "A framework for agricultural pest and disease monitoring based on internet-of-things and unmanned aerial vehicles," *Sensors (Switzerland)*; 20(5): 1487. doi: 10.3390/s20051487.
9. M. V. Suhas, S. Tejas, S. Yaji, and S. Salvi, 2018. "AgrOne: An Agricultural Drone using Internet of Things, Data Analytics and Cloud Computing Features," *2018 4th International Conference for Convergence in Technology. I2CT 2018*; 2018: 1-6. doi: 10.1109/I2CT42659.2018.9057995.
10. M. Romero, Y. Luo, B. Su, and S. Fuentes, "Vineyard water status estimation using multispectral imagery from an UAV platform and machine learning algorithms for irrigation scheduling management," *Computers and Electronics in Agriculture.*; 147: 109-117. doi: 10.1016/j.compag.2018.02.013.
11. M. Reinecke and T. Prinsloo, 2017. "The influence of drone monitoring on crop health and harvest size," *2017 1st International Conference on Next Generation. Computing Applications NextComp 2017*; 2017: 5-10. doi: 10.1109/NEXTCOMP.2017.8016168.
12. L. G. Santesteban, S. F. Di Gennaro, A. Herrero-Langreo, C. Miranda, J. B. Royo, and A. Matese, 2017. "High-resolution UAV-based thermal imaging to estimate the instantaneous and seasonal variability of plant water status within a vineyard," *Agricultural Water Management.*; 183:49-59, doi: 10.1016/j.agwat.2016.08.026.
13. B. Allred, N. Eash, R. Freeland, L. Martinez, and D. B. Wishart, 2018. "Effective and efficient agricultural drainage pipe mapping with UAS thermal infrared imagery: A case study," *Agricultural Water Management.*; 197:132-137, doi: 10.1016/j.agwat.2017.11.011.
14. I. Wahab, O. Hall, and M. Jirstrom, 2018. "Remote Sensing of Yields: Application of UAV Imagery-Derived NDVI for Estimating Maize Vigor and Yields in Complex Farming Systems in Sub-Saharan Africa," *Drones*; 2(3): 28. doi: 10.3390/drones2030028.
15. J. Huuskonen and T. Oksanen, 2018. "Soil sampling with drones and augmented reality in precision agriculture," *Computers and Electronics in Agriculture.*; 154: 25-35. doi: 10.1016/j.compag.2018.08.039.
16. S. Spoorthi, B. Shadaksharappa, S. Suraj, and V. K. Manasa, "Freyr drone: Pesticide/fertilizers spraying drone - An agricultural approach, 2017." in *Proceedings of the 2017 2nd International Conference on Computing and Communications Technologies, ICCCT 2017*; 2017: 252-255. doi: 10.1109/ICCCT2.2017.7972289.
17. C. KOÇ, 2017. "Tarımda Pestisit Uygulama Amacıyla Ekonomik Bir Drone Tasarımı ve İmalatı," *Journal of Agricultural Faculty Gaziosmanpasa Univ.*; 34(2017-1): 94-103. doi: 10.13002/jafag4274.
18. B. Dai, Y. He, F. Gu, L. Yang, J. Han, and W. Xu, "A vision-based autonomous aerial spray system for precision agriculture, 2017." in *2017 IEEE International Conference on Robotics and Biomimetics*; 2018:1-7, doi: 10.1109/ROBIO.2017.8324467
19. "Shane Colton: Fun with the Complementary Filter / MultiWii." <http://scolton.blogspot.com/2012/09/fun-with-complementary-filter-multiwii.html> (accessed Aug. 15, 2020).
20. "Remote control - 2: Sample your remote | Jumping Jack Flashweblog." <https://jumpjack.wordpress.com/2008/05/22/remote-control-2/> (accessed Aug. 16, 2020).

Design and Manufacturing of The Prototype System for Recycling Waste Generated in 3 Dimensional Production to Filaments by Fused Deposition Modeling Method

İlker Ertuna^{1*} , Uğur Can Topçu¹ , Çağrı Yalçınkaya¹ , Defne Açıköz¹ , Ezgi Cırık¹ , Ceren Göde² 

¹ Menderes Tekstil A.Ş. R&D Center, Denizli, Turkey

² Pamukkale University, Vocational School of Technical Sciences, Machinery and Metal Technologies Department, Denizli, Turkey

*ilkerertuna@menderes.com

*Orcid: 0000-0001-5388-6819

Received: 28 January 2021

Accepted: 31 August 2021

DOI: 10.18466/cbayarfb.869473

Abstract

Nowadays, three-dimensional (3D) printers have come to an important place in many sectors with the development of technology. 3D Printers that provide layered manufacturing have different raw materials requirements to be able to work the substance called filament is one of the raw materials of 3D printers. The most preferred raw material for a 3D printer is filament compared to other raw materials. The layered manufacturing device may take wrong printing or undesired printing for any reason. It is important to be able to recycle the product resulting from these printings. The aim of this work is to make the filament re-usable for layered manufacturing. The importance of this study is to create the desired diameter filament and make it usable in the industrial field. With a structure consisting of crushers, extrusion, water and air cooling units, pulling, rotary, wrapper and automatic control units, a system including mechanical, electronic and software processes was designed. With this designed system, an average of 1.75 mm diameter filament to be used in 3D printers was successfully obtained in the wrapper unit and filaments of desired dimensions were obtained within the scope of the study.

Keywords: Filament, waste recycling, layered manufacturing, 3D printer, prototype

1. Introduction

Fused Deposition Modeling technique (FDM) is one of the solid-based rapid prototyping systems. In this system, there are all forms in solid state. The solid state in the system can be in the form of filaments, rolls, sheets and granules [1]. The use of some filaments is more preferred in 3D printers. Polylactic acid (PLA) is a lactic acid-based polymer composed of renewable resources that have a greater impact area than petroleum-based plastics [2]. Acrylonitrile butadiene-styrene (ABS) material is one of the polymers used in rapid prototyping technology, which is widely preferred in FDM that was developed by Stratasy Inc. [3-4]. The gain in pre-selection of ABS and PLA filaments emerged after exchanging ideas with 3D printer suppliers [5]. In the FDM printer, the feedstock containing filament is contained in the wrapper and connected to the extrusion nozzle.

The nozzle has a heater block that melts a thermoplastic polymer. The parameters to be arranged in the printer ¹software are flow and temperature. These parameters should be arranged according to the desired printing [6].

Studies on the temperature range of ABS and PLA filaments to be heated and determining the filling parameters to be arranged during the re-printing of the filament successfully obtained within the scope of this study play an important role in terms of prediction. The inferences for the determination and use of ABS and PLA filaments in the prototype designed and manufactured waste recycling system within the scope of the study were determined by researching academic sources [7-14]. Some of the information during the printing of the filaments manufactured as a result of the study were obtained by analyzing the article [15]. Waste materials

¹ Presented at the 3rd National University-Industry Cooperation, R&D and Innovation Congress

generated during 3D printing such as filament ends, scraps and backers importance to the environmental side of FDM.

Generating recycled filaments to actualize waste management is very important for sustainability [16]. Commercial printing filaments are generally polymers such as PLA or ABS while composites are used to create objects by way of conductive, dielectric, and magnetic materials. 3D prints that are printed using plastics are advantageous [17]. These advantages are especially precious for research apparatus and specialist equipment where new designs need to be tested in biomedical applications such as 3D printed aortic valves [18]. Many companies around the world develop and improve their extruders with variations during printing. The decreasing in the cost of both material extrusion printers and plastic extruders was the starting point for recycling polymer waste and parts such as scrap support. In addition, significant economic profits are provided with the filament produced from polymer pellets. The concept of recycling enriched by layered manufacturing has increased its interest from 2008 to the present and has become a reason for the preference for many countries. Typically, non-recyclable polymers such as ABS and PLA were also obtainable in a recyclable format [19]. 3D printers, which play an active role in layered manufacturing technology, cause damage due to go for prints waste caused by the inability to present the desired product to the user and the drying of the filament on the printer (i.e. the raw material of the printer), which has not been properly protected. As a result of the damage, the idea of recycling the filament has emerged and this has been the main problem of this study. In the literature studies, a commercial PLA filament has an average tensile strength of 60 MPa; it is expected that the tensile strength of any piece to be produced in the same cross-sections from the pure PLA filament is also close to that value [20]. In literature has many different studies of PLA. For example, this study investigated the effects of FDM (Fused Deposition Modeling) process parameters on mechanical properties (tensile strength, elongation, and impact strength) of 3D (three dimensional) printed PA12 (Polyamide12) samples using Taguchi method. In the experimental design (L8), four different layer thickness (0.1, 0.15, 0.2, 0.25 mm), extruder temperature (250 and 260°C), filling structure (Rectilinear and Full Honeycomb), and occupancy rate (25 and 50%) were determined [21]. The aim of our study is to recycle the wrong prints created by 3D printers during printing, the unused parts of the support pieces in the main print, as well as the waste filament that was not completed due to any defect. Subsequently, it is melted at desired temperatures (PLA: 200 °C, ABS: 225, °C) after

passing through the crusher unit and cooled by cooling units at the end of the extrusion unit. After adjusting the tension of the line with the pulling and rotary units, it is made ready for the 3D printer by virtue of the wrapper unit.

2. Material and Methods

2.1 Crusher Unit

Firstly, the filaments to be recycled were specified within the scope of this study. The filaments specified by using the crusher unit consisting of 2 stages were made to suitable sizes for the extruder entrance. A double-stage and screen crusher design was commenced. In the current layout, the blade thickness is 5 mm in the rough breaking (1st Stage) section. The blade thickness is 3 mm in the fine breaking (2nd Stage) section. Each stage is driven by a separate DC gearmotor.

Table 1. Materials Used in Crusher Unit

Quantity	Product name	Description
2	Gear	M1.5 DP= 42 DE=45 Z=28 d=30 D=12
2	Gear	M1 DP= 22 DE=24 Z=22 d=18 D=8
2	Coupler	8x8 Aluminum Shaft Coupling
2	Motor	12v 15 Rpm L Dc Gearmotor
10	Bearing	16x8x5 radial bearing
4	Square shaft	8x8mm 215mm Square shaft
4	Sigma Profile	20x20 266mm Sigma profile
2	Sigma Profile	20x20 300mm Sigma profile
1	Sigma Profile	20x20 280mm Sigma profile
4	Sigma Profile	20x20 148mm Sigma profile
2	Sigma Profile	20x20 190mm Sigma profile
2	Sigma Profile	20x20 104mm Sigma profile
2	Shaft	5x148mm Shaft
2	Motor Driver	Dc Motor Driver
200	Bolt	YSB M5x10
100	Bolt	YSB M5x15
200	Nut	M5/20 Sigma Profile knurled channel nut
150	Corner joint	20x20 Sigma Profile Corner Joint
1	Laser Cut	Laser cutting for crusher

Roller bearings are used to provide movement at each stage and gears with a 1: 1 ratio to transfer the movement. The materials used in the crusher unit are shown in Table 1.

The crusher unit is shown in Figure 1.

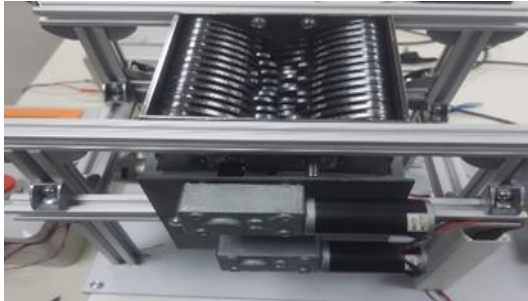


Figure 1. Crusher Unit

2.2. Extrusion Unit

The extrusion unit is essentially designed as 7 pieces. These are reducer motor, input feed silo, extrusion shaft, extrusion shaft sleeve, nozzle, heater cartridge and thermocouple. Extrusion shaft and sleeve on the system are determined according to ABS plastic material. The number of spirals on the extrusion shaft, the distance between the spirals and the helix angle are determined according to the type of material to be melted. Subsequently, the power of the heater cartridges was determined and a sleeve design proper for the shaft was made [22].

As a result of the tests and evaluations made, it was seen that ABS plastic was melted in the desired properties. The choice of dc gearmotor was determined after calculating the power required for pushing the molten, semi-melted and solid plastic. The entire extrusion unit is shown in Figure 2.



Figure 2. Extrusion Unit

2.3. Cooler Units

The cooling section on the system consists of two parts. These are water-cooling unit and air-cooling unit.

2.3.1. Water-Cooling Unit

In the water-cooling unit, the hot filament coming out of the extrusion unit is passed directly through the water and cooled. The water in the overflow chamber and the water in the main chamber were circulated with the help of the water pump on the unit. The water was ventilated and the heat on it was removed. The water-cooling unit is shown in Figure 3.



Figure 3. Water-Cooling Unit

2.3.2. Air-Cooling Unit

An air-cooling unit is designed to dry the wet filament coming out of the water-cooling unit and to remove the remaining heat. The air-cooling unit is shown in Figure 4. The materials concerning to the cooling units are given in Table 2.

Table 2. Materials of Refrigerating Units

Material Type	Quantity / Description
Ø5x100mm shaft	2
626zz roller	6
3d printer prints	Refrigeration unit auxiliary materials
Ø5x60mm shaft	1

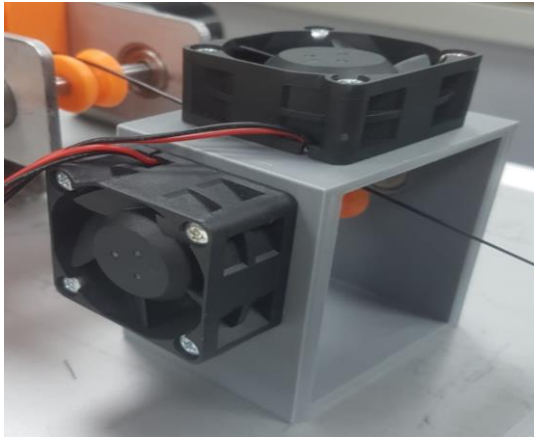


Figure 4. Air Cooling Unit

2.4. Pulling Unit

A suitable diameter of filament is formed by calibrating the speed of the line with the pulling unit. Silicone wheels are used in the unit due to pull the filament more effectively. The suitable torque is provided for the maximum and minimum speeds of the line with the DC gearmotor used on the system. The length of the filament produced on the line is determined with the encoder on the system [23]. The materials used in the pulling unit are given in Table 3.

Table 3. Materials of Pulling Unit

Material Type	Quantity / Description
DC gearmotor	12V-30 revolution per minute
Silicon wheels	51x30mm 2 pieces
6x100 mm shaft	2 pieces
6x60 mm shaft	2 pieces
Tow spring	2 pieces
Encoder	Omron encoder
Sheet metal cutting production	Auxiliary parts
3d printer parts	Pulling unit auxiliary materials
6x8 Coupler	2 pieces
6x6 Coupler	2 pieces
626zz Roller	6 pieces

Pulling unit is as shown in Figure 5.

3. Results and Discussion

The following results are obtained, if the innovative aspects and determinations of the filament recycling system designed and manufactured are analyzed.

- By virtue of the designed filament recycling system, the inert filaments formed in

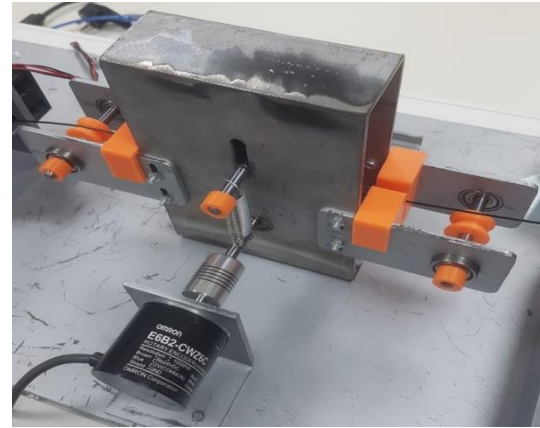


Figure 5. Pulling Unit

2.5. Wrapper Unit

The wrapper unit consists of two parts. These are divided into rotary and pulley winding. It is aimed to reel up the filament properly in the rotary part. For this reason, it operates automatically at a speed that can be arranged linearly on the screen. A conical plug-in system is designed that can be easily demounted and mounted to the wrapper part. However, the pulley can be easily mounted with its full or empty state. With the DC gearmotor in the wrapper part, speed arranged and torque control can be done in empty or loaded state. The image of the wrapper unit is given in Figure 6.

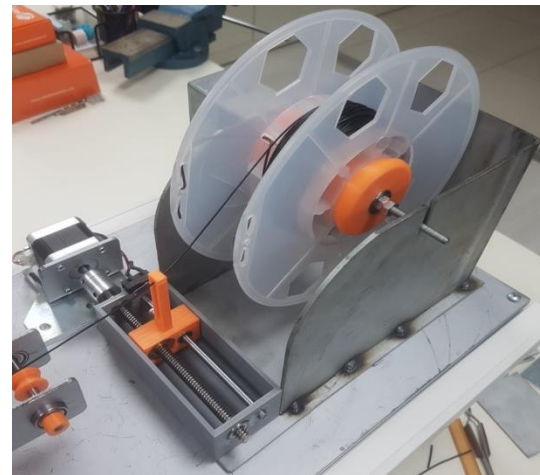


Figure 6. Wrapper Unit

cases such as calibration, power cut, filament depletion, and extruder clogging up have been enabled to produce the desired filaments with contributing to nature.

- Waste support pieces were recycled.
- Recycling of inert filaments was recovered.

- With the prospective studies, it is foreseen some materials such as plastic cups, plastic bottles etc. that can be crushed in the crusher unit and recovered.
- It is thought that bronze, fiber, wood, carbon fiber, elastic reinforced fibers can be obtained from waste filaments in consequence of prospective ideas.
- The designed wrapper unit had performed the wrapper synchronously with the other units and there was no speed problem.

During the testing and start-up stage of the filament recycling system, prototype manufacturing and assembly were completed and the production tests of ABS material were carried out between 5-9 revolution per minute and at 200-235 degrees Celsius. A filament with an average diameter of 1.75 mm was obtained that suitable for FDM printers. It gave the best result among the previous studies, with an output of 11.3 Volts from the ABS filament extruder motor at 200 degrees at 5 rpm. As the number of revolutions increases, the tension of the filament at the exit of the extruder increases and the balance between the other units gradually disappears. In order to prevent this, the filament is moved in the right-left direction in the traversing unit, so that it has a diameter of approximately 1.75 mm before it comes to the wrapper unit.

4. Conclusion

Successfully completed filament recycling system, prototype design and manufacturing enabled the desired filament to be obtained on a product basis. Some of the 3D printers using FDM technology require a filament diameter of 1.75 mm. In this study, 1.75 mm filament diameter was realized with 2% tolerance and made suitable for material production. ABS type filament gave more successful results than PLA type filament. Robust, highly resistant and flexible materials can be produced with ABS filament with a melting temperature of 220 degrees. In this way, the filament to be used for the 3D printer can be recycled with high efficiency and an important contribution is made to us and the relevant units economically. In case of urgent raw material need arising from additive production technology, the recycling system will be easily put into use. It has provided great convenience in terms of time for the production process, especially when material supply is needed. The entire filament recycling system is shown in Figure 7.

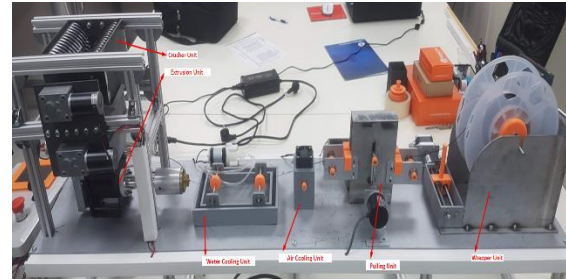


Figure 7. Experimental Setup Equipment.

Crusher unit is first equipment in this study. Its mission is crushing waste filaments and transport to extruder unit. The second equipment is extruder unit that heating the filament until 225 degrees and set the revolution per minute. When the filament is heated it has been ready for cooling. The third one is cooling units that cooling the heated filaments on air and water. Cooling step is necessary for hardness because the filaments must be high steaminess. The fourth one is pulling unit which set the tension on the filaments. This tension is important for system. Because filaments diameter is set by this equipment. The fifth one is wrapper unit which wrap the filaments. Filaments is ready for print on 3D printers in this section.

Acknowledgement

We would like to thank the employees of Menderes Tekstil R&D Center for their unwavering support in the emergence of this study.

Author's Contributions

İlker ERTUNA: Drafted and wrote the manuscript, performed the experiment and result analysis.

Ceren Göde: As the project consultant, supervised the works and helped prepare the manuscript.

Uğur Can TOPÇU: Assisted in analytical analysis on the structure, supervised the experiment's progress, result interpretation and helped in manuscript preparation.

Çağrı YALÇINKAYA: Assisted in analytical analysis on the structure, supervised the experiment's progress, result interpretation and helped in manuscript preparation.

Defne AÇIKGÖZ: Searched the literature and helped in manuscript preparation.

Ezgi CIRİK: Searched the literature and helped in manuscript preparation.

Ethics

There are no ethical issues after the publication of this manuscript.

References

1. Çelik, İ., Karakoç, F., Çakır, M. C., Duysak, A. 2013. Hızlı Prototipleme Teknolojileri ve Uygulama Alanları. Dumlupınar Üniversitesi Fen Bilimleri Enstitüsü Dergisi, 31, 53-69.
2. Mirón, V., Ferrándiz, S., Juárez, D., and Mengual, A. 2017. Manufacturing and characterization of 3D printer filament using tailoring materials. *Procedia Manufacturing*, 13, 888-894.
3. Sa'ude, N., Kamarudin, K., Ibrahim, M., Ibrahim, M.H.I., 2015. Melt flow index of recycle ABS for fused deposition modeling (FDM) filament. *Appl. Mech. Mater.* 773-774, 3-7.
4. Dudek, P., 2013. FDM 3D printing technology in manufacturing composite elements, *Arch. Metall. Mater.* 58 (4) , 1415-1418.
5. Oussai, A., Barftai, Z., Katai, L., and Szalkai, I., 2019. Development of a Small Scale Plastic Recycling Technology and a Special Filament Product for 3D Printing. *International Journal of Engineering and Management Science*, 4.1 : 365-371
6. Angatkina, K. 2018. Recycling of HDPE from MSW waste to 3D printing filaments. *Degree Thesis Materials Processing Technology*.
7. Romero-Alva V, Alvarado-Diaz W, Roman-Gonzalez A 2018. Design of a 3D printer and integrated supply system. *IEEE XXV International conference on electronics, electrical engineering and computing*.
8. Mohammed, M.I.; Das, A.; Gomez-Kervin, E.; Wilson, D.; Gibson, I. 2017. EcoPrinting: Investigating the use of 100% recycled Acrylonitrile Butadiene Styrene (ABS) for Additive Manufacturing. Solid Freeform Fabrication. *In Proceedings of the 28th Annual International Solid Freeform Fabrication Symposium*.
9. Zander, N.E., 2019. Recycled polymer feedstocks for material extrusion additive manufacturing. *Polymer-Based Additive Manufacturing: Recent Developments; ACS Symposium Series. 1315. American Chemical Society.* 37-51.
10. Yeşil, Ö., Mazanoğlu, K. 2018. Effects Of Filling Ratio, Orientation And Print Temperature On Bending Properties Of 3d Printed Pla Beams. *Usak University Journal of Engineering Sciences.* 1(2): 66-75.
11. Corcione CE, Palumbo E, Masciullo A, Montagna F, Torricelli MC. 2018. Fused Deposition Modeling (FDM): an innovative technique aimed at reusing Lecce stone waste for industrial design and building applications. *Constr Build Mater* 158:276–284.
12. Mohammed MI, Wilson D, Gomez-Kervin E, Rosson L, Long J. 2019. EcoPrinting: Investigation of Solar Powered Plastic Recycling and Additive Manufacturing for Enhanced Waste Management and Sustainable Manufacturing. *IEEE Conf. Technol. Sustain. SusTech*.
13. Mohammed, M. I.; Mohan, M.; Das, A.; Johnson, M. D.; Singh Badwal, P.; McLean, D.; Gibson, I. 2017. A low carbon footprint approach to the reconstitution of plastics into 3D-printer filament for enhanced waste reduction. *KnE Eng.* 2 (2), 234–241.
14. Chacón, J.M.; Caminero, M.A.; García-Plaza, E.; Núñez, P.J.; Reverte, J.M.; Becar, J.P. 2019. Additive Manufacturing of PLA-Based Composites Using Fused Filament Fabrication: Effect of Graphene Nanoplatelet Reinforcement on Mechanical Properties, Dimensional Accuracy and Texture. *Polymers*, 11, 799.
15. Öz, Ö, Aydın, M, Kara, A, Sancak, M. 2018. Üç Boyutlu Yazıcılarda Kullanılan Doluluk Oranının Hasar Yüküne Olan Etkisinin Belirlenmesi. *International Journal of 3D Printing Technologies and Digital Industry*, 2 (1), 32-39
16. Pakkanen J, Manfredi D, Minetola P, Iuliano L 2017. About the use of recycled or biodegradable filaments for sustainability of 3d printing. *In: International conference on sustainable design and manufacturing.* 776–785
17. Rahimzadeh, A.; Kalman, J.; Fayazbakhsh, K.; Lessard, L. 2019. Recycling of fiberglass wind turbine blades into reinforced filaments for use in Additive Manufacturing. *Compos. Part B* 175, 107101.
18. Lehrer, J., Scanlon, MR., The Development of a Sustainable Technology for 3D Printing Using Recycled Materials. 2017. *Mid-Atlantic ASEE Conference*.
19. Dubashi, J., Grau, B. and McKernan, A. 2015. AkaBot 2.0: pet 3D printing filament from waste plastic. *Santa Clara: Santa Clara University*.
20. A Review Study on Mechanical Properties of Obtained Products by FDM Method and Metal/Polymer Composite Filament Production. *Journal of Nanomaterials*, 2020.
21. Investigation of the effect of FDM process parameters on mechanical properties of 3D printed PA12 samples using Taguchi method, 2021.
22. Aydın, M, Güler, B, Çetinkaya, K. 2018. Dikey Ekstrüzyon (Filament) Sistemi Tasarım ve Prototip İmalatı. *International Journal of 3D Printing Technologies and Digital Industry*, 2 (1), 1-10.
23. Haq, RHA., Wahab, S., Jaimi, NI., 2013. Fabrication Process of Polymer Nano-Composite Filament for Fused Deposition Modeling. *Applied Mechanics and Materials.* 465-466.

Experimental and response surface methodology investigation of cast material obtained by melting and recycling of chips

Harun AKKUŞ^{1*} , Harun YAKA² 

¹ Nigde Vocational School of Technical Sciences, Nigde Omer Halisdemir University, Niğde, Turkey

² Engineering Faculty, Amasya University, Amasya, Turkey

* harunakkus@windowslive.com

*Orcid: 0000-0002-9033-309X

Received: 17 March 2021

Accepted: 1 June 2021

DOI: 10.18466/cbayarfbe.898972

Abstract

In this study, it is aimed to draw attention to the new materials and recycling produced by the melt-casting process of chips in industry. For this purpose, the aluminum 5000 material with 90 HB hardness was turned. The chips obtained by turning were melted in melting furnace and molded as a cylinder mold. The hardness value of the material Recycled Al 5000 obtained by casting method was measured as 95 HB. Materials were examined by surface microscopy. Experimental design, analysis of surface roughness values of Al 5000 and Recycled Al 5000 material, regression equations, coefficients of determination, optimum point, cutting parameters interaction graphs were carried out with response surface methodology (RSM). It was concluded that the surface roughness values decreased in the Recycled Al 5000 material. In order to determine this reduction, the surfaces of the chips and materials were examined. Optimum parameter levels for Ra were found as cutting speed 222 m/min, feed rate 0,14 mm/rev, depth of cut 1,77 mm. Feed rate was the most effective parameter for surface roughness in both materials. In prediction experiments, it was observed that the RSM model yielded 90% reliability.

Keywords: turning, chips, recycling, casting, RSM.

1. Introduction

Nowadays, the consumption of available resources increases rapidly due to the increasing population. With the rapid depletion of the resources used, the important institutions in the world about how to use the resources efficiently need to do various studies. While meeting our current needs, we should not endanger the potential of future generations to meet their needs [1]. The main subject of our study is to provide recycling of waste aluminum chips. We support the conservation of both our natural resources and our resources.

Waste shavings or materials resulting from machining can be collected and recycled through scrap work. Metal materials take a long time to disappear in nature. Aluminum is lost in nature in about one hundred years. Energy and material savings are ensured by recycling.

The casting processes of different materials, which are important in industrial production, constitute the basis of many studies. Metalworking and shaping with the discovery of metals in human history has been practiced

almost simultaneously. In this sense, the foundry and casting technique has continued its development throughout the ages, and it continues to be popular in today's information age [2, 3].

Aluminum is one of the most common metals used in many sectors (automotive, construction, aerospace, electric-electronics, etc.) due to its advantages (such as lightness, process ability, oxidation resistance and electrical conductivity). Recycling of scrap or waste materials for aluminum production saves approximately 90% energy from ore to aluminum production. This shows how important recycling of aluminum is. Aluminum is produced from primary aluminum and scrap as secondary aluminum [4-6].

Nowadays, it is aimed to obtain high quality products with low manpower in a short time [7]. For this purpose, the use of CNC machine has become widespread in order to be able to produce flexible and mass production. A wide variety of metal removal methods are available in the manufacturing industry. Turning is an important chip removal method because it is faster

than other operations and gives better results in surface quality [8]. There are several factors that influence the surface roughness in turning. The most important of these are the cutting speed, feed and chips depth known as cutting parameters [9-11]. Generally, the desired cutting parameters are determined according to the experience or according to the catalogs determined by the cutting tool manufacturers [12]. However, in order to obtain a better result in surface roughness, optimization of cutting parameters and surface roughness should be modeled [13]. Developing technology and increasing product diversity force manufacturers to produce more quality and faster. Therefore, cutting tool technology is constantly evolving. Recently, the improvement of cutting tools has not only increased the removed chip ratio but also reduced processing costs and processing time as well as increasing the quality of the desired surface [14]. In order to obtain a smooth surface, many experimental and statistical studies were performed on the optimization of the cutting parameters. In order to find the optimum value by decreasing the number of experiments, Taguchi method was used in studies and unnecessary experiments were avoided [15]. Bensouilah et al. Used surface roughness and shear force analysis in the hard turning process with and without coating using Taguchi method. In the experiments, the surface roughness was better at the coated ceramic ends and the cutting force was lower at the uncoated ceramic ends [16]. In his work, Noordin and his colleagues subjected AISI 1040 steel material to a lathe operation with a coated insert and investigated the effect of cutting parameters on surface roughness. At the end of their studies, they found that the most important parameter affecting the surface roughness was the progress [17]. In addition, in the literature, optimization with the response surface methodology (RSM) is widely used to determine optimum cutting parameters [18-20].

The main purpose of this study is to investigate the machinability of the new material obtained by the melt-casting method of the chip pieces produced by the machining in the enterprises or workshops. The surface roughness of the material obtained as a result of the process and the internal structure of the material were investigated. In this way, it was aimed to create awareness in the department students and to cooperate

with the industry in accordance with the data we obtained.

2. Materials and Methods

In this study, aluminum 5000 work piece used in heating and cooling equipment, roof coverings, writing signs, panels, traffic lights, architectural applications, chemical industry, parts requiring coating.

First, aluminum 5000 cylindrical material is machined on the lathe. The chips formed during turning are deposited and pressed into the box placed on the lathe to keep them away from any contaminants such as oil and dirt. The pressed chips are melted in the crucible in our own melting furnace and poured into a cylindrical hollow material. Charcoal was used to heat the melting furnace. Slag formed during melting were removed. During melting, the average temperature reached 730 °C. After casting, the material was cooled to room temperature. Before the material was used, it was processed on the lathe to smooth the surface and the residues were removed. In Figure 1, flow chart is given. The parameters and definitions related to the experiment are given in Table 1. In the experiments, a cylindrical piece with dimensions of Ø50x175 mm was used. Process length was selected as 60 mm.

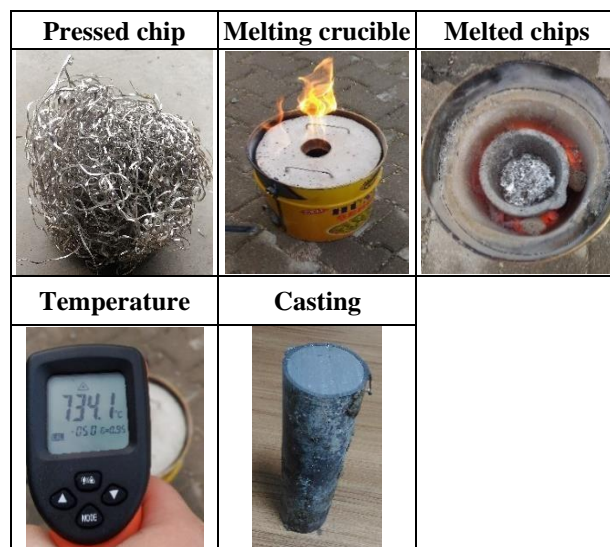


Figure 1. Flow chart.

Table 1. Experimental parameters.

Processing Conditions	Definitions
Workpiece	Aluminum 5000
Workpiece hardness (Al 5000)	90 HB
Workpiece hardness (Al 5000, Recycled from chips)	95 HB
Workpiece dimensions	Ø50x175 mm
Process length	60 mm
Lathe	ACE Micromatic Designers LT-20C

Cutting speed (m/min)	222-308-394
Feed rate (mm/rev)	0,14-0,21-0,28
Depth of cut (mm)	0,33-1,77-3,21
Cutting media	Dry
Cutter tips	Lamina Technologies VBMT 160404 NN LT10<100
Tools holder	TIMAXIP SVHBR 2525 M16
Measured value	Average surface roughness (Ra)
Roughness measuring instrument	Mitutoyo Surftest SJ-210
Temperature measuring instrument	Infrared Thermometer DT 8016H
Hardness measuring instrument	BMS Digirock RSR
Metallographic grinding and polishing machine	Metkon FORCIPOL 2V Grinder-Polisher
Microscope	Leica DMC 2900
Used programs	Design Expert, Microsoft Excell

Experimental design Design Experiment 11 program with a Box Behnken approach was created with 15 experimental lists. Experimental design and obtained test results are given in Table 2.

3. Experimental Results

Table 2 shows the experimental results and the graph of the test results in Figure 2. When the results of the experiment are examined, it is seen that the surface roughness values of the Recycled Al 5000 material decreased. It is determined that this decrease is caused by material hardness, internal structure of material and chip form.

Table 2. Experimental design and experimental results.

No	V (m/min)	f (mm/rev)	a (mm)	Al 5000 Ra (µm)	Recycled Al 5000 Ra (µm)
1	308	0,21	1,77	3,535	1,741
2	308	0,28	3,21	5,444	3,991
3	308	0,28	0,33	5,899	4,486
4	394	0,28	1,77	5,742	5,382
5	222	0,14	1,77	2,159	1,479
6	222	0,21	0,33	3,077	1,989
7	222	0,28	1,77	5,288	4,250
8	222	0,21	3,21	3,365	3,096
9	308	0,14	0,33	2,342	2,010
10	394	0,14	1,77	2,220	1,946
11	308	0,21	1,77	3,718	3,205
12	308	0,21	1,77	3,341	3,054
13	394	0,21	0,33	3,516	3,269
14	308	0,14	3,21	2,329	1,983
15	394	0,21	3,21	4,599	3,419

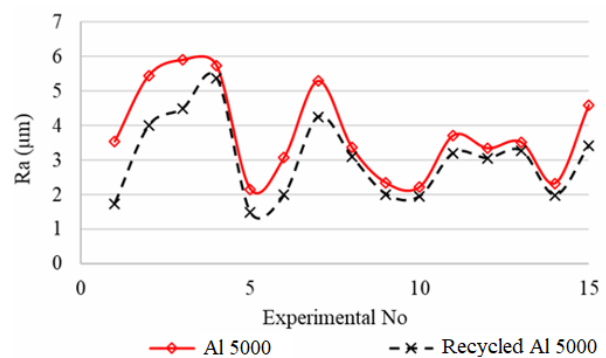


Figure 2. The roughness comparison of Al 5000 and Recycled Al 5000 material.

Figure 3 shows the chips of Al 5000 materials and the Recycled Al 5000. When the chips are examined, the chips in the Recycled Al 5000 material are not coiled in any way because of the short structure. As the Al 5000 material is being processed, the chips are not fragile, so the roughness values are increased. In other words, during the turning process of the Al 5000 material, the chips entrained in the part caused scratches on the surface. This situation increased the surface roughness of scratches.

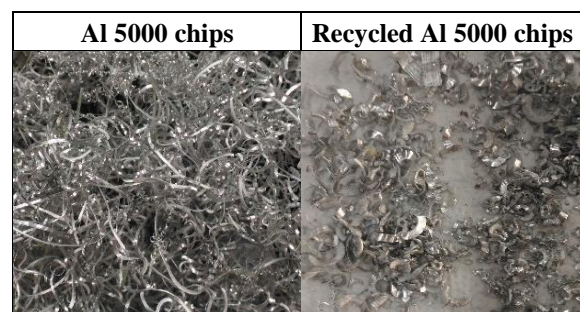


Figure 3. The chips structures formed during the processing of Al 5000 material and Recycled Al 5000 material.

In order to examine the differences in the chips structure as a result of the processing of Al 5000 material and Recycled Al 5000 material, the sections were taken from the samples and examined by Leica DMC 2900 microscope. The surfaces of the samples were prepared with Metkon FORCIPOL 2V Grinder-Polisher before the examination. The samples were ground in liquid medium with 180, 800 and 1200 sandpaper. Grinding surfaces are polished by using special liquid with felt. Figure 4 shows microscope images for 20x magnification. When the shape is examined, the surface of Al 5000 material is seen as a whole, but cracks and gaps are seen on the surface of the Recycled Al 5000 material. These images also explain the difference in the chips structures in Figure 3.

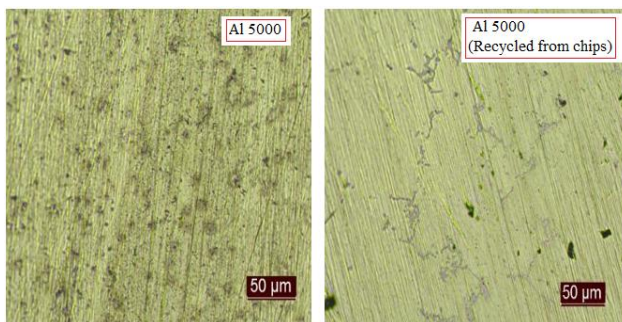


Figure 4. Microscope images.

4. Respond Surface Methodology (RSM)

The statistical analyzes of the experimental results were performed by Design Expert program. For optimum surface roughness of linear, quadratic, cubic equations have been tried. The most appropriate model was created by the quadratic equation. According to coefficients calculated in Design Expert program, quadratic model equations are obtained.

$$Ra_{Al\ 5000} = 3,531 + 0,273 * V + 1,665 * f + 0,112875 * a + 0,098 * V * f + 0,198 * V * a - 0,1105 * f * a - 0,0216 * V^2 + 0,342 * f^2 + 0,129 * a^2$$

$$Ra_{Recycled\ Al\ 5000} = 2,666 + 0,401 * V + 1,336 * f + 0,091 * a + 0,166 * V * f - 0,239 * V * a - 0,117 * f * a + 0,211 * V^2 + 0,385 * f^2 + 0,064 * a^2$$

R² was obtained as 89% for Al 5000 material. R² of the Recycled Al 5000 material was 97%. Table 3 and Table 4 show the results of ANOVA. When Table 3 and Table 4 show the equation coefficients, it is seen that the effective and important parameter on the roughness is progress. Table 3 and Table 4 also show that the model created for the Al 5000 material is not important and the

model created for the Recycled Al 5000 material is important.

Table 3. ANOVA results for Al 5000 material.

Source	Sum of Squares	df	Mean Square	F-value	p-value
Model	16,71	9	1,86	4,5	0,0562
A-v	1,28	1	1,28	3,11	0,1383
B-f	14,29	1	14,29	34,62	0,002
C-a	0,0675	1	0,0675	0,1636	0,7026
AB	0,1106	1	0,1106	0,2679	0,6268
AC	0,229	1	0,229	0,5548	0,4899
BC	0,0548	1	0,0548	0,1327	0,7306
A ²	0,1654	1	0,1654	0,4009	0,5545
B ²	0,5499	1	0,5499	1,33	0,3005
C ²	0,0156	1	0,0156	0,0377	0,8537
Residual	2,06	5	0,4127		

Table 4. ANOVA results for Recycled Al 5000 material.

Source	Sum of Squares	df	Mean Square	F-value	p-value
Model	23,62	9	2,62	19,84	0,0021
A-v	0,5984	1	0,5984	4,52	0,0868
B-f	22,19	1	22,19	167,71	0,0001
C-a	0,1019	1	0,1019	0,7704	0,4203
AB	0,0386	1	0,0386	0,2919	0,6122
AC	0,158	1	0,158	1,19	0,3243
BC	0,0488	1	0,0488	0,3692	0,57
A ²	0,0017	1	0,0017	0,0131	0,9133
B ²	0,4333	1	0,4333	3,28	0,1301
C ²	0,062	1	0,062	0,4686	0,5241
Residual	0,6615	5	0,1323		

Figure 5 shows the graphs V-f, V-a and f-a. When Figure 5 is examined, it is seen that the parameter having the most effect on the surface roughness from the cutting parameters for Al 5000 and Recycled Al 5000 material is progress. It confirms our study in the literature [17, 21, 22].

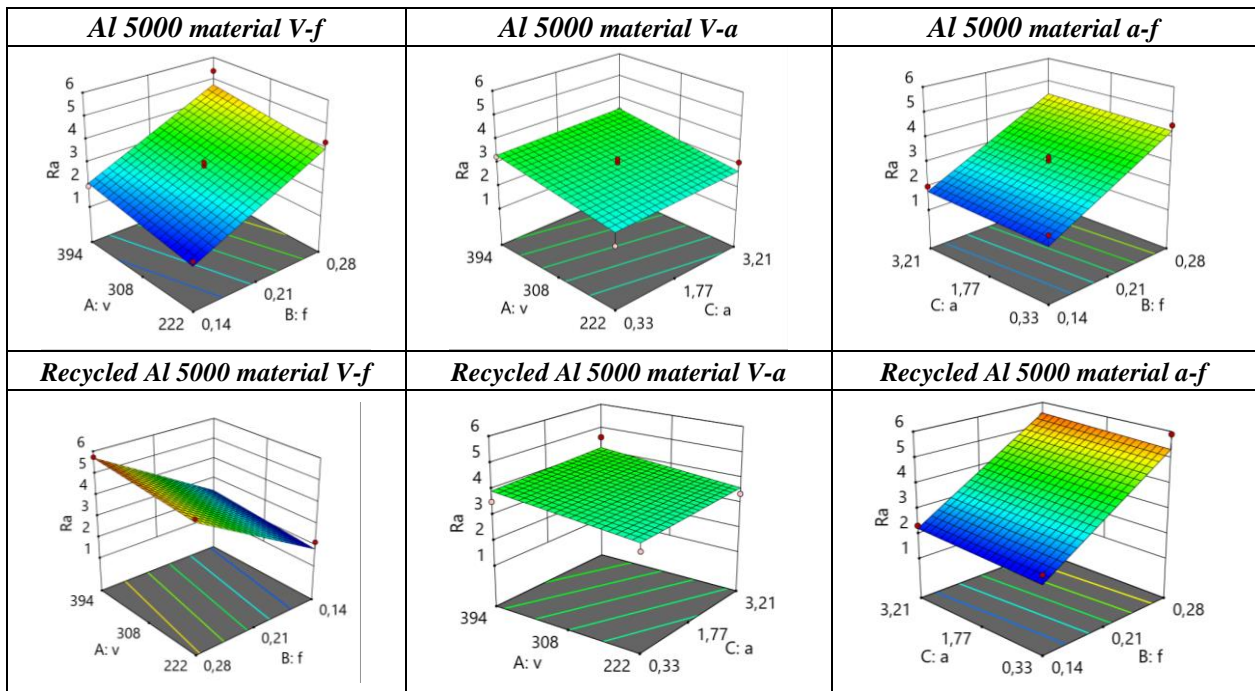


Figure 5. Al 5000 material and Recycled Al 5000 material for V-f, V-a, f-a graphics.

The optimum points for RSM models are determined in the Design Expert program. The determined optimum points and roughness values are given in Figure 6. Figure 6 shows that the cutting parameters ($V = 222$ m/min - $f = 0,14$ mm/rev - $a = 1,77$ mm) are the same

for Al 5000 and Recycled Al 5000 material. For the same cutting parameters, $Ra = 2,01 \mu\text{m}$ for Al 5000 material and $Ra = 1,28 \mu\text{m}$ for Recycled Al 5000 material. The Ra value is low for the Recycled Al 5000 material.

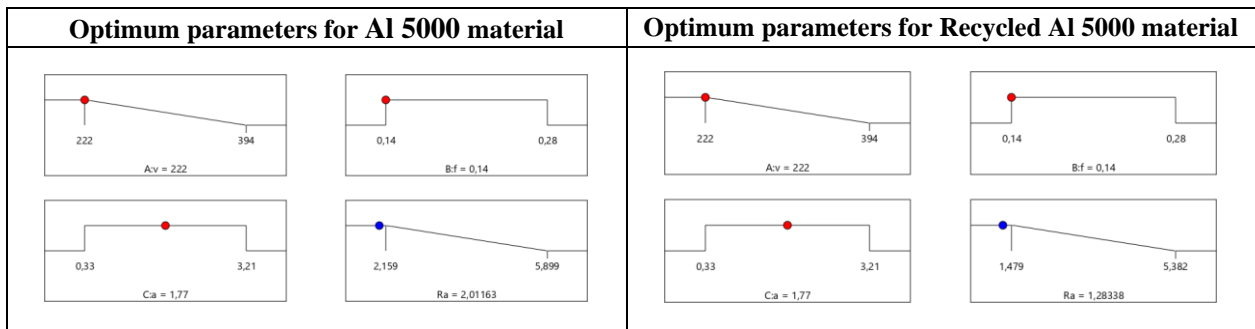


Figure 6. Optimum parameters for Al 5000 and Recycled Al 5000 material.

The result estimation and the experiments were performed for the cutting parameters determined in the Design Expert program for the RSM models. When Table 5 and Table 6 are examined, the estimation

models for Al 5000 material and Recycled Al 5000 material approached approximately 90% of the experimental results. This has demonstrated the reliability of estimation models.

Table 5. Estimation experiments for Al 5000 material.

Test no	V (m/min)	f (mm/rev)	a (mm)	Actual	Predict	Absolute difference	Absolute error (%)
1	222	0,14	1,77	2,219	2,011	0,21	9,37
2	250	0,2	1,03	3,435	3,152	0,28	8,24
3	380	0,27	3,2	6,342	5,805	0,54	8,47

Table 6. Estimation experiments for Recycled Al 5000 material.

Test no	V (m/min)	f (mm/rev)	a (mm)	Actual	Predict	Absolute difference	Absolute error (%)
1	222	0,14	1,77	1,381	1,283	0,10	7,10
2	250	0,2	1,03	2,785	2,511	0,27	9,84
3	380	0,27	3,2	5,012	4,591	0,42	8,40

5. Conclusion

In this study, aluminum 5000 material is turned. The chips formed during the turning process were collected and melted in our own design melting pot and a new cylindrical material was produced. Recycling of chips is provided.

The hardness of the Al 5000 material was 90 HB and the hardness of the Recycled Al 5000 material was 95 HB. The obtained surface roughness values were reduced in the Recycled Al 5000 material for the same cutting parameters. The reason for this decrease is due to the increased hardness of the material due to the fact that the chips are more fragile and do not wrap the surface and create scratches on the surface.

Sections were examined by microscope. While the surface of Al 5000 material is seen as a whole, cracks and gaps in the surface of the Recycled Al 5000 material is noteworthy. This explains why the chips structures are broken in the Recycled Al 5000 material.

Optimum parameter levels for Ra were found as cutting speed 222 m/min, feed rate 0,14 mm/rev, depth of cut 1,77 mm. Feed rate was the most effective parameter for surface roughness in both materials.

RSM models for Ra values were obtained by Design Expert statistical program. Quadratic regression models were created for Ra values. ANOVA tables are given in the RSM results. In the RSM model, the graphs V-f, V-a and f-a are given. In the equations and graphs obtained, it is concluded that the most effective parameter is Ra.

Three experimental parameters were determined to determine the reliability of the predicted part of the RSM model. In this experiment and model comparison, approximately 90% of the results were obtained.

Different materials and different methods can be used in future manuscripts. We made the process of recycling with the charcoal smelting due to impossibility. Electric or natural gas melting furnaces can be used to reduce environmental damage.

Acknowledgement

This study was supported by Amasya University Scientific Research Projects Coordination Unit with the projects of FMB-BAP 18-0316 and FMB-BAP 20-0447.

Author's Contributions

Harun AKKUŞ: Conceptualization, Methodology, Software, Validation, Verification, Formal analysis, Investigation, Resources, Data Curation, Writing - Original Draft, Writing - Review & Editing, Visualization, Supervision, Project administration, Funding acquisition.

Harun YAKA: Conceptualization, Methodology, Validation, Verification, Investigation, Resources, Writing - Original Draft, Writing - Review & Editing, Visualization.

Ethics

There are no ethical issues after the publication of this manuscript.

References

- Akbulut H., Içaga Y., Gürer C. 2003. The Possibility of Recycle of Waste Agregates in the Asphalt Pavement and CEN Standards. *III National Kırmataş Symposium*, 3-4.
- Akar M. 2018. Casting errors and design methods for prevention, *Pamukkale University Graduate School of Natural and Applied Sciences*.
- Cooper D. R., Song J., Gerard R. 2018. Metal recovery during melting of extruded machining chips. *Journal of Cleaner Production*; 200: 282-292.
- Jirang C. U. I., Roven H. J. 2010. Recycling of automotive aluminum. *Transactions of Nonferrous Metals Society of China*; 20: 11: 2057-2063.
- Martínez V.P., Torres J.T., Valdes A.F. 2017. Recycling of aluminum beverage cans for metallic foams manufacturing. *Journal of Porous Materials*; 24: 3: 707-712.
- Gürbüz M. 2018. Effect of the cold working on mechanical properties of aluminum produced from waste beverage cans. *Journal of Science and Engineering*; 20: 58: 28-35.
- Özel T., Karpat Y. 2005. Predictive modeling of surface roughness and tool wear in hard turning using regression and neural networks. *International Journal of Machine Tools and Manufacture*; 45: 467-479.
- Gupta M.K., Sood P.K. 2016. Optimizing multi characteristics in machining of AISI 4340 steel using Taguchi's approach and utility concept. *Journal of The Institution of Engineers (India): Series C*; 97: 63-69.
- Kopac J., Bahor M., Soković M. 2002. Optimal machining parameters for achieving the desired surface roughness in fine turning of cold pre-formed steel workpieces. *International Journal of Machine Tools and Manufacture*; 42: 707-716.

10. Özlü B. 2021. Investigation of the effect of cutting parameters on cutting force, surface roughness and chip shape in turning of Sleipner cold work tool steel. *Journal of the Faculty of Engineering and Architecture of Gazi University*, 36(3), 1241-1251.
11. Özlü B., Akgün M., Demir H. 2019. Analysis and optimization of effects on surface roughness of cutting parameters on turning of AA6061 alloy. *Gazi Müh Bilim Derg*, 5, 151-158.
12. Sahoo P. 2011. Optimization of turning parameters for surface roughness using RSM and GA. *Advances in Production Engineering and Management*; 6: 197-208.
13. Tzeng C.J., Lin Y.H., Yang Y.K., Jeng M.C. 2009. Optimization of turning operations with multiple performance characteristics using the Taguchi method and grey relational analysis. *Journal of Materials Processing Technology*; 209: 2753-2759.
14. Bhattacharya A., Das S., Majumder P., Batish A. 2009. Estimating the effect of cutting parameters on surface finish and power consumption during high speed machining of AISI 1045 steel using Taguchi design and ANOVA. *Production Engineering*; 3: 31-40.
15. Kurt M., Bagci E., Kaynak Y. 2009. Application of Taguchi methods in the optimization of cutting parameters for surface finish and hole diameter accuracy in dry drilling processes. *The International Journal of Advanced Manufacturing Technology*; 40: 458-469.
16. Bensouilah H., Aouici H., Meddour I., Yallese M.A., Mabrouki T., Girardin F. 2016. Performance of coated and uncoated mixed ceramic tools in hard turning process. *Measurement*; 82: 1-18.
17. Noordin M.Y., Venkatesh V.C., Sharif S., Elting S., Abdullah A. 2004. Application of response surface methodology in describing the performance of coated carbide tools when turning AISI 1045 steel. *Journal of Materials Processing Technology*; 145: 46-58.
18. Aslan A. 2020. Optimization and analysis of process parameters for flank wear, cutting forces and vibration in turning of AISI 5140: A comprehensive study. *Measurement*, 163, 107959.
19. Kuntoğlu M., Aslan A., Pimenov D. Y., Giasin K., Mikolajczyk T., Sharma S. 2020. Modeling of cutting parameters and tool geometry for multi-criteria optimization of surface roughness and vibration via response surface methodology in turning of AISI 5140 steel. *Materials*, 13(19), 4242.
20. Kuntoğlu M., Aslan A., Pimenov D. Y., Giasin K., Mikolajczyk T., Sharma S. 2020. Modeling of cutting parameters and tool geometry for multi-criteria optimization of surface roughness and vibration via response surface methodology in turning of AISI 5140 steel. *Materials*, 13(19), 4242.
21. Akkuş H. 2018. Optimising the effect of cutting parameters on the average surface roughness in a turning process with the Taguchi method. *Materiali in Tehnologije*; 52: 6: 781-785.
22. Akkuş H. 2021. Multiple optimization analysis of MRR, surface roughness, sound intensity, energy consumption, and vibration values in machinability of TC4 titanium alloy. *Surface Review and Letters*, 2150072.

Determination Of the Effect Of Cooling Rate And Strontium Amount On Eutectic Si Modification Performance Of A356 Alloy Via Casting Simulation

Batuhan Dođdu^{1, 2*} , Uđur Aybarç² , Serkan Gündođdu¹ , Onur Ertuđrul¹ 

¹Material Science and Engineering Department, İzmir Katip Celebi University, İzmir, Turkey

²CMS Jant ve Makina San. R&D Center, İzmir, Turkey

*bdogdu@cms.com.tr

*Orcid:0000-0003-4110-7341

Received: 26 January 2021

Accepted: 2 August 2021

DOI: 10.18466/cbayarfbe.869010

Abstract

It is well-known that strontium addition into molten metal as a eutectic modifier increases the elongation and toughness values of the cast parts by refining the eutectic phases. However, when over-modification occurs, porosity increases due to some unwanted physical and chemical reactions that develop within the structure. On the other hand, it has been seen that high cooling rates tend to reduce the porosity of the alloy, decrease grain size and secondary dendrite arm spacing and refine eutectic silicon phase on Al-Si casting alloys. Within the scope of this research, it is aimed to investigate the effects of the cooling rate of cast part and the addition amount of strontium on the silicon modification behavior of Al A356 (AlSi7Mg) alloy parts using casting simulation environment. To examine the effect of strontium amount, 150, 250, 350 and 450 parts per million of strontium additions were selected in accordance with the aluminum wheel production limits that given by OEM customers. After the casting session of each Al A356 composition with different strontium amount by using special designed 5-spoke mold on casting simulation, thermal analysis was done by obtained thermocouple data from casting part's each spoke. Obtained thermal analysis data was interpreted with the casting simulation outputs. Within all aspects, the 150 parts per million strontium addition on Al A356 alloy have been identified as the most useful simulation model in terms of casting performance.

Keywords: A356 alloy, casting simulation, cooling rate, eutectic modification

1. Introduction

Aluminum (Al)-Silicon (Si) casting alloys as one of the most popular family of the cast Al alloys which have been used in industry for decades, especially for the advantages of their light weight, recyclability and high specific strength [1]. The most common composition of Al-Si casting alloy is A356 (Al7Si0.3Mg) which contains needle-like hard and brittle eutectic Si phase and ductile α -Al phase as alloy matrix. This eutectic phase, inside solidified commercially pure (CP) A356 alloy, has a needle-like structure and results an increment on inner stress due to increased stress sharp edges inside microstructure. Modification is a must in order to refine the eutectic Si phase to obtain finer morphology. Unmodified Si phase inside Al-Si casting alloy degrades tensile strength and fatigue properties of cast part to eliminate this negative effect and increase mechanical properties such as tensile strength, toughness and elongation, eutectic modification and

grain refinement procedures have been used for most of the Al cast parts. This modification can be obtained by either chemically, by using master alloys, and physically by increasing the rate of solidification by extracting the heat energy of alloy with mold adaptations and external cooling channels.

Chemical modifiers are master alloys including Sr, sodium (Na), barium (Ba), calcium (Ca) and europium (Eu) elements used to obtain eutectic modification which avoids eutectic Si growth by the mechanism of impurity induced twinning (IIT) growth and twin plane re-entrant (TPRE) poisoning [2-4]. Besides that ability, Sr melt treatment increases the H concentration in the melt. Consequently, Iwahori et.al. investigated that Sr addition to the melt effects the porosity formation in Al-7%Si alloys. Also, they proposed that there was a correlation between the observed oxide number and porosity for (Sr) modified A356 alloy [5]. Additionally, besides the benefits of Sr on modification, it is believed

that Sr reduces the surface tension of the molten alloy which may cause to porosity formation with increased wt. % content [6].

Grain refinement also can be acquired chemically by using master alloy contribution inside Al melt, such as titanium (Ti), niobium (Nb), beryllium (Be), boron (B) and lanthanum (La) based, by the mechanism of creating potential nucleation sites for α -Al dendrites [7]. It is also known that Ti-B master alloys which have been used as a commercial grain refiner, have a chironical problem such as fading and poisoning mechanism, which also has a negative influence on mechanical properties of A356 alloy. As a consequence of higher density of the nucleant TiB_2 and $TiAl_3$ particles, than molten Al, settlement of nucleants through the crucible can be observed by the function of time and gravity. This mechanism is known as fading. On the other hand, TiB_2 particle surface interface is an energetically favorable site for Si growth, compared to the Al-matrix grain boundaries. Ti-Si included compound coats $TiAl_3$ surface and degrades the influence of the nucleant that exists in the Ti-B master alloy, based on Sigworth and Guzewaski's work [8]. On both fading and poisoning effect, grain refinement efficiency decreases dramatically, which have deleterious consequences on strength and toughness of the cast part [9]. Commercially, foundries have been using Sr and Ti-B based master alloys for eutectic modification and grain refinement respectively, on the process of melt treatment before actual casting stage. Moreover, heat extraction velocity from molten metal can influence the temperature gradient in the mold, thus, solidification rate of the alloy itself, and is one of the most important variable which influences microstructure and mechanical characteristic of castings. At elevated solidification rates, more α -Al dendrites with smaller arm spacing will be formed, resulting in lower and more uniform distribution of shrinkage porosity due to enhanced mass feeding [10-12]. In addition, high cooling rate ensures eutectic Si phase refining by blocking the growth of eutectic Si which greatly affects mechanical properties positively [13].

Ferdian et al. proposed that to determine the optimum amount of eutectic modification, the needed eutectic depression must be at least 7 °C which is slightly higher than the value previously proposed by Apelian et al. as 5.5°C [14]. Additionally, the authors suggested that the only values of solidification rate higher than 0.7 °C/s relate to sufficient modification of A356 alloy in either sand or metallic molds.

The innovative approach of this study is to investigate the effect of Sr content and cooling rate on Si modification with the help of casting simulation analysis. In order to execute detailed investigations on melt treatment performances, thermal analysis technique

has been examined for determination of melt treatment level and quality assessment of casting. Normally, thermal analysis examination proceeds by extracting analog data from molten metal, at the time of where molten metal solidifies, and transforming the data into digital one on an analog to digital converter device. Instead of this standard procedure, casting simulation's virtual thermocouple's data was used in this work. By obtained T /t graphs, $T_{nucleation}$ (T_n), $T_{minimum}$ (T_m) and T_{growth} (T_g) temperatures can be analyzed by first derivate method of T/t graph itself, for eutectic modification which is dealt with in the current paper. Finally, the effects of Sr amount and cooling rate are summarized by comprising the whole results consisting of macroporosity formation, eutectic grain radius, Sr macrosegregation and thermal analysis data outcomes.

2. Materials and Methods

Firstly, a mold design was studied on Catia V5 CAD software, by considering the cooling rate differences on each spoke. The five spoke mold was designed on two different section volume by referencing of middle point of the casting part, as it seems on Figure 1. That section differences were designed to obtain different thermal gradient on the same mold. Therefore, on the thick section part, two air cooling nozzle holes were implemented to get much higher cooling rates due to obtain different cooling rates on edge to edge (higher values on thick section, lower values on thin section). After the design step, the CAD mold was appended on Magmasoft casting simulation software. 4 mm tetrahedral mesh was implied on whole cast and mold data. To examine the efficacy of Sr contribution, thanks to material Jmat Pro database of Magmasoft, thermodynamic calculations were made for 150, 250, 350 and 450 ppm of Sr addition. Lever equation was used for each Sr concentration. Based on the standard casting parameters (700°C molten metal temperature, 350°C mold temperature), numbers of experiments were designed through the whole process to correlate to solidification of A356 alloy by real casting examinations. Nevertheless, in order to observe only the eutectic modification performance of each casting version on the casting simulation, grain refiner was not defined on elemental composition of A356 alloy, so that data noise that may be occurred by thermodynamic calculation of Ti and B was eliminated. Detailed casting simulation parameters data are given in Table 1. Thermal regime of the mold and cooling curves of the middle point of each spoke were obtained by virtual thermocouples. By these thermocouple data, T_n , T_m and T_g were considered to compare the effect of cooling rate and Sr amount on eutectic modification performance for each spoke. As a final step, macroporosity formation, eutectic grain radius, Sr macrosegregation and thermal analysis data outcomes were examined based on each Sr addition and cooling behavior of each spoke of the cast part.

Table 1. Casting Parameters.

Parameter	Material	Specification
Cast Part Temperature	Al7Si0.3Mg (A356)	700°C
Modifier Element	Sr	150,250,350 and 450 ppm
Mold Temperature	X40CrMoV 5-1 (H13)	350°C
Heat Transfer Between Cast Part and Mold	-	1-548°C # 1000 W/m ² . K 548-613°C # linear increment 613-1000°C # 2700 W/m ² . K
Cooling Channel (x2)	Air (6 bar, 20°C)	1450 W/m ² . K
Heat Transfer Between Mold and Medium	-	$\epsilon = 0.3$ $h = 20W/m^2.K$
Heat Transfer Between Cast Part and Medium	-	$\epsilon = 0.8$ $h = 20W/m^2.K$
Die Coating	Dycote34	Thickness= 0.1 mm
Molten Metal Inlet Mass Flow Rate	Al7Si0.3Mg (A356)	0.285 gr/s

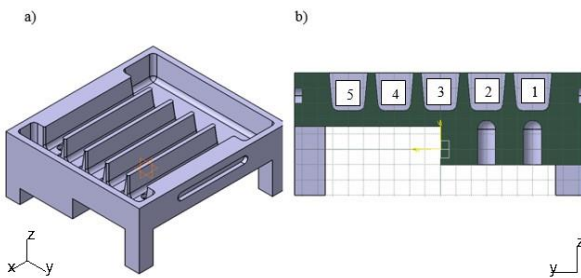


Figure 1. a) Isometric view, and b) mid-section of the mold, where cooling channel hubs and spoke numbers can be seen.

3. Results and Discussion

In this part, the whole experimental results are analyzed in 5 different perspectives as Cooling Design of the Mold, Eutectic Grain Radius, Sr Macrosegregation, Shrinkage Porosity, and Thermal Analysis.

3.1 Cooling Design of the Mold

Cooling system of the mold was designed for obtaining various cooling rates on each spoke of the casting part. For purpose of obtaining different solidification rate from each spoke, mold thickness difference and cooling channel implementation were applied to the mold on Catia V5 CAD software. Thanks to bulk mold mass on thick section, it was thought that thick section will absorb more heat by relying on the principle of $Q=mc\Delta t$. Conversely, it was seen that thin section's temperature was increased due to decreased mold mass on that area, as indicated in Figure 2. On the other hand, implemented external cooling channels extract the heat of the mold, so that, heat flow through casting part to mold can be forced.

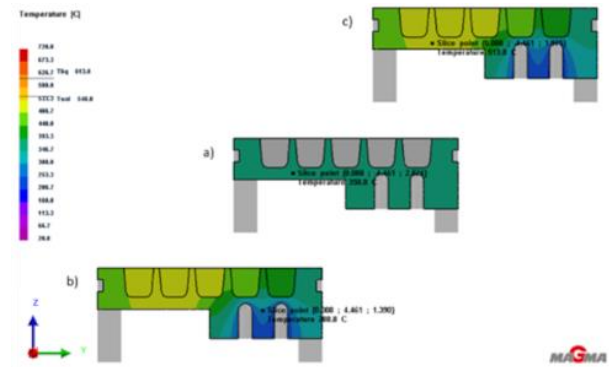


Figure 2. Temperature Scale of zy plane section of the a) $T=350^{\circ}C$ at $t=0$, b) $T=288.8^{\circ}C$ at $t=final$ (Thick section with cooling channel implementation.) and c) $T=513^{\circ}C$ at $t=final$ (Thin section).

As it seems in Figure 3., spoke 1 has solidified primarily on cast part. After the solidification of spoke 1, spoke 5 tend to become solid on $t=65s$. And then, thermal gradient difference between thick section and thin section of the mold was exposed, as spoke 2, 3 and 4 has is solidified, respectively. It is seen that, while the solidification has been proceeding, the warmest part of the casting where the molten metal get poured into the mold and where solidification occurred lastly, has shrunk because of density difference between molten alloy and solidified alloy. The warmer the area, higher possibility to get shrank. However, that bulk shrinkage formation is acceptable on design criteria since only the spokes of the casting part were taken into consideration.

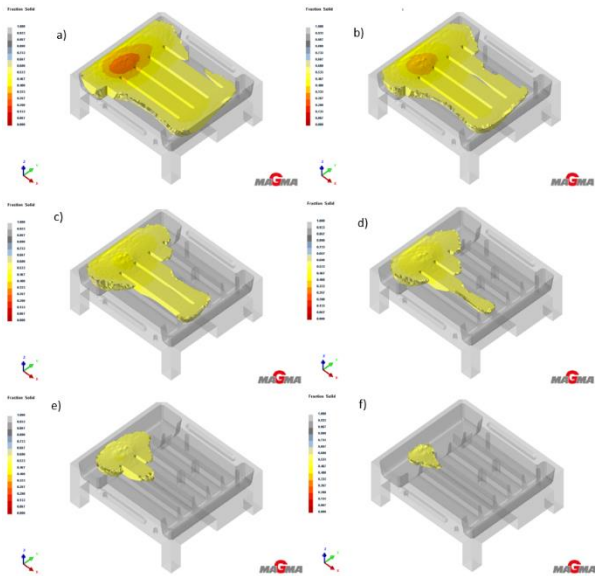


Figure 3. Solidification Sequence of A356 Alloy on Magmasoft Casting Simulation at a) 65s, b) 75s, c) 95s, d) 115s, e) 135s, f) 175s as a result of % fraction solid.

3.2 Eutectic Grain Radius

On casting simulations, eutectic grain radius (EGR) module shows amount of the eutectic phase formation between dendrites. In the scope of the work of Ferdian et al., eutectic Si shape and size on Al-Si alloys are directly related with cooling rate and the amount of eutectic growth restrictor element, like Sr, Na [15].

In Figure 4, EGR values tend to decrease on every step of Sr addition on spoke 4, except of other four spoke on 150 ppm Sr casting setup. It can be interpreted that even if on the spoke 4, which has lowest solidification rate, 150 ppm Sr addition has the ability to modify eutectic Si. After 250 ppm Sr addition, overall eutectic radius increment has been seen. On the following compositions of 350 and 450 ppm Sr addition, overall EGR values have a tendency to decrease linearly but not remarkably.

3.3 Sr Macrosegregation

In the consideration of a solid solution, solvent atoms have the possibility to tend to freeze before the solute atoms, which causes a composition gradient in molten alloy under non-equilibrium conditions [16]. The thermal and compositional condition responsible for this

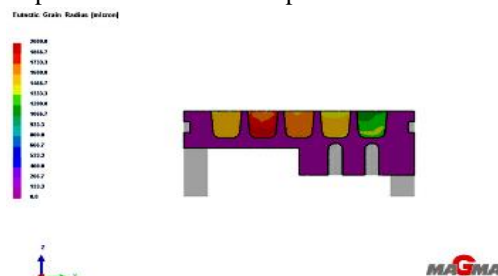


Figure 4. EGR value representation based on Sr amount.

cellular micro and macrosegregation is named as constitutional undercooling. Cooling characteristic related segregation values are listed below.

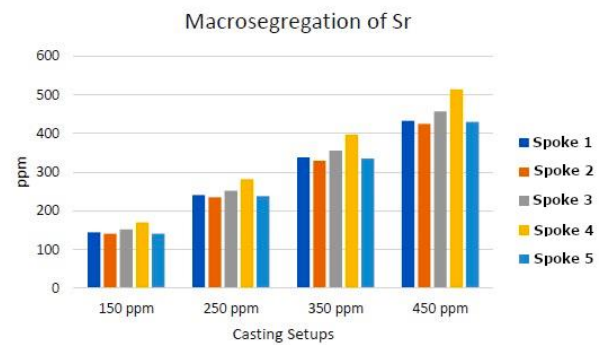
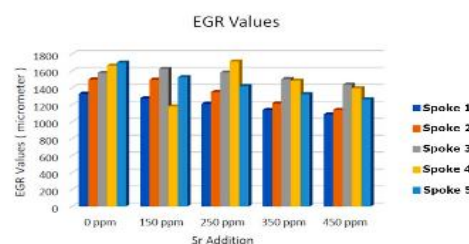


Figure 5. Macrosegregation value schematic in terms of ppm.

Based on simulation data, Sr macrosegregation is highly caused by solidification rate. There might be some other reasons such as oxide film density, filling properties of molten metal into the mold and etc. Therefore, because of the linear increment on the values of macrosegregation of Sr in terms of ppm, it can be said that, theoretically the Sr addition amount on A356 alloy does not have any impact, as it seems in Figure 5, the ppm difference ratio between each spoke is different.

3.4 Shrinkage Porosity

According to Nampoothiri et al., the addition of Sr triggers the porosity formation in the interdendritic region of alloy which terminates the advantageous influence obtained by morphological transformation of eutectic Si [12]. Also, it is known that lack of feeding is a cause for macroshrinkage during solidification where the density of alloy has change by heat extraction from melt. Macroshrinkage can be avoided by rapid and directional solidification through the whole part. Interdendritic feeding is the key for the solution of macroporosity. As it was indicated in Figure 6, minimum porosity formation was obtained on 150 ppm Sr addition (Figure 6b). Conversely, maximum porosity formation was observed on 250 ppm Sr included A356 alloy (Figure 6c)



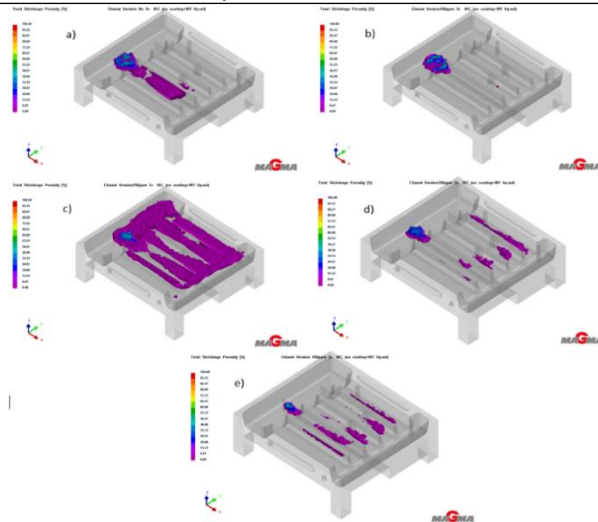


Figure 6. Total Shrinkage Porosity formation of a) CP. A356, b) 150 ppm Sr, c) 250 ppm Sr, d) 350 ppm Sr and e) 450 ppm Sr.

3.5 Thermal Analysis

Thermal analysis on Al-Si alloys has critical importance on defining the solidification path of the alloy itself. To specify the α Al dendrite solidification temperature, eutectic Si nucleation temperature (T_n), eutectic minimum temperature (T_m), eutectic growth temperature (T_g) and the other intermetallic phases such as β -Al₅FeSi, π -Al₈FeMg₃Si₆ and β -Mg₂Si, derivative point analysis is necessary. Ferdian et al. suggested that eutectic depression ($T_g - T_m$) should be examined to observe eutectic modification [15]. The only way for reliable examination is derivative curve analysis.

The thermal analysis curves were obtained from virtual thermocouples on Magmasoft software. For each spoke and Sr addition, T_n , T_m and T_g temperatures have been extracted from these curves. In Figure 7, T/t curve (blue dots) and its derivative (green dots) of spoke 5 of CP. A356 casting setup was indicated, as an example.

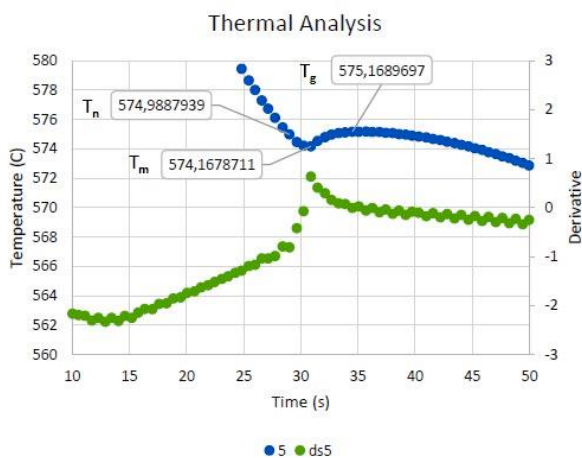


Figure 7. Thermal analysis of spoke 5, (T/t curve with blue dots and its derivative curve with green dots) on CP. A356.

Based on T/t graphs of all the casting simulation setups, it can be clearly said that Sr addition on A356 alloy has a direct influence on the eutectic formation temperatures. It decreases eutectic nucleation temperature up to 560 °C in overall, without considering the effect of cooling rate. Up to 450 ppm from 150 ppm Sr addition, just slight differences exist. On the other hand, cooling rate calculations have been made based on Equation 1. Negative slope of T/t curve between the point of where α Al dendrites start to solidify and the eutectic nucleation spot, has been calculated. On Table 2, it can be seen that aimed cooling rate difference through the spokes has obtained. By this variation, it is obvious that cooling rate has a strong influence on eutectic formation mechanism, according to simulation calculations. When liquid molten alloy is solidified at an elevated solidification rate, the actual supercooling of the solidified alloy is large and thus the nucleation rate of eutectic phase is increased.

Both T_n and eutectic depression undercooling mechanisms are important to obtain modified eutectic Si in microstructure of Al-Si hypoeutectic alloys. The importance of undercooling of nucleation has been proposed in the literature. It is mentioned that the decreased T_n is attributed to the potential nucleation sites (AIP) poisoned by Sr [17-20]. Therefore, the decreased T_n also suggests that the required nucleation undercooling is increased. This also shows that the addition of Sr ensures the nucleation of the eutectic phase more difficult at high temperature. The decrease on the temperature of T_m indicates the present undercooling of the melt is increased when more of nucleation events occur.

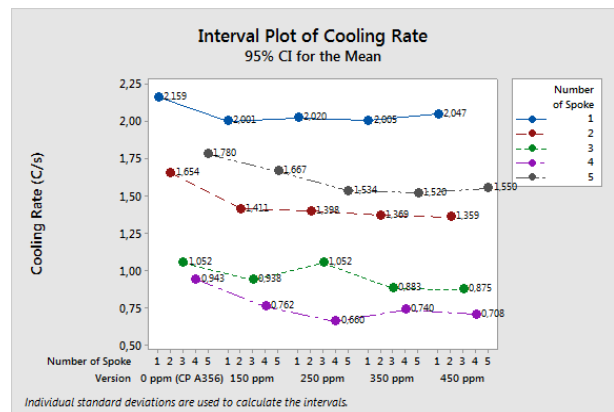


Figure 8. Representation of Cooling Rate change according to Sr addition and spoke.

Table 2. Thermal Analysis Values of Casting Simulation.

Version	Temperature (°C)	Spoke Number				
		5	4	3	2	1
CP. A356	T _n	574.4	575.5	576.0	577.0	574.7
	T _m	574.2	574.8	574.6	574.3	573.8
	T _g	575.1	575.4	575.1	575.0	574.9
	Cooling Rate (°C/s)	1.7	0.9	1.0	1.6	2.1
150 ppm Sr	T _n	565.8	565.6	565.9	563.1	560.4
	T _m	560.4	565.5	562.3	560.3	557.3
	T _g	560.7	565.8	562.5	559.8	556.2
	Cooling Rate (°C/s)	1.6	0.7	0.9	1.4	2.0
250 ppm Sr	T _n	562.9	564.9	562.7	560.8	558.8
	T _m	558.1	563.1	560.0	558.1	554.7
	T _g	560.5	565.3	561.6	557.5	554.7
	Cooling Rate (°C/s)	1.5	0.6	1.0	1.3	2.0
350 ppm Sr	T _n	560.5	566.1	565.3	563.1	561.7
	T _m	558.0	563.1	559.9	558.1	554.9
	T _g	560.4	565.3	561.0	557.3	554.7
	Cooling Rate (°C/s)	1.5	0.7	0.8	1.3	2.0
450 ppm Sr	T _n	562.0	566.1	564.1	562.6	558.7
	T _m	558.3	563.1	559.9	557.9	554.8
	T _g	560.5	565.3	561.6	557.2	554.7
	Cooling Rate (°C/s)	1.5	0.7	0.8	1.3	2.0

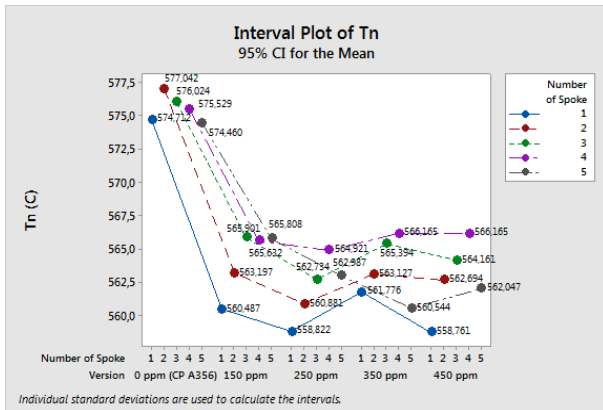


Figure 9. Representation of T_n change according to Sr addition and spoke.

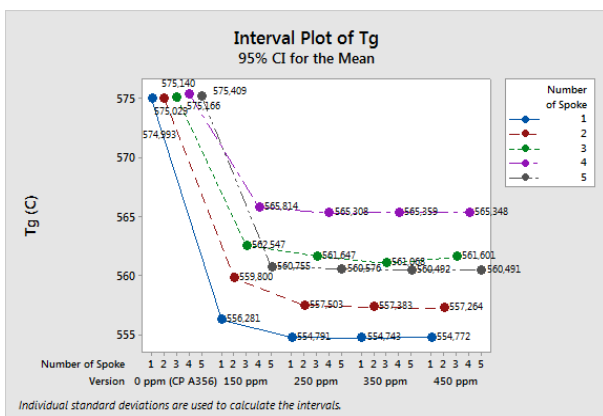


Figure 10. Representation of T_g change according to Sr addition and spoke.

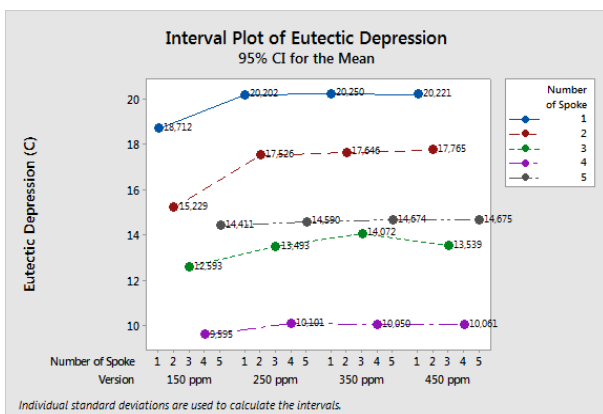


Figure 11. Representation of Eutectic Depression change according to Sr addition and spoke.

Whole data was analyzed with the help of Minitab 18 software. Figure 8-11 show the Cooling Rate, T_n , T_g and Eutectic Depression changes according to Sr addition and spoke number, respectively. In Figure 8, it was seen that Sr addition affected the solidification rate of each casting part even if mold and molten metal temperatures are exactly same for all versions. This effect may have

occurred due to thermodynamic reaction calculations during solidification of the alloy. In Figure 9 and Figure 10, minimum T_n and T_g were achieved, respectively, for 250 ppm Sr contribution. For the addition amount higher than 250 ppm, the increment was observed for the T_n at Figure 9. It was proven that solidification rate of alloy has a significant impact on T_n and T_g . Moreover, it was indicated on Minitab graph that 250 ppm Sr addition is influenced by the Eutectic Depression mechanism mostly which was represented in Figure 11. However, it was also shown that there was no significant change more than 250 ppm Sr addition.

4. Conclusions

On foundry applications, casting simulations takes critical role due to ability and advantages of detecting casting defects, solidification path of alloy and other major parameters before actual casting process. Thus, it is also possible to predict Sr addition and cooling rate's association on to eutectic modification thanks to accessible modules of Magmasoft Software.

As a result, it can be concluded that;

- With correct parameters of heat transfer between cast part, mold and medium, composition properties and meshing precision, reasonable results can be obtained. Also, it was seen that thermal analysis studies can be proceeded as computer-based, instead of real-time casting work.
- Theoretical Eutectic Grain Radius (EGR) calculations showed that Sr addition decreases the eutectic density between dendrites. On spoke 4, 150 ppm Sr has proceeded very well due to color representation although it has lowest cooling rate. On wheel casting, low cooling rates can be observed on hub section. It is important to obtain eutectic modification even these kind of areas on casting. So that, it is reasonable that 150 ppm Sr can be a good choice for foundry applications on hypoeutectic Al-Si casting alloys.
- Distribution of macrosegregation of Sr on each spoke can be seen on the related Magmasoft module. The effect of cooling rate on segregations are significantly observable. Sr amount just only changes the mean value of deviation.
- Shrinkage porosity formation has dramatically increased on 250 ppm Sr addition. Correlation studies are necessary to prove that claim.
- Thermal analysis results show that the maximum development has occurred on 150 ppm Sr. After that, undercooling on eutectic formation temperatures tend to increase with just a lower ratio. Even if the maximum improvement on modification has obtained by 250 ppm Sr based on eutectic depression data, due to maximum porosity level observation on that composition, theoretical delimitation has obtained. 150 ppm Sr addition on A356 alloy seems to be best solution for eutectic modification.

- According to Ferdian et al, minimum eutectic depression limit has obtained as 7°C, and minimum cooling rate has mentioned as 0.7°C/s, for optimum eutectic modification. It can be concluded that, minimum required modification can be observed even on spoke 4 which has lowest cooling rate among all spokes of casting part. Simulation data has given eutectic depression values more than 7°C (Minimum value was obtained on spoke 4, 150 ppm Sr level as 9,995°C).
- It was also exposed that cooling rate and Sr addition correlation can only get done by further real casting comparison with same setup. Actual microstructure and mechanical properties result such as eutectic Si aspect ratio and yield-tensile strength and elongation results are noteworthy to consider.

Acknowledgments

This work was co-supported by Tübitak 2209-B Industry/Undergraduate Thesis Support Programme and also by CMS Jant ve Makina San. R&D Center.

Author's Contributions

Batuhan Dođdu: Drafted and wrote the manuscript, performed the experiment and result analysis.

Uđur Aybarç: Assisted in analytical analysis on the structure, supervised the experiment's progress, result interpretation and helped in manuscript preparation.

Serkan Gündođdu: Assisted in analytical analysis and helped in manuscript preparation.

Onur Ertuđrul: Assisted in analytical analysis on the structure, supervised the experiment's progress, result interpretation and helped in manuscript preparation.

Ethics

There are no ethical issues after the publication of this manuscript.

References

1. Sigworth, G. K., Fundamentals Of Solidification In Aluminum Castings. 2014. *International Journal of Metalcasting*; 8: 7-20.
2. Pramod, Ravikirana, A. K. Prasada Rao, Murty B. S., Bakshi S. R. 2016. Effect of Sc addition and T6 aging treatment on the microstructure modification and mechanical properties of A356 alloy, *Materials Science and Engineering: A*; 674:438-450.
3. Lu, S Z., Hellawell 1987. A. The mechanism of silicon modification in aluminum-silicon alloys: Impurity induced twinning. *Metallurgical and Materials Transactions A*; 18:1721-1733.
4. Hanna, M.D., Lu, SZ. & Hellawell 1984. A. Modification in the aluminum silicon system *Metallurgical and Materials Transactions A*; 15, 459-469.
5. Iwahori, H., Yonekura, K., Yamamoto, Y., Nakamura, M., 1990. Occuring Behaviour Of Porosity And Feeding Capabilities Of Sodium And Strontium Modified Al-Si Alloys. *AFS Transactions*; 98:167-173.
6. Fang, Q. T., Granger, D. A. 1989. Porosity Formation In Modified And Unmodified A356 Alloy Castings. *Transactions of the American Foundry Society*; 97.10: 989-1000.
7. Murty B. S., Kori S. A. & Chakraborty M. 2002. Grain refinement of aluminium and its alloys by heterogeneous nucleation and alloying. *International Materials Reviews*; 47:1, 3-29
8. Sigworth G.K. and Guzowski M.M. 1985. Grain refining of Hypo-eutectic Al-Si Alloys. *AFS Transactions*; 93:907-12.
9. Kori, S. A., Auradi V., Murty, B. S.; Chakraborty, M. 2004. Poisoning and fading mechanism of grain refinement in Al-7Si alloy *Proceedings of 3rd International Conference on Advanced Materials Processing (ICAMP-3)*; pp. 387-393.
10. Zhang L.Y., Jiang A Y.H., Ma Z., Shan S.F., Jiab Y.Z., Fan C.Z., Wang W.K. 2008. Effect of Cooling Rate on Solidified Microstructure and Mechanical Properties of Aluminium-A356 Alloy. *Journal of Materials Processing Technology*; 207:107-111
11. James G. Conley, Julie Huang, Jo Asada, Kenji Akiba, 2000. Modeling the Effects of Cooling Rate, Hydrogen Content, Grain Refiner and Modifier on Microporosity Formation In Al A356 Alloys. *Materials Science and Engineering*; 285:49-55.
12. Tiryakiođlu, M., Campbell, J., Alexopoulos, N. D. 2009. On the Ductility of Cast Al-7 Pct Si-Mg Alloys. *Metallurgical and Materials Transactions A*; 40(4):1000-1007.
13. Eskin D, Du Q, Ruvalcaba D. 2005. Experimental Study of Structure Formation in Binary Al-Cu Alloys at Different Cooling Rates. *Materials Science and Engineering A*; 404: 1-10.
14. Liao H C, Sun Y, Sun G X. 2002. Correlation Between Mechanical Properties and Amount of Dendritic A-Al Phase in As-Cast Near-Eutectic Al-11.6%Si Alloys Modifies with Strontium. *Material Science and Engineering A*; 335:62-66.
15. Ferdian, D., Lacaze, J., Lizarralde, I., Niklas, A., & Fernandez-Calvo, A. I. 2013. Study of The Effect of Cooling Rate on Eutectic Modification in A356 Aluminium Alloys. *Materials Science Forum*; 765:130-134.
16. K. Nogita; H. Yasuda; K. Yoshida; K. Uesugi; A. Takeuchi; Y. Suzuki; A.K. Dahle 2006. Determination of strontium segregation in modified hypoeutectic Al-Si alloy by micro-X-ray fluorescence analysis. *Scripta materialia*; 55(9), 787-790.
17. Stuart D. McDonald; Kazuhiro Nogita; Arne K. Dahle 2006. Eutectic grain size and strontium concentration in hypoeutectic aluminium-silicon alloys. *Journal of alloys and compounds*; 422(1-2), 0-191.
18. Sumanth Shankar; Yancy W Riddle; Makhlof M Makhlof 2004. Nucleation mechanism of the eutectic



phases in aluminum–silicon hypoeutectic alloys. *Acta Materialia* 52.15; 4447–4460.

19. Nogita, K., McDonald, S. D., & Dahle, A. K. 2004. Solidification mechanisms of unmodified and strontium-modified hypereutectic aluminium-silicon alloys. *Philosophical Magazine*; 84(17), 1683-1696.
20. McDonald, S.D., Dahle, A.K., Taylor, J.A. *et al.* 2004. Eutectic grains in unmodified and strontium-modified hypoeutectic aluminum-silicon alloys. *Metallurgical and materials transactions A*;35(6), 1829-1837.

Synthesis, Spectroscopic Characterization, Crystal Structure and Theoretical Studies on New Organic Single Crystal of 1-(3,5-Difluorophenyl)-3-(2-Nitrophenyl)Urea

Tuğba Güngör^{1*}, Tuncay Karakurt², Zarife Sibel Şahin³

¹ Department of Chemistry, Faculty of Sciences and Arts, Natural Products and Drug Research Laboratory, Çanakkale Onsekiz Mart University, Çanakkale, Turkey

² Department of Chemical Engineering, Faculty of Engineering-Architecture, Kırşehir Ahi Evran University, Kırşehir, Turkey

³ Department of Energy Systems Engineering, Faculty of Engineering and Architecture, Sinop University, Sinop, Turkey

*tgungor@comu.edu.tr

*Orcid: 0000-0001-5261-1856

Received: 27 February 2021

Accepted: 1 June 2021

DOI: 10.18466/cbayarfbe.887714

Abstract

A new organic compound, 1-(3,5-difluorophenyl)-3-(2-nitrophenyl)urea was synthesized from 2-nitroaniline, 3,5-difluoroaniline and triphosgene in sequential two steps with 92% yield. The product was crystallized by the slow evaporation using THF and ethyl acetate solvent system to obtain its single crystal. The pure crystals were characterized with melting point, FT-IR, ¹H NMR, ¹³C NMR and MS. The structure of the compound was brought to light by X-ray single-crystal structure determination. Density functional theory calculations were applied by using (DFT/B3LYP) method with the 6-311G(d,p) basis set level. The potential energy surface (PES) scanning was performed to determine the stability of the molecule. Frontier molecular orbitals of the compound were calculated. AIM charge and MEP analyzes were performed.

Keywords: Crystal structure, DFT calculations, diphenylurea, triphosgene, XRD

1. Introduction

In recent years, there has been an increasing interest in 1,3-diphenylureas which are also known as *N,N'*-diphenylureas due to their wide range of chemical and biological applications [1,2]. It is known that these compounds show good pharmacological activities including anticancer [3-5], antimalarial [6,7], anti-Alzheimer [8], antiviral [9], carbonic anhydrase I and II inhibitors [2], anti-tuberculosis [10] and antidepressant [11,12]. Regorafenib named 4-(4-(((4-chloro-3-(trifluoromethyl)phenyl)carbamoyl}amino)-3-fluorophenoxy)-*N*-methylpyridine-2-carboxamide which is a diphenylurea derivative drug shows the pharmaceutical properties as multikinase inhibitor of VEGFR-2, -3, c-Kit, p38 MAP kinase *etc.* and uses at the treatment of colorectal, hepatocellular and gastrointestinal stromal cancers [3]. In addition, sorafenib is another effective kinase inhibitor drug containing diphenylurea moiety

uses for the treatment of kidney, liver and thyroid cancers [5]. Also, 1,3-diphenylureas were reported acting like auxins and cytokinins which are important plant growth regulators in agrochemical applications [13].

The synthesis of unsymmetrical diphenylurea derivatives is an important issue due to their superior biological applications and chemical treatments including usage as intermediate, linker in complex synthesis and also protection of amino groups. Synthesis of target structures can be carried out with aniline derivatives and phosgene [14,15], triphosgene (BTC, bis(trichloromethyl) carbonate) [16], 1,1'-carbonyldiimidazole (CDI) [7], *S,S*-dimethyl dithiocarbonate [17], 1,1-carbonylbis benzotriazole [18] or carbon monoxide/dioxide with catalysts [19,20] as CO sources. In addition, alternative synthesis method is Curtius rearrangement which begins with a different

starting material, substituted benzoyl chlorides. The first step of this method is the reaction of benzoyl chloride derivative and sodium azide to obtain benzoyl azide derivative. In the second step, *in situ* generation of isocyanate occurs through the removal of nitrogen gas and the reaction of aniline derivative with intermediate isocyanate results in the target diphenylurea product [21].

The density functional theory (DFT) is an approach that determines the quantum chemical model of structures and is presently one of the most successful methods. DFT predicts many molecular properties such as molecular structures, vibrational frequencies, molecular energies, and electric properties. The fact that the simulation results are very close to experimental studies is one of the reasons why DFT is a preferred method.

In this study, we synthesized a new *N,N'*-diphenylurea derivative (compound **4**) successfully using a two-step synthesis approach with high yield. The well-shaped crystals of product were obtained by using slow evaporation technique and characterized with melting point and various spectral analyses such as FT-IR, ¹H NMR, ¹³C NMR, MS and X-ray single diffraction. Theoretical calculations were performed using the DFT(B3LYP) method and 6-311G(d,p) basis set to determine and characterize the molecular and electronic structure properties of the compound. NMR and IR values of the optimized structure were compared to the experimental values. The potential energy surface (PES) scanning was performed to determine the stability of molecule. Frontier molecular orbitals of the compound were calculated. Also, AIM charge and MEP analyzes were performed.

2. Materials and Methods

All chemicals and solvents used in the experimental studies were provided from commercial suppliers and used without further purification. Reaction tracking was conducted by using thin-layer chromatography with Merck precoated Kieselgel 60GF₂₅₄ plates. Melting point was recorded with X-4 melting-point apparatus. Infrared spectra were measured with a Perkin Elmer Spectrum 100 FTIR spectrophotometer in the range 4000-600 cm⁻¹ with attenuated total reflectance (ATR) sampling accessory. NMR spectra were registered with a Jeol High-Performance Digital FT-NMR spectrometer (400 and 100 MHz for ¹H and ¹³C, respectively) using DMSO-d₆ as solvent. The molecular weight of product was determined with Shimadzu LC-MS/MS 8040 Liquid Chromatograph Mass Spectrometer with an ESI source. The single crystal X-ray diffraction (XRD) data was collected at ambient temperature on an Agilent Supernova X-Ray Diffractometer using Molybdenum X-ray source and CCD detector. Literature search of compound was done using Reaxys database.

2.1. Synthesis of 1-(3,5-difluorophenyl)-3-(2-nitrophenyl)urea (compound **4**)

2-Nitroaniline (**1**, 1.0 mmol; 0.138 g) was dissolved in 2 mL DCM. Bis(trichloromethyl)carbonate (triphosgene, 1.0 mmol; 0.296 g) in 1 mL DCM and triethylamine (0.3 mL) were added slowly in an ice bath. The mixture was stirred at 0-5 °C for 30 min and then room temperature for 2 hours. Solvent was evaporated in vacuo to dryness and the residue (**2**) was dissolved in a mixture of THF:DCM (1:1, 6 mL). 3,5-Difluoroaniline (**3**, 1.0 mmol; 0.129 g) was added to the reaction medium and was stirred at reflux condition for 4 hours. Upon completion as shown by TLC, solvent mixture was evaporated in vacuo to dryness. Crude product was dissolved in acetone (8 mL) and distilled water (8 mL) was added on it. Obtained orange solid was filtered, washed with water (20 mL) and dried at room temperature. (0.27 g, 92% yield) mp 200-202 °C; IR (ATR) ν 3404, 3332, 3127, 3098, 1728, 1630, 1605, 1502, 1477, 1415, 1335, 1269, 1168, 1140, 1113, 1087, 1047, 1002, 975, 872, 850, 837, 746, 706, 666 cm⁻¹; ¹H NMR (400 MHz, DMSO-d₆) δ 10.15 (s, 1H), 9.60 (s, 1H), 8.18 (dd, J= 8.45 and 1.15 Hz, 1H), 8.06 (dd, J= 8.33 and 1.45 Hz, 1H), 7.69 (td, J= 7.86 and 1.53 Hz, 1H), 7.22 (td, J= 7.80 and 1.26 Hz, 1H), 7.14 (dd, J= 9.87 and 2.25 Hz, 2H), 6.82 (tt, J= 9.39 and 2.31 Hz, 1H); ¹³C NMR (100 MHz, DMSO-d₆) δ 164.41 and 164.26 (d, J_{C-F}=15.65 Hz), 161.99 and 161.84 (d, J_{C-F}=15.42 Hz), 152.26, 142.64-142.36 (t, J_{C-F}=13.96 Hz), 138.82, 135.50, 134.63, 125.95, 123.44, 101.97 and 101.68 (d, J_{C-F}=29.28 Hz), 98.27-97.75 (t, J_{C-F}=26.28 Hz); MS (ESI): m/z (%) 294 (M⁺, 100), 279 (44), 163 (36).

2.2. Growth of Crystal

A saturated solution of product was prepared from the pure solid using THF as solvent and filtered. Vapor diffusion technique which use volatile-less volatile binary solvent system for better crystallization was applied to get single crystals. For this purpose, ethyl acetate was used as outer solvent and the solution was kept at room temperature. The orange needle crystals suitable for single-crystal diffraction experiments were obtained after ten days.

2.3. X-Ray Diffraction Analysis

Suitable crystal of compound **4** was selected for data collection which was performed on a SuperNova diffractometer equipped with a graphite-monochromatic Mo-K α radiation at 296 K. The H atoms of C atoms were located from different maps and then treated as riding atoms with C-H distance of 0.93 Å. Other H atoms were located in a difference map and refined freely. We used these procedures for our analysis: solved by direct methods; SHELXS-2013 [22]; refined by full-matrix least-squares methods; SHELXL-2013

[23]; data collection: Bruker APEX2 [24]; molecular graphics: MERCURY [25]; solution: WinGX [26]. Details of data collection and crystal structure determinations were given in Table 3.

2.4. Theoretical Calculations

The molecular modeling studies of the compound were performed with the DFT/B3LYP method [27,28] and 6-311G(d,p) basis set [29] by using Gaussian 09 software package [30]. Aim charge analysis was done using AIMAll [31] suite of programs to examine intermolecular and intramolecular interactions. Molecular orbitals of the molecule were calculated and visualized using the Multiwfn program [32].

3. Results and Discussion

3.1. Synthesis of Title Compound

One-pot, sequential two-step synthesis was performed to the formation of target unsymmetrical urea derivative **4** (Figure 1). The first step was the synthesis of isocyanate intermediate (**2**) from 2-nitroaniline (**1**) and triphosgene by using triethylamine as base at room temperature. Mechanistically, triphosgene reagent causes to the by-product formation of 2 moles phosgene and HCl. While the reactive intermediate phosgene continues to the similar reaction with 2-nitroaniline to form isocyanate **2**, hydrochloric acid gives triethylammonium chloride with triethylamine base. Also, triethylamine helps to the removing of acidic hydrogens of -NH₂ group on 2-nitroaniline, increasing the nucleophilic power and accelerating the formation of the isocyanate **2**. The second step, a typical urea synthesis was carried out between intermediate **2** which was used directly without further purification and 3,5-difluoroaniline at reflux conditions in DCM/THF solvent mixture. As a result, 1-(3,5-difluorophenyl)-3-(2-nitrophenyl)urea (**4**) was obtained with high purity and high yield, 92% (Figure 1). Product was identified by melting point, FT-IR, ¹H NMR, ¹³C NMR and LC-MS analyses (See experimental part and supplementary information). It is determined that compound is air-stable and soluble in common organic solvents such as acetone, ethyl alcohol, ethyl acetate, THF, DCM *etc.* but insoluble in water.

3.2. Spectroscopic Analysis

All spectra and data of the compound **4** were given in the Experimental part and Supplementary information. The calculated and experimental FT-IR spectrum and some of the compared characteristic frequencies were given in Figure 2 and Table 1. The compound has 84 normal modes of vibration (Table 1 and S1). The free vibration frequencies of the N-H group, which does not contain an intramolecular or intermolecular hydrogen bonding are in the range of 3700 and 3550 cm⁻¹, while the free vibration frequencies of the N-H group containing hydrogen bonding are observed in the range of 3200–2400 cm⁻¹ [33]. In this study, the free vibration frequencies of the N-H mode of asymmetric ureas have been observed as 3404 and 3332 cm⁻¹ experimentally, and this frequency is reported as 3179 cm⁻¹ in the literature [34]. The calculated values were observed at 3476 and 3318 cm⁻¹ with a contribution of 100 and 98% of PED (Potential Energy Distribution). In the presence of the N-H group which contains intermolecular or intramolecular hydrogen bonds within the molecule, the stretching vibration frequency values of this group decreased while the bending vibration frequency values increase [35]. The experimental/calculated values of the in-plane angle bending vibration frequency of N-H mode were obtained as 1630/1587-1485 cm⁻¹, while this value in literature is 1494 cm⁻¹ [36]. The experimental/calculated values of the out-of-plane angle bending vibration frequency of N-H mode were obtained as 666/673 cm⁻¹.

Other major feature of compound was strong carbonyl (C=O) band at 1728 cm⁻¹ and also this band appeared at 1714 cm⁻¹ as pure strain vibration with 74% PED additive in the theoretical spectrum. The experimental band at 1502 and 1335 cm⁻¹ corresponds to the asymmetrical and symmetrical stretching vibrations of the NO₂ group while N-O vibration frequencies (with PED additive) are calculated as 1595 (10%) cm⁻¹, 1541 (30%) cm⁻¹, 1435 (24%) cm⁻¹, 1313 (31%) cm⁻¹ and 1252 (22%) cm⁻¹. Characteristic C-H vibration frequency values of aromatic compounds are observed in the range of 3100-3000 cm⁻¹ [37], while C-C aromatic stretching vibrations are observed in the range of 1600-1400 cm⁻¹ [38].

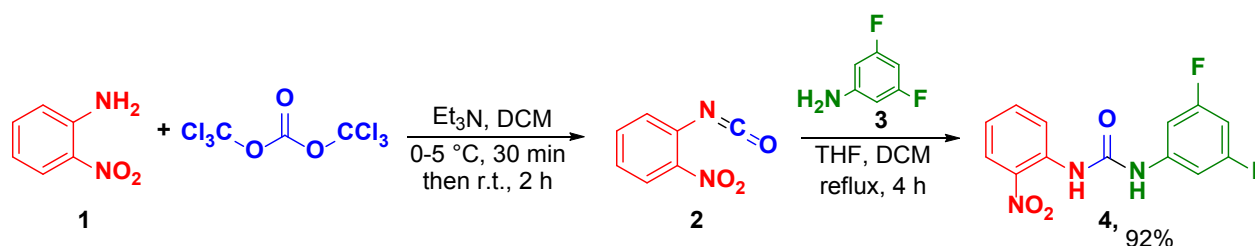


Figure 1. Two-step synthesis scheme of 1-(3,5-difluorophenyl)-3-(2-nitrophenyl) urea.

In our study, symmetrical C-H and C-C vibration frequencies were experimentally observed in the range of 3127, 3098 and 1605 cm^{-1} , respectively, and agree with the literature values 3110-3003 and 1666-1535 cm^{-1} [39].

Theoretically, C-H vibration frequency values (with PED contribution) were observed in 3134 (99%) cm^{-1} , 3126 (99%) cm^{-1} , 3106 (95%) cm^{-1} , 3102 (100%) cm^{-1} , 3076 (96%) cm^{-1} , 3066 (100%) cm^{-1} and 3056 (93%) cm^{-1} as pure C-H vibration while C-C mode was calculated as 1601 cm^{-1} with 45% of PED contribution. In-plane C-H angle bending vibration frequencies in the aromatic ring are experimentally observed between 1400–1000 cm^{-1} [40]. In our study, this vibration frequency was observed experimentally as 1477, 1415 cm^{-1} and calculated with the PED contributions theoretically as 1211 (26%) cm^{-1} , 1195 (55%) cm^{-1} , 1138 (66%) cm^{-1} and 1128 (30%) cm^{-1} . The stretching of the C-F bond was confirmed at 1113 cm^{-1} while this band appeared at 1092, 985, 953 cm^{-1} in the theoretical spectrum. Also, 1,2- and 1,3- C-H vibrations of di/trisubstitutedbenzene were determined as strong peaks at the fingerprint region (837 and 746 cm^{-1}) of experimental spectra. Other calculated vibration modes were given in Table S1.

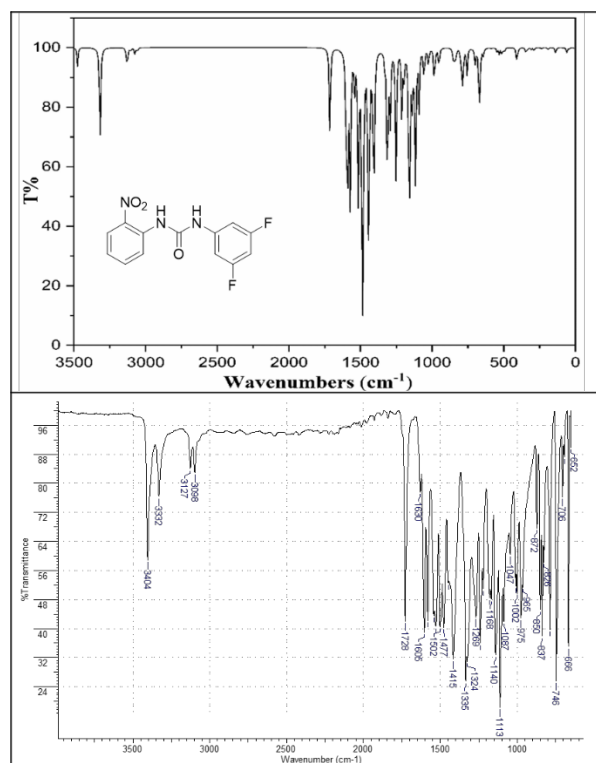


Figure 2. Theoretical and experimental IR spectra of the title compound.

To investigate NMR chemical shifts of the molecules, GIAO (Gauge-Independent Atomic Orbital) method [41,42] was used. ^1H and ^{13}C chemical shift values were calculated using the DFT/B3LYP method with 6-

311G(d,p) basis set. The geometry of compound, together with that of tetramethylsilane (TMS, $\text{Si}(\text{CH}_3)_4$) were fully optimized choosing dimethyl sulfoxide (DMSO) solvent. The ^1H and ^{13}C NMR chemical shifts were converted to the TMS scale by subtracting the calculated absolute chemical shielding of TMS with values of 32.10 ppm (^1H) and 189.40 ppm (^{13}C). All ^1H and ^{13}C NMR peaks of compound **4** were monitored at the expected regions (Figure 3 and supplementary information) and confirmed the target structure (Table 2). When compound was examined spectroscopically in detail, signals were detected in the range of 10.15-6.82 ppm in ^1H NMR spectrum. Two characteristic broad singlet signals with 1H integration (10.15 and 9.60 ppm) confirm the presence of -NH groups of urea. The calculated shift values for these protons were found as 11.31 and 6.31 ppm. Four split peaks (H2-H5) with 1H integration on nitroaromatic ring (Ring A) were observed at 8.18, 8.06, 7.69 and 7.22 ppm and calculated as 9.37-7.16 ppm for theoretical spectrum. Also, three protons of fluoro atoms containing aromatic ring (Ring B) were shifted in the high-field of spectrum when compared Ring B. While doublet of doublets peak at 7.14 ppm corresponded to the protons H9 and H13 with 2H integration, the signal of H11 was appeared as triplets of triplet at 6.82 ppm due to splitting with two fluorine atoms in orto position and two hydrogen atom in meta position. In addition, these Ring B protons were calculated in the range of 8.31-6.38 ppm according to the DFT/6-311G(d,p) method.

In the ^{13}C NMR spectrum, the signal of carbonyl carbon of urea (C7) was located at 152.26 ppm and calculated as 153.11 ppm (Figure 3 and Table 2). Other aromatic carbons were observed in the region of 164.34-98.01 ppm as expected. The highest chemical shifts 164.34 and 161.92 ppm were belong to the fluorine-bound carbons C10 and C12 as doublet peaks because of the high deshielding effect of the electronegative fluorine atom. These carbons were found as 171.52, 170.83 ppm by theoretical calculations. However, the lowest value (98.01 ppm) which was splitted as a triplet peak by two neighbor fluorine atoms correspond to the C11 carbon and is calculated as 100.02 ppm. Also, triplet peak at 142.50 ppm was belong to carbon C8 and doublet peaks of 101.97 and 101.68 ppm were belong to the carbons C9 and C13. The chemical shifts of carbons C8, C9 and C13 were calculated as 146.96, 102.63 and 102.59 ppm, respectively. Carbons C1-C6 in the Ring A were observed at 134.63, 125.95, 123.44, 135.50 and 138.82 ppm as singlet peaks. It is noted that the strong peak at 123.44 ppm correspond to overlapped two carbons named C3 and C5 (Figure 3). Also, Ring A carbons (C1-C6) were calculated in the range of 144.43-121.98 ppm.

In addition to FT-IR and NMR analyses, molecular weight of title compound (**4**) was confirmed as 293.23 g/mol ($\text{C}_{13}\text{H}_9\text{F}_2\text{N}_3\text{O}_3$) with LC-MS analysis in negative and positive modes (see supplementary information).



Table 1. Comparison of the observed and calculated vibrational spectra of title compound.

Experimental		Theoretical		
Assignment	Frequency (cm ⁻¹)	Frequency (cm ⁻¹)	Assignment PED (%)	Intensity (kcal/mol)
urea N-H	3404	3476	ν NH 100	29
	3332	3318	ν NH 98	216
aromatic C-H stretching	3127, 3098	3134	ν CH 99	22
		3126	ν CH 99	19
		3106	ν CH 95	4
		3102	ν CH 100	2
		3076	ν CH 96	11
		3066	ν CH 100	2
		3056	ν CH 93	7
urea C=O	1728	1714	ν OC 74	355
aromatic C=C	1605	1601	ν CC 45	298
aromatic C-H bending	1477, 1415	1211	ν NC 10+ δ HCC 13+ δ HCC 13	732
		1195	δ HCC 25+ δ HCC 15+ δ HCC 26	370
		1138	ν CC 12+ δ HCC 15+ δ HCC 40	1482
		1128	ν NC 14+ ν NC 15+ δ HCC 17+ δ HCC 13	332
asymmetric NO ₂	1502	1595	ν ON 10+ ν CC 21+ ν CC 10	272
		1541	ν ON 17+ ν CC 14+ ν ON 13+ ν CC 11	151
		1435	ν ON 24+ δ HNC 10+ δ HCC 10	201
symmetric NO ₂	1335	1313	ν ON 10+ ν ON 21+ ν NC 14	63
		1252	ν ON 22+ ν CC 17+ ν NC 10	23
C-F	1113	1092	ν FC 25+ ν FC 21+ δ HCC 40	847
		985	ν CC 13+ ν CC 11+ ν FC 16+ δ HCC 12	75
		953	ν FC 12	11

ν : stretching, δ : in plane bending

Table 2. Theoretical and experimental ¹H and ¹³C chemical shifts for 1-(3,5-difluorophenyl)-3-(2-nitrophenyl)urea.

Assign. ^a	¹ H NMR		Assign. ^a	¹³ C NMR	
	Experimental ^b (ppm)	Calculated ^c (ppm)		Experimental ^b (ppm)	Calculated ^c (ppm)
H2	8.18	9.37-7.16	C1	134.63	140.17
H3	7.69	(Ring A)	C2	125.95	130.57
H4	7.22		C3, C5	123.44 ^d	124.22, 121.98
H5	8.06		C4	135.50	142.75
H9, H13	7.14	8.31-6.38	C6	138.82	144.43
H11	6.82	(Ring B)	C7	152.26	153.11
H(N2)	10.15	11.31	C8	142.50	146.96
H(N3)	9.60	6.31	C9, C13	101.97, 101.68	102.63, 102.59
			C10, C12	164.34 ^e , 161.92 ^e	171.52, 170.83
			C11	98.01	100.02

a The assignments of atoms are according to the ORTEP numbering

b NMR solvent: DMSO-d₆

c DFT/6-311G(d,p)

d Overlapped

e Average

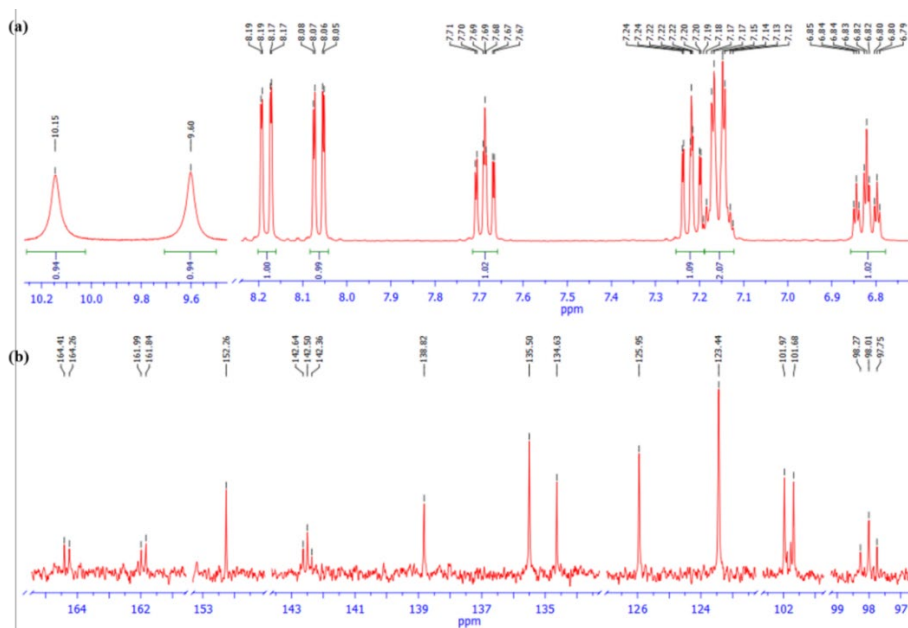


Figure 3. ^1H NMR (a) and ^{13}C NMR (b) spectra of compound 4.

3.3. X-ray Crystal Structure of Compound 4

The molecular structure of compound 4 with the atom labeling was shown in Figure 4. The parameters for data collection and structure refinement of the compound were listed in Table 3. The nitro group is equivalent and typical of N=O double bonds [N1-O1=1.2184(19) Å and N1-O2=1.2277(19) Å]. The dihedral angle between phenyl rings is 35.62(5)°. The selected bond lengths and bond angles were given in Table 4. The molecules of 4 are connected by N-H \cdots O hydrogen bonds (Table 5). Atom N3 atom acts as hydrogen-bond donor, via atom H3A, to nitro atom O2ⁱ [(i) 1-x, -y, 1-z], forming a centrosymmetric R₂²(16) ring centered at (1/2, 0, 1/2). Compound 4 also contains two $\pi\cdots\pi$ interactions. The intermolecular $\pi\cdots\pi$ interactions occur between the two symmetry-related phenyl rings of neighboring molecules. The distances between the ring's centroids are 3.814 Å and 3.817 Å. The combination of $\pi\cdots\pi$ interactions produces one-dimensional supramolecular network which is running parallel to the [010] direction (Figure 5).

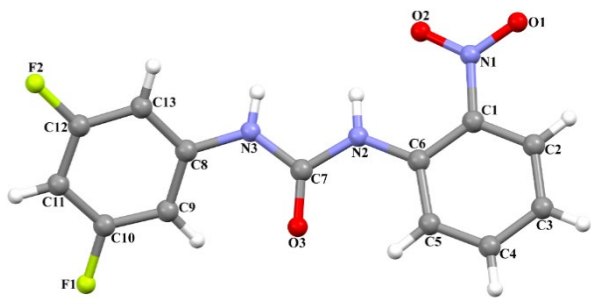


Figure 4. The molecular structure of 4 showing the atom numbering scheme.

3.4. Conformational Analysis

To determine stability of the molecule, 2D potential energy surface scanning (PES) was performed. Single point energies were calculated by changing θ_1 (C6-N2-C14-S1) dihedral angle for $-180^\circ/+180^\circ$ angle range and 10° steps. As a result of PES (Figure 6) analysis, 4 conformations (Conf 1-4) corresponding to global and local minimum points were obtained. The molecular structures of these 4 conformations were optimized using DFT/B3LYP/6-311g (d, p) methods.

Table 3. Crystal data and structure refinement parameters for compound 4.

Empirical formula	C₁₃H₉F₂N₃O₃
Formula weight	293.23
Crystal system	Monoclinic
Space group	I2/a
a (Å)	25.8745 (16)
b (Å)	3.8143 (3)
c (Å)	24.7392 (19)
β (°)	94.051 (6) ^o
V (Å³)	2435.5 (3)
Z	8
D_c (g cm⁻³)	1.599
μ (mm⁻¹)	0.14
θ range (°)	4.4-28.1
Measured refls.	4365
Independent refls.	2391
R_{int}	0.015
S	1.03
R1/wR2	0.043/0.110
$\Delta\rho_{\text{max}}/\Delta\rho_{\text{min}}$ (eÅ⁻³)	0.23/-0.23

Table 4. Selected bond distances and angles for compound **4** (Å, °).

N1-O1	1.2184 (19)	N1-O2	1.2277 (19)
C7-O3	1.2029 (19)		
N3-C7-N2-C6	176.09 (18)	N2-C7-N3-C8	-176.24 (18)

Table 5. Hydrogen bonds parameters for compound **4** (Å, °).

D-H...A	D-H	H...A	D...A	D-H...A
N2—H2A...O2	0.88 (2)	1.95 (2)	2.6383 (18)	133
C5—H5...O3	0.93	2.18	2.811 (2)	124
N3—H3A...O2 ⁱ	0.83 (2)	2.55 (2)	3.2824 (19)	148

As seen in Table 6, conf 1 and conf 4 are the most stable structures. Hence, theoretical calculations were continued with the conf 1 structure (Figure 7).

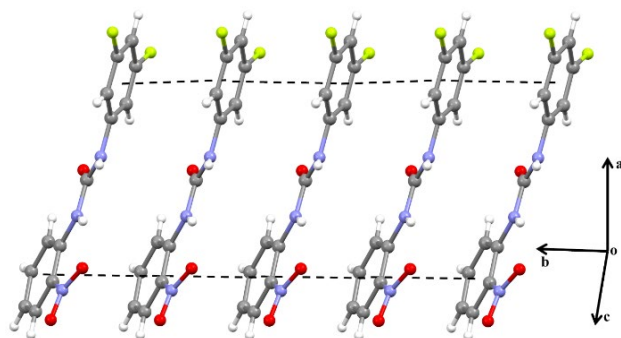


Figure 5. Crystal structure of **4**, showing the formation of a chain along [010] generated by $\pi \cdots \pi$ interactions.

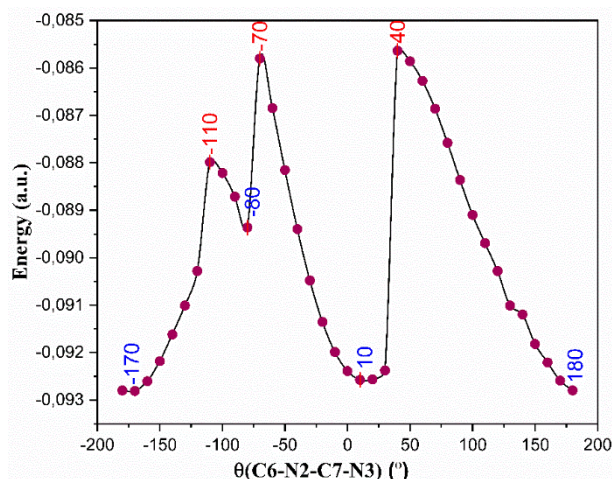


Figure 6. Molecular energy profile versus the selected torsional degree of freedom.

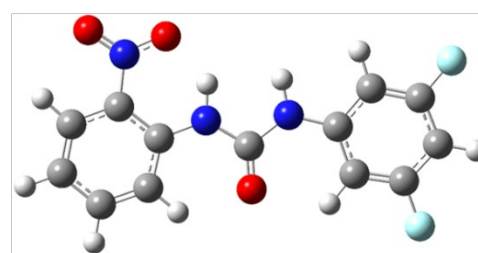
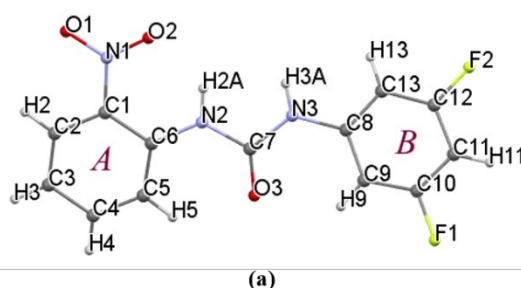


Figure 7. The X-ray (a) and optimized (b) structure (conf1) of the title compound.

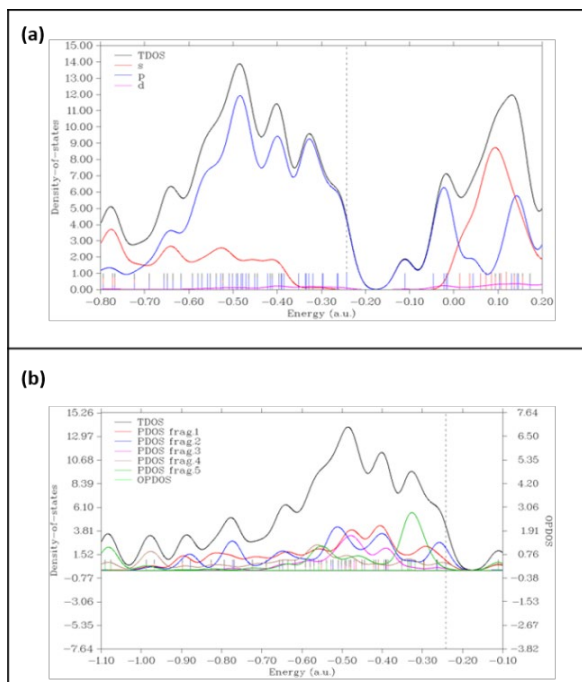
Table 6. Conformation structures of the title molecule.

E= -1090.629173 Conf1	E= -1090.621512 Conf2	E= -1090.621512 Conf3	E= -1090.629173 Conf4

3.5. Frontier Molecular Orbitals

The Density-of-States (DOS) is an important concept in solid state physics and describes the number of states that are to be occupied by the system at each level of energy. The s, p, d atomic orbitals forming the molecule and Total Density-of-States (TDOS)

were shown in Figure 8a. It was observed that atomic orbitals consist mainly of s and p orbitals. Besides, atomic orbital contributions of fragments are also shown in Figure 8b. It is also seen that the most contribution to the formation of molecular orbitals was provided by fragment 1 and fragment 2.



frag. 1: A ring; frag. 2: B ring; frag. 3: C11 and C1 2 atoms; frag. 4: N1, N2 and N3 atoms; frag. 5: O1, O2 and O3 atoms

Figure 8. Plot TDOS, PDOS and OPDOS a) s, p and d orbitals b) specific fragments.

The frontier molecular orbitals (HOMO and LUMO) are the most important molecular orbitals. HOMO is molecular orbital of the highest energy that is occupied by electrons, while LUMO is the molecular orbital of the lowest energy that is not occupied by electrons. HOMO and LUMO orbitals of a molecule are also known as electron donor and acceptor groups [43-46]. They can be used to determine intermolecular charge transfers. Besides, molecular properties such as ionization potential, electron affinity, chemical reactivity, kinetic stability, polarization, conjugation can be calculated by considering these orbitals [47-50].

Figure 9 contains the orbital distributions of HOMO, HOMO-1, LUMO and LUMO+1 of the molecule. The highest 5 atomic contributions to these orbitals were calculated as LUMO + 1: C3 (16%) + C5 (14%) + C2 (12%) + C6 (12%) + C7 (12%), LUMO: N1 (26%) + O1 (21%) + O2 (19%) + C4 (10%) + C2 (9%), HOMO: N2 (10%) + N3 (18%) + C3 (7%) + C11 (18%) + C5 (5%), HOMO- 1: C13 (25%) + C10 (15%) + C9 (10%) + C12 (6%) + C3 (5%). As can be seen, these 5 atoms are expected to be the most active in a reaction or interaction in the HOMO, HOMO-1, LUMO and LUMO + 1 orbitals of the title compound.

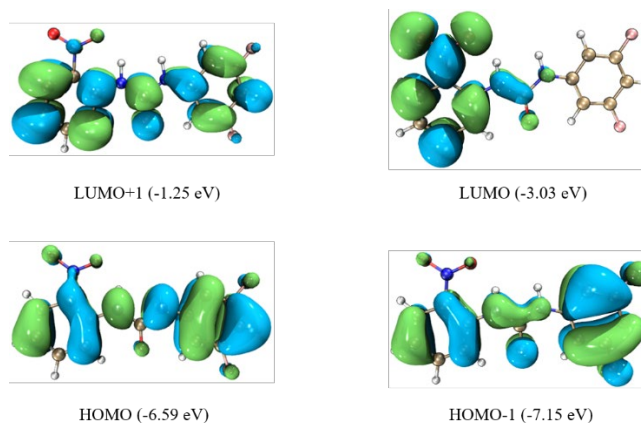


Figure 9. Molecular orbital surfaces and energy levels.

3.6. AIM Charge and MEP Analyzes

Bader's QTAIM theory has been used for details about the nature and strength of intra- and inter-molecular hydrogen bonds [51]. The strength and interaction type of the intra- and inter-molecular bonds in the compound were obtained by using the electron density (ρ_{BCP}), the Laplacian of electron density ($\nabla^2(\rho_{BCP})$), the potential energy density ($V(r)$), the kinetic energy density ($G(r)$) and electronic energy density ($H(r)$) in the BCPs (different bond critical points). $\nabla^2(\rho_{BCP})$ is negative in covalent bonds, while it is positive in the bonds formed by ionic, Van der Waals and hydrogen interactions. Rozas et al. [52] evaluated that $\nabla^2(\rho_{BCP}) < 0$ and $H_{BCP} < 0$ for the strong hydrogen bonds that have covalent character, $\nabla^2(\rho_{BCP}) > 0$ and $H_{BCP} < 0$ for the medium-strong hydrogen interactions that have partial covalent character, and

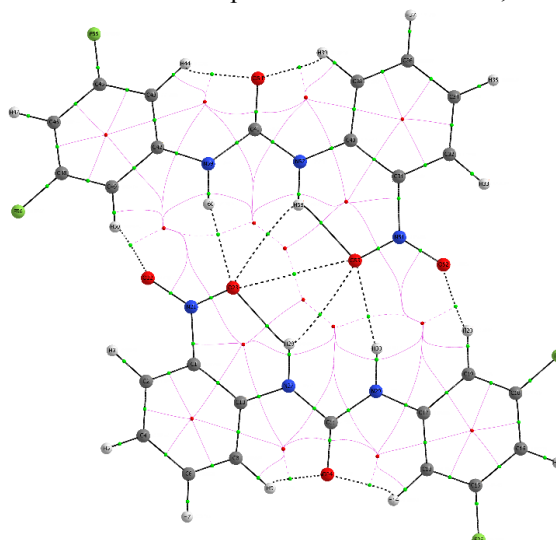


Figure 10. Molecular graph of dimer: bond critical points (small green spheres), ring critical points (small red sphere).

$\nabla^2(\rho_{BCP}) > 0$ and $H_{BCP} > 0$ for the weak hydrogen bonds that have electrostatic character. The molecular graph of the compound's dimer structure is shown in Figure 10.

Table 7 shows the intra-molecular and inter-molecular interactions observed in the molecule. Interaction energies (E_{int}) were calculated to determine the significances of these interactions. The

relationship between E_{int} and potential energy density was given as $E_{int} = 1/2 (V_{BCP})$ by Espinoza [53]. In Table 7, it was found that the interaction energy of the N2-H2A...O2 hydrogen bond is greater than other interactions ($E_{int} = -9.37$ kcal/mol). The positive ρ_{BCP} and H_{BCP} values of the three interactions also showed that these interactions are weak hydrogen bonds that have electrostatic character.

Table 7. Topological parameters for bonds of interacting atoms.

Interaction	ρ_{BCP} (a.u.)	$\nabla^2\rho_{BCP}$ (a.u.)	G_{BCP} (a.u.)	V_{BCP} (a.u.)	H_{BCP} (a.u.)	E_{int} (kcal/mol)
N2-H2A...O2	+0.034478	+0.133038	+0.031571	-0.029883	+0.001688	-9.37
N2-H2A...O2 ⁱ	+0.007258	+0.028038	+0.005847	-0.004685	+0.001162	-1.47
N3-H3A...O2 ⁱⁱ	+0.016754	+0.056357	+0.012333	-0.010576	+0.001757	-3.32

$$H(r) = G(r) + V(r)$$

When the molecular electrostatic potential (MEP) map (Figure 11) of the optimized molecule is examined, the regions coded with red (the most negative region) and blue (the most positive region) are clearly visible. As can be seen in Figure 11, negative regions in the molecule were found around the O1, O2, O3, F1 and F2 atoms. The most negative region was found around the O1 (MEP value is -0.036 a.b.). MEP values for O2, O3, F1 and F2 atoms are -0.031, -0.030, -0.021 and -0.018 a.b., respectively. According to this result, these five atoms are the most suitable regions for electrophilic attack reaction. The positive regions in MEP map were localized on the hydrogen atoms. The most positive region for the nucleophilic attack is around the H3A atom and the MEP value is defined as +0.067 a.b.

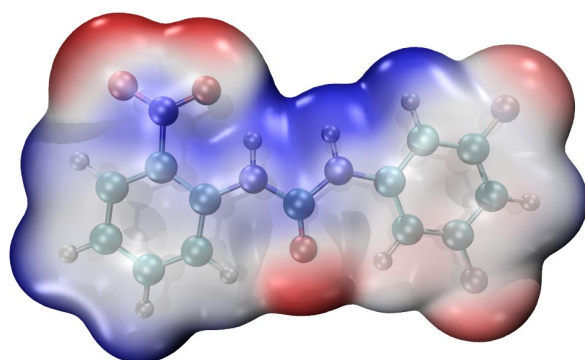


Figure 11. MEP surface obtained from the electron density of the title compound.

In particular, O1 and O2 atoms to LUMO orbitals, N2 and N3 atoms also contribute to HOMO orbitals in Figure 9 and these atoms are in the most negative and positive region in the MEP map. These two

situations show the congruence of molecular orbitals and MEP calculations.

4. Conclusion

In summary, the target compound, 1-(3,5-difluorophenyl)-3-(2-nitrophenyl) urea was successfully synthesized in 92% yield using 2-nitroaniline, 3,5-difluoroaniline and triphosgene as readily available starting materials with two-step synthesis method. The orange crystals of product were grown by the slow evaporation technique using THF and ethyl acetate solvent system as inner and outer solvent, respectively. The obtained crystals were identified by various characterization techniques such as melting point, FT-IR, ¹H NMR, ¹³C NMR, MS and X-ray single diffraction analysis. Besides, calculated IR and NMR results were given by comparing to experimental results. Slight differences were observed because the experimental results were obtained at the solid phase and in silico calculations pertain to the gaseous phase. To determine the stability of the molecule, 2D potential energy surface scanning (PES) was performed. As a result of PES analysis, the most stable conformations were obtained and compared with X-ray structure of compound. Frontier molecular orbitals and MEP analyzes of the optimized structure were calculated. Molecular electrostatic potential confirm the compound electrophile and nucleophile attack of the reactive centers. According to the MEP map, the most negative and positive regions of the molecule were determined. We hope the results of this study will help the researchers to analyze and synthesize new materials.



Acknowledgement

T. Güngör wish to thank Dr. Mehmet AY and Dr. Fatma Aydın for their support.

Author's Contributions

Tuğba Güngör: Designed all study, performed the synthesis and characterization studies, interpreted the results and wrote the manuscript.

Tuncay Karakurt: Performed the theoretical studies and wrote the manuscript.

Z. Sibel Şahin: Performed the X-ray and conformational analysis and wrote the manuscript.

Ethics

There are no ethical issues after the publication of this manuscript.

Supplementary Information

Supplementary data consists of all characterization data of the product. Crystallographic data for the structural analysis has been deposited with the Cambridge Crystallographic Data Centre, CCDC No. 2009298. Copies of this information may be obtained free of charge from the Director, CCDC, 12 Union Road, Cambridge CB2 1EZ, UK (fax: +44-1223-336033; e-mail: deposit@ccdc.cam.ac.uk or www: <http://www.ccdc.cam.ac.uk>).

For Supporting Information:

http://fbc.mcbu.edu.tr/db_images/file/T.Gungor-supporting_information.pdf

References

1. Al-Masoudi, NA, Essa, AH, Alwaaly, AAS, Saeed, BA, Langer, P. 2017. Synthesis and conformational analysis of new arylated-diphenylurea derivatives related to sorafenib drug via Suzuki-Miyaura crosscoupling reaction. *Journal of Molecular Structure*; 1146: 522-529.
2. Atahan, A, Gencer, N, Bilen, Ç, Yavuz, E, Genç, H, Sonmez, F, Zengin, M, Ceylan, M, Kucukislamoglu, M. 2018. Synthesis, biological activity and structure-activity relationship of novel diphenylurea derivatives containing tetrahydroquinoline as carbonic anhydrase I and II inhibitors. *ChemistrySelect*; 3: 529-534.
3. Strumberg, D, Schultheis, B. 2012. Regorafenib for cancer. *Expert Opinion on Investigational Drugs*; 21(6): 879-889.
4. Ruan, BF, Lin, MX, Shao, Q, Wang, TH, Zhang, Q, Dong, Y, Bu, C, Xu, H, Zhou, B, Li, Q. 2018. Modification, biological evaluation and SAR studies of novel 1H-Pyrazol derivatives containing N,Ni-disubstituted urea moiety as potential anti-melanoma agents. *Chemistry & Biodiversity*; 15: 1700504, 1-9.
5. Gentile, C, Martorana, A, Lauria, A, Bonsignore, R. 2017. Kinase inhibitors in multitargeted cancer therapy. *Current Medicinal Chemistry*; 24: 1671-1686.
6. Bobrovs, R, Jaudzems, K, Jirgensons, A. 2019. Exploiting structural dynamics to design open-flap inhibitors of malarial aspartic proteases. *Journal of Medicinal Chemistry*; 62: 8931-8950.
7. Zhang, Y, Anderson, M, Weisman, JL, Lu, M, Choy, CJ, Boyd, VA, Price, J, Sigal, M, Clark, J, Connelly, M et al. 2010. Evaluation of diarylureas for activity against Plasmodium falciparum. *ACS Medicinal Chemistry Letters*; 1: 460-465.
8. Huang, W, Lv, D, Yu, H, Sheng, R, Kim, SC, Wu, P, Luo, K, Li, J, Hu, Y. 2010. Dual-target-directed 1,3-diphenylurea derivatives: BACE 1 inhibitor and metal chelator against Alzheimer's disease. *Bioorganic & Medicinal Chemistry*; 18: 5610-5615.
9. Tang, C, Loeliger, E, Kinde, I, Kyere, S, Mayo, K, Barklis, E, Sun, Y, Huang, M, Summers, MF. 2003. Antiviral inhibition of the HIV-1 capsid protein. *Journal of Molecular Biology*; 327: 1013-1020.
10. Biswal, BK, Morisseau, C, Garen, G, Cherney, MM, Garen, C, Niu, C, Hammock, BD, James, MNG. 2008. The molecular structure of epoxide hydrolase B from Mycobacterium tuberculosis and its complex with a urea-based inhibitor. *Journal of Molecular Biology*; 381: 897-912.
11. Sikka, P, Sahu, JK, Mishra, AK, Hashim, SR. 2015. Role of Aryl Urea Containing Compounds in Medicinal Chemistry. *Medicinal Chemistry*; 5(11): 479-483.
12. Perveen, S, Mustafa, S, Khan, MA, Dar, A, Khan, KM, Voelter, W. 2012. Substituted urea derivatives: a potent class of antidepressant agents. *Medicinal Chemistry*; 8: 330-336.
13. Carra, A, Del Signore, MB, Sottile, F, Ricci, A, Carimi, F. 2012. Potential use of new diphenylurea derivatives in micropropagation of Capparis spinosa L. *Plant Growth Regulation*; 66: 229-237.
14. Bigi, F, Maggi, R, Sartori, G. 2000. Selected syntheses of ureas through phosgene substitutes. *Green Chemistry*; 2(4): 140-148.
15. Asakawa, C, Ogawa, M, Fujinaga, M, Kumata, K, Xie, L, Yamasaki, T, Yui, J, Fukumura, T, Zhang, M. 2012. Utilization of [11C] phosgene for radiosynthesis of N-(2-{3-[3,5-bis(trifluoromethyl)]phenyl}[11C]ure2;ido)ethyl)glycyrrhetinamid, an inhibitory agent for proteasome and kinase in tumors. *Bioorganic & Medicinal Chemistry Letters*; 22(11): 3594-3597.
16. Majer, P, Randad, RS. 1994. A Safe and Efficient Method for Preparation of N,N'-Unsymmetrically Disubstituted Ureas Utilizing Triphosgene. *Journal of Organic Chemistry*; 59: 1937-1938.
17. Artuso, E, Degani, I, Fochi, R, Magistris, C. 2007. Preparation of Mono-, Di-, and Trisubstituted Ureas by Carbonylation of Aliphatic Amines with S,S-Dimethyl Dithiocarbonate. *Synthesis*; 22: 3497-3506.
18. Katritzky, AR, Pleyne, DPM, Yang, B. 1997. A General Synthesis of Unsymmetrical Tetrasubstituted Ureas. *Journal of Organic Chemistry*; 62: 4155-4158.
19. Sonoda, N. 1993. Selenium assisted carbonylation with carbon monoxide. *Pure & Applied Chemistry*; 65(4): 699-706.
20. Shi, F, Deng, Y, SiMa, T, Peng, J, Gu, Y, Qiao, B. 2003. Alternatives to Phosgene and Carbon Monoxide: Synthesis of Symmetric Urea Derivatives with Carbon Dioxide in Ionic Liquids. *Angewandte Chemie International Edition*; 42: 3257-3260.



21. Semenov, AV, Tarasova, IV, Khramov, VS, Semenova, EV, Inchina, VI, Vakaeva, SS. 2018. Glucokinase activators based on N-Aryl-Ni-Pyridin-2-ylurea derivatives. *Pharmaceutical Chemistry Journal*; 52(3): 209-212.
22. Sheldrick, GM. 2008. A short history of SHELX. *Acta Crystallographica Section A*; A64: 112-122.
23. Sheldrick, GM. 2015. Crystal structure refinement with SHELXL. *Acta Crystallographica Section C*; C71: 3-8.
24. APEX2, Bruker AXS Inc. Madison Wisconsin USA (2013).
25. Macrae, CF, Sovago, I, Cottrell, SJ, Galek, PTA, McCabe, P, Pidcock, E, Platings, M, Shields, GP, Stevens, JS, Towler, M et al. 2020. Mercury 4.0: From visualization to analysis, design and prediction. *Journal of Applied Crystallography*; 53: 226-235.
26. Farrugia, LJ. 2012. WinGX and ORTEP for Windows: an update. *Journal of Applied Crystallography*; 45: 849-854.
27. Becke, AD. 1993. Density-functional thermochemistry. III. The role of exact exchange. *The Journal of Chemical Physics*; 98: 5648-5652.
28. Lee, C, Yang, W, Parr, RG. 1988. Development of the Colle-Salvetti correlation-energy formula into a functional of the electron density. *Physical Review B*; 37: 785.
29. Foresman, JB, Frisch, A. Exploring chemistry with electronic structure methods: a guide to using Gaussian, 1996.
30. Frisch, M, Trucks, G, Schlegel, HB, Scuseria, G, Robb, M, Cheeseman, JR, Scalmani, G, Barone, V, Petersson, GA, Nakatsuji, H, et al. Gaussian 09, revision a. 02, Gaussian, Inc., Wallingford, CT, 200, 2009.
31. Keith, TA, AIMAll (Version 15.09.27), T.K. Gristmill Software, Overland Park K.S., USA, 2016.
32. Lu, T, Chen, F. 2012. Multiwfn: A multifunctional wavefunction analyzer. *Journal of Computational Chemistry*; 33(5): 580-592.
33. Çukurovalı, A, Karakurt, T. 2019. Synthesis, spectroscopic, X-ray diffraction and tautomeric properties of 5-(diethylamino)-2-((2-(5-(3-methyl-3-phenylcyclobutyl)-6H-1,3,4-thiadiazin-2-yl) hydrazono)methyl)phenol: A combined experimental and theoretical study. *Journal of Molecular Structure*; 1189: 328-337.
34. Karakurt, T, Çukurovalı, A, Subaşı, NT, Kani, I. 2016. Molecular structure and computational studies on 2-((2-(4-(3-(2,5-dimethylphenyl)-3-methylcyclobutyl)thiazol-2-yl)hydrazono)methyl)phenol monomer and dimer by DFT calculations. *Journal of Molecular Structure*; 1125: 433-442.
35. Karakurt, T, Çukurovalı, A, Subaşı, NT, Onaran, A, Ece, A, Eker, S, Kani, I. 2018. Experimental and theoretical studies on tautomeric structures of a newly synthesized 2,2'-(hydrazine-1,2-diylidenebis(propan-1-yl-1-ylidene))diphenol. *Chemical Physics Letters*; 693: 132-145.
36. Karakurt, T, Çukurovalı, A, Kani, İ. 2020. Structure of 2-(2-(anthracen-9-ylmethylene) hydrazinyl)-4-(3-methyl-3-phenylcyclobutyl)thiazole by combined X-Ray crystallographic and molecular modelling studies. *Molecular Physics*; 1-17.
37. Varsányi, G. Assignments for Vibrational Spectra of Seven Hundred Benzene Derivatives, Halsted Press, 1974.
38. Furic, K, Mohacek, V, Bonifacic, M, Štefanic, I. 1992. Raman spectroscopic study of H₂O and D₂O water solutions of glycine. *Journal of Molecular Structure*; 267: 39-44.
39. Avcı, D, Atalay, Y, Şekerci, M, Dinçer, M. 2009. Molecular structure and vibrational and chemical shift assignments of 3-(2-hydroxyphenyl)-4-phenyl-1H-1,2,4-triazole-5-(4H)-thione by DFT and ab initio HF calculations. *Spectrochimica acta. Part A, Molecular and Biomolecular Spectroscopy*; 73: 212-217.
40. Mohan, Organic Spectroscopy: Principles and Applications, Crc Press, 2004.
41. Ditchfield, R. 1972. Molecular Orbital Theory of Magnetic Shielding and Magnetic Susceptibility. *The Journal of Chemical Physics*; 56: 5688-5691.
42. Wolinski, K, Hinton, JF, Pulay, P. 1990. Efficient implementation of the gauge-independent atomic orbital method for NMR chemical shift calculations. *Journal of American Chemical Society*; 112(23): 8251-8260.
43. Fukui, K. 1982. Role of frontier orbitals in chemical reactions. *Science*; 218: 747-754.
44. Büyüksulu, H, Akdoğan, M, Yıldırım, G, Parlak, C. 2010. Ab initio Hartree-Fock and density functional theory study on characterization of 3-(5-methylthiazol-2-ylidiazonyl)-2-phenyl-1H-indole. *Spectrochimica Acta Part A: Molecular and Biomolecular Spectroscopy*; 75: 1362-1369.
45. Chaudhary, T, Chaudhary, MK, Joshi, BD, Santana, MSA, Ayala, AP. 2021. Spectroscopic (FT-IR, Raman) analysis and computational study on conformational geometry, AIM and biological activity of cephalixin from DFT and molecular docking approach. *Journal of Molecular Structure*; 1240: 130597.
46. Al-Otaibi, JS, Mary, YS, Armaković, S, Thomas, R. 2020. Hybrid and bioactive cocrystals of pyrazinamide with hydroxybenzoic acids: detailed study of structure, spectroscopic characteristics, other potential applications and noncovalent interactions using SAPT. *Journal of Molecular Structure*, 1202: 127316.
47. Parr, RG, Pearson, RG. 1983. Absolute hardness: companion parameter to absolute electronegativity. *Journal of the American Chemical Society*; 105: 7512-7516.
48. Parr, RG, Donnelly, RA, Levy, M, Palke, WE. 1978. Electronegativity: the density functional viewpoint. *The Journal of Chemical Physics*; 68: 3801-3807.
49. Parr, RG, Szentpály, LV, Liu, S. 1999. Electrophilicity index. *Journal of the American Chemical Society*; 121: 1922-1924.
50. Jeelani, A, Muthu, S, Narayana, B. 2021. Molecular structure determination, Bioactivity score, Spectroscopic and Quantum computational studies on (E)-N'-(4-Chlorobenzylidene)-2-(naphthalen-2-yloxy) acetohydrazide. *Journal of Molecular Structure*; 1241: 130558.
51. Bader, RFW. 2006. Pauli Repulsions Exist Only in the Eye of the Beholder. *Chemistry-A European Journal*; 12(10): 2896-2901.
52. Rozas, I, Alkorta, I, Elguero, J. 2000. Behavior of Ylides Containing N, O, and C Atoms as Hydrogen Bond Acceptors. *Journal of the American Chemical Society*; 122(45): 11154-11161.
53. Espinosa, E, Molins, E, Lecomte, C. 1998. Hydrogen bond strengths revealed by topological analyses of experimentally observed electron densities. *Chemical Physics Letters*; 285(3): 170-173.

Experimental and Theoretical Investigation of a new β -Diketimate Derivative

İlkay Yıldırım^{1*} 

¹ Department of Radiotherapy, Vocational School, Biruni University, 34010 İstanbul, TURKEY

* iyildirim@biruni.edu.tr

* Orcid: 0000-0002-7423-5043

Received: 13 November 2020

Accepted: 2 June 2021

DOI: 10.18466/cbayarfbe.825395

Abstract

A new β -diketimate compound (**I**) was synthesized, and its structure was determined by a single-crystal X-ray diffraction study. The molecule crystallizes as a salt in the monoclinic system, and the crystal structure is stabilized by intermolecular N–H \cdots Cl hydrogen bonds. The structural and energetic properties were examined using the HSEH1PBE density functional method with cc-pvdz basis set. The optimized structure represents well the experimental structure. In addition, the noncovalent interactions have been also analyzed using Hirshfeld surface analysis. Hirshfeld surface analysis shows that H \cdots H and H \cdots Cl/Cl \cdots H interactions contribute to about 94% of the total intermolecular interactions. Frontier molecular orbitals (HOMO-LUMO), their energy gap and associated parameters were determined.

Keywords: β -diketimate, crystal structure, DFT, Hirshfeld surface.

1. Introduction

The β -diketimate class, also known NacNac or $[\{ArNC(R)\}_2CH^-]$ (where Ar = aryl and R = Me or another organic group), occupies a rightful place among other ancillary supports, which applications change from structural inorganic/organometallic chemistry to bioinorganic systems and catalysis [1-4]. The β -diketimate ligands are known to provide monoanionic, bidentate support for metal complexes and a high degree of steric control can be achieved depending on the choice of N-substituents [5]. The reactivity of these class of the ligands can also be improved significantly, by tuning the steric and electronic properties of the supporting β -diketimate ligands [6,7].

Since the first such metal NacNac complexes were reported by McGeachin [8] and Holm [9], these ligand class has been often used to stabilize many elements in the periodic table and in unusual oxidation states [10]. A lot of complexes can be derived from variation of substituents on nitrogen atom of 1,3-diketimates by different hydrogen/alkyl/aryl/silyl/germanyl groups, as well metal ions [11-14]. Consequently, the resulting ligands become good σ donors and poor π acceptors like N-heterocyclic carbenes (NHCs), and thus have the potential to exhibit carbene-like chemistry.

In this paper, we report the synthesis and crystal structure of *N*-[(2*Z*,3*E*)-4-(isopropylamino)pent-3-en-2-ylidene]propan-2-aminium chloride salt (**I**) formed unexpectedly (Figure 1).

2. Materials and Methods

2.1. Synthesis

Two moles of ⁱPr₂-nacnacH (1) (0.5 g) in 10 mL toluene were mixed with one mole of 1,2-bis(dimethylamino) diborane dichloride (2) (0.248 g) in 5 mL toluene for 2 hours, and stand for two days. The precipitated colorless crystal (**I**) was filtered and washed cold ether. (Yield: % 48).

2.2. XRD Analysis

XRD data of **I** were collected at room temperature using a Mo K α radiation with STOE IPDS II diffractometer. During the process the ω -scan method was applied. X-Area [15] and X-RED32 [15] were used to perform for data collection and cell refinement and for data reduction, respectively. Direct methods were used to solve the structure with SIR2019 [16]. Refinement of the structure was processed with SHELXL-2018 [17] on *F*² by means of the full matrix least-squares calculations. All of the H atoms bonded to C atoms were first located in Fourier difference maps then trade

as riding atoms, fixing the bond lengths at 0.93 Å for aromatic CH, 0.98 Å for methine CH and 0.96 Å for CH₃ atoms. Also, the H atoms bonded to N atoms were located from the Fourier-difference map but refined freely. All the details of the process are given in Table 1. The OLEX2 [18] was used to generate the molecular graphics.

The supplementary crystallographic data for the compound reported here is deposited at CCDC 2024442 and can be provided free of charge upon request to CCDC, 12 Union Road, Cambridge CB2 1EZ, UK [Fax: +44 1223 336 033, e-mail: deposit@ccdc.cam.ac.uk, <https://www.ccdc.cam.ac.uk/structures/>].

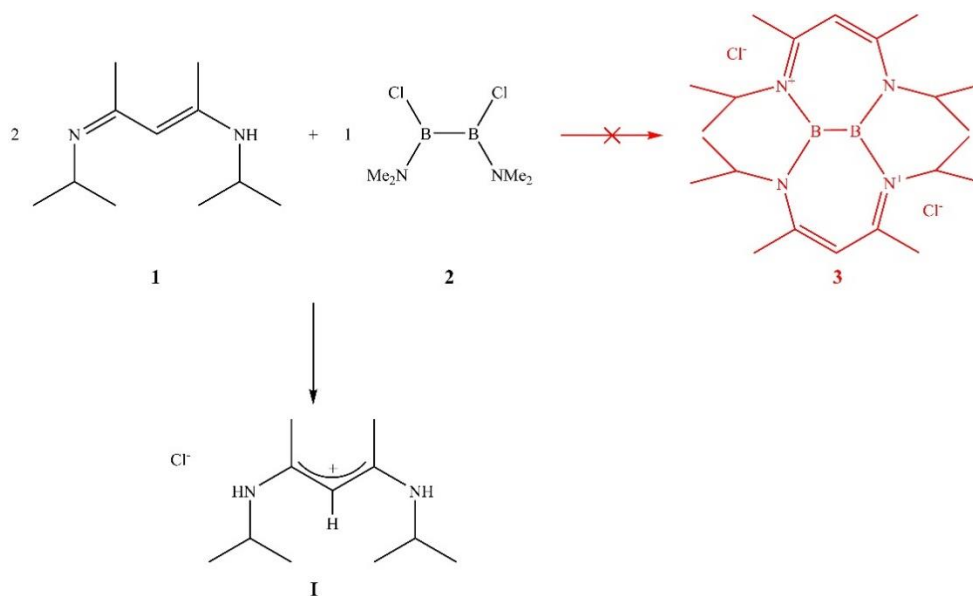


Figure 1. Chemical formula of **I**.

2.3. Computational Procedure

Theoretical calculations were carried out with the aid of GaussView 5 [19] molecular visualization software and Gaussian 09 program package [20]. The structural and other electronic properties of **I** were obtained using the HSEH1PBE density functional method [21-23] with cc-pvdz basis set [24]. The optimized geometry was confirmed to be real minima by frequency calculation (no imaginary frequencies).

3. Results and Discussion

To obtain dicationic bicyclic diborane derivative (**3**), 1,2-bis(dimethylamino)diborane dichloride (**2**) [25] was reacted with two equivalents ⁱPr₂-nacnacH (**1**) [26] in toluene at room temperature. Unfortunately, desired product (**3**) could not be produced from the reaction. Presumably, compound **3** is very unstable so it immediately decomposes in the reaction media. By the diboran compound acts as reducing agent, imine group is converted to iminium cation salt through secondary amine group. Compound **I** is a decomposition product that is crystallized in a reaction mixture at room temperature. The compound **I** is stable in air atmosphere. Reaction was monitored by IR spectrum during the formation of compound **I**. In the spectrum, β-Diketimine (**1**) showed the bands

at 3333 and 1648 cm⁻¹ attributed to enamine and imine groups, respectively. Upon formation of iminium cation salt, the monitored bands at 3501 cm⁻¹ and at 2085, 1593 cm⁻¹ on the spectrum were attributed to secondary amine and iminium salt, respectively (Figure 2).

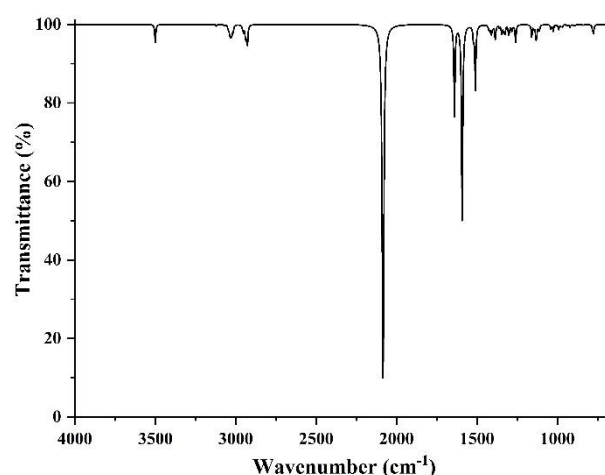


Figure 2. IR spectrum of **I**.

Table 1. Crystal data and structure refinement parameters for **I**.

CCDC depository	2024442
Color/shape	Colorless/prism
Chemical formula	$C_{11}H_{23}N_2^+Cl^-$
Formula weight	218.76
Temperature (K)	296(2)
Wavelength (Å)	0.71073 Mo $K\alpha$
Crystal system	Monoclinic
Space group	$P2_1/c$ (No. 14)
Unit cell parameters	
a, b, c (Å)	11.6986(10), 11.9408(9), 19.8065(18)
α, β, γ (°)	90, 101.002(7), 90
Volume (Å ³)	2715.9(4)
Z	8
$D_{calc.}$ (g/cm ³)	1.070
μ (mm ⁻¹)	0.253
Absorption correction	Integration
$T_{min.}, T_{max.}$	0.8941, 0.9846
F_{000}	960
Crystal size (mm ³)	0.56 × 0.31 × 0.05
Diffractometer	STOE IPDS II
Measurement method	ω scan
Index ranges	$-13 \leq h \leq 13, -14 \leq k \leq 13, -23 \leq l \leq 23$
θ range for data collection (°)	$1.773 \leq \theta \leq 25.048$
Reflections collected	20101
Independent/observed reflections	4797/1949
$R_{int.}$	0.1543
Refinement method	Full-matrix least-squares on F^2
Data/restraints/parameters	4797/0/281
Goodness-of-fit on F^2	0.802
Final R indices [$I > 2\sigma(I)$]	$R_1 = 0.0544, wR_2 = 0.0715$
R indices (all data)	$R_1 = 0.1646, wR_2 = 0.0928$
$\Delta\rho_{max.}, \Delta\rho_{min.}$ (e/Å ³)	0.16, -0.16

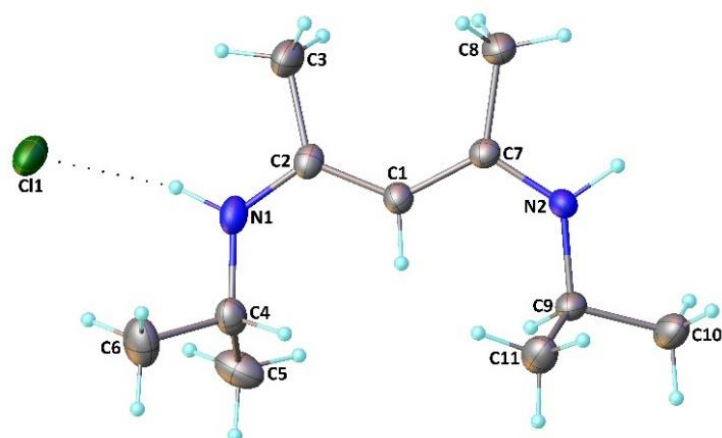


Figure 3. The molecular structure of one (A) of the two independent molecules present in the crystals of **I**. Dotted lines show the intermolecular H-bonding.

3.1. Experimental and Theoretical Structure

The solid-state structure of **I** has been unambiguously determined by single-crystal X-ray diffraction analysis (XRD), and its structural plot is presented in Figure 3, whilst some of the experimental and theoretical parameters are quoted in Table 2. Colorless crystals of **I** crystallize as a salt in the monoclinic system $P21/c$ with two crystallographically independent molecules, A and B, in the asymmetric unit. In the following discussion, parameters related to the second molecule (B) are given in square brackets.

The compound is composed of an $N-[(2Z,3E)-4-(isopropylamino)pent-3-en-2-ylidene]propan-2-$ aminium cation and one chloride anion. There are no chemically significant differences between the two cationic molecules in the asymmetric unit. The central C1–C2 and C1–C7 bond distances of 1.384(4) and 1.390(4) Å [1.389(4) and 1.380(4) Å], respectively, are almost equal to each other, and show an intermediate character between single (1.54 Å) and double bonds (1.34 Å) [27], indicating dispersion of positive charge over C2–C1–C7 atoms. These

bonds were calculated at 1.432 and 1.380 Å, respectively. Although the N1–C4 and N2–C9 bond distances of 1.463(4) and 1.468(4) Å [1.469(4) and 1.463(4) Å], respectively, conform to a C–N single bond (1.48 Å), the N1–C2 and N2–C7 bond distances of 1.318(4) and 1.328(4) Å [1.327(4) and 1.332(4) Å], respectively, are shorter than a C–N single bond but longer than a C=N double bond (1.28 Å). These bonds were theoretically determined at 1.457, 1.455, 1.306 and 1.353 Å, respectively. So, this data suggests an extended electron delocalization over the N1–C2 and N2–C7 bonds since the C2–C3 and C7–C8 bond distances of 1.512(5) and 1.504(4) Å [1.498(4) and 1.495(4) Å] correspond to a C–C single bond, which were computed at 1.502 and 1.503 Å, respectively.

The molecular structure of **I** contains no intramolecular interactions. In the crystal structure, the cation is linked to the chloride anions by means of N–H···Cl hydrogen bonds, so forming $C_2^1(8)$ [28] chains along the c axis (Figure 4). Details of these interactions are given in Table 3.

Table 2. Selected geometric parameters for **I**.

Parameters	X-ray		DFT
	Molecule A	Molecule B	
Bond lengths (Å)			
N1–C2	1.318(4)	1.327(4)	1.306
N1–C4	1.463(4)	1.469(4)	1.457
N2–C7	1.328(4)	1.332(4)	1.353
N2–C9	1.468(4)	1.463(4)	1.455
C1–C2	1.384(4)	1.389(4)	1.432
C1–C7	1.390(4)	1.380(4)	1.380
C2–C3	1.512(5)	1.498(4)	1.502
C7–C8	1.504(4)	1.495(4)	1.503
Bond angles (°)			
C2–N1–C4	127.0(3)	126.6(3)	129.02
C7–N2–C9	126.8(3)	126.5(3)	127.25
N1–C2–C1	121.7(4)	122.0(3)	121.56
N1–C2–C3	114.1(3)	113.3(3)	114.03
N2–C7–C1	119.9(3)	120.5(3)	121.24
N2–C7–C8	114.8(3)	113.7(3)	113.10
C2–C1–C7	130.4(3)	129.6(3)	128.84
C1–C2–C3	124.3(3)	124.7(3)	124.39
C1–C7–C8	125.2(3)	125.8(3)	125.66
Torsion angles (°)			
C3–C2–N1–C4	–179.2(3)	–175.4(3)	179.13
C8–C7–N2–C9	–177.1(3)	177.3(3)	179.74
N1–C2–C1–C7	–172.4(3)	179.3(3)	–173.18
N2–C7–C1–C2	–177.9(4)	175.7(3)	–175.10
C2–C1–C7–C8	2.5(6)	–4.3(6)	4.32
C7–C1–C2–C3	8.9(6)	–0.9(6)	8.37

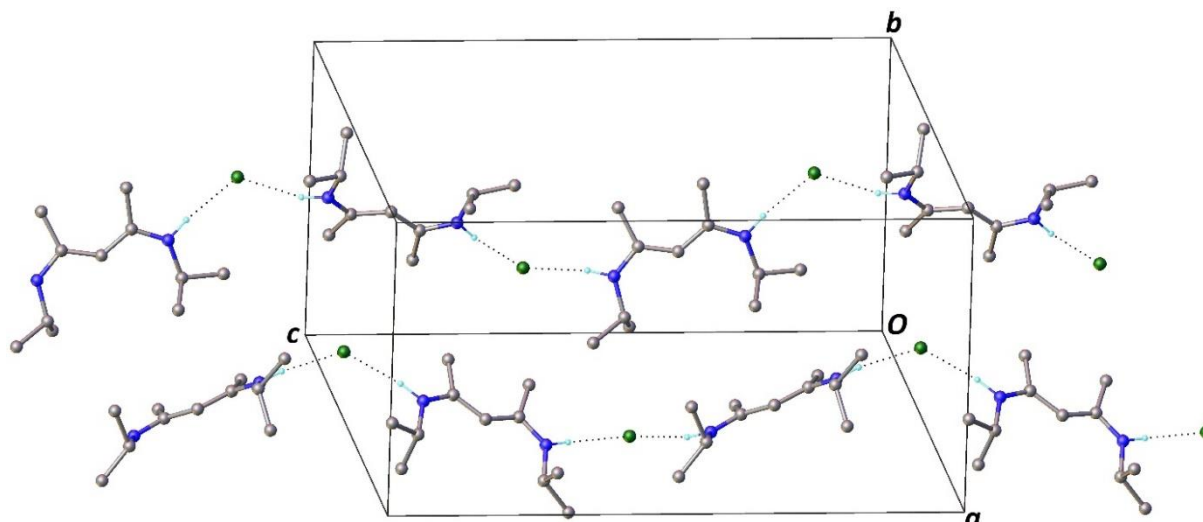


Figure 4. Part of the crystal structure of **I**, showing the formation of $C_2^1(8)$ chains along [001] built from N–H···Cl hydrogen bonds. For clarity, only H atoms involved in hydrogen bonding have been included.

Table 3. Hydrogen bonding geometry for **I**.

D–H···A	D–H (Å)	H···A (Å)	D···A (Å)	D–H···A (°)
N2A–H2A1···Cl1A ⁱ	0.95(3)	2.32(3)	3.261(3)	171(3)
N2B–H2B1···Cl1B ⁱⁱ	0.91(3)	2.32(4)	3.216(3)	170(3)
N1B–H1B1···Cl1B	0.98(4)	2.27(4)	3.240(3)	168(3)
N1A–H1A1···Cl1A	0.93(4)	2.32(4)	3.222(3)	163(3)

Symmetry codes: (i) $x, -y+3/2, z-1/2$; (ii) $x, -y+1/2, z-1/2$.

3.2. Hirshfeld Surface (HS) Analysis

HS analysis is very useful to picturize and examine important intra- or intermolecular interactions within the crystal structure.

The distance external to the surface d_e measures the distance between a surface to the neighboring nucleus while the distance internal to the surface d_i measures the distance between a surface to nearest atom in the molecule itself. The two-dimensional (2D) fingerprint plots based on HS analysis can provide the contributions of each specific contact pairs to HS [29]. The 2D fingerprint plots for **I** were generated by Crystal Explorer 17.5 program [30] and shown in Figure 5.

The fingerprint plots show that the main intermolecular interactions in **I** are H···H and H···Cl/Cl···H. The highest contribution to the total Hirshfeld surface occurs due to H···H close contacts with 73.2%. The proportion of H···Cl/Cl···H interactions comprises 20.2% of the surface. These intermolecular contacts correspond to about 94% of all noncovalent interactions. Missing percentages are H···C/C···H 4.9% and H···N/N···H 1.7% contacts.

3.3. Energetics and Stability

One way to get an idea on how compound interacts with other species is to analyze the highest occupied molecular orbital (HOMO) and the lowest unoccupied molecular orbital (LUMO) which are frontier molecular orbitals. In many reactions, electrons located in HOMO are donated first while a compound accepts electrons to its LUMO. Thus, one can easily measure chemical hardness, reactivity and many more parameters from the energy gap (ΔE) between HOMO and LUMO [31]. The global chemical reactivity descriptors (GCRD) such as the absolute electronegativity [$\chi = (I+A)/2$], the chemical potential [$\mu = -(I+A)/2$], the absolute hardness [$\eta = (I-A)/2$], softness ($S = 1/2\eta$) and electrophilicity index ($\omega = \mu^2/2\eta$) were calculated by taking the energies of HOMO as ionization potential ($I = -E_{\text{HOMO}}$) and LUMO as electron affinity ($A = -E_{\text{LUMO}}$) according to Koopmans Theorem [32].

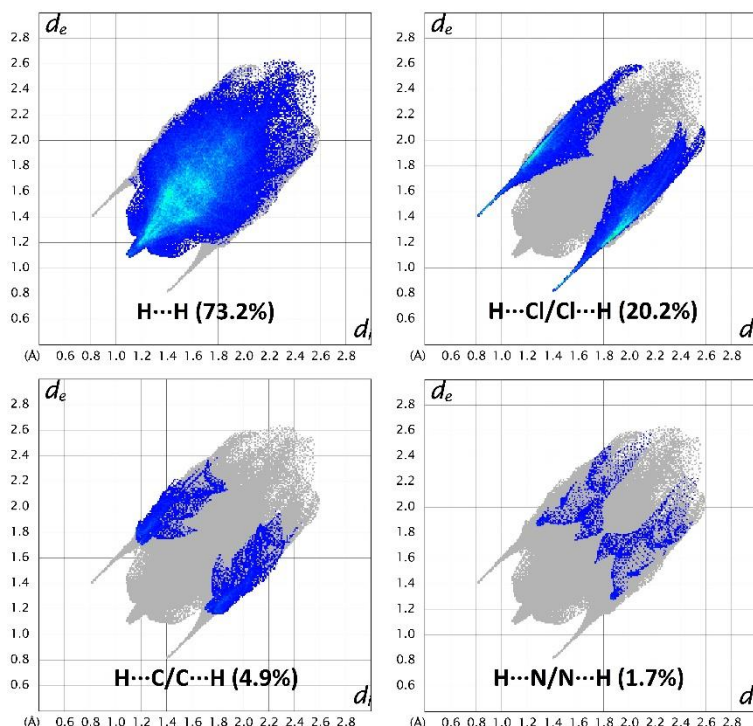


Figure 5. The 2D fingerprint plots with decomposition of dominant types of the intermolecular contacts of **I**.

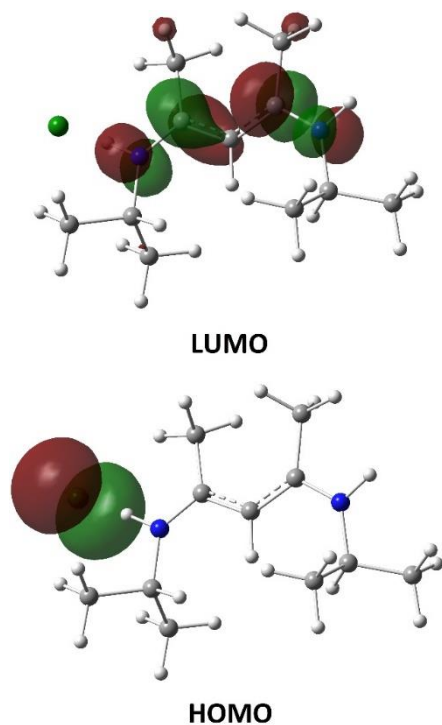


Figure 6. Frontier molecular orbital surfaces of compound **I**.

The contour plot of HOMO and LUMO orbitals of **I** is shown in Figure 6 while the GCRDs values are collected in Table 4. The calculated E_{HOMO} , E_{LUMO} and ΔE energies are 4.92, 1.85 and 3.07 eV,

respectively. If the molecule is hard, the larger ΔE corresponds to the more hardness molecule. In this case, the compound has higher kinetic stability and thus, lower chemical reactivity. The molecules are kinetically stable with the hardness and chemical potential values of 1.54 and -3.39 eV, respectively. The other parameters such as softness (0.33 eV $^{-1}$), electronegativity (3.39 eV), and electrophilic index (3.73 eV) also suggest that the compound holds stability and chemical strength.

Table 4. Calculated energy values of **I**.

E_{HOMO} (eV)	-4.92
E_{LUMO} (eV)	-1.85
Energy gap (ΔE) (eV)	3.07
Electronegativity (χ) (eV)	3.39
Chemical potential (μ) (eV)	-3.39
Chemical hardness (η) (eV)	1.54
Chemical softness (S) (eV $^{-1}$)	0.33
Electrophilicity index (ω) (eV)	3.73

4. Conclusion

In summary, compound **I** is investigated by using XRD and computational methods. Theoretical geometric parameters are in good agreement with the experimental findings. XRD results indicate that the compound crystallizes as a salt. The intermolecular N—H \cdots Cl interactions are responsible for the stabilization of the crystal structure. In an effort to investigate the intermolecular interactions, HS

analysis was also carried out. The contributions of total HS were analyzed by plotting the fingerprint plots. The highest contribution of total HS was found as $H\cdots H$: 73.2% and $H\cdots Cl/Cl\cdots H$: 20.2%. The calculated descriptors related to chemical reactivity showed a high energy gap between HOMO and LUMO which concluded that the compound has high kinetic stability and shows low intramolecular charge transfer and low chemical reactivity.

Acknowledgement

The support of Dr. Erkan FIRINCI is appreciated. In addition, for the X-ray data collection, I would like to thank to the support of the Crystallography Laboratory Unit supported by the University Research Fund (Project No: PYO.FEN.1906.19.001) from Ondokuz Mayıs University. I also thank Amasya University for providing the access to GaussView 5.0 and Gaussian 09W software packages.

Author's Contributions

İlkay Yıldırım: Drafted and wrote the manuscript, performed the experiment and result analysis.

Ethics

There are no ethical issues after the publication of this manuscript.

References

1. Dindar, S, Kharat, AN, Safarkoopayeh, B, Abbasi, A. 2021. Ruthenium (II) β -diketimine as hydroamination catalyst, crystal structure and DFT computations. *Transition Metal Chemistry*; 46(5): 403-413.
2. Rinke, P, Görls, H, Kretschmer, R. 2021. Calcium and Magnesium Bis(β -diketiminato) Complexes: Impact of the Alkylene Bridge on Schlenk-Type Rearrangements. *Inorganic Chemistry*; 60(7): 5310-5321.
3. Zhu, L, Xu, Y, Yuan, D, Wang, Y, Yao, Y. 2021. Synthesis and structural characterization of lanthanide monoborohydride complexes supported by 2-tertbutylphenyl substituted β -diketiminato, and their application in the ring-opening polymerization of lactide. *Journal of Organometallic Chemistry*; 934(15): 121662.
4. Li, B, Yang, Y, Zhu, H, Roesky, HW. 2021. (β -Diketiminato)aluminum hydroxides and the chalcogenide derivatives: Precursors for homo- and heterometallic complexes with Al-E-M (E = chalcogen, M = metal) frameworks. *Coordination Chemistry Reviews*; 429(15): 213625.
5. Zhong, M, Sinhababu, S, Roesky, HW. 2020. The unique β -diketiminato ligand in aluminum(I) and gallium(I) chemistry. *Dalton Transactions*; 49(5): 1351-1364.
6. Jones, C. 2017. Dimeric magnesium(I) β -diketiminates: a new class of quasi-universal reducing agent. *Nature Reviews Chemistry*; 1: 0059.
7. McWilliams, SF, Holland, PL. 2015. Dinitrogen Binding and Cleavage by Multinuclear Iron Complexes. *Accounts of Chemical Research*; 48(7): 2059-2065.
8. McGeachin, SG. 1968. Synthesis and properties of some β -diketiminates derived from acetylacetone, and their metal complexes. *Canadian Journal of Chemistry*; 46(11): 1903-1912.
9. Parks, JE, Holm, RH. 1968. Synthesis, solution stereochemistry, and electron delocalization properties of bis(β -iminoamino)nickel(II) complexes. *Inorganic Chemistry*; 7(7): 1408-1416.
10. Tsai, Y-C. 2012. The chemistry of univalent metal β -diketiminates. *Coordination Chemistry Reviews*; 256(5-8): 722-758.
11. Liddle, ST, Arnold, PL. 2007. Synthesis and characterisation of yttrium complexes supported by the β -diketiminato ligand $\{ArNC(CH_3)CHC(CH_3)NAr\}^-$ (Ar = 2,6-Pr₂C₆H₃). *Dalton Transactions*; 30: 3305-3313.
12. Xiao, X, Hao, X, Bai, J, Chao, J, Cao, W, Chen, X. 2016. Synthesis, mechanism and ethylene polymerization catalysis of Ge(IV), Sn(II) and Zr(IV) complexes derived from substituted β -diketiminates. *RSC Advances*; 6(65): 60723-60728.
13. Xiong, Y, Yao, S, Kostenko, A, Driess, M. 2018. An isolable β -diketiminato chlorosilylene. *Dalton Transactions*; 47(7): 2152-2155.
14. Bourget-Merle, L, Lappert, MF, Severn, JR. 2002. The chemistry of β -diketiminato metal complexes. *Chemical Reviews*; 102(9): 3031-3066.
15. X-Area (version 1.18) and X-RED32 (version 1.04), Stoe & Cie, Darmstadt, Germany, 2002.
16. Burla, MC, Caliandro, R, Carrozzini, B, Cascarano, GL, Cuocci, C, Giacovazzo, C, Mallamo, M, Mazzone, A, Polidori, G. 2015. Crystal structure determination and refinement via SIR2014. *Journal of Applied Crystallography*; 48(1): 306-309.
17. Sheldrick, GM. 2015. Crystal structure refinement with SHELXL. *Acta Crystallographica Section C: Structural Chemistry*; 71(1): 3-8.
18. Dolomanov, OV, Bourhis, LJ, Gildea, RJ, Howard, JAK, Puschmann, H. 2009. OLEX2: a complete structure solution, refinement and analysis program. *Journal of Applied Crystallography*; 42(2): 339-341.
19. Dennington, R, Keith, T, Millam, J. GaussView, Version 5, Semicem Inc., Shawnee Mission KS, 2009.
20. Frisch, MJ, Trucks, GW, Schlegel, HB, Scuseria, GE, Robb, MA, Cheeseman, JR, Scalmani, G, Barone, V, Mennucci, B, Petersson, GA, Nakatsuji, H, Caricato, M, Li, X, Hratchian, HP, Izmaylov, AF, Bloino, J, Zheng, G, Sonnenberg, JL, Hada, M, Ehara, M, Toyota, K, Fukuda, R, Hasegawa, J, Ishida, M, Nakajima, T, Honda, Y, Kitao, O, Nakai, H, Vreven, T, Montgomery, JA, Jr, Peralta, JE, Ogliaro, F, Bearpark, M, Heyd, JJ, Brothers, E, Kudin, KN, Staroverov, VN, Kobayashi, R, Normand, J, Raghavachari, K, Rendell, A, Burant, JC, Iyengar, SS, Tomasi, J, Cossi, M, Rega, N, Millam, NJ, Klene, M, Knox, JE, Cross, JB, Bakken, V, Adamo, C, Jaramillo, J, Gomperts, R, Stratmann, RE, Yazyev, O, Austin, A J, Cammi, R, Pomelli, C, Ochterski, J W, Martin, RL, Morokuma, K, Zakrzewski, VG, Voth, GA, Salvador, P, Dannenberg, JJ, Dapprich, S, Daniels, AD, Farkas, Ö,



- Foresman, JB, Ortiz, JV, Cioslowski, J, Fox, DJ. Gaussian 09, Revision C.01, Gaussian, Inc., Wallingford CT, 2009.
21. Heyd, J, Scuseria, GE. 2004. Assessment and validation of a screened Coulomb hybrid density functional. *Journal of Chemical Physics*; 120(16): 7274-7280.
22. Heyd, J, Scuseria, GE. 2004. Efficient hybrid density functional calculations in solids: Assessment of the Heyd–Scuseria–Ernzerhof screened Coulomb hybrid functional. *Journal of Chemical Physics*; 121(3): 1187-1192.
23. Heyd, J, Peralta, JE, Scuseria, GE, Martin, RL. 2005. Energy band gaps and lattice parameters evaluated with the Heyd-Scuseria-Ernzerhof screened hybrid functional. *Journal of Chemical Physics*; 123(17): 1-8.
24. Dunning Jr, TH. 1989. Gaussian basis sets for use in correlated molecular calculations. I. The atoms boron through neon and hydrogen. *Journal of Chemical Physics*; 90(2): 1007-1023.
25. Nöth, H, Meister, W. 1961. Beiträge zur Chemie des Bors, VI: Über Subverbindungen des Bors. Hypoborsäure-tetrakis-dialkylamide und Hypoborsäure-ester. *Chemische Berichte*; 94(2): 509-514.
26. Tian, X, Goddard, R, Pörschke, KR. 2006. (β -Diketiminato)palladium Complexes. *Organometallics*; 25(25): 5854-5862.
27. Allen, FH, Kennard, O, Watson, DG, Brammer, L, Orpen, AG, Taylor, R. 1987. Tables of bond lengths determined by X-ray and neutron diffraction. Part 1. Bond lengths in organic compounds. *Journal of the Chemical Society, Perkin Transactions 2*; 12: S1-S19.
28. Bernstein, J, Davis, RE, Shimoni, L, Chang, NL. 1995. Patterns in Hydrogen Bonding: Functionality and Graph Set Analysis in Crystals. *Angewandte Chemie International Edition*; 34(15): 1555-1573.
29. Spackman, MA, McKinnon, JJ. 2002. Fingerprinting intermolecular interactions in molecular crystals. *Crystal Engineering Community*; 4(66): 378-392.
30. Turner, MJ, MacKinnon, JJ, Wolff, SK, Grimwood, DJ, Spackman, PR, Jayatilaka, D, Spackman, MA. Crystal Explorer, Version 17.5, University of Western Australia, Perth, 2017.
31. Ece, A, Pejin, B. 2014. A computational insight into acetylcholinesterase inhibitory activity of a new lichen depsidone. *Journal of Enzyme Inhibition and Medicinal Chemistry*; 30(4): 528-532.
32. Koopmans, T. 1934. Über die Zuordnung von Wellenfunktionen und Eigenwerten zu den einzelnen Elektronen eines Atoms. *Physica*; 1(1-6): 104-113.

Investigation of the effects on dose calculations of correction-based algorithms in different tissue medium

Serhat ARAS^{1,2,*} 

¹Medical Imaging Techniques Program, University of Health Sciences Turkey, Istanbul, Turkey

²Department of Radiation Oncology, Haydarpasa Numune Training and Research Hospital, University of Health Sciences Turkey, Istanbul, Turkey

*serhat.aras@sbu.edu.tr

*Orcid: 0000-0002-4825-5921

Received: 16 December 2020

Accepted: 24 June 2021

DOI: 10.18466/cbayarfbe.841547

Abstract

The aim of this study is to investigate the effects of Modified Batho and Equivalent Tissue-Air Ratio (ETAR) correction-based algorithms on dose distributions in the inhomogeneous media and left-sided breast and lung cancer. Distribution profiles at lateral depth and percentage depth dose (PDD) values were obtained for soft tissue, bone and air rectilinear virtual phantoms in the Eclipse treatment planning system (TPS). In addition, intensity modulated radiotherapy (IMRT) treatment planning technique was applied to 20 patients with left-sided breast and lung cancer diagnosis on computed tomography (CT) sections. The maximum dose, mean dose, D₉₅, Monitor Unit (MU) and segment numbers in planning target volume (PTV) were calculated. Although the effect of correction-based algorithms on (PDD) values and dose distribution profiles in lateral depth were calculated below 1% in soft tissue virtual phantom, dose profiles were obtained as approximately 20% in bone and air media. No statistical differences were observed in dosimetric parameters except for PTVmean and D95 values due to the differences in correction-based algorithms in left-sided breast IMRT treatment planning ($p>0.05$). However, significant statistical differences were obtained in the values of lung IMRT treatment plans ($p<0.05$). It was concluded that correction-based algorithms in the different inhomogeneous mediums have a significant effect on the dose values calculated in TPS.

Keywords: Radiotherapy, inhomogeneous medium, correction methods, dose calculation, pencil beam convolution.

1. Introduction

Human anatomy is heterogeneous and has tissue and air spaces with different physical density values. These tissues and organs have different electron density, atomic number, and mass density. Ionizing X-ray passing through the patient can pass through air spaces, lungs, bones and soft tissues [1]. These different inhomogeneous structures cause changes in the transport of photons and electrons and the absorption of the dose. To determine more accurately absorbed dose in irradiated tissues, precise dose calculations are required in inhomogeneous structures [2]. Dose distributions obtained in heterogeneous medium without water equivalent change depending on the energy of radiation and the physical properties of the medium [3].

Percentage depth dose (PDD) and isodose curves used in dosimetric procedures in radiotherapy are obtained from water or water equivalent homogeneous medium. Various methods and algorithms are developed and used in treatment planning systems (TPS) to precisely calculate and correct these changes due to physical parameters in dose distribution [4]. The dose distribution that occurs in the patient's body during radiotherapy treatment is determined by dose calculation algorithms in TPS. Correct dose calculation of algorithms is a very important factor for success in radiotherapy [5].

Correction-based dose calculation algorithms used in TPS make dose calculations by interpolating and extrapolating the depth-dose curves measured in the water phantom and dose profiles taken at various depths.

Dose distributions are calculated with standard measurements and correction factors [6]. Correction-based algorithms are stated that are not suitable for stereotactic treatments with small treatment fields. In regions with tissue heterogeneity, they may cause inaccurate dose calculations in the target volume and surrounding healthy tissues [7]. In addition, the dose distributions calculated in the radiotherapy treatment plans are based on the correction of the measurements previously obtained in the water phantom. Many correction factors are applied to accurately calculate the patient dose [8]. Power Law (Batho) method, tissue-air ratio method (TAR), equivalent tissue-air ratio (ETAR) method are the main inhomogeneity correction methods. These methods are based on measurement data and precise dose calculation principles [9, 10]. The Pencil Beam Convolution (PBC) algorithm used in calculating photon dose distributions in TPS calculates by convolution of kernels defined as the stored dose around the primary photon pencil beam. It considers inhomogeneous structures using a correction factor such as the Modified Batho, ETAR method [11]. In this study, dose distributions for different inhomogeneous media and tissues were obtained in Eclipse TPS, where the PBC dose calculation algorithm was used. Using these correction-based algorithms, the calculation and comparison of dose values were performed in different treatment fields [12].

The purpose of this study is to dosimetrically compare the effects of different correction-based algorithms on

dose distributions in lung ve breast inhomogeneous tissues using PBC dose calculation algorithm and to determine which method would be more appropriate to use in TPSs.

2. Materials and Methods

In this study, dose values for soft tissue, bone and air media s on the rectilinear phantom in Eclipse TPS were primarily examined before obtaining different dosimetric parameters in breast and lung treatment planning. In TPS, different correction-based algorithms were used in soft tissue and inhomogeneous medium, including Modified Batho, Equivalent Tissue-Air Ratio (ETAR) and "none" when the inhomogeneity correction method was not used, and dose calculations were achieved. Before comparing the effects of correction-based algorithms on dose distributions for the PBC dose calculation method in TPS, dose distribution profiles obtained in the inhomogeneous medium were obtained in virtual phantoms and dose calculations were performed. In V_{8.9.08} version (Varian, USA) Eclipse TPS, under 2 homogeneous 25x2x25cm³ cubic phantoms, 25x9x25cm³ soft tissue, bone and air materials were defined separately for Hounsfield Unit (HU) values and three rectilinear virtual phantoms were created (Figure 1).

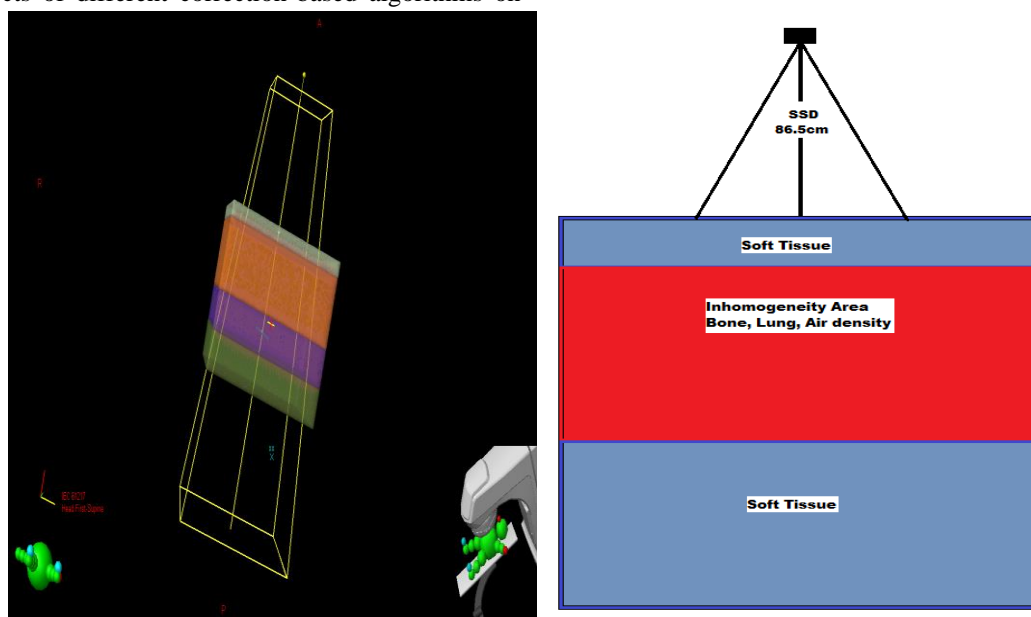


Figure 1. Rectilinear virtual phantom consisting of 25x9x25cm³ soft tissue, bone and air materials under 2 homogeneous 25x2x25cm³ cubic phantoms.

Rectilinear virtual phantoms were created by defining the Hounsfield Unit (HU) and density (g/cm^3) values in Table 1, and their effects due to the difference in density compared to water in the medium in high and low-density medium transitions were shown.

Table 1. Hounsfield Unit and medium densities of homogeneous and inhomogeneous virtual phantoms.

Medium	Hounsfield Unit (HU)	Density (g/cm^3)	Ratio by Water
Soft Tissue (Water equivalent)	0	1.000	1.0
Air	1000-	0.0012	1/800
Lung	740-	0.2-0.3	1/5
Bone	600+	1.6	1.6X

While creating the set-up phase, phantoms on bone, lung, air, and soft tissue-like material formed the build-up region and were placed to maintain an electronic-equilibrium condition. Other phantoms 10cm thick were placed due to backscattering. All calculations were made on heterogeneous virtual phantoms with 18MV photon energy, Gantry: 0° irradiation angle, $20 \times 20 \text{cm}^2$ beam field size, 2Gy dose and skin source distance (SSD) 86.5cm. In inhomogeneous media where PBC dose calculation algorithm is used, Modified Batho, Equivalent Tissue-Air Ratio (ETAR) and “none” situations; percentage depth dose (%) and dose distribution profiles at lateral depth were calculated and compared in three separate phantoms.

To examine the effect of different inhomogeneity correction methods on the dose distribution in the plans calculated with PBC, Modified Batho plans were copied without any changes, and the plans were obtained by calculating them separately with the ETAR and “none”

inhomogeneity correction-method. In order to reveal the effects of correction-based algorithms on dose distributions in different tissues, dose simulation was performed using intensity modulated radiotherapy (IMRT) treatment technique in 20 patients with left-sided breast (50Gy/25fr) and lung (66Gy/33fr) cancers. The maximum dose, mean dose, D_{95} , Monitor Unit (MU) and segment numbers in planning target volume (PTV) were calculated and compared. Later, IMRT based Modified Batho plans were copied without any changes, and the plans were obtained by calculating them separately using the ETAR and “none” inhomogeneity correction method.

3. Statistical Analysis

Analysis of the data was obtained using the SPSS 25 package program. Differences between dose calculation algorithms in terms of mean \pm SD measurement values were performed using the independent sample t-test. Differences were considered significant when the p value was <0.05 .

4. Results and Discussion

In Figure 2-4, dose distributions at lateral depth and PDD profiles depending on the depth were calculated separately in soft tissue, air and bone media using different dose correction-based algorithms in the rectilinear virtual phantom. In dose calculations performed on soft tissue phantom, the effect of correction-based algorithms on dose distributions were calculated below 1% in PDD values depending on the depth and dose distribution profiles at lateral depth. However, dosimetric differences due to correction-based algorithms were obtained about 20% in PDD values and dose distribution profiles at lateral depth in dose calculations using air and bone media.

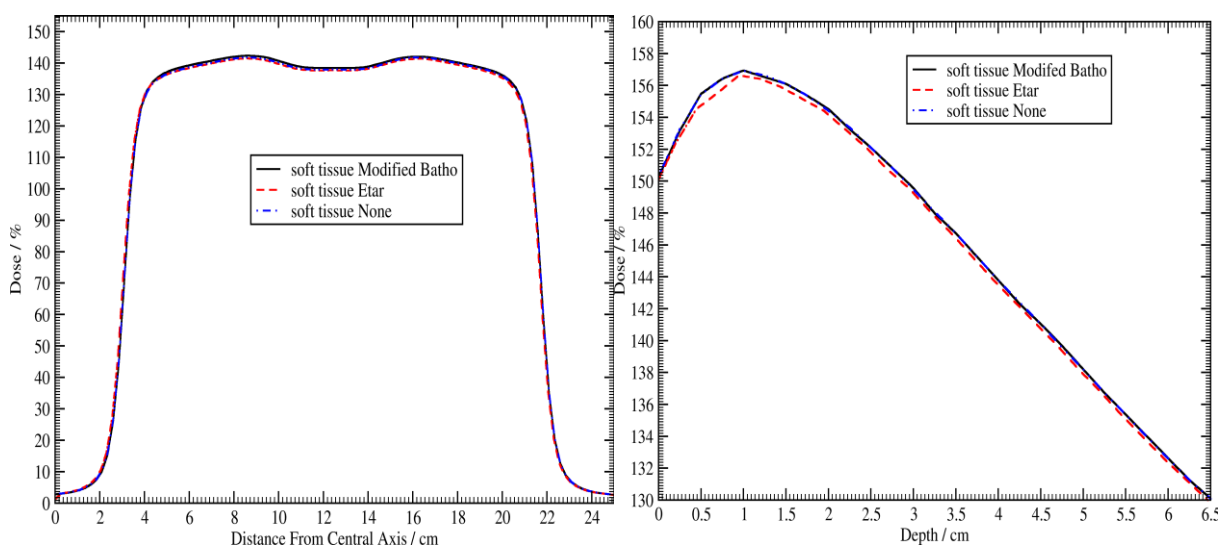


Figure 2. Dose distributions at lateral depth and dose distribution profiles depending on the depth obtained in soft tissue by using different dose correction based algorithms in rectilinear virtual phantom.

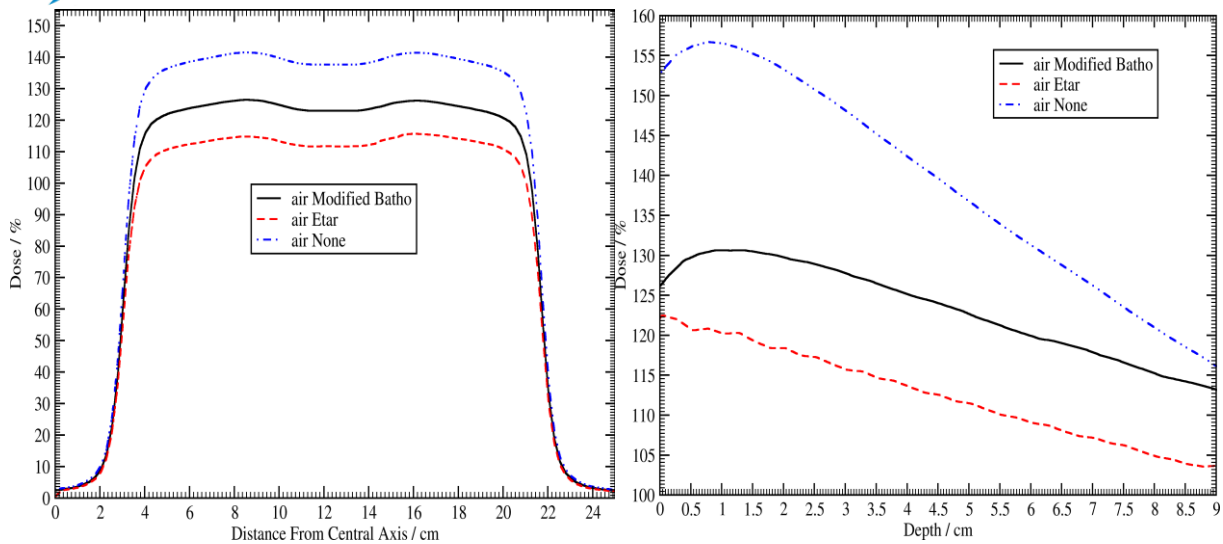


Figure 3. Dose distributions at lateral depth and dose distribution profiles depending on the depth obtained in air medium by using different dose correction based algorithms in rectilinear virtual phantom.

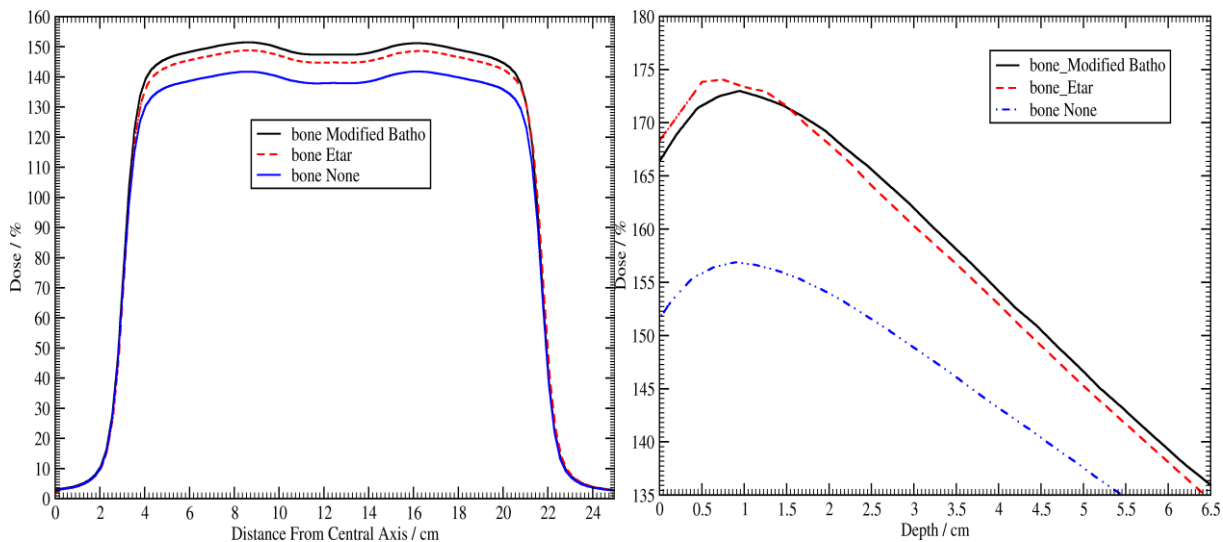


Figure 4. Dose distributions at lateral depth and dose distribution profiles depending on the depth obtained in bone medium by using different dose correction based algorithms in rectilinear virtual phantom.

In dose simulations based on correction-based algorithms performed on computed tomography sections of 20 patients with left-sided breast and lung cancer, dosimetric differences of <2% in breast IMRT treatment technique were obtained in the maximum dose, mean dose, D_{95} in PTV, MU and segment numbers, while lung IMRT treatment technique was calculated an average of 1-10% dose differences in these dosimetric parameters. Although no statistically dose differences were observed in dosimetric parameters (except PTVmean and D_{95} values) due to the differences of correction-based algorithms in left-sided breast IMRT treatment planning ($p>0.05$) (Table 2), significant statistical differences were obtained in the values of lung IMRT treatment plans ($p<0.05$) (Table 3).

Organ doses in external radiotherapy are calculated with the dose calculation algorithms in TPS and it is assumed that they are close to the actual dose distribution between the measurement data loaded into the system and the calculated dose. Different correction-based algorithms are used to obtain the closest dose calculations to reality in patient dose procedures using computed tomography in TPS [13].

The fact that the dose calculated in TPS's is slightly different from the dose administered to the patient is directly related to the capabilities of dose calculation algorithms in inhomogeneous structures.

Table 2. Left-sided breast treatment plan values obtained for different correction-based algorithms

Left sided breast (50Gy/25fr)	PTV Max mean±SD	PTV Mean mean±SD	PTV D ₉₅ mean±SD	Total MU mean±SD	Segment Number mean±SD
Modified Batho	109±1.8	5107±14.7	4885±12.4	580±12.8	113±5.4
ETAR	109±2.8	5048±18.3	4789±19.8	574±10.7	113±3.9
None	108.8±2.3	5078±11.1	4827±23.4	583±11.5	112±6.5
p Value					
	M.B. vs. Etar	M.B. vs. None	Etar vs. None		
PTVmax	>0.05	>0.05	>0.05		
PTVmean	0.012*	0.007*	0.002*		
PTV D ₉₅	0.023*	0.002*	0.005*		
MU	>0.05	>0.05	>0.05		
Segment Number	>0.05	>0.05	>0.05		

**Statistically significant values (p<0.05), MU: Monitor Unit, PTV: Planning target volume, D₉₅: Dose covering 95% of the volume, M.B: Modified Batho, SD: Standard deviation*

Table 3. Lung treatment plan values obtained for different correction-based algorithms

Lung (66Gy/33fr)	PTV Max mean±SD	PTV Mean mean±SD	PTV D ₉₅ mean±SD	Total MU mean±SD	Segment Number mean±SD
Modified Batho	106±2.3	6357±22.6	6094±15.4	564±13.2	94±7.8
ETAR	108±2.1	6380±18.7	6116±32.2	591±19.8	104±6.5
None	116.5±2.8	6441±15.8	6011±54.7	659±20.7	102±6.9
p Value					
	M.B. vs. Etar	M.B. vs. None	Etar vs. None		
PTVmax	>0.05	0.041*	0.018*		
PTVmean	>0.05	0.017*	0.007*		
PTV D ₉₅	>0.05	0.004*	0.013*		
MU	>0.05	0.022*	0.004*		
Segment Number	>0.05	>0.05	>0.05		

**Statistically significant values (p<0.05), MU: Monitor Unit, PTV: Planning target volume, D₉₅: Dose covering 95% of the volume, M.B: Modified Batho, SD: Standard deviation*

Different correction-based algorithms have advantages and disadvantages against each other due to the different dose values obtained in low and high-density heterogeneous mediums such as soft tissue, lung, air and bone [14]. Correction-based algorithms are mainly based on measured data obtained from the cubic water phantom. The total dose at any point is usually obtained by summing up its primary and scatter components calculated separately [15]. The accuracy of correction-based algorithms is limited, especially for 3-D heterogeneity corrections in lung and tissue-cross sections where electronic-equilibrium cannot be fully achieved [16]. Actual dose values in different tissues are found by taking into account some correction factors such as tissue inhomogeneity. Dose calculation algorithms calculate dose by interpolating between depth doses measured in the water phantom and use dose profiles taken at various depths [17]. In TPS-based dose calculation algorithms, it is important to correctly determine the electronic equilibrium perpendicular and parallel to the beam direction to calculate the total absorbed dose correctly. Vertical electronic-equilibrium is especially important in treatment planning for cases where tissue heterogeneity is intense such as lung and breast. In these treatment fields, vertical electronic-equilibrium cannot be calculated effectively due to the fact that TPS algorithms have many heterogeneous in area close to the skin. Therefore, the calculated dose in the skin area is slightly different from the measured dose [18]. The PBC dose calculation algorithm calculates the absorbed dose faster because it does not effectively account for the horizontal electronic equilibrium and scattered electrons. Although vertical electronic equilibrium has been determined, dose calculation accuracy is especially more limited than other dose calculation algorithms in the heterogeneous medium [19].

In this study, no significant dose difference was calculated between the PDD profiles depending on the depth and the dose distribution profiles at the lateral depth in the dose calculations of soft tissue virtual phantoms using different correction-based algorithms. However, we showed that there are significant dosimetric differences in both the depth-dependent PDD distribution profiles and the lateral depth dose distribution profiles in dose calculations using air and bone virtual phantoms. Inhomogeneity correction is required to accurately calculate dose distributions in radiotherapy applications where heterogeneity is dominant, such as lung, breast, head&neck and esophageal cancer.

M. Bragg et al did not observe a significant difference in prostate and head and neck in the study in which they compared the effect of Anisotropic Analytical Algorithm (AAA) and PBC algorithms on dose distribution in lung, prostate and head and neck cancers, but reported significant dose differences in lung cancers [20]. Knöös et al acquired plans with conformal or conventional techniques and compared the results of AAA

convolution/superposition algorithms and PBC inhomogeneity correction algorithms in patients with lung, prostate, head-neck and breast cancer. While no significant difference was reported in the prostate and head and neck regions, a significant difference was reported in the lung and breast plans in the neighborhood of low-density inhomogeneous tissue. In addition, these two algorithms were compared with Monte Carlo and it was noted that convolution/superposition algorithms were more compatible with Monte Carlo. They emphasized that the use of IMRT technique may cause new problems [21]. It is desirable that the homogeneous distribution of the dose in the PTV and the dosimetric parameter values should be close to each other for different correction-based algorithms in radiotherapy planning.

Although only statistical differences were observed in mean and D_{95} values in PTV between Modified Batho, ETAR and "none" correction-based algorithms for IMRT plans with 20 left-sided breast cancer diagnoses in this study, significant statistical differences were obtained in all other dosimetric parameters except segment numbers in lung IMRT plans. In addition, we think that the Modified Batho correction-based algorithm can give more accurate results in dose calculations of inhomogeneous structures and in dose distribution profiles depending on depth and lateral depth. Considering the literature studies [22, 23], it was observed that different correction-based algorithms using the PBC dose calculation algorithm were especially insufficient in media where the heterogeneity of the tissue such as lung and bone is dominant and much more complex IMRT treatment planning technique.

We think that it should be compared dosimetrically with dose calculation algorithms such as Monte Carlo, AAA and Acuros, as well as PBC dose calculation algorithm to obtain much more precise and accurate patient dose calculations. In addition, it was concluded that the most ideal patient dose treatment plan can be achieved by using appropriate correction-based algorithms according to the treatment plan.

5. Conclusion

It was concluded that the Modified Batho correction-based algorithm can give more accurate and precise results in dose calculations of such structures in anatomical regions where inhomogeneity is dominant such as head-neck and lung cancer, where the PBC dose calculation algorithm is used.

Author's Contributions

Serhat Aras: Drafted and wrote the manuscript, performed the experiment and result analysis.



Ethics

Ethics committee approval was given by University of Health Sciences Turkey, Hamidiye Scientific Research Ethics Committee.

6. References

1. Wilcox EE, Daskalov GM. Accuracy of dose measurements and calculations within and beyond heterogeneous tissues for 6 MV photon fields smaller than 4 cm produced by Cyberknife. *Medical Physics* 2008; 35: 2259–2266.
2. Butts JR. Comparison of commercially available three-dimensional treatment planning algorithms for monitor unit calculations in the presence of heterogeneities. *Journal of Applied Clinical Medical Physics* 2001; 2: 32.
3. Cilla S, Digesù C, Macchia G, et al. Clinical implications of different calculation algorithms in breast radiotherapy: A comparison between pencil beam and collapsed cone convolution. *Physica Medica* 2014; 30: 473–481.
4. Lu L, Yembi-Goma G, Wang JZ, et al. A Practical Method to Evaluate and Verify Dose Calculation Algorithms in the Treatment Planning System of Radiation Therapy. *International Journal of Medical Physics, Clinical Engineering and Radiation Oncology* 2013; 02: 76–87.
5. Ahnesjö A, Aspradakis MM. Dose calculations for external photon beams in radiotherapy. *Physics in Medicine and Biology*; 44. Epub ahead of print 1999. DOI: 10.1088/0031-9155/44/11/201.
6. Engelsman M, Damen EMF, Koken PW, et al. Impact of simple tissue inhomogeneity correction algorithms on conformal radiotherapy of lung tumours. *Radiotherapy and Oncology* 2001; 60: 299–309.
7. Dorje T. Limitation of Pencil Beam Convolution (PBC) Algorithm for Photon Dose Calculations in Inhomogeneous Medium. *Journal of Cancer Treatment and Research* 2014; 2: 1.
8. Papanikolaou N, Stathakis S. Dose-calculation algorithms in the context of inhomogeneity corrections for high energy photon beams. *Medical Physics* 2009; 36: 4765–4775.
9. Sontag MR, Cunningham JR. The equivalent tissue-air ratio method for making absorbed dose calculations in a heterogeneous medium. *Radiology* 1978; 129: 787–794.
10. Stathakis S, Kappas C, Theodorou K, et al. An inhomogeneity correction algorithm for irregular fields of high-energy photon beams based on Clarkson integration and the 3D beam subtraction method. *Journal of Applied Clinical Medical Physics* 2006; 7: 1–13.
11. Nyholm T, Olofsson J, Ahnesjö A, et al. Modelling lateral beam quality variations in pencil kernel based photon dose calculations. *Physics in Medicine and Biology* 2006; 51: 4111–4118.
12. Lax I, Panettieri V, Wennberg B, et al. Dose distributions in SBRT of lung tumors: Comparison between two different treatment planning algorithms and Monte-Carlo simulation including breathing motions. *Acta Oncologica* 2006; 45: 978–988.
13. Kry SF, Alvarez P, Molineu A, et al. Algorithms used in heterogeneous dose calculations show systematic differences as measured with the radiological physics center's anthropomorphic thorax phantom used for RTOG credentialing. *International Journal of Radiation Oncology Biology Physics* 2013; 85: e95–e100.
14. Antonella F, Giorgia N, Alessandro C, et al. Dosimetric validation of the Acuros XB Advanced Dose Calculation algorithm: fundamental characterization in water. *Physics in Medicine and Biology* 2011; 56: 2885.
15. Buzdar SA, Afzal M, Todd-Pokropek A. Comparison of pencil beam and collapsed cone algorithms, in radiotherapy treatment planning for 6 and 10 MV photon. *Journal of Ayub Medical College, Abbottabad: JAMC* 2010; 22: 152–154.
16. Ding GX, Duggan DM, Lu B, et al. Impact of inhomogeneity corrections on dose coverage in the treatment of lung cancer using stereotactic body radiation therapy. *Medical Physics* 2007; 34: 2985–2994.
17. Mackie TR, El khatib E, Battista J, et al. Lung dose corrections for 6 and 15 MV x rays. *Medical Physics* 1985; 12: 327–332.
18. Kim YL, Suh TS, Choe BY, et al. Dose distribution evaluation of various dose calculation algorithms in inhomogeneous media. *International Journal of Radiation Research* 2016; 14: 269–278.
19. Chen H, Lohr F, Fritz P, et al. Stereotactic, single-dose irradiation of lung tumors: A comparison of absolute dose and dose distribution between pencil beam and monte carlo algorithms based on actual patient ct scans. *International Journal of Radiation Oncology Biology Physics* 2010; 78: 955–963.
20. Bragg CM, Wingate K, Conway J. Clinical implications of the anisotropic analytical algorithm for IMRT treatment planning and verification. *Radiotherapy and Oncology* 2008; 86: 276–284.
21. Knöös T, Wieslander E, Cozzi L, et al. Comparison of dose calculation algorithms for treatment planning in external photon beam therapy for clinical situations. *Physics in Medicine and Biology* 2006; 51: 5785–5807.
22. Mesbahi A, Thwaites DI, Reilly AJ. Experimental and Monte Carlo evaluation of Eclipse treatment planning system for lung dose calculations. *Reports of Practical Oncology and Radiotherapy* 2006; 11: 123–133.
23. Durmus IF, Atalay ED. Output Measurements of Monte Carlo, Collapse Cone and Pencil Beam Algorithms in Homogeneous and Inhomogeneous Phantom. *Çanakkale Onsekiz Mart University Journal of Graduate School of Natural and Applied Sciences* 2019; 5(2): 251-260.

On Iteration Method to The Solution of More General Volterra Integral Equation in Two Variables and a Data Dependence Result

Samet MALDAR^{1*} 

¹ Aksaray University, Faculty of Science and Letters, Department of Mathematics, Aksaray, Turkey

*mmaldar@aksaray.edu.tr

*Orcid: 0000-0002-2083-899X

Received: 7 December 2020

Accepted: 16 September 2021

DOI: 10.18466/cbayarfbe.837062

Abstract

Fixed point theory is one of the most important theories and has been studied extensively by researchers in many disciplines. One of these studies is its application to integral equations. In this work, we have shown that the iteration method given in [30] converges to the solution of the more general Volterra integral equation in two variables by using Bielecki's norm. Also, a data dependence result for the solution of this integral equation has been proven.

Keywords: convergence, data dependence, integral equation, iteration method

Mathematics Subject Classification: 47H06; 47H10, 54H25.

1. Introduction

Various problems in nature can be expressed in nonlinear equations. Reaching the solution of nonlinear equations is significant for many disciplines. There are many methods to obtain this solution in mathematics. One of them is the fixed-point theory. One of the study areas of nonlinear analysis is integral equations and one way to show the existence and uniqueness of the solutions of integral equations is iteration methods in fixed point theory. Iteration methods have become an intriguing method for solving nonlinear equations. In this context, a large literature has emerged with the definition of new iteration methods (see [1-5]). Fixed point iteration methods have been studied by many researchers to solve integral equations (see [8-29]). The basic approach in this method is to construct iteration methods by including the integral equations in an operator classification under certain conditions and to determine the appropriate conditions for the sequence obtained from this iteration to converge to the fixed point of the operator, in other words, to the solution of the integral equation. In this regard, Lungu and Rus [6] have proved that defined Volterra-Fredholm integral equation (1.1) under the conditions given below (c1-c6) has only unique solution.

In more general form, Volterra-Fredholm integral equation [6] in two variables can be seen as

$$g(x, y) = f(x, y, (h(g))(x, y)) + \int_0^x \int_0^y K(x, y, s, t, g(s, t)) ds dt \quad x, y \in \mathbb{R}_+. \quad (1.1)$$

Let $(E, \|\cdot\|)$ be a Banach space. Let $K \in C(\mathbb{R}_+^4 \times E, E)$ be class of continuous functions. Bielecki's norm [7] on X_τ defined as

$$\|g\|_\tau = \sup_{x, y \in \mathbb{R}_+} (\|g(x, y)\|) e^{-\tau(x+y)} \quad (1.2)$$

such that

$$X_\tau = \{g \in C(\mathbb{R}_+^2, E) \mid \exists M(g) > 0: |g(x, y)| \leq e^{-\tau(x+y)} \leq M(g)\}. \quad (1.3)$$

for $\tau > 0$.

It is clear that $(X_\tau, \|\cdot\|_\tau)$ is a Banach space.

Theorem 1.1 Let us assume that the following conditions are satisfied:

$$(c1) f \in C(\mathbb{R}_+^2 \times E, E), K \in C(\mathbb{R}_+^4 \times E, E),$$

$$(c2) \forall x, y \in \mathbb{R}_+, \forall u, v \in X_\tau, h: X_\tau \rightarrow X_\tau \text{ such that} \\ \exists L_h > 0: \|(h(u))(x, y) - (h(v))(x, y)\| \\ \leq L_h \|u - v\|_\tau e^{\tau(x+y)},$$

$$(c3) \forall x, y \in \mathbb{R}_+, \forall w_1, w_2 \in E;$$

$$\exists L_f > 0: \|f(x, y, w_1) - f(x, y, w_2)\| \leq L_f \|w_1 - w_2\|,$$

- (c4) $\forall x, y, s, t \in \mathbb{R}_+, \forall w_1, w_2 \in E;$
 $\exists L_K(x, y, s, t) > 0: \|K(x, y, s, t, w_1) - K(x, y, s, t, w_2)\|$
 $\leq L_K(x, y, s, t) \|w_1 - w_2\|,$
 (c5) $\forall x, y \in \mathbb{R}_+,$
 $L_K \in C(\mathbb{R}^4_+, \mathbb{R}_+)$ and $\int_0^x \int_0^y L_K(x, y, s, t) e^{\tau(s+t)} ds dt \leq$
 $L e^{\tau(x+y)},$
 (c6) $L_h L_f + L < 1.$

Then (1.1) has a unique solution [6].

The following iteration method has defined in [30].

$$\begin{cases} x_0 \in X, \\ x_{n+1} = T \left(\frac{(1-\alpha_n)}{k} T x_n + \left(1 - \frac{(1-\alpha_n)}{k} \right) T y_n \right) \\ y_n = T \left(\frac{(1-\beta_n)}{k} x_n + \left(1 - \frac{(1-\beta_n)}{k} \right) T x_n \right) \end{cases} \quad (1.4)$$

where $\{\alpha_n\}_{n=1}^\infty$ and $\{\beta_n\}_{n=1}^\infty$ are real sequences in $[0,1]$, $k, n \in \mathbb{N}$ and T is any self-operator. The iteration method (1.4) can be demonstrated as follows:

$$\begin{cases} x_0 \in X, \\ x_{n+1} = T u_n \\ u_n = \frac{(1-\alpha_n)}{k} T x_n + \left(1 - \frac{(1-\alpha_n)}{k} \right) T y_n \\ y_n = T v_n \\ v_n = \frac{(1-\beta_n)}{k} x_n + \left(1 - \frac{(1-\beta_n)}{k} \right) T x_n. \end{cases} \quad (1.5)$$

Definition 1.2 Let X be a Banach space and C be a nonempty, closed, convex subset of X . Let $S, T: C \rightarrow C$ be two mappings. We say that the S is an approximate mapping pair of T if for all $x \in C$ and for a fixed $\epsilon \geq 0$, we have $\|Tx - Sx\| \leq \epsilon$ [31].

Lemma 1.3 Let $\{\sigma_n\}_{n=0}^\infty$ be nonnegative real sequence. Assume that there exists $n_0 \in \mathbb{N}$, such that for all the $n \geq n_0$ one has the inequality

$$\sigma_{n+1} \leq (1 - \lambda_n) \sigma_n + \lambda_n m_n$$

where $\lambda_n \in (0,1)$ for all $n \in \mathbb{N}$, $\sum_{n=0}^\infty \lambda_n = \infty$, and $m_n \geq 0$. Then the following inequality holds:

$$0 \leq \limsup_{n \rightarrow \infty} \sigma_n \leq \limsup_{n \rightarrow \infty} m_n \quad [31].$$

Consider the equation (1.1), we have $T: X_\tau \rightarrow X_\tau$ defined by

$$\begin{aligned} T(x_n(x, y)) &= f(x, y, (h(x_n))(x, y)) \\ &+ \int_0^x \int_0^y K(x, y, s, t, x_n(s, t)) ds dt \quad x, y \in \mathbb{R}_+. \end{aligned} \quad (1.6)$$

In this work, we have shown that the iteration method (1.5) converges to the solution of Volterra-Fredholm integral equation given by (1.1) in Banach space X for the initial point $x_0 \in X$. Also, we have obtained the data dependence result for the solution of equation (1.1) under conditions in Theorem 1.1.

2. Main Results

Theorem 2.1 Let $\{\alpha_n\}_{n=1}^\infty$ and $\{\beta_n\}_{n=1}^\infty$ are real sequences in $[0,1]$. Then under the assumptions of Theorem 1.1, the equation (1.1) has a unique solution, say x_p , and the iteration method (1.5) is convergent strongly to x_p .

Proof Let $\{x_n\}_{n=1}^\infty$ be an iterative sequence generated by iteration method (1.5) as follows:

$$\begin{aligned} T(x_n(x, y)) &= f(x, y, (h(x_n))(x, y)) + \\ &\int_0^x \int_0^y K(x, y, s, t, x_n(s, t)) ds dt \quad x, y \in \mathbb{R}_+ \end{aligned} \quad (2.1)$$

where $T: X_\tau \rightarrow X_\tau$.

We will show that $x_n \rightarrow x_p$ as $n \rightarrow \infty$. From (1.1), iteration method (1.5), and the assumptions (c1)-(c6) of Theorem 1.1, we obtain

$$\begin{aligned} \|x_{n+1} - x_p\|_\tau &= \|T u_n - T x_p\|_\tau = \\ &\sup_{x, y \in \mathbb{R}_+} (\|T u_n(x, y) - T x_p(x, y)\| e^{-\tau(x+y)}) \end{aligned} \quad (2.2)$$

and

$$\begin{aligned} &\|T u_n(x, y) - T x_p(x, y)\| = \\ &\left\| \begin{aligned} &f(x, y, (h(u_n))(x, y)) \\ &+ \int_0^x \int_0^y K(x, y, s, t, u_n(s, t)) ds dt \\ &- f(x, y, h(x_p(x, y))) \\ &- \int_0^x \int_0^y K(x, y, s, t, x_p(s, t)) ds dt \end{aligned} \right\| \\ &\leq \|f(x, y, (h(u_n))(x, y)) - \\ &f(x, y, (h(x_p))(x, y))\| + \\ &\left\| \int_0^x \int_0^y K(x, y, s, t, u_n(s, t)) ds dt - \right. \\ &\left. \int_0^x \int_0^y K(x, y, s, t, x_p(s, t)) ds dt \right\| \\ &\leq L_f \| (h(u_n))(x, y) - (h(x_p))(x, y) \| + \\ &\int_0^x \int_0^y \| K(x, y, s, t, u_n(s, t)) - \\ &K(x, y, s, t, x_p(s, t)) \| ds dt \\ &\leq L_f L_h \|u_n - x_p\|_\tau e^{\tau(x+y)} + \\ &\int_0^x \int_0^y L_K(x, y, s, t) \|u_n(s, t) - x_p(s, t)\| ds dt \\ &\leq L_f L_h \|u_n - x_p\|_\tau e^{\tau(x+y)} + \|u_n - \\ &x_p\|_\tau \int_0^x \int_0^y L_K(x, y, s, t) e^{\tau(s+t)} ds dt \\ &\leq L_f L_h \|u_n - x_p\|_\tau e^{\tau(x+y)} + L \|u_n - x_p\|_\tau e^{\tau(x+y)} \\ &\leq (L_f L_h + L) \|u_n - x_p\|_\tau e^{\tau(x+y)} \end{aligned}$$

and we have

$$\|x_{n+1} - x_p\|_\tau \leq (L_f L_h + L) \|u_n - x_p\|_\tau \quad (2.3)$$

and

$$\begin{aligned} & \|Tx_n(x, y) - Tx_p(x, y)\| = \\ & \left\| \begin{aligned} & f(x, y, (h(x_n))(x, y)) \\ & + \int_0^x \int_0^y K(x, y, s, t, x_n(s, t)) ds dt \\ & - f(x, y, (h(x_p))(x, y)) \\ & - \int_0^x \int_0^y K(x, y, s, t, x_p(s, t)) ds dt \end{aligned} \right\| \\ & \leq \left\| f(x, y, (h(x_n))(x, y)) - f(x, y, (h(x_p))(x, y)) \right\| + \\ & \left\| \int_0^x \int_0^y K(x, y, s, t, x_n(s, t)) ds dt - \int_0^x \int_0^y K(x, y, s, t, x_p(s, t)) ds dt \right\| \\ & \leq L_f \| (h(x_n))(x, y) - (h(x_p))(x, y) \| + \\ & \int_0^x \int_0^y \| K(x, y, s, t, x_n(s, t)) - K(x, y, s, t, x_p(s, t)) \| ds dt \\ & \leq L_f L_h \|x_n - x_p\|_\tau e^{\tau(x+y)} + \\ & \int_0^x \int_0^y L_K(x, y, s, t) \|x_n(s, t) - x_p(s, t)\| ds dt \\ & \leq L_f L_h \|x_n - x_p\|_\tau e^{\tau(x+y)} \\ & + L \|x_n - x_p\|_\tau e^{\tau(x+y)} \\ & \leq (L_f L_h + L) \|x_n - x_p\|_\tau e^{\tau(x+y)} \end{aligned}$$

and we obtain

$$\|Tx_n - Tx_p\|_\tau \leq (L_f L_h + L) \|x_n - x_p\|_\tau. \quad (2.4)$$

Similarly,

$$\|Ty_n - Tx_p\|_\tau = \sup_{x, y \in \mathbb{R}_+} (\|Ty_n(x, y) - Tx_p(x, y)\| e^{-\tau(x+y)})$$

and we have

$$\|Ty_n - Tx_p\|_\tau = (L_f L_h + L) \|y_n - x_p\|_\tau \quad (2.5)$$

and similarly,

$$\|y_n - x_p\|_\tau = \sup_{x, y \in \mathbb{R}_+} (\|y_n(x, y) - x_p(x, y)\| e^{-\tau(x+y)})$$

and

$$\begin{aligned} & \|y_n(x, y) - x_p(x, y)\| = \|Tv_n(x, y) - Tx_p(x, y)\| = \\ & \left\| \begin{aligned} & f(x, y, (h(v_n))(x, y)) \\ & + \int_0^x \int_0^y K(x, y, s, t, v_n(s, t)) ds dt \\ & - f(x, y, (h(x_p))(x, y)) \\ & - \int_0^x \int_0^y K(x, y, s, t, x_p(s, t)) ds dt \end{aligned} \right\| \\ & \leq \left\| f(x, y, (h(v_n))(x, y)) - f(x, y, (h(x_p))(x, y)) \right\| + \\ & \left\| \int_0^x \int_0^y K(x, y, s, t, v_n(s, t)) ds dt - \int_0^x \int_0^y K(x, y, s, t, x_p(s, t)) ds dt \right\| \end{aligned}$$

$$\begin{aligned} & \leq L_f \| (h(v_n))(x, y) - (h(x_p))(x, y) \| + \\ & \int_0^x \int_0^y \| K(x, y, s, t, v_n(s, t)) - K(x, y, s, t, x_p(s, t)) \| ds dt \\ & \leq L_f L_h \|v_n - x_p\|_\tau e^{\tau(x+y)} + \\ & \int_0^x \int_0^y L_K(x, y, s, t) \|v_n(s, t) - x_p(s, t)\| ds dt \\ & \leq L_f L_h \|v_n - x_p\|_\tau e^{\tau(x+y)} + L \|v_n - x_p\|_\tau e^{\tau(x+y)} \\ & \leq (L_f L_h + L) \|v_n - x_p\|_\tau e^{\tau(x+y)}. \end{aligned}$$

Then, we have

$$\|y_n - x_p\|_\tau \leq (L_f L_h + L) \|v_n - x_p\|_\tau. \quad (2.6)$$

By using (2.4), we obtain

$$\begin{aligned} & \|v_n - x_p\|_\tau = \left\| \frac{(1-\beta_n)}{k} x_n + \left(1 - \frac{(1-\beta_n)}{k}\right) Tx_n - x_p \right\|_\tau \\ & \leq \frac{(1-\beta_n)}{k} \|x_n - x_p\|_\tau + \left(1 - \frac{(1-\beta_n)}{k}\right) \|Tx_n - x_p\|_\tau \\ & \leq \frac{(1-\beta_n)}{k} \|x_n - x_p\|_\tau + (L_f L_h + L) \left(1 - \frac{(1-\beta_n)}{k}\right) \|x_n - x_p\|_\tau \leq \|x_n - x_p\|_\tau \end{aligned} \quad (2.7)$$

and combining (2.4), (2.5), (2.6), and (2.7)

$$\begin{aligned} & \|u_n - x_p\|_\tau = \left\| \frac{(1-\alpha_n)}{k} Tx_n + \left(1 - \frac{(1-\alpha_n)}{k}\right) Ty_n - x_p \right\|_\tau \\ & \leq \frac{(1-\alpha_n)}{k} \|Tx_n - x_p\|_\tau + \left(1 - \frac{(1-\alpha_n)}{k}\right) \|Ty_n - x_p\|_\tau \\ & \leq \frac{(1-\alpha_n)}{k} (L_f L_h + L) \|x_n - x_p\|_\tau + (L_f L_h + L) \left(1 - \frac{(1-\alpha_n)}{k}\right) \|y_n - x_p\|_\tau \\ & \leq \frac{(1-\alpha_n)}{k} (L_f L_h + L) \|x_n - x_p\|_\tau + (L_f L_h + L)^2 \left(1 - \frac{(1-\alpha_n)}{k}\right) \|v_n - x_p\|_\tau \\ & \leq \frac{(1-\alpha_n)}{k} (L_f L_h + L) \|x_n - x_p\|_\tau + (L_f L_h + L)^2 \left(1 - \frac{(1-\alpha_n)}{k}\right) \|x_n - x_p\|_\tau \\ & \leq (L_f L_h + L) \|x_n - x_p\|_\tau \end{aligned} \quad (2.8)$$

and we have

$$\begin{aligned} & \|x_{n+1} - x_p\|_\tau \leq \|Tu_n - x_p\|_\tau \\ & \leq (L_f L_h + L) \|u_n - x_p\|_\tau \\ & \leq (L_f L_h + L)^2 \|x_n - x_p\|_\tau \end{aligned}$$

by induction we obtain

$$\|x_{n+1} - x_p\|_\tau \leq (L_f L_h + L)^{2n} \|x_0 - x_p\|_\tau \quad (2.9)$$

Taking the limit on both sides of (2.9) and using $(L_f L_h + L) < 1$, we obtain

$$\lim_{n \rightarrow \infty} \|x_n - x_p\|_\tau = 0.$$

We consider the equation (1.1), we have

$$S(w_n(x, y)) = f_1(x, y, (h(w_n))(x, y)) + \int_0^x \int_0^y K_1(x, y, s, t, w_n(s, t)) ds dt \quad x, y \in \mathbb{R}_+. \quad (2.10)$$

We have

Theorem 2.2 We suppose that

i) f, K, f_1, K_1, h satisfy conditions c1-c6 in Theorem 1.1

ii) there exists $\varepsilon_1 > 0$ such that

$$\|f(x, y, w) - f_1(x, y, w)\|_\tau \leq \varepsilon_1$$

for all $x, y \in \mathbb{R}_+, w \in E$;

iii) there exists $\varepsilon_2 > 0$ such that

$$\|K(x, y, s, t, w) - K_1(x, y, s, t, w)\|_\tau \leq L\varepsilon_2$$

for all $x, y, s, t \in \mathbb{R}_+, \forall w \in E$;

iv) $\{w_n\}_{n=1}^\infty$ be an iterative sequence generated by

$$\begin{cases} w_{n+1} = S\eta_n \\ \eta_n = \frac{(1-\alpha_n)}{k} S w_n + \left(1 - \frac{(1-\alpha_n)}{k}\right) S \mu_n \\ \mu_n = S \zeta_n \\ \zeta_n = \frac{(1-\beta_n)}{k} w_n + \left(1 - \frac{(1-\beta_n)}{k}\right) S w_n. \end{cases}$$

Then

a) the equations (1.6) and (2.10) have a unique solution x_p, w_p respectively;

$$b) \quad \|w_p - x_p\| \leq \left[\frac{1+(L_f L_h + L) + (L_f L_h + L)^2 + (L_f L_h + L)^3}{1 - (L_f L_h + L)} \right] (\varepsilon_1 + L\varepsilon_2).$$

Proof The assumptions (c1)-(c6) of Theorem 1.1, we obtain

$$\|Tx_n - Sw_n\|_\tau = \sup_{x, y \in \mathbb{R}_+} (\|Tx_n(x, y) - Sw_n(x, y)\| e^{-\tau(x+y)})$$

and

$$\begin{aligned} & \|Tx_n(x, y) - Sw_n(x, y)\| \leq \\ & \left\| \begin{aligned} & f(x, y, (h(x_n))(x, y)) \\ & + \int_0^x \int_0^y K(x, y, s, t, x_n(s, t)) ds dt \\ & - f_1(x, y, (h(w_n))(x, y)) \\ & - \int_0^x \int_0^y K_1(x, y, s, t, w_n(s, t)) ds dt \end{aligned} \right\| \\ & \leq \|f(x, y, (h(x_n))(x, y)) - f(x, y, (h(w_n))(x, y))\| + \\ & \|f(x, y, (h(w_n))(x, y)) - f_1(x, y, (h(w_n))(x, y))\| + \end{aligned}$$

$$\begin{aligned} & \left\| \int_0^x \int_0^y K(x, y, s, t, x_n(s, t)) ds dt - \int_0^x \int_0^y K(x, y, s, t, w_n(s, t)) ds dt \right\| + \\ & \left\| \int_0^x \int_0^y K(x, y, s, t, w_n(s, t)) ds dt - \int_0^x \int_0^y K_1(x, y, s, t, w_n(s, t)) ds dt \right\| \\ & \leq L_f \| (h(x_n))(x, y) - (h(w_n))(x, y) \| + \varepsilon_1 e^{\tau(x+y)} + \\ & \int_0^x \int_0^y L_K(x, y, s, t) \|x_n(s, t) - w_n(s, t)\| ds dt + \\ & L\varepsilon_2 e^{\tau(x+y)} \\ & \leq L_f L_h \|x_n - w_n\|_\tau e^{\tau(x+y)} + \varepsilon_1 e^{\tau(x+y)} + L \|x_n - w_n\|_\tau e^{\tau(x+y)} + L\varepsilon_2 e^{\tau(x+y)} \\ & \leq [(L_f L_h + L) \|x_n - w_n\|_\tau + (\varepsilon_1 + L\varepsilon_2)] e^{\tau(x+y)}. \quad (2.11) \end{aligned}$$

By using (2.11), we have

$$\|Tx_n - Sw_n\|_\tau \leq (L_f L_h + L) \|x_n - w_n\|_\tau + \varepsilon_1 + L\varepsilon_2 \quad (2.12)$$

and we obtain

$$\begin{aligned} \|v_n - \zeta_n\|_\tau & \leq \left\| \frac{(1-\beta_n)}{k} x_n + \left(1 - \frac{(1-\beta_n)}{k}\right) T x_n - \frac{(1-\beta_n)}{k} w_n - \left(1 - \frac{(1-\beta_n)}{k}\right) S w_n \right\| \\ & \leq \frac{(1-\beta_n)}{k} \|x_n - w_n\|_\tau + \left(1 - \frac{(1-\beta_n)}{k}\right) \|T x_n - S w_n\|_\tau \\ & \leq \frac{(1-\beta_n)}{k} \|x_n - w_n\|_\tau + \left(1 - \frac{(1-\beta_n)}{k}\right) (L_f L_h + L) \|x_n - w_n\|_\tau + \left(1 - \frac{(1-\beta_n)}{k}\right) (\varepsilon_1 + L\varepsilon_2) \\ & \leq \|x_n - w_n\|_\tau + \left(1 - \frac{(1-\beta_n)}{k}\right) (\varepsilon_1 + L\varepsilon_2). \quad (2.13) \end{aligned}$$

Similarly to (2.11),

$$\|y_n - \mu_n\| = \|T v_n - S \zeta_n\| \leq [(L_f L_h + L) \|v_n - \zeta_n\|_\tau + (\varepsilon_1 + L\varepsilon_2)] e^{\tau(x+y)}.$$

Thus, we have

$$\|y_n - \mu_n\|_\tau = \|T v_n - S \zeta_n\|_\tau \leq (L_f L_h + L) \|v_n - \zeta_n\|_\tau + (\varepsilon_1 + L\varepsilon_2) \quad (2.14)$$

and

$$\|Ty_n - S\mu_n\|_\tau = \sup_{x, y \in \mathbb{R}_+} (\|Ty_n(x, y) - S\mu_n(x, y)\| e^{-\tau(x+y)})$$

and

$$\begin{aligned} \|Ty_n - S\mu_n\| & \leq \|f(x, y, (h(y_n(x, y)))) - f(x, y, (h(\mu_n)(x, y)))\| + \|f(x, y, (h(\mu_n)(x, y))) - f_1(x, y, (h(\mu_n)(x, y)))\| + \\ & \left\| \int_0^x \int_0^y K(x, y, s, t, y_n(s, t)) ds dt - \int_0^x \int_0^y K(x, y, s, t, \mu_n(s, t)) ds dt \right\| + \\ & \left\| \int_0^x \int_0^y K(x, y, s, t, \mu_n(s, t)) ds dt - \int_0^x \int_0^y K_1(x, y, s, t, \mu_n(s, t)) ds dt \right\| \end{aligned}$$

$$\begin{aligned} &\leq L_f \| (h(y_n))(x, y) - (h(\mu_n))(x, y) \| + \varepsilon_1 e^{\tau(x+y)} + \\ &\int_0^x \int_0^y L_K(x, y, s, t) \| y_n(s, t) - \mu_n(s, t) \| ds dt + \\ &L \varepsilon_2 e^{\tau(x+y)} \\ &\leq [(L_f L_h + L) \| y_n - \mu_n \|_\tau + (\varepsilon_1 + L \varepsilon_2)] e^{\tau(x+y)}. \end{aligned} \quad (2.15)$$

By using (2.15), we have

$$\| T y_n - S \mu_n \|_\tau \leq (L_f L_h + L) \| y_n - \mu_n \|_\tau + \varepsilon_1 + L \varepsilon_2. \quad (2.16)$$

Combining (2.12), (2.13), (2.14), and (2.16), we have

$$\begin{aligned} \| \eta_n - u_n \|_\tau &\leq \frac{(1-\alpha_n)}{k} \| T x_n - S w_n \|_\tau + \left(1 - \frac{(1-\alpha_n)}{k} \right) \| T y_n - S \mu_n \|_\tau \\ &\leq \frac{(1-\alpha_n)}{k} [(L_f L_h + L) \| x_n - w_n \|_\tau + \varepsilon_1 + L \varepsilon_2] + \\ &\left(1 - \frac{(1-\alpha_n)}{k} \right) [(L_f L_h + L) \| y_n - \mu_n \|_\tau + \varepsilon_1 + L \varepsilon_2] \\ &\leq \frac{(1-\alpha_n)}{k} (L_f L_h + L) \| x_n - w_n \|_\tau + \frac{(1-\alpha_n)}{k} \varepsilon_1 + \\ &L \frac{(1-\alpha_n)}{k} \varepsilon_2 + \left(1 - \frac{(1-\alpha_n)}{k} \right) (L_f L_h + L) \| y_n - \mu_n \|_\tau + \\ &\left(1 - \frac{(1-\alpha_n)}{k} \right) \varepsilon_1 + L \left(1 - \frac{(1-\alpha_n)}{k} \right) \varepsilon_2 \\ &\leq \frac{(1-\alpha_n)}{k} (L_f L_h + L) \| x_n - w_n \|_\tau + \varepsilon_1 + L \varepsilon_2 + \\ &\left(1 - \frac{(1-\alpha_n)}{k} \right) (L_f L_h + L) \| y_n - \mu_n \|_\tau \\ &\leq \frac{(1-\alpha_n)}{k} (L_f L_h + L) \| x_n - w_n \|_\tau + \varepsilon_1 + L \varepsilon_2 + \\ &\left(1 - \frac{(1-\alpha_n)}{k} \right) (L_f L_h + L) [(L_f L_h + L) \| v_n - \zeta_n \|_\tau + \\ &\varepsilon_1 + L \varepsilon_2] \\ &\leq \frac{(1-\alpha_n)}{k} (L_f L_h + L) \| x_n - w_n \|_\tau + \varepsilon_1 + L \varepsilon_2 + \\ &\left(1 - \frac{(1-\alpha_n)}{k} \right) (L_f L_h + L)^2 \| v_n - \zeta_n \|_\tau + (L_f L_h + \\ &L) \left(1 - \frac{(1-\alpha_n)}{k} \right) \varepsilon_1 + L \left(1 - \frac{(1-\alpha_n)}{k} \right) (L_f L_h + L) \varepsilon_2 \\ &\leq \frac{(1-\alpha_n)}{k} (L_f L_h + L) \| x_n - w_n \|_\tau + \varepsilon_1 + L \varepsilon_2 + \\ &\left(1 - \frac{(1-\alpha_n)}{k} \right) (L_f L_h + L)^2 \| x_n - w_n \|_\tau + \left(1 - \frac{(1-\alpha_n)}{k} \right) \left(1 - \frac{(1-\beta_n)}{k} \right) (L_f L_h + L)^2 \varepsilon_1 + L \left(1 - \frac{(1-\alpha_n)}{k} \right) \left(1 - \frac{(1-\beta_n)}{k} \right) (L_f L_h + L)^2 \varepsilon_2 + \left(1 - \frac{(1-\alpha_n)}{k} \right) (L_f L_h + L) \varepsilon_1 + L \left(1 - \frac{(1-\alpha_n)}{k} \right) (L_f L_h + L) \varepsilon_2 \\ &\leq (L_f L_h + L) \| x_n - w_n \|_\tau + \varepsilon_1 + L \varepsilon_2 + \left(1 - \frac{(1-\alpha_n)}{k} \right) \left(1 - \frac{(1-\beta_n)}{k} \right) (L_f L_h + L)^2 \varepsilon_1 + L \left(1 - \frac{(1-\alpha_n)}{k} \right) \left(1 - \frac{(1-\beta_n)}{k} \right) (L_f L_h + L)^2 \varepsilon_2 + \left(1 - \frac{(1-\alpha_n)}{k} \right) (L_f L_h + L) \varepsilon_1 + L \left(1 - \frac{(1-\alpha_n)}{k} \right) (L_f L_h + L) \varepsilon_2 \end{aligned}$$

and similarly

$$\begin{aligned} \| x_{n+1} - w_{n+1} \|_\tau &\leq \| T u_n - S \eta_n \|_\tau \leq (L_f L_h + \\ &L) \| u_n - \eta_n \|_\tau + \varepsilon_1 + L \varepsilon_2 \\ &\leq (L_f L_h + L)^2 \| x_n - w_n \|_\tau + (L_f L_h + L) \varepsilon_1 + \\ &L (L_f L_h + L) \varepsilon_2 + \varepsilon_1 + L \varepsilon_2 + \left(1 - \frac{(1-\alpha_n)}{k} \right) \left(1 - \frac{(1-\beta_n)}{k} \right) (L_f L_h + L)^3 \varepsilon_1 + L \left(1 - \frac{(1-\alpha_n)}{k} \right) \left(1 - \frac{(1-\beta_n)}{k} \right) (L_f L_h + L)^3 \varepsilon_2 \end{aligned}$$

$$\frac{(1-\beta_n)}{k} (L_f L_h + L)^3 \varepsilon_2 + \left(1 - \frac{(1-\alpha_n)}{k} \right) (L_f L_h + L)^2 \varepsilon_1 + L \left(1 - \frac{(1-\alpha_n)}{k} \right) (L_f L_h + L)^2 \varepsilon_2$$

and we get

$$(L_f L_h + L)^2 = (1 - \theta)$$

Then, we have

$$\| x_{n+1} - w_{n+1} \| \leq (1 - \theta) \| x_n - w_n \| + \theta \left[\frac{1+(L_f L_h+L)}{\theta} + \frac{(L_f L_h+L)^2+(L_f L_h+L)^3}{\theta} \right] (\varepsilon_1 + L \varepsilon_2). \quad (2.17)$$

Denote that

$$\begin{aligned} \sigma_{n+1} &= \| x_{n+1} - w_{n+1} \| \\ \sigma_n &= \| x_n - w_n \| \\ \lambda_n &= \theta = 1 - (L_f L_h + L)^2 \\ m_n &= \left[\frac{1+(L_f L_h+L)}{1-(L_f L_h+L)^2} + \frac{(L_f L_h+L)^2+(L_f L_h+L)^3}{1-(L_f L_h+L)^2} \right] (\varepsilon_1 + L \varepsilon_2). \end{aligned}$$

It can be seen that (2.17) satisfies all the conditions in Lemma 1.3, and hence it follows from its conclusion that

$$\| x_p - w_p \| = \left[\frac{1+(L_f L_h+L)+(L_f L_h+L)^2+(L_f L_h+L)^3}{1-(L_f L_h+L)^2} \right] (\varepsilon_1 + L \varepsilon_2).$$

3. Conclusion

In this work, we have shown that the iteration method (1.5) converges to the solution of the more general Volterra integral equation in two variables (1.1). Finally, we have proved a data dependence result can be obtained for the solution of the integral equation (1.1).

Author's Contributions

Samet Maldar compiled information from the literature and wrote the manuscript.

Ethics

There are no ethical issues after the publication of this manuscript.

References

1. Rawat, S., Dimri, R. C., and Bartwal, A. 2021. A New Iterative Scheme for Approximation of Fixed Points of Suzuki's Generalized Nonexpansive Mappings. doi: 10.20944/preprints202105.0125.v1.
2. Akewe, H. 2016. The stability of a modified Jungck-Mann hybrid fixed point iteration procedure. *International Journal of*



- Mathematical Analysis and Optimization: Theory and Applications*; 2016, 95-104.
3. Dogan, K. 2018. Daha Hızlı Mann Sabit Nokta Yinelemesi Üzerine Bir Çalışma. *Afyon Kocatepe Üniversitesi Fen ve Mühendislik Bilimleri Dergisi*; 18(3), 852-860.
 4. Başarır M and Şahin A. 2017. Some Results of The New Iterative Scheme in Hyperbolic Space. *Communications of the Korean Mathematical Society*; 32 (4), 1009-1024.
 5. Gürsoy, F., Karakaya, V., and Rhoades, B. E. 2014, January. Some convergence and stability results for the Kirk multistep and Kirk-SP fixed point iterative algorithms. *In Abstract and Applied Analysis*; 2014, 1-12.
 6. Lungu, N. ve Rus, I. A. 2009. On a Functional Volterra-Fredholm Integral Equation via Picard Operator. *Journal of Mathematical Inequalities*; 3 (4), 519-527.
 7. Bielecki, A. 1956. Un Remarque sur L'application de la Méthode de Banach-Cacciopoli-Tikhonov dans la Théorie de L'equation $s=f(x, y, z, p, q)$. *Bull. Acad. Polon. Sci. Sér. Sci. Math. Phys. Astr*; 4, 265-268.
 8. Banas, J., and Lecko, M. 2002. Fixed points of the product of operators in Banach algebra. *Panamerican Mathematical Journal*; 12(2), 101-109.
 9. Hadizadeh, M., and Asgary, M. 2005. An efficient numerical approximation for the linear class of mixed integral equations. *Applied mathematics and computation*; 167(2), 1090-1100.
 10. Çakan, Ü., and Özdemir, İ. 2015. An application of Darbo fixed-point theorem to a class of functional integral equations. *Numerical Functional Analysis and Optimization*; 36(1), 29-40.
 11. Çakan, Ü., and Özdemir, İ. 2017. Applications of measure of noncompactness and Darbo's fixed point theorem to nonlinear integral equations in Banach spaces. *Numerical Functional Analysis and Optimization*; 38(5), 641-673.
 12. Çakan, Ü. 2017. On monotonic solutions of some nonlinear fractional integral equations. *Nonlinear Funct. Anal. Appl.*; 22(2), 259-273.
 13. Dobritoiu M. 2008. System of Integral Equations with Modified Argument. *Carpathian J. Math*, 24(2): 26-36.
 14. Craciun, C., and Serban, M. A. 2011. A nonlinear integral equation via Picard operators. *Fixed point theory*; 12(1), 57-70.
 15. Gursoy, F. 2014. Applications of normal S-iterative method to a nonlinear integral equation. *The Scientific World Journal*; 2014, 1-5.
 16. Atalan, Y., and Karakaya, V. 2017. Stability of nonlinear Volterra-Fredholm integro differential equation: A fixed point approach. *Creat. Math. Inform.* 26 (2017), No. 3, 247-254.
 17. Atalan, Y., and Karakaya, V. 2017. Iterative Solution of Functional Volterra-Fredholm Integral Equation with Deviating Argument. *J. Nonlinear and Convex Analysis*; 18(4), 675-684.
 18. Karapinar, E., Kumari, P. S., and Lateef, D. 2018. A new approach to the solution of the Fredholm integral equation via a fixed point on extended b-metric spaces. *Symmetry*; 10(10), 512.
 19. Garodia, C., and Uddin, I. 2018. Solution of a nonlinear integral equation via new fixed point iteration process. arXiv preprint arXiv:1809.03771.
 20. Abbas, M., Ibrahim, Y., Khan, A. R., and De la Sen, M. 2019. Strong Convergence of a System of Generalized Mixed Equilibrium Problem, Split Variational Inclusion Problem and Fixed-Point Problem in Banach Spaces. *Symmetry*, 11(5), 722
 21. Atalan, Y. 2019. İteratif Yaklaşım Altında Bir Fonksiyonel-İntegral Denklem Sınıfının Çözümünün İncelenmesi. *Iğdır Üniversitesi Fen Bilimleri Enstitüsü Dergisi*; 9(3), 1622-1632.
 22. Ilea, V., and Otrocol, D. 2020. Existence and Uniqueness of the Solution for an Integral Equation with Supremum, via w-Distances. *Symmetry*; 12(9), 1554.
 23. Ciplea, S. A., Lungu, N., Marian, D., and Rassias, T. M. 2020. On Hyers-Ulam-Rassias stability of a Volterra-Hammerstein functional integral equation. arXiv preprint arXiv:2001.07760.
 24. Abdou, M. A., Soliman, A. A., and Abdel-Aty, M. A. 2020. On a discussion of Volterra-Fredholm integral equation with discontinuous kernel. *Journal of the Egyptian Mathematical Society*; 28(1), 1-10.
 25. Beiglo, H., and Gachpazan, M. 2020. Numerical solution of nonlinear mixed Volterra-Fredholm integral equations in complex plane via PQWs. *Applied Mathematics and Computation*; 369, 124828, 1-9.
 26. Panda, S. K., Abdeljawad, T., & Ravichandran, C. 2020. Novel fixed-point approach to Atangana-Baleanu fractional and Lp-Fredholm integral equations. *Alexandria Engineering Journal*; 59, 4, 1959-1970.
 27. Okeke, G. A., & Abbas, M. 2020. Fejér monotonicity and fixed-point theorems with applications to a nonlinear integral equation in complex valued Banach spaces. *Applied General Topology*; 21(1), 135-158.
 28. Gutiérrez, J. M., Hernández-Verón, M. Á., and Martínez, E. 2020. Improved Iterative Solution of Linear Fredholm Integral Equations of Second Kind via Inverse-Free Iterative Schemes. *Mathematics*; 8 (10), 1747.
 29. Hacıoğlu, E., Gürsoy, F., Maldar, S., Atalan, Y., and Milovanović, G. V. 2021. Iterative approximation of fixed points and applications to two-point second-order boundary value problems and to machine learning. *Applied Numerical Mathematics*; 167, 143-172.
 30. Maldar, S. 2020. Yeni Bir İterasyon Yöntemi İçin Yakınsaklık Hızı. *Iğdır Üniversitesi Fen Bilimleri Enstitüsü Dergisi*; 10(2), 1263-1272.
 31. Soltuz S. M. and Grosan T. 2008. Data dependence for Ishikawa iteration when dealing with contractive like operators. *Fixed Point Theory Appl.*; 2008 (2008), 1-7.

The Effects of Magnetic Iron oxide Nanoparticles (Fe_3O_4) on Some Biological Aspects of *Galleria mellonella* L. (Lepidoptera: Pyralidae)

Ayşe Nazan Eskin^{1*} , Şahlan Öztürk¹ , Ata Eskin^{2**} 

¹Environmental Engineering Department, Nevşehir Hacı Bektaş Veli University, Nevşehir, Turkey

²Department of Plant and Animal Production, Avanos Vocational School, Nevşehir Hacı Bektaş Veli University, Nevşehir, Turkey

**ataeskin@nevsehir.edu.tr

**<https://orcid.org/0000-0002-7953-654X>

Received: 19 April 2021

Accepted: 2 August 2021

DOI: 10.18466/cbayarfbe.920637

Abstract

In this study, 18-38 nm-sized and spherical-shaped nanopowder Fe_3O_4 NPs concentrations (0.4, 2, 10, 50, 250 $\mu\text{g}/10 \mu\text{l}$) was force-fed to sixth instar ($180 \pm 20 \text{ mg}$) *Galleria mellonella* (Lepidoptera: Pyralidae) larvae under laboratory conditions. The effects of magnetic iron oxide nanoparticles (Fe_3O_4) on the pupal and adult developmental times, pupal and adult weights and adult longevity of *G. mellonella* were recorded. Results showed that treating *G. mellonella* with 250 $\mu\text{g}/10 \mu\text{l}$ Fe_3O_4 NPs significantly increased pupal weights. Additionally, while adult developmental time increased post 250 $\mu\text{g}/10 \mu\text{l}$ Fe_3O_4 NPs treatment, it was observed that pupal developmental time, pupal and adult weights, and adult longevity were not statistically significantly different when compared to the control.

Keywords: Biology, *Galleria mellonella*, Iron Oxide, Nanoparticle.

* The data of the present study were obtained from master's thesis of the first author

1. Introduction

Nanotechnology is a technology for the development of functional materials, devices, and systems at the level of atomic and molecular structures [1]. Nanotechnology is also the science of particles measuring nanometers (usually 1-100 nm) [2]. Iron (III) oxide (Fe_2O_3) is a reddish-brown and an inorganic compound that is paramagnetic in nature. It is also one of the three main iron oxides. The other two of them are FeO and Fe_3O_4 . Because of their very small size, magnetic properties, and biocompatibility, Fe_3O_4 NPs is used in various fields such as cancer, diabetes, atherosclerosis, inflammatory diseases, early diagnosis of contrast agents, drug magnetic resonance imaging, targeted drug delivery, hyperthermia, gene therapy, molecular/cellular tracking and in biomedical applications [3-4]. There are some studies on the use of Fe_3O_4 NPs iron oxide in terms of using as nutrients in agricultural studies [5-7]. During their widespread use, NPs come into contact with water. Subsequently, they are separated from the materials that are included in and pass into the water environment. As a result, they can turn into toxic substances [8]. *Galleria mellonella* L. (Lepidoptera:

Pyralidae) is an important pest species for beekeepers and causes important problems in beekeeping activities by opening galleries on honeycombs. It can be produced in large numbers in a short time under laboratory conditions. Furthermore, *G. mellonella* is a very low costly insect species and is used as a model experimental organism in toxicological studies. Several previous studies reported that different chemical NPs caused adverse effects on hemocyte counts, biology and antioxidant system, bioaccumulation, antioxidant defense, and immune system on *G. mellonella* [9-12]. The force-feeding method is the forcible delivery of the calories, protein, macro and micro elements, and vitamins that a living thing needs to the body without free will. This method is generally used in toxicity studies [13]. The aim of this study is to obtain data on Fe_3O_4 NP toxicity on a model experimental organism's life cycle. For this, we investigated the effects of various concentrations (0.4-250 $\mu\text{g}/10 \mu\text{l}$) of Fe_3O_4 NPs on the pupal and adult developmental times, pupal and adult weights, and adult longevity of *G. mellonella* by the force-feeding method.

2. Materials and Methods

2.1. Insects

Different life stages (egg, larvae, and pupae) of *G. mellonella* were obtained from the infested midrib of the wax combs.

2.1.1. Insect Diet

The collected samples were placed and reared with wax combs in jars (1 l capacity). The eggs laid by the adult moths who had emerged were also collected. The first stage larvae hatched from the eggs were again placed and reared with wax combs in jars (1 L capacity). The control (untreated) and experiment group larvae (NP treated) were reared in dark conditions at 27 ± 4 °C with $55 \pm 5\%$ relative humidity. All insect rearing cultures and experimental studies of NPs were studied at Avanos Vocational School of Higher Education, Avanos, Nevşehir, Turkey. Sixth instar (180 ± 20 mg) *G. mellonella* larvae were used in all force-feeding studies [10].

2.2. Chemicals and Materials

In this study, 18-38 nm-sized and spherical-shaped nanopowder Fe₃O₄ NPs (Nanokar, Istanbul/TURKEY) were used. Distilled water, 29 gauges micro-fine insulin syringe, 70% ethanol, ultrasonic bath sonicator (Isolab, Turkey), 20 ml plastic containers were formed the basic materials of the study.

2.3. Characterization of Fe₃O₄ NPs

The morphology of the Fe₃O₄ NPs was examined using field emission scanning electron microscopy (FESEM) at the Erciyes University Technology Research and Application Center (TAUM). The images of the Fe₃O₄ NPs were taken by using a Zeiss GEMINI 500 device which was connected to the FESEM detector at 25 kV [11]. X-ray diffraction (XRD) pattern of the Fe₃O₄ NPs was recorded at Marmara University, Faculty of Engineering, Metallurgical and Materials Engineering Department with reference code 98-001-7149. The diffractogram was compared with the standard powder diffraction card of the JCPDS iron file and previous studies.

2.4. Determination of Lethal Concentration 50 and 90 (LC₅₀ and LC₉₀) Values of Fe₃O₄ NPs in *G. mellonella* Larvae

The toxicity test protocol was performed according to [10] and [11]. Fe₃O₄ NPs were added to distilled water and dissolved to prepare a stock solution of $\mu\text{g}/10 \mu\text{l}$. The concentrations of Fe₃O₄ NPs (1, 10, 50, 100, 200, 400 $\mu\text{g}/10 \mu\text{l}/\text{larva}$) were prepared to determine the lethal concentration 50 and 90 (LC₅₀ and LC₉₀) values of Fe₃O₄ NPs in *G. mellonella* for 30 days (d). We used

only distilled water as a control solution. The NP suspensions were homogenized by a bath-type sonicator for 10 min at 40 °C. Sixty larvae (180 ± 20 mg) and three replicates, each replicate consisted of 20 larvae) were used for every treatment (control and for each experiment groups). The larvae, which were determined to be used in all experiments, were starved for 3 hours [10]. Then, larvae were force-fed with different Fe₃O₄ NPs concentrations (1, 10, 50, 100, 200, 400 $\mu\text{g}/10 \mu\text{l}/\text{larva}$) or only 10 μl distilled water (control group) with a micro-fine insulin syringe (29 gauges) [10]. Postforce-feeding treatment, each larva was maintained in a sterile plastic container (20 ml, with 20 pinhole holes on the top cover) without any diet in dark conditions at 27 ± 4 °C with $55 \pm 5\%$ relative humidity. The numbers of dead larvae and the numbers of viable larvae were counted in 30 d for probit analysis. The lethal concentrations (LC₅₀ and LC₉₀ values) of Fe₃O₄ NPs on the sixth instar *G. mellonella* larvae were determined by probit analysis using IBM-SPSS (2011) software on the 30th d [14]. According to LC₅₀ values of Fe₃O₄ NPs, (0.4, 2, 10, 50, 250 $\mu\text{g}/10 \mu\text{l}$) Fe₃O₄ NP concentrations were determined as experimental (treated) concentrations for all *G. mellonella* life cycle studies.

2.5. The Determination of Effects of the Magnetic Iron oxide NPs (Fe₃O₄) on Some Biological Aspects of *Galleria mellonella*

For bioassays, larvae (180 ± 20 mg) were force-fed with different Fe₃O₄ NPs concentrations (0.4, 2, 10, 50, 250 $\mu\text{g}/10 \mu\text{l}$). Each of these concentrations formed the experimental groups of the study. Only 10 μl of distilled water was given to the control group larvae. These studies were carried out under the stereomicroscope with using a micro-fine insulin syringe (29 gauges) [10]. Then, *G. mellonella* larvae were transferred individually into each in a sterile plastic container. The development of sixth instar larvae was monitored daily until the pupation to determine the pupal developmental time. Each pupa was weighed on an analytical scale to investigate the effect of Fe₃O₄ NPs on the pupal weight of *G. mellonella*. The individuals in both experimental and control groups were observed daily and adult developmental times were recorded. Each adult was weighed on an analytical scale with high sensitivity (1 mg to 500 g) to investigate the effect of Fe₃O₄ NPs on adult weight. Adult longevity time (day) was also recorded in treated with different doses of Fe₃O₄ NPs and untreated groups. Each biological assay was replicated three times with 20 sixth instar larvae.

2.6. Statistical Analysis

IBM-SPSS (Version 20.0) was used for the probit and pupal and adult developmental times, pupal and adult weights, and adult longevity data analysis of *G. mellonella*. Nonparametric Kruskal–Wallis test was

used for biological assays of the insect when data were not normally distributed [14].

3. Results and Discussion

3.1. Characterization of Fe₃O₄ NPs

Figure 1 display the FESEM image of Fe₃O₄ NP powder. The FESEM image showed that Fe₃O₄ NPs were in a spherical morphology (Figure 1).

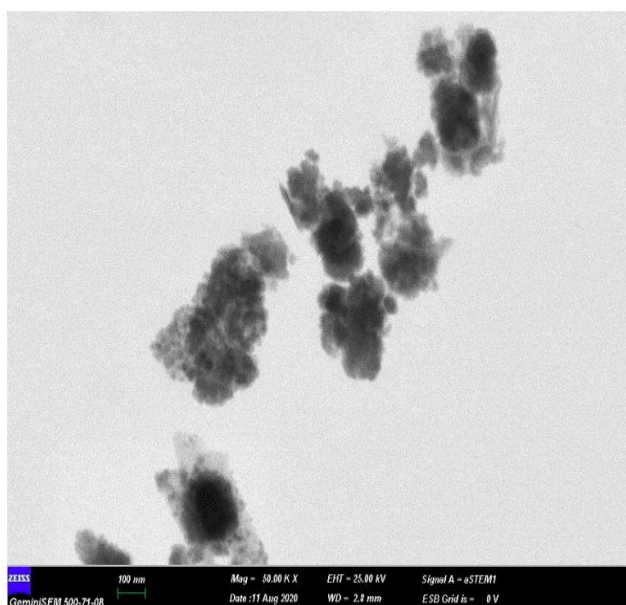


Figure 1. FESEM image of Fe₃O₄ NP powder (50.000x). The scale bar shows 100nm.

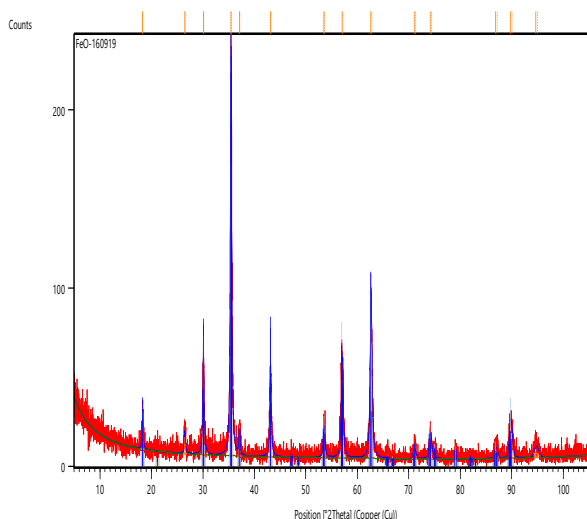


Figure 2. The XRD diffractogram of Fe₃O₄ NPs.

The XRD results showed that Fe₃O₄ NPs matched by [15] with magnetite low property (Table 1). All peaks in the XRD patterns are well matched to the standard PDF Cards for Fe₃O₄ NP (ICSD Number: 98-001-7149) (Figure 2). Peaks for Fe₃O₄ NPs appear at $2\theta = 30.09$ (220), 35.45 (311), 43.10 (400), 53.50 (422), 57.02

(511), and 62.62 (440) respectively (Table 1 and Figure 2) [16]. The peaks confirmed that the studied nanomaterial is Fe₃O₄ NP and has a low magnetic property.

Table 1. XRD peak list of Fe₃O₄ NPs

Pos. [°2Th.]	Height [cts]	FWHM Left [°2Th.]	d-spacing [Å]	Rel. Int. [%]	Tip Width	Matched by
18.27(1)	14(2)	0.23(6)	4.85134	8.42	0.2763	98-001-7149
30.091(7)	41(3)	0.30(3)	2.96744	24.86	0.3582	98-001-7149
35.453(3)	163(6)	0.27(2)	2.52994	100	0.3265	98-001-7149
37.08(2)	10(1)	0.28(5)	2.42286	5.92	0.3368	98-001-7149
43.109(7)	36(3)	0.30(4)	2.09671	22.31	0.3576	98-001-7149
53.50(2)	13(2)	0.36(9)	1.71152	8.09	0.4313	98-001-7149
57.022(7)	43(3)	0.38(4)	1.61376	26.27	0.4573	98-001-7149
62.625(6)	74(4)	0.35(3)	1.48218	45.16	0.4249	98-001-7149
71.05(4)	4(1)	0.6(1)	1.32576	2.47	0.7187	98-001-7149
74.17(2)	11(2)	0.5(1)	1.27749	6.77	0.5440	98-001-7149
86.88(4)	4(1)	0.6(1)	1.12025	2.74	0.7405	98-001-7149
89.75(1)	17(1)	0.57(6)	1.09172	10.67	0.6853	98-001-7149

3.2. LC₅₀ and LC₉₀ Values of Fe₃O₄ NPs

LC₅₀ and LC₉₀ values of Fe₃O₄ NPs were determined on *G. mellonella* larvae as 482.72 µg/10 µl and 1843.89 µg/10 µl (Probit, Chi-square= 30.383, df = 5, P = 0.00, $y=0.65+1.09E-5*x$) respectively for 30 d. Therefore, 0.4, 2, 10, 50, 250 µg/10 µl Fe₃O₄ NP concentrations were determined as experimental (treated) concentrations for all biological studies.

3.3. Effects of Iron Oxide Nanoparticles (Fe₃O₄) on Some Biological Aspects of *G. mellonella*

We tested the effects of Fe₃O₄ NPs on some life parameters (developmental time to pupal stage, pupal weight, developmental time to adult stage, adult weight, and adult longevity) of *G. mellonella*, to determine its sublethal toxicity on the insect by force-feeding method at concentrations of 0.4, 2, 10, 50, 250 µg/10 µl. Results were given in Table 2 below.

The mean of pupal developmental time increased significantly at 250 µg/10 µl concentration when compared with 2 and 50 µg/10 µl concentrations of Fe₃O₄ NPs ($\chi^2 = 30.294$, df= 5, P= 0.00). But there were no significant differences between experimental groups and control group exist in the mean pupal developmental time. Under the influence of increasing concentrations of Fe₃O₄ NP, an increase in pupal weight was observed.

Table 2. The effects of iron oxide nanoparticles on some life parameters of *G. mellonella*

Concentrations of Fe ₃ O ₄ NPs (µg/10 µl)	Pupal development time (day) (Mean ^b ± SE) ^c	Pupal weight (mg) (Mean ^b ± SE) ^c	Adult development time (day) (Mean ^b ± SE) ^c	Adult weight (mg) (Mean ^b ± SE) ^c	Adult longevity time (day) (Mean ^b ± SE) ^c
0 ^a	10.08 ± 0.63 ^{ab}	110.61 ± 2.69 ^a	14.08 ± 0.43 ^a	65.29 ± 1.99 ^a	7.61 ± 0.59 ^a
0.4	10.42 ± 0.74 ^{ab}	118.39 ± 2.69 ^{ab}	15.65 ± 0.47 ^{ab}	68.47 ± 2.04 ^a	7.73 ± 1.00 ^a
2	9.04 ± 0.39 ^a	112.40 ± 1.75 ^{ab}	15.43 ± 0.22 ^{ab}	69.00 ± 1.85 ^a	7.97 ± 0.65 ^a
10	10.48 ± 0.44 ^{ab}	112.00 ± 2.23 ^{ab}	16.69 ± 0.37 ^b	63.97 ± 1.82 ^a	8.13 ± 0.45 ^a
50	9.76 ± 0.44 ^a	116.12 ± 2.20 ^{ab}	14.97 ± 0.57 ^{ab}	65.76 ± 2.03 ^a	6.25 ± 0.31 ^a
250	11.65 ± 0.63 ^b	121.73 ± 3.64 ^b	15.47 ± 0.39 ^{ab}	69.82 ± 3.5 ^a	7.00 ± 0.81 ^a
SPSS test:	Kruskal Wallis Test, P=0.00 < 0.05	Kruskal Wallis Test, P=0.008 < 0.05	Kruskal Wallis Test, P=0.000 < 0.05	Kruskal Wallis Test, P=0.340 > 0.05	Kruskal Wallis Test, P=0.178 > 0.05

^a "0" control group.

^b Values are the means of three replicates with 20 larvae. Larvae who could not reach the adult stage were not included in the calculation.

^c The difference between groups with different letters in the same column is statistically significant.

The pupa mean weight was significantly increased to 121.73 at 250 µg/10 µl Fe₃O₄ NP concentration ($\chi^2=15.585$, $df=5$, $P=0.008$). Pupal weight in treated larvae ranged from 112 to 121.73 mg as compared with 110.61 mg in the control group (Table 2). We found that adult developmental time significantly increased at 10 µg/10 µl concentration of Fe₃O₄ NP when compared with the control group ($\chi^2=22.339$, $df=5$, $P=0.000$). Mean adult weight did not differ significantly ($\chi^2=5.668$, $df=5$, $P=0.340$) and ranged from 63.97 to 69.82 mg. Similarly, mean adult longevity was insignificant ($\chi^2=7.631$, $df=5$, $P=0.178$) in all Fe₃O₄ NP treatments when compared to the control group and values ranged from 6.25 to 8.13 (d) (Table 2).

Currently, studies on the toxic effects of magnetic Fe₃O₄ NPs on *G. mellonella* are scarce. In this study, it was observed that mean of the pupal development time was prolonged at the highest Fe₃O₄ NPs concentration when compared to the lower concentrations of Fe₃O₄ NPs (Table 2). The reason why nanoparticles cause delays in the biological parameter of insects is explained as follows by [17-18]. According to them, after NPs entering the gut, they were able to induce apoptosis by crossing the peritrophic membrane [17-18]. So, this

toxicity within the gut resulted in delays in development. There are some studies conducted with metal oxide NPs and showing that metal oxide NPs cause apoptosis in cell cellular systems of insects [11, 19-21]. We believe that there may be apoptotic mechanisms that occur as a result of NP stress in the larva, which prolongs the pupal development period in response to the increasing concentration of NPs. Changes in pup weights as a result of physiological stress resulting from exposure to silver NPs were obtained by [22] in two lepidopteran pests of the castor plant (*Ricinus communis* L.) namely Asian armyworm, *Spodoptera litura* F. (Lepidoptera: Noctuidae) and castor semi looper, *Achaea janata* L. (Lepidoptera: Noctuidae) larvae. They showed that larval and pupal body weights decreased along with the decrease in the concentrations of AgNPs and AgNO₃ in both the test insects [22]. However, in our study, the mean pup weight increased significantly at the highest Fe₃O₄ NP concentration (250 µg/10 µl) when compared to the control group. We speculate that the increase in pupal weights of *G. mellonella* may be related to the upregulation of expression of juvenile hormone-binding proteins (JHBPs) after treatment with Fe₃O₄ NPs as explained by [23]. Adult developmental time extended significantly at 10 µg/10 µl Fe₃O₄ NPs concentration when compared with control group ($\chi^2=22.339$, $df=5$, $P=0.00$) (Table 2). Juvenile hormone is secreted from the corpus allatum, inhibits insect metamorphosis, and regulates development, reproduction, diapause, polyphenism, behavior throughout insect life [24]. Juvenile hormone metabolism may also affect the larval development time and can cause a prolongation in adult developmental time in *G. mellonella* [25]. So as a result, it is also thought that the increase adult developmental time in our study may be due to an irregularity in the balance of hormones associated with metamorphosis such as the juvenile hormone because of Fe₃O₄ NPs.

4. Conclusion

The purpose of this work was to determine the effects of Fe₃O₄ NPs on some biological aspects of *G. mellonella*. In this context, different concentrations of nanopowder Fe₃O₄ were force-fed to sixth instar larvae. The toxic effects of Fe₃O₄ NPs on the pupal and adult developmental times, pupal and adult weights, and adult longevity of *G. mellonella* were studied. Also, the morphology of the Fe₃O₄ NPs was examined using field emission scanning electron microscopy (FESEM). Finally, X-ray diffraction (XRD) pattern of the Fe₃O₄ NPs was recorded. As a result of these analyzes, it was understood that the Fe₃O₄ NPs have magnetite low property and were in a spherical morphology. Thus, the toxic effects of spherical-shaped and magnetite low

property Fe₃O₄ NPs on some biological stages of the model experimental organism *G. mellonella* were determined with this study.

Acknowledgements

This study was supported by Nevşehir Hacı Bektaş Veli University Scientific Research Projects Unit with the project number ABAP21F9. Thanks to Nevşehir Hacı Bektaş Veli University Scientific Research Projects Unit for financially supported our study.

Author's Contributions

Ayşe Nazan Eskin: Carried out the toxicity studies. Read, wrote, and approved the final manuscript.

Şahlan Öztürk: Managed and coordinated the toxicity studies. Read, wrote, and approved the final manuscript.

Ata Eskin: Participated in the design of the study, interpreted the chemical analysis results and performed the statistical analysis. Read, wrote and approved the final manuscript.

Ethics

Ethical approval is not applicable, because this article does not contain any studies with human or animal subjects.

References

1. Tunca Üçüncü, E. 2015. Nanoteknolojinin temeli nanopartiküller ve nanopartiküllerin fitoremediasyon, *Ordu Üniversitesi Bilim ve Teknoloji Dergisi* 5, 2: 23-34.
2. Marangoz, Ö, & Yavuz, O. 2020. Nano-ilaç taşıma sistemleri ve toksikolojik değerlendirmeleri, *Turkish Bulletin of Hygiene & Experimental Biology/Türk Hijyen ve Deneysel Biyoloji*, 77(4).
3. Pandey P, Dahtya M. A Brief review on inorganic nanoparticles, *Journal of Critical Reviews*, 3(3):18-26.
4. Uyanıkgil, E. Ö. Ç, & Salmanoğlu, D. S. 2020. Metalik nanopartiküllerin hedeflendirilmesi, *Ege Tıp Dergisi*, 59(1), 71-81.
5. Abou El-Nasr M. K, El-Hennawy H. M, El-Kereamy A. M. H, Abou ElYazied A, Salah Eldin A. T. 2015. Effect of magnetite nanoparticles (Fe₃O₄) as nutritive supplement on pear saplings. *Middle East Journal of Applied Sciences*, 5:777-785.
6. Rezapour-Osalou, P, Tajbakhsh, M, Asri-Rezaei, S, & Hasanzadeh, A. 2015. Foliar application of nano-Fe₃O₄ induced iron content and phytase activity in corn seed Single Cross 704, *Cumhuriyet Üniversitesi Fen-Edebiyat Fakültesi Fen Bilimleri Dergisi*, 36(3), 664-671.
7. Jalali, M, Ghanati, F, & Modarres-Sanavi, A. M. 2016. Effect of Fe₃O₄ nanoparticles and iron chelate on the antioxidant capacity and nutritional value of soil-cultivated maize (*Zea mays*) plants. *Crop and Pasture Science*, 67(6), 621-628.
8. Ünşar, E. K, & Perendeci, N. A. 2016. Nanopartiküllerin çevresel akıbetleri ve anaerobik parçalanma prosesine etkileri. *Pamukkale Üniversitesi Mühendislik Bilimleri Dergisi*, 22(6), 503-512.
9. Zorlu T, Nurulloğlu Z. U, Altuntaş, H. 2018. Influence of dietary titanium dioxide nanoparticles on the biology and antioxidant system of model insect, *Galleria mellonella* (L.) (Lepidoptera: Pyralidae), *Journal of the Entomological Research Society*, 20(3):89-103.
10. Eskin, A, Öztürk, Ş, & Körükçü, M. 2019. Determination of the acute toxic effects of zinc oxide nanoparticles (ZnO NPs) in total hemocytes counts of *Galleria mellonella* (Lepidoptera: Pyralidae) with two different methods, *Ecotoxicology*, 28(7), 801-808.
11. Eskin, A, & Bozdoğan, H. 2021. Effects of the copper oxide nanoparticles (CuO NPs) on *Galleria mellonella* hemocytes, *Drug and Chemical Toxicology*, 1-11.
12. Tuncsoy, B, & Mese, Y. 2021. Influence of titanium dioxide nanoparticles on bioaccumulation, antioxidant defense and immune system of *Galleria mellonella* L., *Environmental Science and Pollution Research*, 1-9.
13. Ramarao N, Nielsen-Leroux C, Lereclus D. 2012. The insect *Galleria mellonella* as a powerful infection model to investigate bacterial pathogenesis, *Journal of Visualized Experiments*, 70: 4392.
14. IBM-SPSS Statistics for Windows. 2011. Version 20.0. Elsevier, London, UK. IBM Corp. Released. Armonk, NY: IBM Corp.
15. Manna, M, Bhave, K, & Pathak, A. S. 2021. Adhesive scale formation on low silicon steel surface; characterization and mechanism, *ISIJ International*, *ISIJINT-2020*.
16. Morel, M, Martínez, F, & Mosquera, E. 2013. Synthesis and characterization of magnetite nanoparticles from mineral magnetite. *Journal of Magnetism and Magnetic Materials*, 343, 76-81.
17. Pappas, S. A, & Mishra, M. 2018. A drosophila model to decipher the toxicity of nanoparticles taken through oral routes, *Cellular and Molecular Toxicology of Nanoparticles*, 311-322.
18. Malhotra, N, Lee, J. S, Liman, R. A. D, Ruallo, J. M. S, Villaflores, O. B, Ger, T. R, & Hsiao, C. D. 2020. Potential toxicity of iron oxide magnetic nanoparticles: A review. *Molecules*, 25(14), 3159.
19. Qiang X, Hongxia S, Yinghua S, Dexiang U. G, Zhang G. 2005. Apoptosis of *Spodoptera litura* larval hemocytes induced by heavy metal zinc, *Chinese Science Bulletin*, 50(24): 2856-2860.
20. Das S, Debnath N, Patra P, Datta A, Goswami A. 2012. Nanoparticles influence on expression of cell cycle related genes in *Drosophila*: a microarray-based toxicogenomics study, *Toxicological & Environmental Chemistry*, 94:952-7.
21. Chen, H, Wang, B, Feng, W, Du, W, Ouyang, H, Chai, Z, & Bi, X. 2015. Oral magnetite nanoparticles disturb the development of *Drosophila melanogaster* from oogenesis to adult emergence, *Nanotoxicology*, 9(3), 302-312.
22. Yasur, J, & Rani, P. U. 2015. Lepidopteran insect susceptibility to silver nanoparticles and measurement of changes in their growth, development and physiology, *Chemosphere*, 124, 92-102.



23. Meng, X, Abdlli, N, Wang, N, Lü, P, Nie, Z, Dong, X., ... & Chen, K. 2017. Effects of Ag nanoparticles on growth and fat body proteins in silkworms (*Bombyx mori*), *Biological Trace Element Research*, 180(2), 327-337.
24. Shinoda, T. 2016. Methyl farnesoate. In *Handbook of Hormones* (pp. 566-e100). Academic Press.
25. Tüven, A. 2006. Farklı dozlarda konağa verilen gibberellik asitin parazitoid *Apanteles galleriae* Wilkinson (Hymenoptera: Braconidae) biyolojisine etkileri (Master's thesis, Balıkesir Üniversitesi Fen Bilimleri Enstitüsü).

In vitro Micropropagation of Duckweed (*Lemna minor* L.) Plant with Temporary Immersion System Bioreactors

Uğur Sidal^{1*}, Zehra Ergönül¹

¹Manisa Celal Bayar University Faculty of Arts and Sciences Department of Biology Manisa, TURKEY

* ugur.sidal@bayar.edu.tr

*Orcid: 0000-0002-1562-6239

Received: 29 December 2020

Accepted: 1 June 2021

DOI: 10.18466/cbayarfbe.848369

Abstract

Which is very rich in protein in plant *Lemna minor* L. abundant in Turkey ecologically plays a very important role in protecting the elimination of water pollution and aquaculture environment balance. In this study, in vitro propagation of this plant with Temporary Immersion System Bioreactor and determination of the effects of used plant growth regulators on the protein content of the plant were aimed. With this objective different variant of media with and without sucrose, varying pH and concentrations of BAP, kinetin, TDZ in medium were analyzed. Experiments for micropropagation were performed for 8 hours in the dark and 16 hours in white fluorescent light (150 μ mol photons m⁻²s⁻¹) under photoperiod and at 24 \pm 1 ° C. The highest plant growth was observed at pH 7.23 in sugar free liquid MS medium containing 0.2 mg/L BAP. 50.44 plants per explant were recorded in this medium. In addition, the maximum number of plants per explant in liquid MS medium containing 0.05 mg/L kinetin was calculated as 57,823 and the maximum number of plants per explant in liquid MS medium containing 0.6 mg/L TDZ was calculated as 50.74. As a result of nitrogen determination studies with Kjeldahl method, the protein value of the plant was determined as 25.5%. As a result of hormone application, it was seen that protein content in plant increased to 29.18% with 0.5 mg/L BAP. It was concluded that the aim of the study were fulfilled and positive effects of Temporary Immersion System Bioreactors on plant multiplication were found.

Keywords: In vitro, Temporary Immersion System Bioreactors, *Lemna minor*, Micropropagation

1. Introduction

Aquatic plants, the main producers of the aquatic environment, are chlorophyll-containing organisms of various forms, from one cell to multiple cells. These plants, which are the primary producers, carry out photosynthesis using carbon dioxide and light energy present in the water and form plant sources as the first link in the food chain of the aquatic environment [1]. Organic degradation in the aquatic ecosystem is extremely important for the biological cycle. The oxygen supply required for aerobic bacteria and fungi responsible for organic degradation is provided by aquatic plants and indirectly, the plants are important in the aquatic environment for the degradation of organic wastes [2]. As is known, aquatic plants play a role in the removal of pathogenic bacteria and are used for phytoremediation and bioaccumulation as they are indicator plants with a large growth potential in industrial wastewater [3]. *Lemna minor* is a very small

and simple plant in the Lemnaceae family of Arales, which is free-floating or submerged [4]. This species is a nutritional source of energy, studies on it are gaining momentum in recent years and increasing importance. It is a very rich plant in terms of protein [5]. *L. minor* is of great ecological importance. In recent years, the use of plants in the elimination of pollution by various factors in natural waters has been increasing. It has a large growth potential in industrial wastewater and is one of the leading plants used for phytoremediation as it is an indicator plant [3]. Studies have shown that *L. minor* is also effective in eliminating the pollution caused by petroleum hydrocarbons. *L. minor* species synthesize cysteine and other sulfur-containing amino acids by absorbing sulfur from toxic gases such as SO₂ and H₂S. They also have a very high percentage of minerals and essential amino acids such as methionine and lysine [6,7]. *Lemna minor* is also used in proteomic and genomic research. It has been developed for the production of recombinant therapeutic proteins due to

its high protein content. Lemna Expression System (LEX); it allows rapid clonal growth of transgenic plants, release of recombinant proteins, high protein production [8]. Thanks to its rapid propagation and tissue culture techniques, its usage areas are gradually increasing and the studies related to the subject gain momentum.

The proliferation and rooting of plants from organized meristems, somatic cells that have not yet matured or completed maturation, either directly (organogenesis or somatic embryogenesis) or indirect (callus, protoplast, etc.) are generally called micro-propagation [9]. Micropropagation is considered to be one of the most advantageous methods for propagation in tissue culture techniques if appropriate nutrients, hormone and culture requirements are required by plants. With this technique it is possible to obtain disease-free plants. Variety is increasing due to somaclonal variation and production is carried out in a shorter time and using less rootstock than other techniques [10]. In tissue culture techniques, solid nutrient media are generally used. In these studies, explants placed in solid nutrient medium begin to darken due to the presence of gelling agents that solidify the nutrient medium and are therefore transferred periodically to new media after 4-6 weeks. Contamination of the material is very high during these transfers. Micropropagation studies in solid nutrient environments where gelling agents are used are higher contamination risk and more costly applications compared to tissue culture studies in liquid nutrient media [11]. For this reason, liquid culture media without solidifying agents are particularly preferred for commercial micropropagation. In liquid culture media, the entire surface of the plant explants is in contact they absorb the components in the nutrient media better. The use of bioreactors used in liquid culture media in micropropagation studies is therefore increasing [12]. The most common problem in bioreactor systems in which liquid culture media are used is the observation of hyperhydricity due to the fact that the plant material remains in the nutrient medium continuously. Therefore, recently developed temporary immersion system bioreactors are used which enable the plant to move away from the liquid surface at certain intervals. Temporary immersion system bioreactors were first developed by Haris and Mason [13] and the first successful plant regeneration results were obtained from somatic embryos of *Solanum tuberosum* and *Coffea arabica* [11]. Unlike other bioreactor systems in temporary immersion system bioreactors, a surface has been developed which can provide temporary contact between explant and liquid nutrient media from time to time. With the air flow, the environment goes up in certain time intervals and ensures that the plant receives the necessary nutrients. During the dipping process, air flow and nutrient media penetrate the plant and pass to the tissues without damaging the material. Temporary immersion system bioreactors are used as suitable systems for somatic embryogenesis and organogenesis

for this purpose. In this study, in vitro propagation of the plant with temporary immersion system bioreactor is aimed and with the use of bioreactor, it is aimed to keep the ambient conditions at an optimum level and to reproduce the plant in a faster time and healthier than the natural conditions. Also; The aim of this study is to determine the effects of plant growth regulators used for micro-propagation of plant on growth rate and plant protein quality.

2. Materials and methods

2.1. Plant material

Duckweed (*Lemna minor* L.) obtained from Ankara University Faculty of Agriculture Department of Fisheries were used in this study.

2.2. Growth media and culture conditions in in vitro studies

Basic nutrient medium containing MS (Murashige and Skoog basal medium) mineral salt and vitamins and 3% sucrose and solidified with 0.8% agar (Type A, Sigma-Aldrich Corporation St Lo. Mo) or 0.6-0.65% agar (Duchefa Netherlands) were used in the experiments. Agar was not added in liquid culture experiments. Double distilled water was used in the preparation of the medium and plant growth regulators of different constructions were added to the nutrient medium when necessary. The pH of the nutrient medium was adjusted to 5.6-5.8 by using 1N NaOH or 1N HCl, followed by autoclaving at 120 ° C for 20 minutes under a pressure of 118 KPa. All cultures were kept under photoperiod for 16 hours under white fluorescent light (150 $\mu\text{mol photons m}^{-2}\text{s}^{-1}$) at 24 ± 1 ° C [14].

2.3. Plant growth regulators

Plant growth regulators BAP (Benzylaminopurine), TDZ (Thidiazuron) and kinetin used in the study were obtained from Sigma Aldrich and Duchefa. The stock solutions of the growth regulators were prepared in the desired amount and proportion after thawing with suitable solvents as recommended by the company. Prepared stock solutions were stored at 4 ° C for two months. Kinetin was added to the media after autoclaving [14].

2.4. Explant surface sterilization

For surface sterilization, different doses of commercial bleach and H₂O₂ were used in duckweed [14].

2.5. Determination of nitrogen and protein in plant material

Kjeldahl method was used to determine the protein and nitrogen contents of the plants which were micro-propagated and dried [15].

2.6. Statistical evaluation of data

Regeneration experiments were performed with 3 replications. The data obtained from the studies were analyzed by using SPSS 16 for Windows program on the computer according to factorial experiment pattern. Duncan, LSD or t tests were applied to determine the significance level of the media. Percentage values were subjected to arcsin transformation before statistical analysis [16].

3. Results

3.1. Surface sterilization of the explant

Surface sterilization of the explants in vitro experiments, *Lemna minor* plant explants (20 pieces) were first surface sterilized in 20% commercial bleach, then in 10% and 20% H₂O₂ for 5, 6, 7, 8, 9 and 10 min. Data obtained as a result of surface sterilization was subjected to variance analysis [17] and the results are given in Table 3.1.

Table 3.1. Variance analysis of surface sterilization with bleach and H₂O₂ at different time and concentrations.

Variance resources	Degrees of freedom	Average of squares	Frequency
Time (min)	5	2549,63	86,050
Concentration (%)	2	45029,63	1,520x10 ³
Time x concentration	10	2549,63	86,050**
Error	36	29,630	
General total	53		

**p<0.05

Table 3.2. Duncan test results of surface sterilization with bleach and H₂O₂ at different time and concentrations.

Time (min)	Ratio of sterile plants		
	%20 Bleach	%10 H ₂ O ₂	%20 H ₂ O ₂
5	100,00	0,00	30,00d
6	100,00	0,00	50,00c
7	100,00	0,00	60,00b
8	100,00	0,00	100,00a
9	100,00	0,00	100,00a
10	100,00	0,00	100,00a

The difference between the means indicated by different letters in the same column is significant at 0.05 level.

As seen in Table 3.1 as a result of the analysis of variance, 5, 6, 7, 8, 9 and 10 minutes with 20% commercial bleach and 20% and 10% H₂O₂ concentrations in terms of surface sterilization at 0.05 level is important differences were found. Duncan test [18] results to determine the significance level of these differences are given in Table 3.2. As shown in

Table 3.2 Duncan test results according to 20% bleach and different time treatment between 0 and 100.00% sterile plants were obtained. Although the sterilization application was carried out with bleach at different times, 100% sterile plants were obtained, but whitening was observed due to chlorophyll disintegration. 30 to 100% sterile plants were obtained by 20% H₂O₂ treatment. However, bleaching and damage of the plants were detected in 20% H₂O₂ treatment for 9 and 10 minutes. No sterile plants were obtained with different time and 10% H₂O₂ treatment. These parameters were used for surface sterilization in the following studies since 100% sterilization was achieved in plants with 8 minutes and 20% H₂O₂ treatment.

3.2. The effect of different pH values on the growth of duckweed in erlenmayer in non-agitated environment

In vitro study, *Lemna minor* plant explants were cultured in Erlenmayer for 1 week in non-agitated medium using distilled water at different pH values. The data obtained after 1 week were subjected to variance analysis and the results are given in Table 3.3. As shown in Table 3.3 as a result of analysis of variance pH 5, 6, 7, 7.23, 8, and 9 values were found to be significant differences at 0.01 level in reproduction rate, number of plants and total plants per explant. Duncan test results to determine the significance level of these differences are given in Table 3.4. The difference between the means indicated by different letters in the same column is significant at the 0.01 level. Plant growth was observed in all pH values. Amplification rate ranged from 3.87% to 280%. The number of plants per explant ranged between 1.47 and 5. The highest increase in the number of plants was obtained at pH 5 with 5 units and the lowest increase was found at pH 9 values with 1.47 units. The total number of plants varied between 7.33 and 25. The maximum number of plant growths with 5 explants starting at pH 7.23 25 units, the least plant formation was recorded as pH 9 7.33 units. In addition, the number of 19 plants at pH 7 and 25 plants at pH 7.23 were recorded. In addition, 8.33 plants were obtained at pH 8 and 7.33 plants were recorded at pH 9. According to this study, the most ideal pH range for the plant is 7–7.23, pH range is lower than pH 7–7.23 (6–5.8) and pH range is higher than pH 7–7.23 (pH 8–9) the percentage of plant formation has been observed to fall (Table 3.4).

3.3. The effect of different pH values on the growth of duckweed in erlenmayer under agitation

In vitro experiments, *Lemna minor* plant explants were cultured in Erlenmayer for 1 week in shaking medium using distilled water at different pH values. The data obtained after 1 week were subjected to variance analysis and the results are given in Table 3.5. As it is seen in Table 3.5, variance analysis showed that

significant differences were found in pH 5, 6, 7, 7.23, 8 and 9 values in terms of reproduction rate, number of plants per explant, total number of plants, wet weight and dry weight changes. Duncan test results to determine the significance level of these differences are given in Table 3.6. Plant growth was observed in all pH values. The amplification rate ranged from -3.33% to 560%. The number of plants per explant ranged between 0.63 and 6.60.

The highest increase in number of plants was obtained in pH 7 with 6.60 and the least increase in number of plants was in pH 5 with 0.63. The total number of plants ranged from 9.67 to 66.00. The highest plant growth was obtained at pH 7 and the lowest plant growth was at pH 5. The heaviest plants in weight were 0.7 g, pH 7.23 and the lightest plants were 0.04 g, pH 5. Dry weight values in weight of 0.55 g pH 7.23, 0.001 g was observed at pH 9 (Table 3.6).

Table 3.3. Analysis of variance of the effect of different pH values on the plant growth of duckweed in Erlenmayer in non-agitated medium using distilled water.

Variance resources	Degrees of freedom	Number of plants per explant (pcs)		Total number of plants (pcs)	
		Average of squares	F	Average of squares	F
pH	5	5,76	20,56**	143,92	20,56**
Error	12	0,28		7,00	
General total	17				

**p<0.01

Table 3.4. Distilled water using different pH values in the non-agitated environment in the Erlenmayer effect of duckweed on the plant growth of Duncan test results.

pH	Number of plants per explant (pcs)	Total number of plants (pcs)
5	5,00a	10,00cd
6	3,80b	12,67c
7	2,53c	19,00b
7,23	2,00cd	25,00a
8	1,67cd	8,33cd
9	1,47d	7,33d

The difference between the means indicated by different letters in the same column is significant at the 0.01 level.

Table 3.5. Variation analysis of the effect of different pH values on the plant growth of duckweed in Erlenmayer in shaking environment.

V. R	D. F	Number of plants per explant (pcs)		Total number of plants (pcs)		Wet weight (g)		Dry weight (g)	
		A. S	F	A. S	F	A. S	F	A. S	F
pH	5	15,58	62,63**	1470,32	73,93**	0,03	65,02**	0,03	222,42**
Error	12	0,25		19,89		0,00		0,00	
General total	17								

**p<0.01

Table 3.6. Different pH values in the shaking environment of the effect of duckweed plant growth in Erlenmayer Duncan test results.

pH	Number of plants per explant (pcs)	Total number of plants (pcs)	Wet weight (g)	Dry weight (g)
5	0,63e	9,67d	0,04d	0,01c
6	1,26ed	12,67d	0,41d	0,13c
7	6,60a	66,00a	0,12a	0,07a
7,23	4,70b	47,00b	0,70b	0,55b
8	1,77d	17,67d	0,48cd	0,006d
9	2,93c	29,33c	0,05c	0,001d

The difference between the means indicated by different letters in the same column is significant at the 0.01 level.

3.4. Setting the amount of liquid MS (Murashige and Spoo basal medium) suitable for reproduction in temporary immersion system (TIS) bioreactors

After determining the appropriate pH for the plant, the studies were carried out to determine the appropriate MS and sugar concentrations in the liquid culture medium to be used for rapid propagation of the plants in the TIS bioreactor. TIS bioreactors to be used in the study were sterilized twice in each autoclave at 126 °C separately before being used despite any risk of contamination. Afterwards, 20 explants in TIS bioreactors were cultured in medium containing 1/4 MS, 1/2 MS, MS and 30 g sucrose for 1 week. Initially, 350 ml of liquid culture medium was used in the bioreactors, but after 2 weeks the plants in the bioreactor became completely white. It was observed that the plants did not get enough nutrients in 350 ml liquid culture and their development was insufficient.

3.5. Liquid MS medium optimization in TIS bioreactors

Lemna minor plant explants (40 pcs) were cultured in different MS liquid culture medium (400 ml) for 4

weeks. Then the data obtained were subjected to analysis of variance and the results are given in Table 3.7. As seen in Table 3.7, as a result of the analysis of variance in sugar and sugar-free MS, 1/2 MS and 1/4 MS liquid culture media, plant formation rate, number of plants per explant, total number of plants, pH change in terms of significant 0.01 level differences were found. Duncan test results to determine the significance level of these differences are given in Table 3.8. The rate of plant formation in the experiment ranged between 75.00% and 143.33%. The number of plants per explant was observed between 0.51 and 1.90. The maximum number of plant growths was obtained in 1.90, 1/4 MS sugar culture medium and the least plant number was 0.51 in MS 1/4 sugar free culture medium. The highest number of plants (38 pcs) was observed in liquid culture medium with 1/4 MS sugar and the lowest number of plants (15 pcs) was observed in 1/4 MS sugar free liquid culture medium. The effects of cultured explants on the pH of the environment were obtained at the lowest values of 4.88 and 5.66. The lowest change rate pH 4.88 value 1/4 MS sugar culture medium with the highest change rate pH 5.66 value was observed in MS sugar-free environment (Table 3.8).

Table 3.7. Analysis of variance of the effects of plant duckweed on different MS liquid culture media.

V. R	D. F	Number of plants per explant (pcs)		Total number of plants (pcs)		pH end state	
		A. S	F	A. S	F	A. S	F
Different MS medium	5	0,68	16,0**	224,72	61,28**	0,248	424,66**
Error	12	0,043		3,66		0,001	
General total	17						

**p<0.01

Table 3.8. Duncan test results of plant formation effects of duckweed of different MS liquid culture media.

Proportions of MS medium	Number of plants per explant (pcs)	Total number of plants (pcs)	pH end state
1/4 MS with sugar	1,90a	38,00a	4,88e
1/2 MS with sugar	1,43b	28,67b	4,90e
MS with sugar	1,25b	25,00c	5,10c
1/4 MS without sugar	0,51d	15,00d	5,22b
1/2 MS without sugar	1,18bc	23,67c	5,04d
MS without sugar	0,84cd	15,33d	5,66a

The difference between the means indicated by different letters in the same column is significant at the 0.01 level.

3.6. Application of TDZ (Thidiazuron) in different concentrations

In vitro experiment, duckweed plant explants (40) were cultured for 4 weeks in MS liquid culture media (400 ml) by adding different concentrations of TDZ hormone. The data obtained after 4 weeks were subjected to variance analysis and the results are given in Table 3.9. As shown in Table 3.9 as a result of

variance analysis of liquid MS culture medium in different concentrations of TDZ hormone application plant formation rate, number of plants per explant, total number of plants, wet weight and dry weight were found to be significant at the level of 0.01. Duncan test results to determine the significance level of these differences are given in Table 3.10. In this experiment, plant growth was observed in liquid culture MS medium treated with all TDZ hormones. Plant formation ranged

between 276% and 2274%. The number of plants per explant was obtained in liquid MS medium containing up to 50,74 units of 0.6 mg/L TDZ and in liquid nutrient medium containing 0.3 mg/L TDZ as minimum number of plants (8,99 units). Cultured explants showed that the least wet plants were 0.36 g in liquid MS medium containing 0.5 mg/L TDZ and the heaviest plants were found in liquid MS medium containing 1.80 g and 0.1 mg/L TDZ. These results reflected similarly in dry weight. The minimum dry weight in exsplant 0.03 g and

0.3 mg / L TDZ containing liquid nutrient medium and the maximum dry weight of 0.68 g 0.1 mg / L TDZ containing liquid medium was determined (Table 3.10). In the experiment, the protein ratios of the plants treated with different concentrations of TDZ were calculated. The highest protein content was 26.96% in liquid MS medium containing 0.2 mg/L TDZ. The lowest protein content was recorded in liquid MS medium containing 16.48% and 0.6 mg/L TDZ.

Table 3.9. The results of variance analysis of the effects of different concentrations of TDZ hormone application on plant growth of duckweed.

V. R	D. F	Number of plants per explant (pcs)		Total number of plants (pcs)			
		A. S	F	A. S	F		
TDZ hormone	5	164,225	31510**	262983,033	3,6980**		
Error	12	0,005		7,111			
General total	17						
V. R	D. F	Wet weight (g)		Dry weight (g)		Protein content (%)	
		A. S	F	A. S	F	A. S	F
TDZ hormone	5	0,757	621,896**	0,167	755,001**	82,112	157,55**
Error	12	0,001		0,00		0,02	
General total	17						

**p<0.01

Table 3.10. Duncan test results of the effects of different concentrations of TDZ hormone application on liquid culture MS medium to duckweed plant growth.

TDZ (mg/L)	Number of plants per explant (pcs)	Total number of plants (pcs)	Wet weight (g)	Dry weight (g)	Protein content (%)
0,1	23,74a	949,67a	1,80a	0,68a	26,25b
0,2	15,59b	624,67b	1,25b	0,51b	26,96b
0,3	8,99d	359,67d	0,99c	0,03f	22,35cd
0,4	9,13c	365,33c	0,90d	0,36c	23,31c
0,5	3,76f	150,67f	0,36f	0,16e	27,72a
0,6	50,47e	219,00e	0,63e	0,24d	16,48e

The difference between the means indicated by different letters in the same column is significant at the 0.01 level.

3.7.Bap (6-Benzylaminopurine) hormone application at different concentrations

In vitro experiments, duckweed plant explants (40 pcs) were cultured in MS liquid culture media (400 ml) for 4 weeks by adding BAP hormone at different concentrations. The data obtained after 4 weeks were subjected to variance analysis and the results are given in Table 3.11. As seen in Table 3.11 variance analysis results of liquid MS culture medium BAP hormone application in different concentrations of plant formation rate, the number of plants per explant, the total number of plants, wet weight and dry weight were found to be significant difference in the 0.01 level.

Duncan test results to determine the significance level of these differences are given in Table 3.12. In the experiment, plant growth was observed in liquid culture MS media where all BAP hormone applications were performed. Plant formation ranged between 220 and 4944.2%. The number of plants per explant was determined between 2.78 and 50.44 plants. The maximum number of plants was 50.44 in liquid MS medium containing 0.2 mg/L BAP and the least number of plants (2,78 pcs) in liquid MS medium containing 0.4 mg/L BAP. The total number of plants (2017,7 pcs) was obtained in liquid MS medium containing 0.2 mg/L BAP and at least 111.33 in liquid MS medium containing 0.4 mg/L BAP. Cultured explants had a

minimum wet weight of 0.15 g and were detected in liquid MS medium containing 0.4 mg/L BAP. The heaviest plants were 3.65 g and were detected in liquid MS medium containing 0.2 mg/L BAP. In the dry weight calculation of explants, the lightest plants (0.15 g) were obtained in liquid MS medium containing 0.1 mg/L BAP and the heaviest plants (0.7 g) were obtained in liquid MS medium containing 0.4 mg/L BAP (Table 3.12). In the experiment, protein ratios of plants with different concentrations of BAP were calculated. The highest protein content was 29.18% in liquid MS medium containing 0.5 mg/L BAP. The lowest protein

content was recorded in liquid MS medium containing 20.45% and 0.2 mg/L BAP.

3.8. Application of kinetin in different concentrations

In vitro experiments, plant explants of 40 duckweeds were cultured for 4 weeks in MS liquid culture media (400 ml) by adding different concentrations of kinetin hormone; Data obtained after 4 weeks were subjected to variance analysis and the results are given in Table 3.13.

Table 3.11. The results of variance analysis of the effects of different concentrations of BAP hormone administration on duckweed plant growth.

V. R	D. F	Number of plants per explant (pcs)		Total number of plants (pcs)			
		A. S	F	A. S	F		
BAP hormone	5	1072,713	103400**	1716315,689	104000**		
Error	12	0,010		16,500			
General total	17						
V. R	D. F	Wet weight (g)		Dry weight (g)		Protein content (%)	
		A. S	F	A. S	F	A. S	F
BAP hormone	5	6,824	20650**	0,019	264,459**	436,356	51700**
Error	12	0,000		0,000		0,05	
General total	17						

**p<0.01

Table 3.12. Duncan test results of the effects of different concentrations of BAP hormone application on liquid culture MS medium to duckweed plant growth.

BAP (mg/L)	Number of plants per explant (pcs)	Total number of plants (pcs)	Wet weight (g)	Dry weight (g)	Protein content (%)
0,1	3,99d	160,00d	2,89b	0,15d	28.43a
0,2	50,44a	2017,7a	3,65a	0,16d	20.45d
0,3	3,20e	128,33e	0,30e	0,21c	21.00d
0,4	2,78f	111,33f	0,15f	0,70e	27.72b
0,5	5,4c	217,00c	0,48d	0,24b	29.18a
0,6	5,62b	225,0 0b	0,66c	0,30a	26.18bc

The difference between the means indicated by different letters in the same column is significant at the 0.01 level.

As shown in Table 3.13 variance analysis results of liquid MS culture medium kinetin hormone application in different concentrations of plant formation rate, the number of plants per explant, the total number of plants, wet weight and dry weight were found to be significant differences in the 0.01 level. Duncan test results to determine the significance level of these differences are given in Table 3.14. In the experiment, plant growth was observed in liquid culture MS environments where all kinetin hormone applications were performed. Plant formation ranged between 186.67% and 5683.8%. The maximum number of plants per explant was 57,823 and

was obtained in liquid MS medium containing 0.05 mg/L kinetin and in liquid MS medium containing at least 2,86 0.15 mg/L kinetin. The total number of plants (2313,3) was observed in MS medium containing 0.05 mg/L kinetin and at least 114.67 in liquid MS medium containing 0.15 mg/L kinetin. The least wet weight of cultured explants was found to be 0.24 g in liquid MS medium containing 0.15 mg/L kinetin and the heaviest plants were detected in liquid MS medium containing 4.06 g 0.05 mg/L kinetin.

Table 3.13. Variance analysis of the effects of different concentrations of kinetin hormone application on duckweed plant growth.

V. R	D. F	Number of plants per explant (pcs)		Total number of plants (pcs)			
		A. S	F	A. S	F		
Kinetin hormone	5	1367,854	468300**	2189274,356	458200**		
Error	12	0,003		4,778			
General total	17						
V. R	D. F	Wet weight (g)		Dry weight (g)		Protein content (%)	
		A. S	F	A. S	F	A. S	F
Kinetin hormone	5	6,211	44040**	0,44	282,622**	683,927	234150**
Error	12	0,00		0,00		0,006	
General total	17						

**p<0.01

In the calculation of dry weight of explants, the lightest plants were observed in nutrient medium containing 0.02 g and 0.15 mg/L kinetin and the heaviest plants were observed in liquid MS medium containing 0.39 g and 0.1 mg/L kinetin. In the experiment, protein ratios of kinetin treated plants were calculated. The highest protein content was 26.96% and was observed in liquid MS medium containing 0.15 mg/L kinetin. The lowest protein content was recorded in liquid MS medium containing 0.2 mg/L kinetin at 23.18%.

Table 3.14. Duncan test results of the effects of different concentrations of kinetin hormone application on liquid culture MS medium duckweed plant growth.

Kinetin hormone (mg/L)	Number of plants per explant (pcs)	Total number of plants (pcs)	Wet weight (g)	Dry weight (g)	Protein content (%)
0,05	57,82a	2313,3a	4,06a	0,19d	24.68b
0,1	9,11b	364,67b	0,90b	0,39a	25.44ab
0,15	2,86f	114,67f	0,24f	0,02e	26.96a
0,2	6,90c	276,33c	0,70d	0,24c	23.18c
0,5	3,56e	142,67e	0,32e	0,19d	26.18a
0,6	6,67d	267,00d	0,79c	0,29b	26.84a

The difference between the means indicated by different letters in the same column is significant at the 0.01 level.

4. Discussion

The production of aquarium plants in Turkey is made in limited quantities. Aquatic plants in tissue culture work is done in a limited number of countries including Turkey. In this thesis, *Lemna minor*, one of the aquatic plants, is aimed to be propagated with temporary immersion system bioreactors. In this direction, the production limits of the plant are increased in a faster time than the natural conditions. Turkey from *Lemna minor* plant previously made on the very few studies about the availability of temporary system does not have to work with the micropropagation bioreactors. Generally, the studies have been carried out on the elimination of water pollution causing substances such as heavy metal wastes by using *Lemna minor* plant from water sources [19, 20]. Surface sterilization is one of the most important steps in tissue culture studies. When working with the green part of the plant, the chemicals to be applied to the explant for surface sterilization are very likely to damage the plant. Therefore, the chemicals to be used must be treated in the least amount and as soon as possible. Although there are many studies in the literature on the sterilization of land plants, there are not many studies on surface sterilization of aquatic plants. In this study, commercial bleach and H₂O₂ were used for sterilization and the best results were obtained by sterilizing 20% H₂O₂ for 8 minutes. Cook et al. [21] have used sulfuric acid and ethanol in surface sterilization of *Kosteletzkya virginica* seeds. Straub et al. [22] used bleach or ethanol for surface sterilization of *Phragmites australis* seeds. Agrawal and Ram [23] studied in vitro germination and micropropagation of water chestnut (*Trapa sp.*). After surface sterilization, the embryos were placed in NBS (basic semi-solid medium of Nitsch) to obtain plants. Simon and Helliwel [24] found that when the level of chlorophyll a with pure water is lower than pH 8, chlorophyll a rapidly converts to fiophytine a, but in the case where it is greater than pH 8, hydrolysis is found to

leave the phytol group. Studies were carried out to determine the appropriate pH range in surface sterilized plants. pH optimization for the plant took a long time. In order to make the optimization, the plants were placed in the distilled water in different pH levels and were observed in shaking and non-shaking conditions for 1 week. The material was placed in the shaker in the dark medium at 190 rpm and 28 ° C for shaking media. For the shaking environment, it was kept in the climatic chamber in the flasks for 1 week. As a result, the optimum pH range for the plant was determined to be 7.23 in shaking environment. In the experiment, it was observed that the number of plants in pH 8 and 9 was less than that of pH 7.23, and at pH values less than 7.23, it was observed that the plant could not develop and the growth did not occur. Therefore, it was determined that optimum pH range had an effect on plant growth. Similarly, Kim and Jang [25] used *Drosera peltata* micropropagation studies of pH 3.7, 4.7, 5.7 and 6.7 values and 3% (w/v) sucrose containing 1/2 MS medium used. They determined the optimum value for the micropropagation of the plant as pH 5.7. Perica and Berljak [26] found that pH is an effective factor in the micropropagation of *Drosera spatulata* Labill. Simola [27] found that the most effective value of *Drosera rotundifolia* L. in micropropagation is pH 6.00. After determining the appropriate pH for the plant, the studies were carried out to determine the appropriate MS and sugar

concentrations in the liquid culture medium to be used for rapid propagation of the plants in the TIS bioreactor. Plants were cultured in medium containing 1/4 MS, 1/2 MS, MS with 30 g sucrose and without sucrose in TIS bioreactors. According to the optimization results of the liquid culture medium, the best plant growth percentage (90%) and the total number of plant formation (38.00) were determined in the liquid culture medium with sugar 1/4 MS. It was determined that the chemical substances and concentrations of the liquid culture medium to be used were effective in the micropropagation of the plant. Similarly, Houllou-Kido et al. [28] *Nopalea cochenilifera* heterotrophic and photoautotrophic plant micropropagation have made. They added 3% (w/v) sucrose, 0.8% (w/v) agar, 1.0 mg/L BAP and 0.1 mg/L NAA to the MS medium to be used for micropropagation. At the end of their experiments, they found that in sucrose-containing media 10 times more micropropagation occurs than in non-sucrose-containing media. After determining the sugar and MS concentrations of the liquid culture medium, the effects of different doses of TDZ, BAP and kinetin on the rapid growth of the plant were determined. In the studies, it was observed that the number of plants per explant (57,823 units) and the total number of plants (2313,3 units) were obtained more than the BAP and TDZ applications in the application of kinetin at different rates (0.05-0.6 mg/L). Although the number of plants and reproduction rate were high, the

plants were found to be dull and unhealthy, and the plants were found to have hyperhydricity. In another study, TDZ was applied at different doses (0.1–0.6 mg/L) and the maximum number of plants (949.67 pcs) was recorded in liquid culture medium containing 0.1 mg/L TDZ. In the rapid amplification study with the addition of TDZ, although the number of plant propagations and percentage of plants per explant were high, it was observed that plants with lesser doses and smaller leaf sizes were formed than BAP at different doses. Then, BAP hormone was applied to the liquid culture media at different doses (0.1–0.6 mg/L). The maximum number of plants per explant (50.44 units) and the maximum total number of plants (2017.7 units) were obtained at a BAP concentration of 0.2 mg/L. All plants are green and healthy. In addition, no hyperhydricity was observed in plants. Obviously, different doses of plant growth regulators (BAP, kinetin and TDZ) applied in the scope of the study have been found to have effects on plant micropropagation. Micropropagation experiments without hormone supplementation showed no hyperhydricity, whereas hyperhydricity was observed in different concentrations of TDZ and kinetin in plants. This is due to the presence and concentration of some plant growth regulators. In this study, in order to determine the effects of different cytokinin concentrations on the protein content of the plants, microcoproduced dried plants were determined protein and nitrogen by Kjeldahl method. In literature studies, it was not found that protein and nitrogen were determined in *Lemna minor* plant by this method. In the determination of protein with the plant samples taken from the medium where plant growth regulators were added in the experiments, the amount of 29.18% protein in the plants obtained as a result of 0.5 mg/L BAP application, the amount of protein as 27.72% as a result of 0.5 mg/L TDZ application and as a result of the application of 0.15 mg/L kinetin protein amount was determined as 26.96%. Stewart et al. [29] carrot (*Daucus carota* L.) in the in vitro study carried out in plants developed in the bioreactor due to lack of oxygen have found a negative effect on root elongation. In order to overcome this problem and maintain the O₂ balance in the environment, the explants were cultured in auxophyton containing bioreactors and continuous air intake was provided and positive effects were observed in root elongation. It was recorded that the weight of the plant increased 2.6 times after 20 days. Escalant et al. [30] carried out micropropagation of banana plant with temporary immersion system bioreactors and compared the results obtained with the micropropagation test results of banana plant in solid food medium using agar. In the explants cultured in TIS bioreactor, the number of somatic embryos formed after 2 months was recorded as 1375 and the number of embryos in agar containing solids was 450. As a result, the percentage of plant growth in micropropagation by bioreactor application was 3.05 times higher than the percentage of plant growth in micropropagation in agar medium.

As a result, the propagation of *Lemna minor* plant with temporary immersion system bioreactors was carried out successfully and the plant was produced in a shorter time and more number than the natural environment. The negative risks that may occur during the production phase have been completely eliminated under laboratory conditions and production has been carried out in a controlled manner. It was determined that plant growth regulators used during micropropagation did not have a negative effect on plant protein ratio and it was seen that it caused an increase in the protein ratio of the plant. Even though in recent years has accelerated studies on aquatic plants are considered to be especially important open about the work in this field in Turkey. Therefore, especially tissue culture studies with aquatic plants are very important. It is thought that this study carried out with *Lemna minor* plant will contribute to the rapid and intensive production of aquatic plants and will contribute to future aquatic plant biotechnology studies.

Author's Contributions

Ethics

There are no ethical issues after the publication of this manuscript.

References

1. Bornette G and Puijalón S (2011). Response of aquatic plants to abiotic factors: a review. *Aquat. Sci.*, 73:1–14. doi: 10.1007/s00027-010-0162-7
2. Khataee AR, Movafeghi A, Torbati S, Salehi Lisar SY, Zarei M (2012). Phytoremediation potential of duckweed (*Lemna minor* L.) in degradation of C.I. Acid Blue 92: Artificial neural network modeling. *Ecotoxicol. Environ. Saf.*, 80:291–298
3. Wang WC and Freemark K (1995). The use of plants for environmental monitoring and assessment. *Ecotoxicol. Environ. Saf.*, 30: 289-301
4. Steven MD, Egbert H van N, Rudi MMR (2005). Growth limitation of *Lemna minor* due to high plant density. *Aquat. Bot.*, 81: 245–251
5. Rusoff LL, Blakeney Jr. EW, Culley Jr. DD (1980). Duckweeds (*Lemnaceae* family): a potential source of protein and amino acids. *J. Agric. Food Chem.*, 28(4): 848-850
6. Nayyef MA and Amal AS(2012). Efficiency of duckweed (*Lemna minor* L.) in phytotreatment of wastewater pollutants from basrah oil refinery. *J. of Appl. Phytotech. in Environ. Sanitation*, 1 (4): 163-172
7. Uysal Y (2013). Removal of chromium ions from wastewater by duckweed, *Lemna minor* L. by using a pilot system with continuous flow. *J. Hazard. Mater.*, 263: 486–492
8. Cox KM, Sterling DJ and Regan JT (2006).Glycan optimization of a human monoclonal antibody in the aquatic plant *Lemna minor*. *Nat. Biotechnol.*, 12: 1591–1597
9. Brown DCW and Thorpe TA (1995). Crop improvement through tissue culture. *World Journal of Microbiology and Biotechnology*, 11: 409–415
10. Khvatkov P, Chernobrovkina M, Okuneva A, Dolgov S (2019). Creation of culture media for efficient duckweeds micropropagation (*Wolffia arrhiza* and *Lemna minor*) using artificial mathematical optimization models. *Plant Cell Tiss Org Cult* 136: 85–100
11. Etienne H, Berthouly M (2002).Temporary immersion systems in plant micropropagation. *Plant Cell Tiss. Org. Cult.*, 69: 215–231
12. Aitken-Christie J and Davies HE (1988). Development of a semi-automated micropropagation system. *Acta Hort.*, 230, 81-88 doi: 10.17660/ActaHortic.1988.230.7
13. Harris RE and Mason EBB (1983). Two machines for in vitro propagation of plants in liquid media. *Can. J. Plant Sci.*, 63(1): 311-316, doi: 10.4141/cjps83-032
14. Yenice Z (2010). Micropropagation of common duckweed (*Lemna minor* L.) plants using temporary immersion system bioreactors. Master Thesis, Ankara University Biotechnology Institute, Ankara, Turkey
15. Bradstreet RB (1954). Kjeldahl method for organic nitrogen. *Anal. Chem.*, 26(1): 185-187 doi: 10.1021/ac60085a028
16. Snedecor GW and Cochran WG (1967) *Statistical Methods*. 6th edn. Ames Iowa, Iowa State University Press
17. Scott AJ and Knott M (1974). A cluster analysis method for grouping means in the analysis of variance. *Biometrics*, 30: 507-512
18. Duncan DB (1955). Multiple range and multiple F tests. *Biometrics*, 11:1-42
19. Artan RO (2007). Use of duckweed (*Lemna* sp) for further treatment of heavy metal containing wastewater. Master's thesis. Çukurova University. Institute of Science. Adana, Turkey
20. Memmon A (2008). Elimination of Oil, Hydrocarbon and Pollution by Plant, Algae and Microorganisms. *Science and Technology*, January number, p 7-8
21. Cook DA, Decker DM and Gallagher JL (1989). Rejuvenation of *Kosteletzkya virginica* (L.) Presl. (Seashore Mallow) from callus cultures. *Plant Cell Tiss Org Cult.*, 17; 111-119
22. Straub PF, Decker DM and Gallagher JL (1988). Tissue culture and long-term regeneration of *Phragmites australis* (Cav.) Trin. Ex Steud. *Plant Cell Tiss Org Cult.*, 15; 73-78
23. Agrawal A and Mohan Ram HY (1995). In vitro germination and micropropagation of water chestnut (*Trapa* sp.). *Aquatic Botany*, 51; 135-146
24. Simon D and Helliwell S (1998). Extraction and quantification of chlorophyll a from freshwater green algae, *Wat. Res.*, 32:2220-2223
25. Kim KW and Jang GW (2004). Micropropagation of *Drosera peltata*, a tuberous sundew, by shoot tip culture. *Plant Cell Tiss Org Cult.*, 77: 211–214
26. Perica MC and Berljak J (1996). In vitro growth and regeneration of *Drosera spatulata* Labill on various media. *Hortscience* 31: 1033–1034
27. Simola LK (1978). The effect of several amino acids and some inorganic nitrogen sources on the growth of *Drosera rotundifolia* in long and short-day condition. *Z. Pflanzenphysiol.* 90: 61–68
28. Houllou-Kido LM, Costa AF, Lira MA, Farias I, Santos DC, Silva KS, Rivas R, Dias ALF, Alves GD (2009).Viability of *Nopalea*



cochenilifera (cv. Ipa Sertânia) photoautotrophic micropropagation. VI International Congress on Cactus Pear and Cochineal. Acta Hort., 811:309-314, doi: 10.17660 / Acta Hort. 2009.811.42

29. Steward FC, Caplin S & Millar FK (1952). Investigations on growth and metabolism of plant cells. I. New techniques for the investigation of metabolism, nutrition and growth in undifferentiated cells. Ann. Bot. 16: 57–77

30. Escalant JV, Teisson C, Cote F (1994). Amplified somatic embryogenesis from male flowers of triploid banana and plantain cultivars (Musa spp). In Vitro Cell. Dev.Biol.30:181-186.